Im Fachbereich Physik der Freien Universität Berlin eingereichte Dissertation.

Ultrafast hot carrier driven magnetization dynamics

by

Alexandr Alekhin

2015

Die vorliegende Arbeit wurde im Zeitraum von Februar 2011 bis Oktober 2015, im Fritz-Haber Institut der Max-Planck Gesellschaft unter der Betreuung von Prof. Dr. Martin Wolf, angefertigt.

Berlin, Oktober 2015

1. Gutachter: Prof. Dr. Martin Wolf

2. Gutachter: Prof. Dr. Martin Weinelt

Datum der Disputation: 04.02.2016

Abstract

This work investigates ultrafast magnetization dynamics driven by hot carrier (HC) transport in metallic multilayer (ML) structures using femtosecond time-resolved linear and nonlinear optical spectroscopy. The linear magneto-optical Kerr effect (MOKE) and magneto-induced second harmonic (SH) generation (mSHG) have been utilized to study optically induced spin dynamics in highly excited state of matter with 20-femtosecond (fs) time resolution approaching the time scales of underlying elementary processes in metals. The spin transfer from a ferromagnet to a noble metal or from one ferromagnet to another one through a non-magnetic spacer by means of HC transport is of particular interest in this thesis. Investigation of these effects is of great importance for understanding of ultrafast spin dynamics and has a potentially high impact on future spintronic devices. Epitaxial Au/Fe/MgO(001) and Fe/Au/Fe/MgO(001) structures have been used as basic model systems, where in the latter case one Fe layer serves as a spin-emitter and another Fe layer serves as a spin-collector.

As a first step towards understanding of the spin transfer in metallic MLs, HC transport has been investigated in simpler two-layer Au/Fe/MgO(001) structures. It has been shown that pumping the Fe film through a transparent MgO substrate leads to the generation of a spin current (SC) flowing from the ferromagnetic film into the non-magnetic layer. This phenomenon is an analog of the spin Seebeck effect, but in this case the SC is dominated by non-equilibrium (NEQ) HCs propagating in Au in a quasi-ballistic regime. According to the first principle quantum transport calculation, the emission of majority electrons from the Fe film into the Au layer is much more efficient than the emission of other HCs, which provides a net flux of the positive SP into the bulk of Au. Quantitative analysis of the MOKE signals, measured from the Fe side of Au/Fe/MgO(001) structures with different Fe thicknesses, reveals a considerable contribution of the HC transport to ultrafast demagnetization of the Fe film, followed by a build-up of transient magnetization in the Au layer which also contributes to the MOKE signal.

Finally, magnetization dynamics induced in a ferromagnet by the injection of the spin-polarized HCs has been studied on three-layer Fe/Au/Fe/MgO(001) structures. Owing to different coercitivities of the Fe films, the magnetizations in the spin-emitter and the spin-collector can be aligned parallel, antiparallel or orthogonal to each other. For the orthogonal alignment, it has been demonstrated that the optically-driven SC pulse excites standing spin waves in the spin-collector via the spatially non-uniform spin transfer torque (STT) mechanism. Realization of different mutual orientations of the external magnetic field and the magnetizations in the spin-emitter and the spin-collector makes it possible to disentangle STT from laser-induced heating of the sample. Moreover, in the analysis of the mSHG response measured in different magnetic geometries it has been undoubtedly proven that the SC pulse gives rise to the SH field originating in the bulk. All data are in a good agreement with the experimental results obtained on two-layer structures and sustains the model of spin-polarized HC transport.

Deutsche Kurzfassung

Diese Arbeit umfasst die Untersuchung der ultraschnellen Magnetisierungsdynamik durch Transport heißer Ladungträger (HC) in metallischen Multilayer(ML)-Strukturen anhand zeitaufgelöster linearer und nichtlinearer optischer Femtosekundenspektroskopie. Der lineare magneto-optische Kerr-Effekt (MOKE) und die magnetisch induzierte Erzeugung der zweiten Harmonischen (mSHG) wurden verwendet, um lichtinduzierte Spindynamik in hoch angeregten Zuständen der Materie mit 20 Femtosekunden (fs) Zeitauflösung zu untersuchen, was den Zeitskalen zugrundeliegender Elementarprozesse in Metallen entspricht. Der Spintransfer von einem Ferromagneten zu einem Edelmetall, oder von einem Ferromagneten zum anderen Ferromagneten mittels HC-Transport durch eine nichtmagnetische Zwischenschicht hindurch ist von besonderem Interesse in dieser Arbeit. Untersuchungen dieser Effekte sind von großer Bedeutung für das Verständnis der ultraschnellen Spindynamik, und die gewonnenen Erkenntnisse haben möglicherweise einen großen Einfluss auf zukünftige Spintronik-Geräte. Als Modellsysteme wurden epitaktische Au/Fe/MgO(001) und Fe/Au/Fe/MgO(001) Strukturen verwendet, wobei im letztgenannten Fall eine Fe-Schicht als Spinemitter und die andere Fe-Schicht als Spinkollektor dient.

Als erster Schritt zum Verständnis des Spin-Transfers in metallischen MLs, wurde der HC Transport in einfachen Zweischicht-Au/Fe/MgO(001)-strukturen untersucht. Es wurde gezeigt, dass die optische Anregung von Fe zur Erzeugung eines Spin-Stroms führt, der von der ferromagnetischen Schicht in die nicht-magnetische Schicht fließt. Dieses Phänomen ist ein Analogon zum Spin-Seebeck-Effekt, wobei in diesem Fall der Spin-Strom in Gold von nicht-gleichgewichts HCs dominiert wird, die sich im quasi-ballistichen Regime bewegen. Die quantitative Analyse der MOKE Signalen, die von der Fe-Seite der Au/Fe/MgO(001)-Strukturen mit unterschiedlichen Fe-Dicken gemessen wurden, zeigt den bemerkbaren Beitrag des HC-Transports zur ultraschnellen Entmagnetisierung des Fe-Films, gefolgt von einer vorübergehenden Magnetisierung der Au-Schicht, die zusätzlich zum MOKE Signal beiträgt.

Abschließend wurde Magnetisierungsdynamik, die in einem Ferromagneten mittels der Injektion von spinpolarisierten HCs induziert wird, an Dreischicht-Fe/Au/Fe/MgO(001)-strukturen untersucht. Aufgrund unterschiedlicher Koerzitivkräfte in den Fe-Filmen können die Magnetisierungen im Spinemitter und im Spinkollektor parallel, antiparallel oder orthogonal zueinander ausgerichtet werden. In der orthogonalen Ausrichtung zeigt es sich, dass der optisch erzeugte Spinstrompuls stehende Spinwellen im Spinkollektor erzeugt, die durch das räumlich inhomogen Spin-Transfer-Drehmoment (STT) induziert werden. Die Realisierung verschiedener gegenseitigen Orientierungen der äußeren Magnetfeldes und der Magnetisierungen im Spin-emitter und im Spin-kollektor ermöglicht es, das Signal des STT unabhängig vom Signal der laserinduzierter Erwärmung der Probe zu messen. Außerdem in der Analyse der mSHG-Antwort, die in verschiedenen magnetischen Geometrien gemessen wurde, kann es deutlich bewiesen werden, dass der Spinstrompuls resultiert im SH-Feld, das im Volum erzeugt wird. Alle Daten zeigen eine gute Übereinstimmung mit den erhaltenen Versuchsergebnissen der Zweischichtstrukturen und untermauern somit das Modell des spinpolarisierten HC-Transports.

Contents

Chapter 1

Introduction and Motivation

1.1 Why study ultrafast spin dynamics

Since the invention of the integrated circuit in 1958 by Jack S. Kilby [1, 2] electronic device fabrication has come a long way from a feature size of the circuit elements above 10 microns to about few tens of nanometers in the most modern prototypes. In August 2014 Intel announced details of the 14-nm technology [3]. During the last ten years development of material processing and significant increase of the number of transistors per chip made it possible to sustain 60% annual growth of the general-purpose computing capacity [4]. However, the smaller the device gets, the harder it becomes to combine high performance, stability and power efficiency. The data storage is one of the variety of information technologies which have to deal with this problem.

Fast growth and development of cloud services, social networks, data bases and computational facilities have changed priorities of the companies specialized in the production of storage devices. Because of large power costs, huge amount of transient data and demand for higher performance and instant access, for such applications non-volatility, high reliability and low latency become the most important factors. Nowadays there are three most perspective low latency memories: Phase Change Memory (PCM or PRAM), Magnetoresistive Random-Access Memory (MRAM) and Spin-Transfer-Torque Magnetic Random Access Memory (STT-MRAM). In Table 1.1 general characteristics of these three storage devices are shown in comparison with other memory technologies: static RAM (SRAM), dynamic RAM (DRAM), flash memory (NAND), ferroelectric RAM (FeRAM). PRAM is a very strong candidate to replace flash memory due to high density and low cost per bit. However, limited endurance and long write/erase time make it unsuitable as a universal memory. MRAM devices are fast and non-volatile, but they use Oersted field to switch bits from one state to another. It works well for large bit sizes, but when the bit size gets smaller, larger magnetic fields and consequently larger currents are required to switch magnetization in one bit, resulting in higher power consumption.

	SRAM	DRAM	Flash (NAND)	FeRAM	MRAM	PRAM	STT-MRAM
Non-volatile	No	No	Yes	Yes	Yes	Yes	Yes
Cell size (F^2)	50-120	6-10	5	15-34	16-40	6-12	6-20
Read time (ns)	1-100	30	50	20-80	3-20	20-50	2-20
Write/Erase time (ns)	1-100	50/50	1 ms/0.1 ms	50/50	3-20	50/120	2-20
Endurance	10^{16}	10^{16}	10^5	10^{12}	$> 10^{15}$	10^{10}	$> 10^{15}$
Write power	Low	Low	Very high	Low	High	Low	Low
Other power consumption	Current leakage	Refresh current	None	None	None	None	None
High voltage required	No	2 V	16-20 V	2-3 V	3 V	1.5-3 V	0.15 V

Table 1.1: Comparison of different types of storage devices [5]. See description in the text. Cell size is given in units of F^2, where F usually represents the metal line width $\sim 3 - 4$ nm.

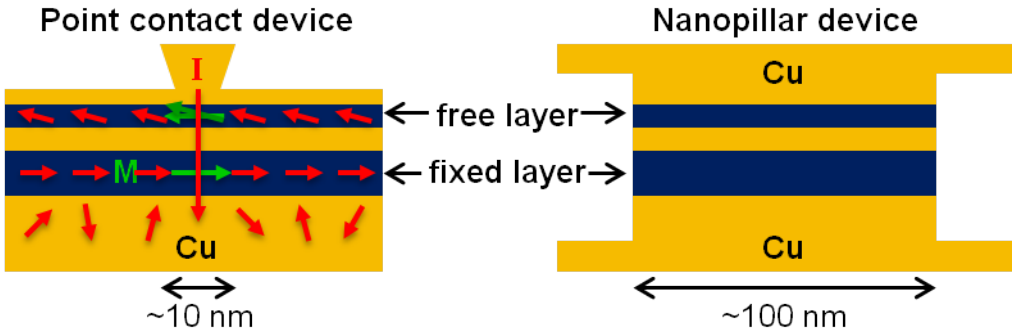

Figure 1.1: Example of STT-MRAM devices: a point contact and nanopillar devices which consist of two ferromagnetic layers, separated by non-magnetic Cu spacer. Green arrows depict magnetizations of the fixed and free ferromagnetic layers. Long red arrow depicts the direction of the current flowing through the ML structure, assuming that it corresponds to the motion of the positive charge. Small red arrows depict SP of the electrons. Initially the electrons in the bottom Cu layer have disordered spin, but when they propagate through the fixed ferromagnetic layer, their spins are aligned parallel to its magnetization. Then the spin-polarized electrons reach the free ferromagnetic layer, where their spins become aligned parallel to its magnetization. On the other hand, due to the conservation of the angular momentum the magnetization of the free ferromagnetic layer tilts towards the magnetization of the fixed ferromagnetic layer and starts to precess afterwards. This figure is redrawn after [10].

STT-MRAM is the next development of the MRAM technology, which uses spin-polarized currents instead of magnetic fields. STT-MRAM device is based on a ML structure, which consists of two ferromagnetic layers with fixed and free magnetization, separated by a non-magnetic spacer (see Figure 1.1). Upon applying electric current through the structure, the fixed ferromagnetic layer serves as a spin filter and generates spin-polarized electric current: magnetic moments of electrons passing through the fixed ferromagnetic layer become aligned parallel to its magnetization. In 1996 Slonczewski [6] and Berger [7] predicted theoretically that current of spin-polarized electrons can transfer its angular momentum to the free ferromagnetic layer and thereby exert a torque on its magnetization. It is a STT (the STT mechanism will be discussed in **Chapter 2**) which drives precession of the magnetization of the free ferromagnetic layer and eventually can switch it parallel or antiparallel to the magnetization of the fixed ferromagnetic layer, depending on the direction of the electrical current. In 1999 Myers employed a sample geometry suggested by Slonczewski [8] to observe the STT-driven magnetization reversal in a stack of two Co layers, separated by a Cu spacer [9]. Typical current densities to induce magnetization reversal are $10^8 - 10^9 A/cm^2$ in point-contact devices and $< 10^7 A/cm^2$ in nanopillar devices [10]. In a few years after the first observations of the current-induced magnetization reversal, time-domain experiments [11–13] including scanning transmission x-ray microscopy [14, 15] were employed to study spin transfer switching driven by electrical current pulses of several hundreds of picoseconds (ps). Recently even laser-induced transfer of spin angular momentum has been demonstrated in MLs [16, 17]. Schellekens et al. reported that optically induced SC pulse can tilt the magnetization of a thin ferromagnetic film and launch its precessional motion [17]. However, magnetization dynamics observed in [17] is limited by the zero standing spin wave mode corresponding to the homogeneous precession of the magnetization $k_0 = 0$, and it was not possible to disentangle the magnetization dynamics induced by laser heating and the HC spin current pulse directly from the experimental results, which made the analysis more complicated. In 2002 Kampen et al. demonstrated two lowest standing spin modes ($k_0 = 0$ and $k_1 = \pi/d$, where d is the film thickness) excited in a permalloy film by a non-homogeneous laser heating [18]. In general, due to stronger localization in space and time, the laser-induced SC pulse is expected to excite higher standing spin wave modes than the laser heating. One of the possible reasons for the absence of the first standing spin wave mode in the experiments performed by Schellekens et al. [17] is that the thicknesses of the ferromagentic films were too small and comparable to the inelastic mean free path of the majority electrons (~ 5 nm [19]).

All theoretical and experimental studies of the STT and STT-induced magnetization dynamics emphasize the role of the spin- and energy-dependent reflection and transmission of the interface between a non-magnet and a ferromagnet [20, 21]. For this reason, the character of the SC (ballistic or diffusive) flowing from one ferromagnet to another is also important, especially for epitaxial MLs with a well-defined energy band structure. Regarding laser-induced SC pulses and SC-induced magnetization dynamics, the present work was motivated by the following questions:

- Which scattering processes are relevant for the transport of spin-polarized HCs?

- What kind of spin dynamics can be induced in the ferromagnetic film by the injection of spin-polarized HCs?
- What are the mechanisms governing this spin dynamics?
- How important is the ballistic character of the HC transport?

In addition to already mentioned SC-induced spin dynamics, laser-induced transport of spin-polarized HCs is of particular interest as a candidate for the origin of ultrafast laser-induced demagnetization [22–24]. One of the main break-through in this field of the magnetization dynamics is the discovery of subpicosecond demagnetization of a thin Ni film in 1996 [25]. These experiments performed by Beaurepaire et al. started a new quest which is troubling scientists even today:

- What is the origin of ultrafast laser-induced demagnetization?

Since then ultrafast laser-induced magnetization dynamics has been observed in a huge variety of magnetic systems, but mechanisms of underlying processes are not well-understood yet. Complexity of different theoretical models and interpretation of the experimental results is related to the fact that a femtosecond laser pulse brings the system in a highly excited state, where magnetic phenomena can not be described in terms of thermodynamics and conventional approximations applied for systems in equilibrium [26]. Besides that, depending on a studied system, several mechanisms may compete with each other. In order to disentangle their influence on the observed magnetization dynamics, further systematic studies are required.

The present thesis addresses all mentioned fundamental challenges with the investigation of the optically induced HC transport in epitaxial metallic MLs. Epitaxially grown sample ensures well-defined structure of the films and the interfaces between them, which simplifies modelling and comparison of the experimental results with ab-initio calculations. The next section gives an overview of the experimental approach.

1.2 Experimental approach

Experimental approach presented here is based on the idea used in STT-MRAM devices, but instead of applying electric current, spin transfer is induced by optically excited HC transport. Basic ML structure is a Fe/Au/Fe structure grown epitaxially on a MgO(001) substrate (see Figure 1.2). Due to the exchange-split energy band structure of a ferromagnet, HCs with different SPs, excited in the first Fe layer (spin-emitter) by the pump laser pulse, have different binding energies, velocities and lifetimes. After the excitation HCs propagate through the non-magnetic Au spacer into the second Fe layer (spin-collector), where they induce variations of the magnetization, which were probed using linear and nonlinear optical spectroscopy. Typical Au thickness is several tens of nanometers. It ensures decoupling of the two Fe layers and suppresses direct interaction of the pump laser pulse with the spin-collector, which is a distinct advantage in comparison with the experiments performed by Schellekens [17], where total thickness of the samples was about 10 nm.

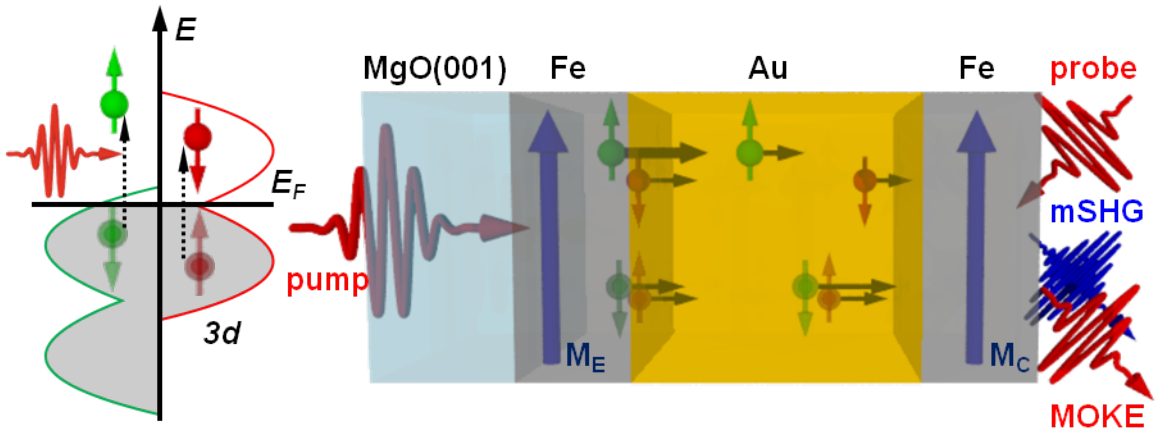

Figure 1.2: Experimental geometry. Optical pumping of the first ferromagnetic layer (spin-emitter) leads to the excitation of majority (non-transparent green balls) and minority (non-transparent red balls) electrons to the states with different binding energies due to the exchange-split d-bands of Fe. Majority electrons and minority holes (transparent red balls) carry positive SP with respect to the magnetization M_E of the spin-emitter, while minority electrons and majority holes (transparent green balls) are responsible for the transport of the negative SP. After the excitation spin-polarized HCs are injected into the non-magnetic Au spacer, where they form spin current pulse. Upon the arrival to the interface between the Au spacer and the second ferromagnetic layer (spin-collector), spin-polarized HCs induces variations of the magnetization M_C, monitored by the transient MOKE and mSHG signals.

In order to distinguish the role of the HC transport in ultrafast demagnetization, first experiments were performed on a 8-nm polycrystalline Fe film grown on a MgO(001) substrate and capped with 3 nm of MgO (see Figure 1.3(a)). For such system laser absorption profile is more or less homogeneous, leading to a uniform HC distribution which in turn ensures the absence of the HC transport. It makes possible to disentangle contributions of the state-filling effects and the magnetization dynamics to the measured signals.

As the next step, the MgO cap layer was replaced with Au which serves as a sink of the spin-polarized HCs excited in Fe (see Figure 1.3(b)). In this case epitaxial growth of the two-layer Fe/Au structures increases the efficiency of the spin injection from the Fe film into the Au layer and ensures well-defined structure which simplifies modelling of the ballistic HC transport, based on the results of the ab-initio calculations. Using a self-consistent 4x4 matrix method developed in [27, 28] together with the knowledge of the spatial HC distributions, one can simulate changes of the magneto-optical response occurring upon laser excitation of the Fe film. Dependence of the transient MOKE and mSHG signals on the Fe thickness d_{Fe} (samples were probed through the MgO substrate) and comparison with the results obtained on the polycrystalline thin Fe

film revealed considerable role of the HC transport in ultrafast demagnetization and allowed us to estimate its efficiency. It has been concluded that the emission of the majority electrons is much more efficient than the emission of other HCs. This result is in a good agreement with ab-initio calculations of the inelastic mean free path λ_{Fe}^{HC} in Fe and the transmission $T_{Fe\rightarrow Au}^{HC}$ of the Fe/Au interface.

After the injection from the Fe film, spin-polarized HCs continue to propagate further into the bulk of the Au layer. Pumping the Fe film and probing the Au side of the Au/Fe/MgO(001) structures with different Au thicknesses, it can be observed that the laser-induced SC pulse is formed predominantly by the majority electrons propagating in Au in a quasi-ballistic regime. In the static regime the mSHG can be considered as a purely surface/interface-sensitive technique. After the optical excitation of Fe, transport of the spin-polarized HCs may give rise to HC-current- and SC-induced SH fields originating in the bulk of the Fe and Au films. Nevertheless, analysis of the mSHG data allows us to monitor arrival of the spin-polarized HCs at the Au surface, thereby realizing a time-of-flight-like experiment (see Figure 1.3(b)). The Fe thickness d_{Fe} also plays a very important role for the HC transport in Au: the ratio between the light penetration depth, the inelastic mean free path, and the Fe thickness d_{Fe} determines the ratio between the optically excited HCs, injected into the Au layer in the ballistic regime, and the secondary HCs.

According to the initial idea of this work presented in Figure 1.2, the final stage of the spin-polarized HCs transport is a HC propagation through the Au/Fe interface into the second Fe layer. Typical Au thickness d_{Au} is several tens of nanometers and the influence of the spin-collector on the HC excitation and the HC emission from the spin-emitter into the Au spacer can be neglected, therefore the experimental results obtained on the two-layer Au/Fe/MgO(001) structures can be applied for the analysis of the magnetization dynamics induced in the spin-collector by the spin-polarized HCs. In order to monitor incoherent magnetization dynamics in the linear and non-linear optical responses, when the SC pulse leads only to the absolute changes of $\vec{M}_C$, one has to realize 8 different mutual orientations of $\vec{M}_E$ and $\vec{M}_C$: two parallel and two anti-parallel magnetic configurations, when both magnetizations in the spin-emitter and spin-collector are either perpendicular to the plane of incidence – transversal magneto-optical geometry, or parallel to the plane of incidence and the film surface – longitudinal magneto-optical geometry (see Figure 1.4(a)) . In all these magnetic configurations HCs emitted from the first Fe layer are either majority or minority with respect to $\vec{M}_C$, and their transport leads to the change of the relative concentration of the majority and minority electrons in the second Fe layer, which is referred in this work as incoherent dynamics. In the previous section it was discussed that the transport of the spin-polarized HCs can lead to the STT effects, which is referred as coherent dynamics. In order to maximize the STT effects, the magnetizations $\vec{M}_E$ and $\vec{M}_C$ should be aligned perpendicular to each other (see Figure 1.4(b)). In this case there are also 8 orthogonal magnetic configurations.

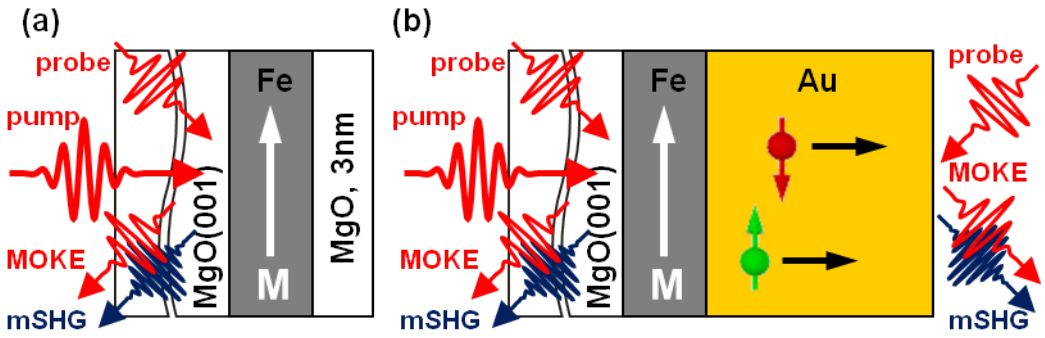

Figure 1.3: Experimental geometries to study (a) ultrafast demagnetization of a 8-nm polycrystalline Fe film in the absence of HC transport, and (b) injection of spin polarized HCs from the Fe film into the Au layer of the epitaxial Au/Fe/MgO(001) structure. In both cases samples were pumped through the MgO substrate. However, Au/Fe/MgO(001) samples were probed either from the back side side to observe HC emission from the Fe film or from the front side to monitor HC transport in Au

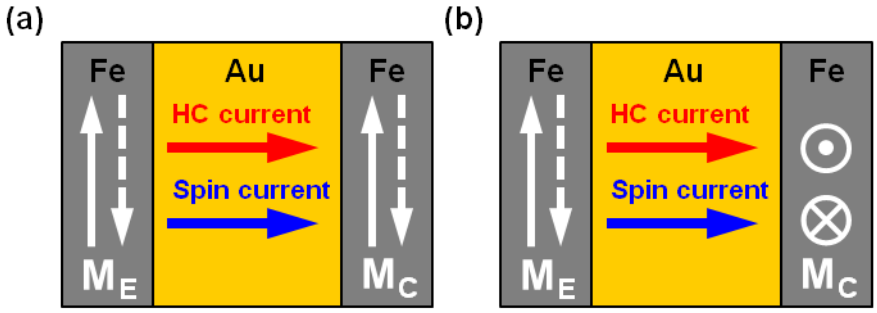

Figure 1.4: Experimental geometries to study spin dynamics induced in the Fe film by the injection of spin-polarized HCs. Optical pumping of the first Fe layer (spin-emitter) leads to emission of spin-polarized HCs into the Au layer, where they form SC pulse, propagating towards the second Fe layer (spin-collector). When M_E is parallel or antiparallel to $\vec{M}_C$ (a), the STT is negligibly small and one can observe only absolute variations of $\vec{M}_C$ (incoherent dynamics), while for the orthogonal alignment of $\vec{M}_E$ and $\vec{M}_C$ (b), the STT can induce standing spin waves in the spin-collector (coherent dynamics).

1.3 Scope of this thesis

After general introduction, magnetism and magnetization dynamics in metals and metallic MLs will be discussed in **Chapter 2**. It starts with properties of the itinerant 3d ferromagnets (Fe, Co, Ni): the origin of ferromagnetism, itinerant behavior and electron density of states. Then processes occurring in metals and metallic MLs upon laser excitation are considered together with experimental works devoted to laser-induced ultrafast HC and magnetization dynamics. In this overview characteristic time constants obtained with different experimental techniques for Fe, Co and Ni, and their dependence on experimental conditions are discussed together with microscopic and phenomenological models describing the observations. Special attention is devoted to superdiffusive spin transport. The last section of **Chapter 2** is devoted to precessional magnetization dynamics and stimuli which can induce it.

In **Chapter 3**, magneto-optical pump-probe techniques for investigation of ultrafast non-local spin dynamics are introduced. The MOKE and the mSHG are discussed in terms of phenomenological description and microscopic formalism. In the last section of **Chapter 3** these two techniques are considered as a tool to probe HC and spin dynamics. In spite of apparent simplicity there are some challenges in correct interpretation of the experimental data, related to the appearance of so-called 'optical artefacts', contributions from different parts of the ML structure to the linear and non-linear magneto-optical signal.

Pump-probe experimental setup and details concerning samples and data analysis are presented in **Chapter 4**. It starts with a brief description of the Coherent Mantis Laser system with cavity dumper as a source of 14-fs laser pulses with central wavelength 820 nm. Then it proceeds with a description of the experimental setup and studied samples. Some special features of the experiments using ultrashort laser pulses are discussed. Further I provide experimental details for the MOKE and mSHG measurements: MOKE detectors with balanced photodiodes, different magneto-optical geometries.

Chapter 5 presents experimental results obtained on a 8-nm polycrystalline Fe film. Owing to homogeneous laser absorption profile and nonconducting MgO substrate and cap layer, the HC spatial distribution is uniform, which allows us to neglect the HC transport. In this case it is possible to evaluate real transient magnetization and disentangle its contribution to the MOKE rotation and ellipticity signals from the variation of the magneto-optical constants. Observed demagnetization of the Fe film occurs on the time scale of approximately 200 fs only due to the spin-flip processes. This time appeared to be close to the characteristic time of the electron thermalization, meaning that ultrafast demagnetization is mostly dominated by the NEQ HCs.

Results presented in **Chapter 5** have been used for the analysis of the HC injection from the Fe film into Au, discussed in **Chapter6**. Pump-probe experiments have been performed on the Au/Fe/MgO(001) structures probing and pumping the Fe side of the samples. Static MOKE data are in a good agreement with theoretical calculations according to the method described in **Chapter 3**. Simple model of the ballistic HC transport has been developed to estimate demagnetization of the Fe film and evaluate the magneto-optical constant of Au. Analysis of the transient MOKE signals reveals

considerable role of the HC transport in the ultrafast demagnetization of the Fe film.

In **Chapter7** it is demonstrated that the HC injection from the Fe film into the Au layer results in the SC pulse with a steep leading part, formed by the optically excited HCs, leaving the ferromagnetic film in the ballistic regime, and a shallow trailing part, formed by the secondary HCs. Analyzing the MOKE and mSHG data, it can be seen that the HC transport in Au has a quasi-ballistic character. Besides that, comparison of the mSHG response measured in the transversal (p-in/p-out) and longitudinal (p-in/45° − out) magneto-optical geometries has brought us to the conclusion that the SC pulse gives rise to the SH field originating in the bulk of Au. At the same time in the static regime the mSHG can be considered as a purely surface/interface sensitive technique.

Chapter8 is devoted to spin dynamics induced in the Fe film by the HC injection. At the beginning of **Chapter8**, it is demonstrated that if two Fe films in a three-layer Fe/Au/Fe structure have different coercitivities, their magnetizations can be aligned parallel, antiparallel or orthogonal to each other. Using the MOKE and the mSHG, it is possible to identify the directions of the static magnetizations $\vec{M}_E$ in the spin-emitter and $\vec{M}_C$ in the spin-collector. Because of a larger variety of the magnetic configurations in comparison with two-layer Au/Fe/MgO(001) structures, the mSHG data obtained on three-layer Fe/Au/Fe structures provide an undoubtful evidence of the appearance of the SC-induced SH field. At the same time, the MOKE is exclusively sensitive to the magnetization. Depending on the initial orientation of $\vec{M}_E$ and $\vec{M}_C$, the injection of the laser-induced SC pulse into the spin-collector can lead to the absolute changes of $\vec{M}_C$ (incoherent dynamics) or even drive its precessional motion (coherent dynamics). These results illuminate the role of spin-dependent HC scattering at the Fe/Au interface.

Chapter 2

Magnetism and magnetization dynamics in metals

The field of magnetization dynamics includes a large variety of processes occurring on different spatial and time scales [29]: from few angstroms to microns, from femtoseconds to picoseconds (see Figure 2.1). This chapter introduces the fundamental concepts for magnetic interactions and magnetization dynamics in metals, providing an overview of theoretical and experimental works.

In the first section the main attention is focused on itinerant ferromagnetism of 3d metals iron (Fe), cobalt (Co) and nickel (Ni). These materials have been under investigation for years, but there is still no basic model which describes all magnetic phenomena. Mostly this problem is related to the fact that such model should include both collective and local aspects of the interactions in the electronic subsystem and between the electronic and lattice subsystems.

Then an overview of laser-induced dynamics in metals and metallic MLs will be given in the second section. In particular, possible mechanisms of ultrafast demagnetization of ferromagnetic films are considered. Typical time scales reported in literature vary from several tens of femtoseconds to few picoseconds. In this case electronic, lattice and spin subsystems are far from equilibrium, and contributions of different processes to the HC and magnetization dynamics can depend on the excitation conditions and vary with time.

Electron transport through an interface between a ferromagnet and a non-magnetic metal may lead to spin wave emission [7]. For this reason, the final section is devoted to precessional magnetization dynamics and mechanisms which can induce such dynamics. Particular interest is related to the excitation of the standing spin waves in ferromagnetic films by injection of spin-polarized HCs.

2.1 Itinerant ferromagnetism of 3d metals

The 3d metals Fe, Co, and Ni are known to be ferromagnets because of spontaneous magnetization in the absense of the external magnetic field and large magnetic susceptibility χ_M which characterizes the ratio of magnetization M to the external magnetic

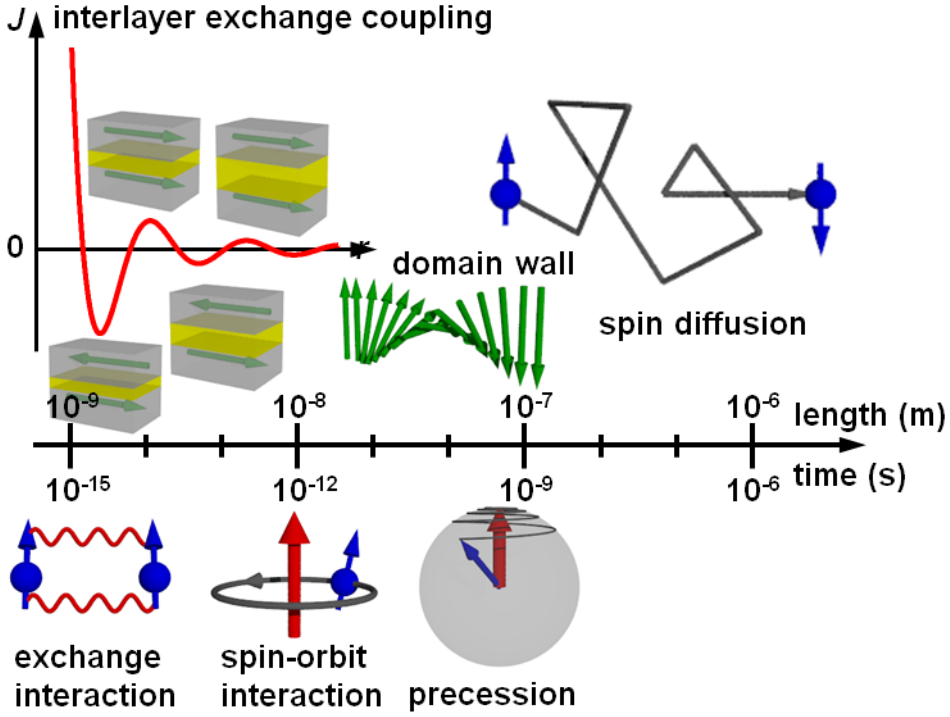

Figure 2.1: Time and length scales in magnetism. Above the axis there is an overview of magnetic phenomena occuring on different spatial scales. Below the axis there is an overview of typical time scales in magnetization dynamics. The data about typical time and length scales were taken from [29].

field H. Magnetic properties of these elements are mostly defined by 3d electrons.

2.1.1 Magnetization and magnetic interactions

State of each electron in a single atom is characterized by four quantum numbers: principal quantum number n, orbital quantum number l, magnetic quantum number m_l and spin quantum number m_s [30]. Electrons with the same principal quantum number n form an electronic shell. The lowest energy state corresponds to $n = 1$. For a given value of the principal quantum number n, the orbital quantum number l has n possible values ranging from 0 to $(n-1)$ and gives the magnitude of the orbital angular momentum $|\vec{l}| = \sqrt{\hbar^2 l(l+1)}$, where $\hbar \approx 6.582 \cdot 10^{-16}$ eV $\cdot$ s is the reduced Planck constant. Electrons with the same principal quantum number n and orbital quantum number l form a subshell. Subshells with orbital quantum numbers $l = 0, 1, 2, 3, 4$ are usually called s, p, d and f subshells, respectively. Magnetic quantum number m_l describes an orbital within a subshell and gives projection of the orbital angular momentum $\vec{l}$ on a specified direction

$$l_z = \hbar m_l. \tag{2.1}$$

Possible values of m_l range from $-l$ to l with integer steps between them. Each electron in atom has a magnetic moment $\vec{\mu}^{orb.}$ associated with its orbital motion around the nucleus. Projection of this magnetic moment on a specified direction is determined by magnetic quantum number m_l

$$\mu_z^{orb.} = -\frac{\mu_B m_l}{\hbar}, \tag{2.2}$$

where $\mu_B = \frac{e\hbar}{2m_e c} = 0.9274 \cdot 10^{-20} Erg \cdot G^{-1}$ is the Bohr magneton, e is the elementary charge, m_e is the electron mass, and c is the speed of light. In addition to the orbital angular momentum, each electron has an intrinsic angular momentum or spin $\vec{s}$. Spin quantum number m_s gives a projection of spin on a specified direction, which can be either $\hbar/2$ or $-\hbar/2$. Electrons are fermions and obey the Pauli exclusion principle formulated by Pauli in 1925. It forbids two identical fermions to occupy the same quantum state simultaneously. Thus electrons with the same values of n, l and m_l should have opposite spins, which means that only two electrons can sit on the same atomic orbital. Electron spin $\vec{s}$ is associated with spin magnetic moment $\vec{\mu}^s$, and m_s gives a projection of $\vec{\mu}^s$ on a specified direction

$$\mu_z^s = -g_s \frac{\mu_B m_s}{\hbar}, \tag{2.3}$$

where $g_s \approx 2$ is the spin g-factor. Protons and neutrons in the atomic nucleus also have magnetic moments, but they are about 1000 times smaller than that of an electron and can be neglected in our consideration.

In the ground state of single Fe, Co and Ni atoms the first ($n = 1$) and second ($n = 2$) shells are completely filled as well as the $3s$, $3p$ and $4s$ subshells [1], therefore their resultant orbital $\vec{L} = \sum_i \vec{l_i}$ and spin $\vec{S} = \sum_i \vec{s_i}$ angular momenta are equal to zero. Occupation of the different orbitals in the $3d$ subshell follows the empirical rules suggested by Hund in 1925. According to the first and second Hund's rules, electronic configuration with the lowest energy has maximum resultant spin $\vec{S}$ and orbital $\vec{L}$ angular momenta. The third Hund's rule is about spin-orbit interaction which couples spin $\vec{S}$ and orbital $\vec{L}$ angular momenta to a total angular momenta $\vec{J} = \vec{L} + \vec{S}$, where $|L - S| \leqslant J \leqslant L + S$. Spin-orbit interaction is a pure relativistic effect. In the rest frame of the nucleus a given electron moves in the Coulomb electric field $\vec{E}$, but in the rest frame of the electron there is a magnetic field $\vec{H} \sim \left[\vec{v} \times \vec{E}\right]/c$ interacting with the spin magnetic moment $\vec{\mu}^s$. In the self-consistent field approximation Hamiltonian operator of the spin-orbit interaction $\hat{H}_{SL}$ is

$$\hat{H}_{SL} = \lambda_{so}(\hat{S} \cdot \hat{L}), \tag{2.4}$$

where $\hat{S}$, $\hat{L}$ are the operators of the resultant spin and orbital momenta, λ_{so} is a constant depending on $\vec{S}$ and L, but not on the total angular momentum J. The constant λ_{so} can be either positive or negative. In the ground state of a single atom with one incompletely filled shell, $\vec{J} = |\vec{L} - \vec{S}|$ ($\lambda_{so} > 0$) if this shell contains not more than half the greatest possible number of electrons for that shell or $\vec{J} = \vec{L} + \vec{S}$

[1] The $3d$ subshell has higher energy than the $4s$ subshell due to the centrifugal potential $\hbar^2 l(l+1)/(2m_e r^2)$, where r is the distance between the electron and the nucleus.

Element	Ground state	Term	$m_{sat}\,[\mu_B]$	$m_{sat}^{orb}\,[\mu_B]$
Fe(bcc)	$3d^6 4s^2$	$^5D_4$	2.216	0.0918
Co(hcp)	$3d^7 4s^2$	$^4F_{9/2}$	1.715	0.1472
Ni(fcc)	$3d^8 4s^2$	$^3F_4$	0.616	0.0507

Table 2.1: Electronic configurations, terms of the ground state of single Fe, Co and Ni atoms, experimental values of the total m_{sat} and orbital m_{sat}^{orb} magnetic moments normalized to the number of atoms per a unit volume in the solid state of Fe, Co and Ni. Values for m_{sat} and m_{sat}^{orb} were obtained from saturation magnetization and the combination of the Einstein-de Haas magnetomechanical and ferromagnetic resonance data [31].

($\lambda_{so} < 0$) if the shell is more than half-full [30]. Electronic states of multielectron atoms are usually called terms or multiplets and denoted as $^{(2S+1)}L_J$. Terms and electronic configurations corresponding to the ground states of single Fe, Co and Ni atoms are shown in the table 2.1.

Projection of the total magnetic moment $\vec{\mu}^J$ of a single atom on a specified direction is

$$\mu_z^J = g_J \frac{\mu_B}{\hbar} m_J, \tag{2.5}$$

where m_J is a projection of the total angular momentum J, and g_J is the Lande g-factor

$$g_J = 1 + \frac{J(J+1) + S(S+1) - L(L+1)}{2J(J+1)}. \tag{2.6}$$

The magnetization M of a solid can be introduced as the number of magnetic dipole moments per a unit volume. If all magnetic moments are aligned parallel by the external magnetic field, the magnetization M can be expressed as

$$M = m\frac{N}{V}, \tag{2.7}$$

where m is the magnetic moment of a single atom, N is the number of atoms, V is the volume of the magnetic material. The $3d$ electrons are localized and conserve their atomic properties in the solid state [29], but atomic model which works for lanthanides, where $4f$ electrons are strongly localized around ion cores, gives wrong estimation for magnetization M in $3d$ ferromagnets. According to the equations (2.2), (2.3), (2.5) and (2.6) orbital, spin and total magnetic moments of single atoms are multiples of the Bohr magneton μ_B. Experimental values of the total magnetic moments m_{sat} normalized to the number of atoms per a unit volume in Fe, Co and Ni are not multiples of the Bohr magneton μ_B (see Table 2.1). Furthermore, interaction with strong crystal field leads to the quenching of the electron orbits and, consequently, small values of the orbital magnetic moment m_{sat}^{orb}. It means that the spin magnetic moments of the electrons give main contribution to the magnetization M.

Broken Bohr magneton numbers in the ferromagnetic metals are related to the itinerant behavior of the d-electrons, meaning that they are not strictly localized. Figure 2.2 shows $3d$ and $4s$ wavefunctions of Ni in the solid state. Overlap of the

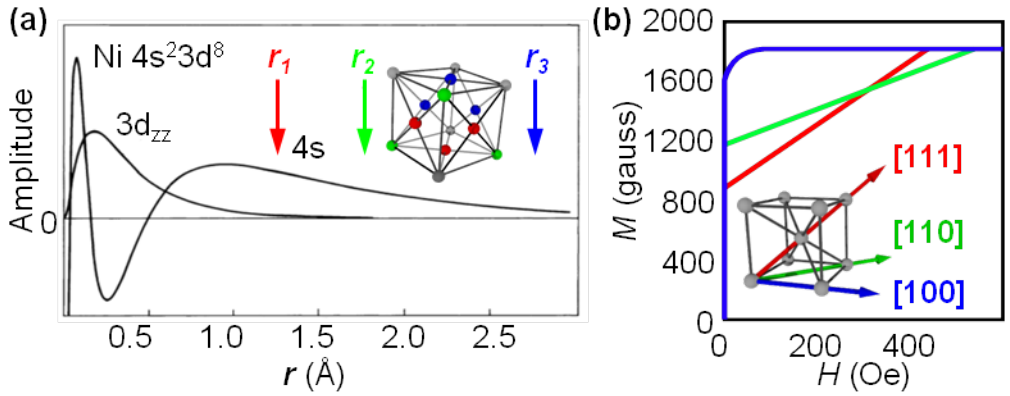

Figure 2.2: (a) The amplitude of the $3d_{zz}$- and $4s$-wavefunctions [32] and a unit cell of the fcc-Ni. The half-distances to the first, second and third nearest neighbors (r_1-red, r_2-green and r_3-blue) are shown for comparison. The plot was redrawn after [33]. (b) Magnetocrystalline anisotropy and a unit cell of the bcc-Fe. The dependences of the magnetization M on the external magnetic field H are shown for three crystallographic directions: [100] (easy axis), [110] (intermediate axis), [111] (hard axis). This figure was redrawn after [34].

$3d$ wavefunctions of the neighboring atoms provides direct exchange interaction between the electron spins, which causes spontaneous long-range parallel alignment of the magnetic moments. The exchange interaction has a quantum mechanical origin and arises from the Coulomb interaction between electrons and the Pauli exclusion principle mentioned before. It is the strongest magnetic interaction (∼1 eV). Also one of the main feature of this interaction is that it acts only on the electron spins, not on the electron orbital magnetic moments. Hamiltonian of the exchange interaction for a many-electron system can be written in the Heisenberg form

$$\hat{H}_{exch} = -\sum_{i \neq j}^{N} J_{ij}^{ex} \cdot \vec{s}_i \cdot \vec{s}_j = -2 \sum_{i<j}^{N} J_{ij}^{ex} \cdot \vec{s}_i \cdot \vec{s}_j, \tag{2.8}$$

where J_{ij}^{ex} is the exchange integral

$$J_{ij}^{ex} = \int \int \psi_i(r_1)\psi_j(r_2)\frac{e^2}{r_{12}}\psi_i^*(r_1)\psi_j^*(r_2)dr_1 dr_2, \tag{2.9}$$

$\psi_i(r)$, $\psi_j(r)$ are the electronic wavefunctions. Thus for J_{ij}^{ex} is positive for ferromagnetic coupling, and negative for antiferromagnetic coupling.

Energy of the spin-orbit interaction (10-100 meV) is much smaller than the exchange interaction in $3d$ transition metals[2]. In spite of that the spin-orbit interaction plays

[2]Considering hydrogen-like atom with nucleus charge Ze, energy of the spin-orbit interaction grows as Z^4, but for multielectron atom it grows as Z^2 [30]. Since for Fe $Z = 26$ and for Au $Z = 79$, the spin-orbit interaction in Au is over nine times larger than in Fe.

very important role. It couples the spin system to the lattice, allowing energy and angular momentum exchange and inducing magnetocrystalline anisotropy. Strong crystal field sets the direction of the orbital angular momentum $\vec{L}$ along the lattice vectors of translational symmetry. Then the orbital angular momentum $\vec{L}$ determines preferential direction of the spin angular momentum $\vec{S}$, corresponding to the minimum of the energy of the spin-orbit interaction (2.4). Figure 2.2(b) shows dependences of the magnetization M on the external magnetic field H. Interaction of the magnetic moments $\vec{\mu}$ with the external magnetic field $\vec{H}$ is called the Zeeman interaction and its energy is given by

$$E_{Zeeman} = -\left(\vec{\mu} \cdot \vec{H}\right). \tag{2.10}$$

In order to align all magnetic moments in a solid parallel to the external magnetic field $\vec{H}$, energy of the Zeeman interaction should compensate the energy of the spin-orbit interaction (2.4). Thus if $\vec{H}_{ext}$ is parallel to the [100] direction (easy axis), the energy of the spin-orbit interaction is minimal and saturation of the magnetization can be achieved for small magnetic fields. If $\vec{H}_{ext}$ is not parallel to the [100] direction, for small magnetic fields all magnetic moments have positive projection on the direction of $\vec{H}_{ext}$ and become parallel to one of the easy axes. Then an increase of the external magnetic field makes magnetic moments parallel to $\vec{H}$: red and green curves in Figure 2.2(b) corresponding to the [111] (hard axis) and [110] (intermediate axis), respectively. In the case of cubic crystals energy of the magnetocrystalline anisotropy can be expressed as

$$\begin{aligned} E_a = K_1 &\left(\cos^2\alpha_1 \cos^2\alpha_2 + \cos^2\alpha_1 \cos^2\alpha_3 + \cos^2\alpha_2 \cos^2\alpha_3\right) \\ &+ K_2 \cos^2\alpha_1 \cos^2\alpha_2 \cos^2\alpha_3, \end{aligned} \tag{2.11}$$

where $\cos\alpha_1$, $\cos\alpha_2$, $\cos\alpha_3$ are the direction cosines with respect to the [100], [010] and [001] directions, respectively. If $|K_2| < \frac{9}{4}|K_1|$ and $K_1 > 0$, [100] directions [3] correspond to the easy axes, and direction [111] corresponds to the hard axis($K_1^{Fe} = 4.6 \cdot 10^5 erg \cdot cm^{-3}$, $K_2^{Fe} = 1.5 \cdot 10^5 erg \cdot cm^{-3}$). If $K_1 < 0$, then the easy axis is parallel to the [111] direction, and the hard axes are the [100] directions(($K_1^{Ni} = -5 \cdot 10^4 erg \cdot cm^{-3}$, $K_2^{Ni} = 2.3 \cdot 10^4 erg \cdot cm^{-3}$)) [35].

In spite of the fact that the orbital angular momentum is important for the appearance of magnetocrystalline anisotropy, its average value and the orbital magnetic moment in 3d ferromagnets (see Table 2.1) are very small due to the strong interaction of the d-electrons with the crystal field, which splits multielectron levels of the d-ions. In the case of 3d metals interaction with the crystal field is comparable to the Coulomb and the exchange interactions, which complicates development of successive quantitative theory for these materials [36].

2.1.2 Energy band structure

In order to explain experimental value of the saturation magnetization and its temperature dependence, the band theory was applied to magnetic systems in 1935 by Mott [37], and in 1936 by Slater [38, 39] and Stoner [40, 41].

[3] In this case [100] is referred to a set of the directions [100], [010], [001].

The simplest band-like model of the ferromagnetic metals is the Stoner-model or the Stoner-Wohlfarth-Slater-model of metallic ferromagnetism. According to this model, electron energies are

$$\begin{aligned} E_\uparrow(k) &= E(k) - In_\uparrow, \\ E_\downarrow(k) &= E(k) - In_\downarrow, \end{aligned} \tag{2.12}$$

where $E(k)$ are the energies in a normal one-electron band structure [4], $n_\uparrow$, $n_\downarrow$ are the number of electrons per a single atom with corresponding spin, and I is the Stoner parameter which describes the energy reduction due to the electron correlation [33]. From equations (2.3) and (2.7) magnetic moment m of a single atom in a solid is

$$m = (n_\uparrow - n_\downarrow)\mu_B. \tag{2.13}$$

Subtracting $I(n_\uparrow + n_\downarrow)/2$ from the one-electron energies, instead of (2.12) we obtain

$$\begin{aligned} E_\uparrow(k) &= \tilde{E}(k) - \frac{Im}{2\mu_B}, \\ E_\downarrow(k) &= \tilde{E}(k) + \frac{Im}{2\mu_B}, \end{aligned} \tag{2.14}$$

where $\tilde{E}(k) = E(k) - I(n_\uparrow + n_\downarrow)/2$. The pair of equations (2.14) corresponds to a k-independent splitting of the energy bands with different spins. It is an approximation, but theory nevertheless says that it holds to within a factor of two. The value of the splitting depends on m determined by the relative occupation $(n_\uparrow - n_\downarrow)$ of the sub-bands. At the absolute zero temperature $T = 0$ K all the states below the Fermi energy E_F are filled, so

$$\begin{aligned} n_\uparrow &= \int_{-\infty}^{E_F} D_\uparrow(E)dE, \\ n_\downarrow &= \int_{-\infty}^{E_F} D_\downarrow(E)dE, \end{aligned} \tag{2.15}$$

where $D_\uparrow(E)$ is the density of states (DOS) in the sub-band with the larger electron population, called the majority sub-band, $D_\downarrow(E)$ is the DOS in the sub-band with the smaller population, called the minority sub-band[5]. In the Stoner model the detailed dependence of the DOS on the electron energy is ignored: it is assumed to have the shape of a semicircle. Real DOSs are more complicated. Nowadays development of the angle-resolved photoemission spectroscopy (ARPES), one of the most direct methods to study the electronic band structure of solids, makes it possible to test and correct theoretical calculations [42–44].

[4] In the one-electron model energy levels and band structure are calculated for an electron in an effective potential consisting of the potential of the ion cores and an average potential due to the other electrons.

[5] Signs $\uparrow$ and $\downarrow$ depict parallel and antiparallel orientation of the electron spin magnetic moments with respect to the magnetization M. Due to the negative charge of the electrons, their spins have the opposite direction with respect to the spin magnetic moment

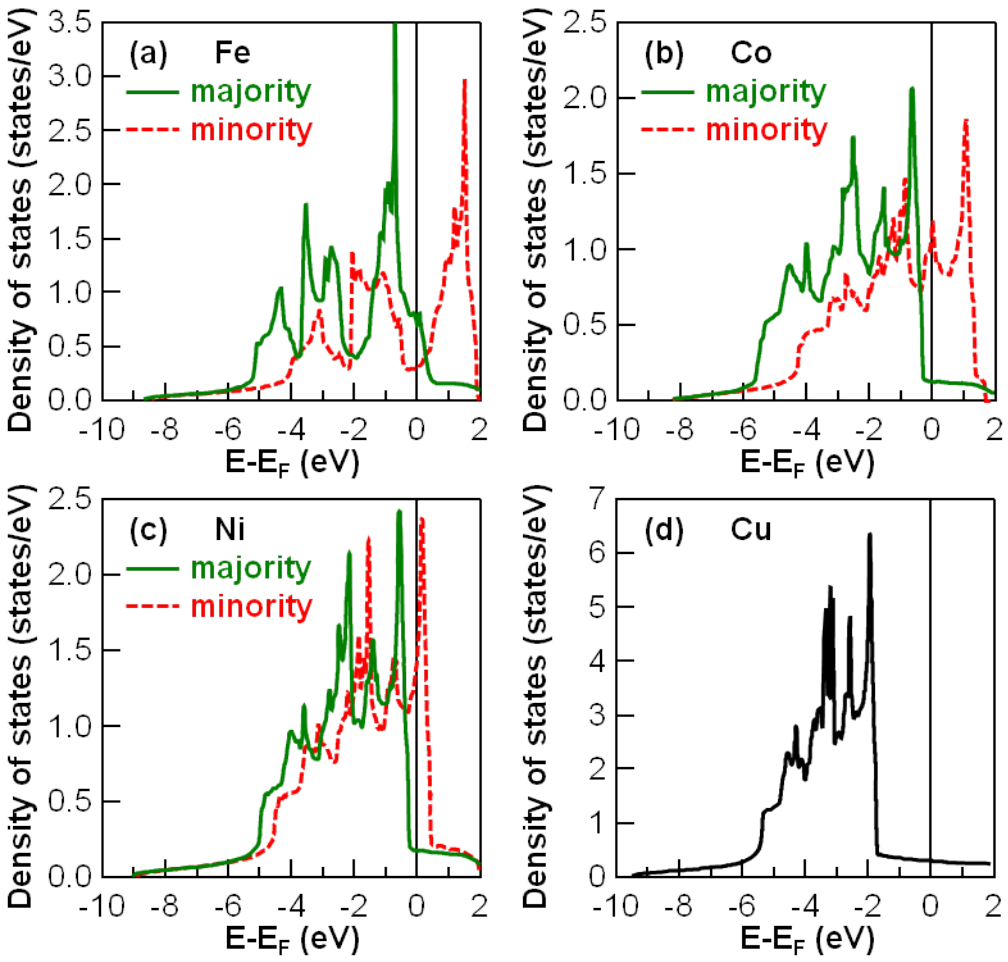

Figure 2.3: Density of states of (a) bcc-Fe, (b) hcp-Co, (b) fcc-Ni for the majority and minority spins. There is no exchange splitting in (d) fcc-Cu, and presented DOS is the sum of DOSs for the majority and minority spins. Figures are redrawn after [45].

Figure 2.3 shows DOSs calculated for Fe, Co, Ni, and nonmagnetic Cu [45]. All four metals have similar shapes of the DOSs, but in Cu there is no exchange splitting and the d-states are far below the Fermi energy $E_F (\approx 2$ eV).

The structure in the DOSs is due to the overlap interactions of the d-states on neighboring atoms with the atoms located on lattice points of well-defined symmetry. Using the positions of the largest peaks in the DOSs in the majority and minority sub-bands, one can estimate the exchange splitting Δ_{ex} about 2.2 eV in Fe, 1.7 eV in Co, and 0.6 eV in Ni, which are in a good agreement with the trend in magnetic moments shown in the table 2.1. Although from the spin-resolved photoemission data it is known that Δ_{ex} varies for different k-vectors. Himpsel et al. give a range of values for Δ_{ex} evaluated at different points in the Brillouin zone: 1.8-2.4 eV for Fe, 0.93-1.05 eV for Co,

and 0.17-0.33 eV for Ni [42, 43]. Typical band width of the d-electrons is comparable to Δ_{ex}, about 3-5 eV. The band width of the s-p electrons is larger, about 10 eV.

One of the most important difference between 3d ferromagnets is the position of the Fermi energy E_F with respect to the d-states in the majority and minority sub-bands (see Figure 2.3). In static regime there are no spin-up d-holes in Ni and Co, therefore they are called 'strong' ferromagnets. Fe is called a 'weak' ferromagnet (but with larger magnetic moment) because of the sizeable d-band contributions in the both sub-bands. Moreover, in bcc-Fe the degree of spin polarization

$$P(E_F) = \frac{D^{\uparrow}(E_F) - D^{\downarrow}(E_F)}{D^{\uparrow}(E_F) + D^{\downarrow}(E_F)} \tag{2.16}$$

at the Fermi energy E_F is positive, while in Co and Ni it is negative. The sign of the spin polarization at E_F is important for a number of experiments, where one measures the sign of the spin polarization of electrons emitted from states near E_F. However, in the experiments with electric current, $P(E_F)$ is not the only factor determining the sign of the spin polarization of the electric current, because conductivity σ is largely determined by the s-d scattering which is spin-dependent and also influences on the spin polarization [29].

In the next section it will be shown that the electronic band structure is very important in terms of light-matter interaction and relaxation processes occuring after optical excitation.

2.2 Laser-induced dynamics in metals and metallic multilayers

Since this work investigates optically excited HC dynamics in metallic MLs, it is worth to summarize typical processes that HCs undergo in metals after excitation by ultrashort laser pulses. Also this section provides an overview of the experimental and theoretical works devoted to laser-induced HC and magnetization dynamics.

2.2.1 Absorption of light in metals

One-photon absorption in metals can be described by the refractive index $n = n'(\omega) + in''(\omega)$ and the dielectric function $\varepsilon = \varepsilon'(\omega) + i\varepsilon''(\omega)$, where

$$\varepsilon = n^2 \Rightarrow \varepsilon' = (n'^2 - n''^2) \text{ and } \varepsilon'' = 2n'n''. \tag{2.17}$$

In the general case the dielectric function is a tensor, but in cubic crystals transverse and logitudinal dielectric functions are identical[6]. Dependence of the diagonal compo-

[6]Considering linear absorption, rotation of the light polarization while propagating in a magnetic medium due to MOKE can be neglected.

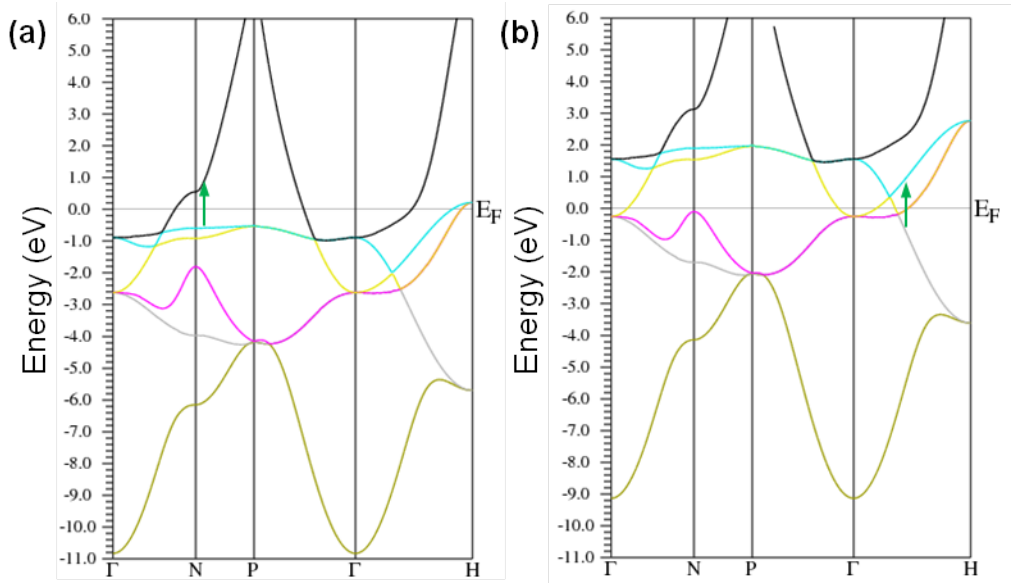

Figure 2.4: E(k) diagram of the majority (a) and minority (b) subbands in Fe. Green arrows denote direct optical transitions. The energy band structure of Fe was calculated by Dr. Tim Wehling and Prof. Dr. Alexander Lichtenstein.

nent of the dielectric tensor $\varepsilon(\omega)$ on the photon energy $\hbar\omega$ is described by this formula

$$\varepsilon_{ii}(\omega) = 1 - \frac{\omega_p^2}{\omega(\omega + i/\tau_c)} - \frac{4\pi e^2}{m^2\omega^2} \sum_{kk'bb'} \frac{(\hbar\omega + i/\tau_{bb'}) \langle bk|p_i|b'k'\rangle\langle b'k'|p_i|bk\rangle}{(E_{b'k'} - E_{bk})(E_{b'k'} - E_{bk} - \hbar\omega - i/\tau_{bb'})} \left[f_0(E_{b'k'}) - f_0(E_{bk})\right], \quad (2.18)$$

where $i = \{x, y, z\}$, ω_p is the plasma frequency, $\tau_c = \tau_0 \left[E_F/(\hbar\omega - E_F)\right]^2$ is the energy-dependent relaxation time of the conduction electrons, $\langle bk|p_i|b'k'\rangle$ is the transition matrix element for $bk \rightarrow b'k'$ transitions, $\tau_{bb'}$ is the corresponding relaxation time, E_{bk} is the energy of the state $|bk\rangle$, and

$$f_0(E_{bk}) = \frac{1}{exp\left[\frac{E_{bk} - E_F(T_e)}{kT_e}\right] + 1} \quad (2.19)$$

is the value of the Fermi function at this energy [46]. The electron temperature dependence of the Fermi energy is given by [47]:

$$E_F(T_e) = E_{F0}\left[1 - \frac{\pi^2}{12}\left(\frac{kT_e}{E_{F0}}\right)^2\right], \quad (2.20)$$

where E_{F0} denotes the Fermi energy at $T_e = 0$.

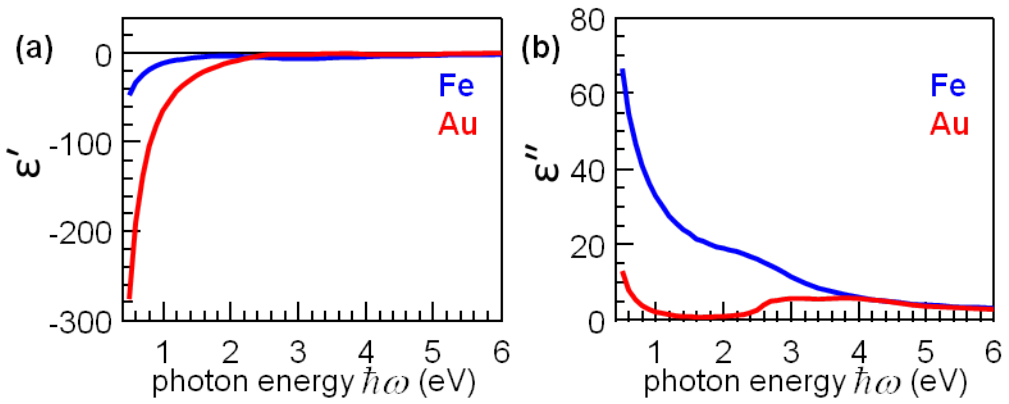

Figure 2.5: Dependence of the real ε' (a) and the imaginary ε'' (b) parts of the dielectric functions of Fe and Au on the photon energy $\hbar\omega$. $\varepsilon'(\omega)$ and $\varepsilon''(\omega)$ were calculated using $n'(\omega)$ and $n''(\omega)$ taken from [48].

The first two terms of (2.18) describe the free-electron absorption or intraband contribution, the last term corresponds to the interband contribution. The momentum conservation condition dictates that

$$\hbar k_f - \hbar k_i = \hbar k. \tag{2.21}$$

Since the photon wave-vector $|k| = 2\pi/\lambda$ is negligibly small for optical frequencies compared to the electron wave-vectors, one can rewrite (2.21):

$$k_f = k_i. \tag{2.22}$$

Therefore direct optical transitions are denoted with vertical arrows on the $E(k)$ diagram (see Figure 2.4).

Figure 2.5 shows the dependence of the real ε' and imaginary ε'' parts of the dielectric function on the photon energy $\hbar\omega$ for Fe and Au. Band structure of Au and hence the density of states is similar to the band structure and the density of states of Cu (see Fig. 2.3(d)). The upper d-band edge in Au is 1.8 eV below the Fermi level. Thus for photon energies $\hbar\omega < 1.8$ eV optical properties of Au are mainly determined by collective excitations of free carriers, while for Fe due to the d-bands around the Fermi level both intraband and interband contributions play significant role. This explains large negative value of the real part of the dielectric function ε'_{Au} of Au (see Fig. 2.5(a)), which results in higher reflectivity, and small imaginary part ε''_{Au}, which results in negligibly small absorption at 1.5 eV. It means that considering hot carrier excitation in the Au/Fe/MgO(001) and Fe/Au/Fe/MgO(001) one can neglect influence of the electrons excited in Au by the pump pulse. However, for ultrashort laser pulses and high intensities two-photon absorption in Au may play a significant role in the HC generation. For photon energies $\hbar\omega >2$ eV, ε'_{Au} is close to 0, and ε''_{Au} becomes comparable to ε''_{Fe}, which corresponds to an increase of the absorption due to the interband transitions.

For plane monochromatic electromagnetic wave with cyclic frequency ω, propagating in a medium in the positive direction of the z axis, electric field is oscillating according to the equation

$$E(z,t) = E_0 \cdot e^{i(kz-\omega t+\phi)}, \tag{2.23}$$

where E_0 and ϕ are the amplitude and phase of the electric field in the point $z = 0$ at the time $t = 0$, respectively, and $k = k' + ik'' = \omega \cdot (n' + in'')/c$ is the wave vector inside the medium. Thus the amplitude of the electric field decreases as $e^{-k''z}$ and the intensity of the electromagnetic wave, which is proportional to $|E_0 \cdot e^{-k''z}|^2$, is governed by the Lamber-Beer's law

$$I(z) = I_0 \cdot e^{-\alpha z}, \tag{2.24}$$

where I_0 is the intensity of the electromagnetic wave in the point $z = 0$, $\alpha = 2 \cdot k'' = 2\omega n''/c$ is the extinction coefficient.

In comparison to the monochromatic wave with a single frequency ω, femtosecond laser pulse has a relatively wide spectrum, different parts of which can have different absorption coefficients $\alpha(\omega)$. However, if $\alpha(\omega)$ does not vary strongly within the spectrum of the short laser pulse, it can be replaced with the average value.

2.2.2 Hot carrier and magnetization dynamics in metals

With the advent of pulsed femtosecond lasers, it has become possible to study a highly excited state of metals where the electron subsystem is far not only from the equilibrium with the lattice, but also from its internal equilibrium. A great effort was done in the investigation of the HC dynamics in normal metals such as Au, Ag and Cu, employing reflectivity, SHG or photoemission spectroscopy [49–71]. Processes induced by a fs laser in normal metals are summarized in Figure 2.6. It was found that hot electron lifetime decreases with the electron energy in accordance with the prediction from the Fermi-Liquid theory (FLT) [73, 74]:

$$\tau_{FLT} \sim \frac{1}{(E - E_F)^2}. \tag{2.25}$$

It may vary from several femtoseconds to hundreds of femtoseconds. In spite of the high electron-electron (e-e) collision rate for HCs with large energies, thermalization of the electronic system is usually established within 300-500 fs. Then the electron energy distribution can be described by the Fermi-Dirac function (2.19) with a certain electron temperature T_e. Subsequent thermalization between the electron subsystem and the lattice occurs on the timescale of several picoseconds via the electron-phonon (e-ph) interaction. In the experiments with metallic films of different thicknesses, it was observed that the hot carrier transport plays significant role in the relaxation process, but its contribution vanishes for thin films ($\sim 10nm$) [69]. After the optical excitation, HCs move in the ballistic regime with velocities $v_{bal.} \sim 10^6 m/s$. Then due to e-e collisions, the HC transport becomes mostly diffusive with the diffusion velocity $v_{dif.} < 10^4 m/s$.

In terms of the HC dynamics, one major difference between noble metals and 3d ferromagnets is that majority $e^{\uparrow}$ and minority $e^{\downarrow}$ electrons are excited to the states

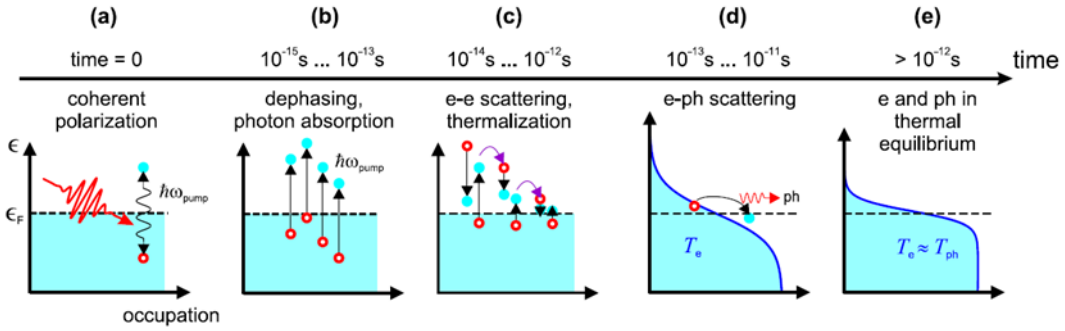

Figure 2.6: Processes induced by a fs laser pulse in metals. This picture was kindly provided and printed with permission from Dr. Tobias Kampfrath [72].

with different binding energies, velocities and lifetimes owing to the exchange-split energy band structure. The second difference is the d-band which provides larger phase space for electrons to scatter [75]. It strongly reduces efficiency of the ballistic transport in transition metals, but leads to faster energy transfer from the electron system to the lattice [69]. However, because of the s/p-band, electron thermalization time constant obtained using the time-resolved photoemission spectroscopy is very close to the values obtained for noble metals [76]. Finally, in magnetic materials one has to consider magnons (quasi-particles of the collective excitations of the magnetic moments). They play very important role in the electron thermalization [77], allowing transitions between the majority and minority sub-bands. Electrons can also flip their spins via the e-ph interaction, but the phonon energy spectrum is limited by the Debay energy $\sim 30-40$ meV, which makes the electron-phonon interaction less efficient than the electron-magnon interaction. In general, both experimental studies and ab-initio calculations show that in 3d ferromagnets the majority HCs have larger lifetimes and inelastic mean free path than the minority HCs [19, 78]. However, there is still a large quantitative difference between experimental observations [71] and different theoretical predictions [19, 78, 79].

Regarding laser-induced magnetization dynamics, the first observation of spin dynamics occurring on the sub-picosecond timescale was made by Beaurepaire et al. [25] in 1996. Pumping a 22-nm Ni film with a 60-fs laser pulse and measuring hysteresis loops in the MOKE signal, they demonstrated that the remanent magnetization undergoes a fast drop by almost 50% within the first picosecond after excitation. In 1997 this result was confirmed by Hohlfeld et. al in the mSHG measurements [80], but rapid variations of the magneto-optical signal made experimentalists call the interpretation of the measured signals into question. Then it was found that the mSHG [81] and MOKE [82] could be affected by state-filling effects, especially in the experiments where $\hbar\omega_{pump} = \hbar\omega_{probe}$. This problem and its solution will be discussed in more detail in the next chapter.

In order to verify previous findings and improve interpretation of the experimental data, Fe, Co and Ni were also studied by other techniques: x-ray magnetic cir-

cular dichroism (XMCD) [83, 84] and spin-resolved two-photon-photoemission (SR-2PPE) [77, 85]. Demagnetization time constants obtained for 3d ferromagnets are similar and on the order of 200 fs. Systematic studies showed that the maximum quenching of magnetization is linearly proportional to the pump fluence for all three 3d ferromagnets [80, 86–88]. Koopmans et al. reported about two demagnetization time scales in Ni [86], while in Fe and Co only one demagnetization time scale has been observed. Two demagnetization time scales are attributed to the situation when coupling between the electron and spin system is weak. Initially at low ambient temperatures and small pump fluence, thin Ni film exhibit only one demagnetization time scale. Appearance of the two demagnetization time scales occurs upon an increase of the pump fluence [86] or the sample termperature [89]. This effect has been observed in rare-earth metals such as Gd and Tb [90], in half-metals [91] and other materials.

2.2.3 Phenomenological description of magnetization dynamics

Together with further improvement of the experimental techniques, one of the main goals in the field of laser-induced spin dynamics is the development of a microscopic model which can successfully describe ultrafast demagnetization. Phenomenological models presented in this subsection, are mostly intended to describe the experimental observations considering the energy flux and the transfer of the angular momentum between three reservoirs: electrons, spins and the lattice (see Figure 2.7). But they do not explicitly include certain microscopic mechanisms responsible for ultrafast demagnetization.

Three-temperature model

In the experiments with picosecond laser pulses HC and lattice dynamics in normal metals can be described by the two-temperature model (2TM) [92, 93] assuming that electron and phonon distributions can be characterized in terms of electron T_e and lattice T_p temperatures, respectively.

In order to describe magnetization dynamics, in 1991 Vaterlaus et al. [94] introduced temperature T_s of the spin system, which was later used by Beaurepaire et al. [25] to develop the three-temperature model (3TM) resulting in the following rate equations for the electron T_e, lattice T_p and spin T_s temperatures:

$$\begin{aligned} C_e \frac{dT_e}{dt} &= I(t) - g_{ep} \cdot (T_e - T_p) - g_{es} \cdot (T_e - T_s)\,, \\ C_p \frac{dT_p}{dt} &= g_{ep} \cdot (T_e - T_p) + g_{sp} \cdot (T_s - T_p)\,, \\ C_s \frac{dT_s}{dt} &= g_{es} \cdot (T_e - T_s) - g_{sp} \cdot (T_s - T_p)\,, \end{aligned} \tag{2.26}$$

where $I(t)$ is the source term related to the laser absorption, C_e, C_p, C_s are the heat capacities. Since spin is conserved in the optical transitions, the pump laser

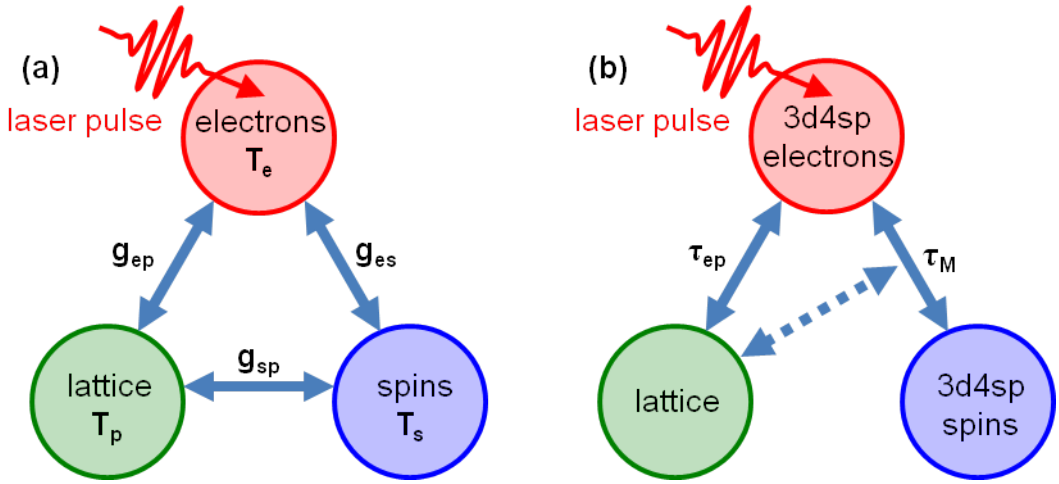

Figure 2.7: Two variants of the three-temperature model: (a) 3TM and (b) M3TM, suggested by Beaurepaire et al. [25] and Koopmans et al. [86] for 3d ferromagnets, respectively. Solid arrows depict the energy flows , and the dash arrow is the transfer of the angular momentum.

pulse excites only the electron system. In all papers using the 3TM, the electron thermalization time is usually neglected, and the electron system is heated instantly to a thermalized distribution. The energy flows between the electron, lattice and spin systems are proportional to the temperature differences between them, g_{ep}, g_{es}, g_{sp} are the corresponding coupling constants (see Figure 2.7(a)). The system of the rate equations 2.26 is written for the homogeneous laser excitation in the absence of HC trasport. In more general case, one should replace total derivatives with partial time derivatives and introduce terms describing HC and energy transport.

The 3TM is a simple and intuitively clear description of the energy equilibration processes. But it has no predictive character, and determination of the magnetization through T_s in a highly NEQ process is very doubtful.

'Microscopic' three-temperature model

Koopmans et al. [86] tried to go beyond the phenomenological 3TM and implemented a microscopic description of the spin dynamics where the main mechanism is the Elliott-Yafet spin-flip electron-phonon scattering discussed in the next subsection. It was suggested that the angular momentum is transferred to the lattice (see Figure 2.7(b)). Complete and detailed derivation of the 'microscopic' 3TM (M3TM) can be found in [95] and results with certain simplifications in the set of three differential equations:

$$\begin{aligned} C_e\frac{dT_e}{dt} &= \nabla_z(\kappa\nabla_z T_e) + g_{ep}(T_p - T_e), \\ C_p\frac{dT_p}{dt} &= g_{ep}(T_e - T_p), \\ \frac{dm}{dt} &= Rm\frac{T_p}{T_C}\left[1 - m\coth\left(\frac{mT_c}{T_e}\right)\right]. \end{aligned} \tag{2.27}$$

This model has been proved to describe magnetization dynamics [86], but it has several significant disadvantages:

- From the measurements of the total heat capacity it can be seen that the magnetic contribution is comparable to the electron contribution at the room temperature, and become comparable to the lattice heat capacity upon strong demagnetization of the ferromagnetic film. Thus energy exchange between electron, lattice and spin systems cannot be neglected, as it is done in the M3TM.

- In the derivation of the spin-flip rate it was assumed that the energy difference between the initial and final electron states in the phonon-mediated spin-flip scattering process is $\pm\Delta_{ex} \pm E_p$, where E_p is a phonon energy. Since $\Delta_{ex} \sim 1eV$ and the typical phonon energy $\sim 30meV$, Carva et al. [96] noted that it is not very probable that an electron can change its energy by Δ_{ex} in the electron-phonon scattering process.

- No suggestions have been made regarding the linear reflectivity.

2.2.4 Microscopic models for the origin of ultrafast demagnetization

Direct interaction with the electric field of the pump pulse

In 2000 Zhang and Hübner suggested that the direct interaction with the electric field of the pump laser pulse is responsible for ultrafast demagnetization [97]. However, there is no experimental evidence that this mechanism really takes place [26]. For instance, Zhang and Hübner predicted that the demagnetization of Ni saturates at about 50 %, but then demagnetization on the order of $70 - 80$ % has been observed by Stamm et al. [83, 84]. Also according to Zhang and Hübner [97], laser-induced demagnetization is almost instantaneous, and the experimental time constants should be determined by the duration of the pump pulse. In the present thesis and some previous works it is demonstrated that in the absence of the HC transport demagnetization time constants are larger than the duration of the applied laser pulses.

Phonon-mediated spin-flip scattering

In a material with the spin-orbit coupling the electronic states are not purely spin-up or spin-down, but a mixture of a dominant spin-up (spin-down) and a small spin-down (spin-up) contribution:

$$\psi_{k,\uparrow} = \left[a_k(r)|\uparrow\rangle + b_k(r)|\downarrow\rangle\right] e^{ik\cdot r}, \tag{2.28}$$

where k is the wave-vector. The interaction of an electron with a phonon with the wave-vector q can be described by the potential consisting of two parts [98]:

$$W_q = W_q^0 + W_q^{spin-orbit}, \tag{2.29}$$

where W_q^0 is the spin-independent part and $W_q^{spin-orbit}$ refers to the spin-dependent part of the scattering potential. The spin-flip matrix element between a spin-up state $\psi_{k,\uparrow}$ and a spin-down state $\psi_{k+q,\downarrow}$ is given by

$$m_{k+q,\downarrow;k,\uparrow} = \langle \psi_{k+q,\downarrow} | W_q^0 + W_q^{spin-orbit} | \psi_{k,\uparrow} \rangle. \tag{2.30}$$

In 1954 Elliott noticed that the first part of this matrix element, related to W_q^0 is non-zero, because it connects the large and small components of the two spinors [99]. Then in 1963 Yafet demonstrated that it is essential to consider both parts of the potential [100]. Thus due to the spin-orbit coupling the electron in the spin-up state $\psi_{k,\uparrow}$ can scatter not only into another spin-up state $\psi_{k',\uparrow}$, but also into the spin-down state $\psi_{k',\downarrow}$. In the theory of Elliott and Yafet the spin-flip probability a_{sf} is related to the spin mixing parameter

$$\langle b^2 \rangle = \overline{min(\langle \psi_k | \uparrow \rangle \langle \uparrow | \psi_k \rangle, \langle \psi_k | \downarrow \rangle \langle \downarrow | \psi_k \rangle)}, \tag{2.31}$$

where the bar stands for a suitable average over all involved states. If $\langle b^2 \rangle = 0$, all relevant states are pure spin states, whereas $\langle b^2 \rangle = 0.5$ corresponds to fully mixed states. The exact relation between a_{sf} and $\langle b^2 \rangle$ is given by:

$$a_{sf} = p \langle b^2 \rangle, \tag{2.32}$$

where p is a material specific parameter.

In 2005 Koopmans et al. [101] suggested that ultrafast demagnetization of a ferromagnet is accompanied with the transfer of the angular momentum to the lattice, which proceeds by means of the Elliott-Yafet spin-flip scattering. Initially the Elliot-Yafet spin-flip mechanism was used only for non-magnetic materials, because theoretical treatment of ferromagnets is rather complex. For this reason, the value of the Elliott-Yafet spin-mixing parameter b^2, calculated for Cu, was used as an estimation for the value of the Elliott-Yafet spin-mixing parameter b^2 in Ni. However, it is very small. Then Steiauf and Fähnle performed ab initio calculations of b^2 for 3d ferromagnets [98]. It appeared that b^2 obtained for Fe, Co and Ni is about 25 times larger than for Cu. This result emphasizes the role of the Elliott-Yafet mechanism in ultrafast spin dynamics.

In the M3TM Koopmans et al. [86] assumed a thermalized electron distribution. However, Carva et al. [96] found that the magnetization change rate calculated for thermalized electron distribution is too small to explain ultrafast demagnetization, and ultrafast spin dynamics is mostly governed by NEQ HCs which provide much larger magnetization change rates. Thus a new model supplemented with NEQ HC dynamics is required (see **Chapter 5**).

Electron-magnon scattering

Electrons can slip their spins, interacting not only with phonons, but also with magnons. In the early measurements performed to determine the heat capacity of ferromagnetic materials [102], the signature of the electron-magnon interaction was identified from the additional term to the total measured heat capacity of the system which should be

accounted for in order to have a good description of the measured data. Carpene et al. [87] suggested the electron-magnon scattering as the origin of ultrafast demagnetization. Nevertheless the electron-magnon spin-flip scattering does not lead itself to the change of the magnetization, in any case the angular momentum has to be transferred to the lattice, which means that an interaction with a phonon is required.

Superdiffusive hot carrier transport

Superdiffusive HC transport is the most recent microscopic model for ultrafast demagnetization, proposed by Battiato et al. [22, 23]. It does not consider transfer of the angular momentum, i.e spin flips, but describes the demagnetization process by spin-dependent transport of charge carriers out of a ferromagnetic layer. 'Superdiffusive' refers to HC transport which starts in the ballistic regime, but becomes diffusive on the time scale of several hundreds of femtoseconds.

According to the model of the superdiffusive HC transport, electrons are excited from quasi-localized d-bands to more mobile sp-bands. This excitation is assumed to be spin conserving. Subsequently, electrons move away from the excited part of the sample. Since the majority and minority electrons have different lifetimes, resulting in a larger mean free path for majority electrons, HC transport lead to the ultrafast demagnetization of the excited region.

2.3 Precessional magnetization dynamics

2.3.1 Homogeneous precession

Precessional motion of a magnetic moment $\vec{m}$ in an magnetic field $\vec{H}$ can be described by the Landau-Lifshitz equation [103]:

$$\frac{d\vec{m}}{dt} = -\gamma \left[\vec{m} \times \vec{H}\right], \tag{2.33}$$

where γ is the gyromagnetic ratio. For an electron with only the spin magnetic moment

$$\frac{\gamma}{2\pi} = g_s \frac{\mu_B}{h} \approx 28 \frac{\mathrm{GHz}}{\mathrm{T}}. \tag{2.34}$$

Considering a homogeneously magnetized ferromagnetic sample with a volume V and N magnetic moments, (2.33) can be written for the magnetization $\vec{M} = N\vec{m}/V$:

$$\frac{d\vec{M}}{dt} = -\gamma \left[\vec{M} \times \vec{H}_{eff}\right], \tag{2.35}$$

where $\vec{H}_{eff}$ is the effective magnetic field, which is the sum of the external magnetic field $\vec{H}_{ext}$, the field of the magneto-crystalline anisotropy $\vec{H}_{anis}$, shape anisotropy, and other sample and material dependent contributions. In the case of non-homogeneous variations of the magnetization $\vec{M}$, one has to consider the exchange field $\vec{H}_{ex}$ originating from the interaction of the neighbouring magnetic moments [104]. It will be considered in the next subsection.

In order to describe the relaxation of the precessional motion to the equilibrium ($\vec{M}_{eq}||\vec{H}_{eff}$), Gilbert suggested a damping term proportional to the magnetization change rate $d\vec{M}/dt$:

$$\frac{d\vec{M}}{dt} = -\gamma \left[\vec{M} \times \vec{H}_{eff}\right] + \frac{\alpha}{|\vec{M}|}\left[\vec{M} \times \frac{d\vec{M}}{dt}\right], \tag{2.36}$$

where α is a dimensionless damping parameter. Equation (2.36) is known as the Landau-Lifshitz-Gilbert (LLG) equation. It is valid for low temperatures and $|\vec{M}| = const.$

At higher temperatures, the change of the magnitude of the magnetization vector $\vec{M}$ can be taken into account, using the Landau-Lifshitz-Bloch (LLB) equation:

$$\frac{d\vec{M}}{dt} = -\gamma \left[\vec{M} \times \vec{H}_{eff}\right] + \gamma\lambda_{\parallel}\frac{\left(\vec{M} \cdot \vec{H}_{eff}\right) \cdot \vec{M}}{|\vec{M}|^2} - \gamma\lambda_{\perp}\frac{\left[\vec{M} \times \left[\vec{M} \times \vec{H}_{eff}\right]\right]}{|\vec{M}|^2}, \tag{2.37}$$

where $\lambda_{\parallel}$ and $\lambda_{\perp}$ are the dimensionless longitudinal and transversal damping parameters [26].

2.3.2 Spin waves

The previous subsection is devoted to a homogeneous precession of the magnetization, when all magnetic moments in a ferromagnetic film precess in-phase and the exchange interaction between them can be omitted from the consideration. In this subsection we consider more general case of collective spin excitation, so-called spin waves, when the neighbouring magnetic moments are not parallel to each other.

In the absence of an external magnetic field, the Hamiltonian for the system of the localized spins includes only the exchange interaction (2.8). The x-, y-, and z-components of the spin operators can be expressed by the Pauli spin matrices [33]:

$$\hat{S}_z = \frac{1}{2}\begin{pmatrix} 1 & 0 \\ 0 & -1 \end{pmatrix},\ \hat{S}_x = \frac{1}{2}\begin{pmatrix} 0 & 1 \\ 1 & 0 \end{pmatrix},\ \hat{S}_y = \frac{1}{2}\begin{pmatrix} 0 & -i \\ i & 0 \end{pmatrix}. \tag{2.38}$$

If we consider the eigenstates of $\hat{S}_z$

$$|\alpha\rangle = \begin{pmatrix} 1 \\ 0 \end{pmatrix},\ |\beta\rangle = \begin{pmatrix} 0 \\ 1 \end{pmatrix}, \tag{2.39}$$

then

$$\hat{S}_z|\alpha\rangle = \frac{1}{2}|\alpha\rangle,\ \hat{S}_z|\beta\rangle = -\frac{1}{2}|\beta\rangle. \tag{2.40}$$

From $\hat{S}_x$, $\hat{S}_y$ we can switch to the spin reversal operators:

$$\hat{S}_+ = S_x + iS_y = \begin{pmatrix} 0 & 1 \\ 0 & 0 \end{pmatrix} \text{ and } \hat{S}_- = S_x - iS_y = \begin{pmatrix} 0 & 0 \\ 1 & 0 \end{pmatrix} \tag{2.41}$$

which act on the states $|\alpha\rangle$ and $|\beta\rangle$ in the following way

$$S_+|\alpha\rangle = 0,\ S_+|\beta\rangle = |\alpha\rangle,\ S_-|\beta\rangle = 0,\ S_-|\alpha\rangle = \beta\rangle. \tag{2.42}$$

Considering the exchange coupling J_{ex} between the nearest neighbours, (2.8) can be rewritten as

$$\hat{H} = -J_{ex}\sum_i\sum_\delta \hat{S}_{i,z}\cdot\hat{S}_{i+\delta,z} + \frac{1}{2}(\hat{S}_{i,+}\hat{S}_{i+\delta,-} + \hat{S}_{i,-}\hat{S}_{i+\delta,+}), \tag{2.43}$$

where the first sum (index i) is the sum over all spins, and the second sum (index δ) corresponds to the sum over the nearest neighbours of the spin i. In the case of the ferromagnetic coupling $J_{ex} > 0$, in the ground state all spins are aligned in the same direction:

$$|0\rangle = \prod_i |\alpha\rangle_i. \tag{2.44}$$

Applying $S_{j,-}$ to the ground state, we obtain a state $|\beta_j\rangle$ with a reversed spin j. This state is not an eigenstate of the Hamiltonian (2.43), because the operators $\hat{S}_{i,+}\hat{S}_{i+\delta,-}$ bring the system to the state $|\beta_{j+\delta}\rangle$. However, the linear combination of such states

$$|\vec{k}\rangle = \frac{1}{\sqrt{N}}\sum_j e^{i\vec{k}\cdot\vec{r}_j}|\beta_j\rangle \tag{2.45}$$

is an eigenstate. This state represents a spin wave: all spins precess around the z axis with a phase shift between different spins, determined by the wave-vector $\vec{k}$. Excitation of a spin wave flips on average one spin.

When the $|\vec{k}|$ is small compared to a reciprocal lattice vector, but large compared to ω/c, where ω is the spin wave frequency, one can use the magnetostatic approximation and describe spin waves with the classical equations of motion. Instead of single spins, one can switch to the continuous model with a space- and time-dependent magnetization $\vec{M}(\vec{r},t)$. When neighbouring magnetic moments are not parallel to each other, it leads to an increase of the exchange energy and an additional contribution to the effective field [104]:

$$\vec{H}_{ex}^{nonuniform} = \frac{D}{M_0}\nabla^2\vec{M}, \tag{2.46}$$

where D is the exchange stiffness (for Fe $D = 280$ Å$^2\cdot meV$ [107, 108]).

Solving the Landau-Lifshitz equation (2.35) with $\vec{H}_{eff} = \vec{H}_{ext} + \vec{H}_{an} + \vec{H}_{dem}$ for an isotropic ferromagnet with the saturation magnetization M_s, one can derive the spin wave dispersion relation [104]:

$$f(k) = \gamma\sqrt{(H_{ext} + H_{anis} + Dk^2)\cdot(H_{ext} + H_{anis} + 4\pi M_s\sin^2\theta_k + Dk^2)}, \tag{2.47}$$

where θ_k is the angle between $\vec{M}_s$ and $\vec{k}$. In the present work we will consider precessional magnetization dynamics in a thin ferromagnetic film with free magnetic moments at its boundary (no pinning).:

$$\frac{\partial\Delta\vec{M}}{\partial z}|_{z=0} = \frac{\partial\Delta\vec{M}}{\partial z}|_{z=d} = 0, \tag{2.48}$$

where $\Delta\vec{M} = \vec{M} - \vec{M}_0$, and d is the film thickness. The boundary conditions (2.48) determine normal spin wave modes: $k = \pi n/d$ ($n = 0,\ 1,\ 2,\ \ldots$).

In the following subsections, we discuss the mechanisms of the laser-induced magnetization precession.

2.3.3 Laser-induced spin precession

There is a variety of mechanisms governing laser-induced spin precession [26]:

- exchange quenching,
- phonon-magnon coupling,
- photoinduced magnetic phase transition,
- invervse Faraday effect,
- impulsive stimulated Raman scattering,
- laser-induced heating,
- spin current injection (Spin Transfer Torque).

However, only two last mechanisms are of great interest in the present work.

Laser-induced heating

As it was already mentioned, the effective magnetic field $\vec{H}_{eff}$ acting on a magnetization $\vec{M}$ of a ferromagnetic film is the sum of the external magnetic field $\vec{H}_{ext}$ and the field of the magneto-crystalline anisotropy. In the static regime without the external magnetic field $\vec{H}_{ext} = 0$, the magnetization $\vec{M}$ is aligned parallel to one of the easy axes. Applying the external magnetic field $\vec{H}_{ext}$ in a different direction brings the magnetization to a new equilibrium orientation $\vec{M}_{eq}$ determined by the effective field $\vec{H}_{eff} = \vec{H}_{anis} + \vec{H}_{ext}$ (see Figure 2.8(a)).

Optical excitation of the ferromagnetic film with the laser pulse leads to an increase of the film temperature and a decrease of the magnetization value. It results in a change of the magneto-crystalline anisotropy, and consequently in a variation of the effective field direction. If this process is fast enough, the magnetization vector $\vec{M}$ is not able to follow the effective magnetic field $\vec{H}_{eff}$ and starts to precess around its new equilibrium direction. Subsequently the equilibrium direction slowly recovers to its initial orientation due to the heat diffusion away from the optically excited area. Thus a non-collinear mutual orientation of $\vec{H}_{ext}$ and $\vec{H}_{anis}$ is essential to modify direction of $\vec{H}_{eff}$ and drive magnetic precession.

In ferromagnetic films with thicknesses larger than the light penetration depth [7], the laser absorption profile is non-uniform, which makes possible to excite not only homogeneous precession, but also higher standing spin wave modes [18].

[7] For Fe and $\hbar\omega = 1.5$ eV the light penetration depth is ~ 17 nm.

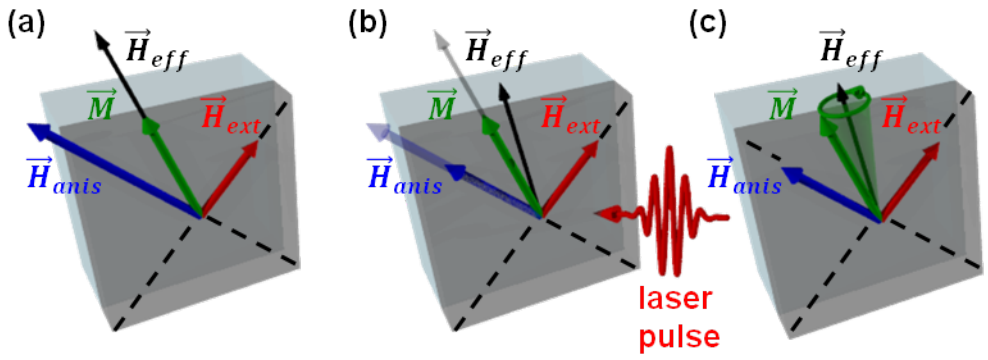

Figure 2.8: Optical excitation of the coherent magnetization precession in a bcc-Fe film grown on a MgO(001) substrate. (a) In the absence of the pump laser pulse ($t < 0$) the magnetization $\vec{M}$ (green arrow) of the Fe film is in equilibrium, and its direction is determined by the effective magnetic field $\vec{H}_{eff}$ (red arrow), i.e. the sum of the external magnetic field $\vec{H}_{ext}$ and the field $\vec{H}_{anis}$ (blue arrow) of the magneto-crystalline anisotropy. (b) Absorption of the pump laser pulse ($0 < t < 1$ ps) heats up the Fe film, resulting in a decrease of the magneto-crystalline anisotropy $\vec{H}_{anis}$. Hence $\vec{H}_{eff}$ also changes, altering the equilibrium direction of the magnetization. (c) The magnetization of the Fe film precesses around $\vec{H}_{eff}$ which slowly recovers to its initial orientation due to the heat diffusion away from the optically excited area. Dash lines depict direction of the easy axes. This figure was redrawn after [26, 105].

Spin transfer torque

In the context of this work, another important mechanism to drive magnetization precession in a ferromagnetic is so-called spin transfer torque (STT). In 1996 Slonczewski [6] and Berger [7] predicted theoretically that current of spin-polarized electrons can transfer its angular momentum to a ferromagnetic film and thereby exert a torque on its magnetization. When an electron with a certain SP penetrates into a ferromagnetic film, its magnetic moment becomes parallel to the magnetization (see Figure 2.9(a)). Considering the ferromagnetic film and the injected electron as a closed system, the total angular momentum is conserved. Thus the change of the angular momentum of the injected electron is compensated by the opposite change of the angular momentum of other electrons in the ferromagentic film. As a result, local magnetization $\vec{M}_{local}$ in the volume of the ferromagnetic film, where the injected electron alters its SP $\vec{\sigma}_{SC}$, tilts towards $\vec{\sigma}_{SC}$ and then starts to precess around the initial direction $\vec{M}_S$ (see Figure 2.9(b)). The SC can be produced either by the electric current flowing through a ferromagnet into a non-magnetic metal or by laser excitation of the ferromagnetic film, followed by an efficient transport of the spin-polarized HCs [106].

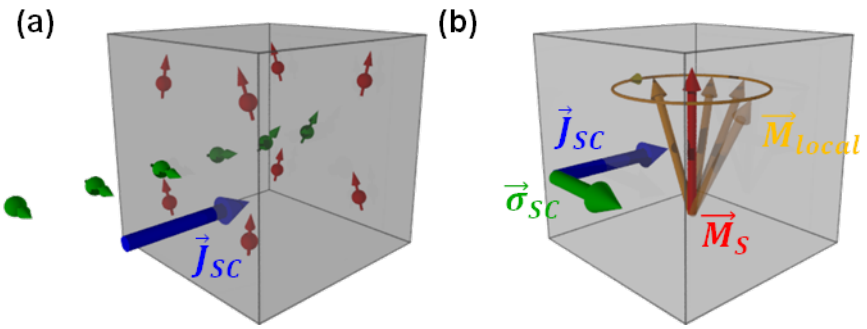

Figure 2.9: (a) Microscopic and (b) macroscopic illustrations of the spin transfer torque (STT). Spin current (SC) $\vec{J}_{SC}$ (blue) can be expressed as a flux of the electrons (green) with the magnetic moments aligned in a certain direction $\vec{\sigma}_{SC}$ (green) which defines SP of the SC. In the absence of the SC, magnetic moments of the electrons (red) in a ferromagnetic film precess around the direction of the magnetization $\vec{M}_S$ (red). When spin-polarized electrons (green) forming the SC $\vec{J}_{SC}$ penetrate into the ferromagnetic film, their magnetic moments tilt towards the magnetization $\vec{M}_S$. Due to the conservation of the angular momentum, a local magnetization $\vec{M}_{local}$ (orange) in the region close to the interface tilts towards $\vec{\sigma}_{SC}$ and starts to precess aroung $\vec{M}_S$.

The influence of the SC on the magnetization of the ferromagnetic film can described by an additional term in the LLG equation (2.36):

$$\frac{d\vec{M}}{dt} = -\gamma\left[\vec{M}\times\vec{H}_{eff}\right] + \frac{\alpha}{|\vec{M}|}\left[\vec{M}\times\frac{d\vec{M}}{dt}\right] + \gamma\frac{J_S}{|\vec{M}|}\left[\vec{M}\times[\vec{\sigma}\times\vec{M}]\right], \tag{2.49}$$

where J_S is the density of the SC, $\vec{\sigma}$ is a unit vector along the polarization direction of the spin current. The first and the last terms in (2.49) behaves differently upon the reversal of the external magnetic field $\vec{H}_{eff}$, static magnetization $\vec{M}_s$ or the polarization direction $\vec{\sigma}$ of the spin current. This circumstance makes it possible to disentangle magnetization dynamics induced by laser-induced heating or laser-induced transport of the spin-polarized HCs. It will be demonstrated in **Chapter 8**.

Chapter 3

Time-resolved magneto-optical probe techniques

In this work variations of magnetization upon laser excitation of the metallic multilayer (ML) structures have been studied on a sub-picosecond time scale. To gain access to this ultrafast dynamics, magneto-optical pump-probe techniques have been applied, employing an intense laser pulse to excite the system and a weak probe pulse to measure its response. This chapter provides an insight into the linear magneto-optical Kerr effect (MOKE) proportional to the bulk magnetization and the magneto-induced second harmonic generation (mSHG) which is primarily sensitive to the spin polarization (SP) at surfaces and interfaces in the case of centrosymmetrical materials, but it can also possess bulk contributions upon inhomogeneous hot carrier (HC) and spin dynamics.

After general introduction into the theory of light-matter interaction, phenomenological description, macro- and microscopic formalisms of the static MOKE and mSHG responses are discussed. The last section is devoted to the interpretation of the HC and spin dynamics probed with these two techniques.

3.1 Light-matter interaction

Theory of light-matter interaction is based on the electromagnetic wave equations and the equations which describe properties of media. The electromagnetic wave equations are the Maxwell's equations:

$$\vec{\nabla} \cdot \vec{D} = 4 \cdot \pi \cdot \rho, \tag{3.1}$$

$$\vec{\nabla} \cdot \vec{B} = 0, \tag{3.2}$$

$$\vec{\nabla} \times \vec{E} = -\frac{1}{c}\frac{\partial \vec{B}}{\partial t}, \tag{3.3}$$

$$\vec{\nabla} \times \vec{H} = \frac{1}{c}\frac{\partial \vec{D}}{\partial t} + \frac{4\pi}{c}\vec{j}, \tag{3.4}$$

where $\vec{E}$, $\vec{D}$ are electric field and electric inductance, $\vec{H}$, $\vec{B}$ are magnetic field and magnetic inductance, ρ is a free charge density, $\vec{j}$ is a current density. The Maxwell's

equations are completed with the constitutive relations

$$\begin{aligned} &\vec{D} = \vec{E} + 4\pi\vec{P}, \quad \vec{P} = \vec{P}(\vec{E}), \\ &\vec{B} = \vec{H} + 4\pi\vec{M}, \quad \vec{M} = \vec{M}(\vec{H}), \\ &\vec{j} = \vec{j}(\vec{E}). \end{aligned} \tag{3.5}$$

These relations describe the response of the medium to electromagnetic field: appearance of polarization $\vec{P}$, magnetization $\vec{M}$ and conduction current $\vec{j}$.

The induced polarization $\vec{P}$ to the electric field $\vec{E}$ of the incident laser pulse is given by [109]

$$\begin{aligned} \vec{P}(\vec{r},t) = &\int_0^{+\infty} dt_1 \int_{-\infty}^{+\infty} \chi^{(1)}(\vec{r}-\vec{r}_1, t-t_1)\vec{E}(\vec{r}_1,t_1)d\vec{r}_1 \\ &+ \int_0^{+\infty} dt_1 dt_2 \int_{-\infty}^{+\infty} \chi^{(2)}(\vec{r}-\vec{r}_1, \vec{r}-\vec{r}_2, t-t_1, t-t_2)\vec{E}(\vec{r}_1,t_1)\vec{E}(\vec{r}_2,t_2)d\vec{r}_1\vec{r}_2 + \ldots, \end{aligned} \tag{3.6}$$

where $\chi^{(n)}$ is the n-th order optical susceptibility tensor of rank $(n+1)$. Here one can note that $\chi^{(n)}$ has nonlocal and non-instantaneous character. It means that the polarization $\vec{P}$ is not a point-like characteristic of a medium and does not change simultaneously with the applied electric field $\vec{E}$. The limits of the time integrals in (3.6) are determined by the causality principle ($t - t_1 > 0$, $t - t_2 > 0$), i.e. only $\vec{E}$ in the past moments affects the current value of $\vec{P}$.

From the Maxwell's equations (3.1), (3.2), (3.3), (3.4) one can derive the optical wave equation for the electric field $\vec{E}(\vec{r},t)$ [109]:

$$\left[\vec{\nabla} \times (\vec{\nabla}\times) + \frac{1}{c^2}\frac{\partial^2}{\partial t^2}\right] \vec{E}(\vec{r},t) = -\frac{4\pi}{c^2}\frac{\partial^2}{\partial t^2}\vec{P}(\vec{r},t). \tag{3.7}$$

Let us assume that the electric field $\vec{E}(\vec{r},t)$ can be expressed as the sum of the monochromatic plane waves:

$$\vec{E}(\vec{r},t) = \sum_l \vec{E}_l(k_l,\omega_l) = \sum_l \vec{\mathcal{E}}_l e^{i(\vec{k}_l\cdot\vec{r}-\omega_l t}. \tag{3.8}$$

If the polarization $\vec{P}(\vec{r},t)$ is a linear function of $\vec{E}(\vec{r},t)$:

$$\vec{P}(\vec{r},t) = \vec{P}^{(1)}(\vec{r},t) = \sum_l \vec{P}_l(k_l,\omega_l) = \sum_l \chi^{(1)}(\omega_l)\vec{E}_l(\vec{k}_l,\omega_l), \tag{3.9}$$

the wave equation (3.7) can be rewritten as a system of the decoupled equations for each frequency component:

$$\left[\vec{\nabla} \times (\vec{\nabla}\times) - \frac{\omega_l^2}{c^2}\varepsilon(\omega_l)\right] \vec{E}_l(\vec{k}_l,\omega) = 0, \tag{3.10}$$

where $\varepsilon(\omega_l) = 1 + 4\pi\chi^{(1)}(\omega_l)$. It means that in this case all monochromatic plane waves propagate in a medium independently from each other and do not produce new frequencies. Instead of the discrete set of the monochromatic waves (3.8), one can consider a wave with a continuous spectrum:

$$E(t) = \frac{1}{2\pi}\int_{-\infty}^{\infty}\tilde{E}(\Omega)e^{i\Omega t}d\Omega, \tag{3.11}$$

where

$$\tilde{E}(\Omega) = \int_{-\infty}^{\infty}E(t)e^{-i\Omega t}dt = |\tilde{E}(\Omega)|e^{i\Phi(\Omega)}. \tag{3.12}$$

(3.11) and (3.12) are known as the inverse and direct Fourier transforms, respectively. $|\tilde{E}(\Omega)|$ is the spectral amplitude, and $\Phi(\Omega)$ is the spectral phase. Since $E(t)$ is a real function, $\tilde{E}(\Omega) = \tilde{E}^*(-\Omega)$.

Presence of the nonlinear terms in the relation (3.6) between $\vec{E}(\vec{r},t)$ and $\vec{P}(\vec{r},t)$ results in the interaction of the different spectral components and the generation of new ones. For instance, the second order susceptibility $\chi^{(2)}$ leads to such effects like second harmonic generation ($2\omega = \omega + \omega$), sum-frequency generation ($\omega = \omega_1 + \omega_2$), difference-frequency generation ($2\omega = \omega_1 - \omega_2$) and optical rectification ($0 = \omega - \omega$. In the following sections, we will consider only the linear MOKE and the mSHG.

3.2 Magneto-optical Kerr effect

In 1845 Michael Faraday found that the polarization of light propagating through a magnetized medium undergoes rotation by an angle proportional to the applied magnetic field [110]. Then thirty two years later John Kerr discovered that the same effect can be observed also in reflection [111].

3.2.1 Phenomenological description and macroscopic formalism

Macroscopic description of the MOKE is based on an analysis of the dielectric tensor. For a medium which is isotropic in the absence of the magnetization, the dielectric tensor can be written in the form [46]

$$\tilde{\varepsilon} = \varepsilon \cdot \begin{pmatrix} 1 & i\cdot Q_z & -i\cdot Q_y \\ -i\cdot Q_z & 1 & i\cdot Q_x \\ i\cdot Q_y & -i\cdot Q_x & 1 \end{pmatrix} \tag{3.13}$$

where $\vec{Q} = (Q_x, Q_y, Q_z)$ is the Voigt vector [112], proportional to the magnetization $\vec{M}$. It can be expressed as a product of the Voigt constant q and the magnetization $\vec{M}$:

$$\vec{Q} = q \cdot \vec{M}. \tag{3.14}$$

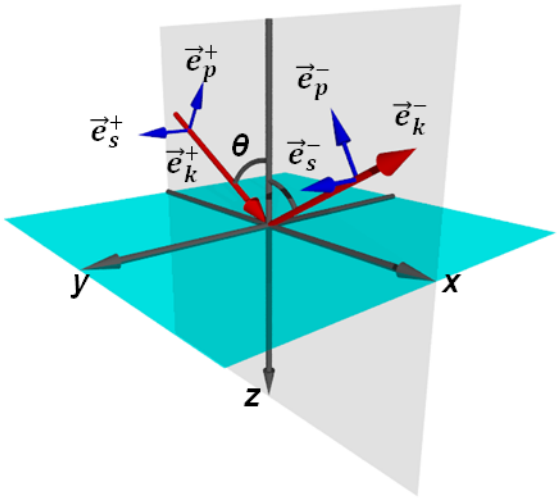

Figure 3.1: Coordinate system. The xy-plane is the boundary between two media. The xz-plane is the plane of incidence.'+' and '-' denote incident and reflected waves, respectively. Set $(\vec{e}_p, \vec{e}_s, \vec{e}_k)$ defines local coordinate system for each wave. Vector $\vec{e}_k$ is a unit vector along the wave vector $\vec{k}$. Vectors $\vec{e}_p$ and $\vec{e}_s$ are unit vectors along p and s directions which are perpendicular to $\vec{e}_k$, parallel and perpendicular to the plane of incidence, respectively.

Considering a wave $\sim \exp(ikx - i\omega t)$ and assuming that the magnetic permeability is 1, the relations between $\vec{D}$ and $\vec{E}$, $\vec{B}$ and $\vec{H}$, are

$$\vec{D} = \varepsilon\vec{E} + i\varepsilon\vec{E} \times \vec{Q} \text{ and } \vec{B} = \vec{H}. \tag{3.15}$$

Then the Maxwell's equations give

$$\begin{aligned} &\vec{k} \cdot \vec{E} + i\vec{k} \cdot \left[\vec{E} \times \vec{Q}\right] = 0, \\ &\vec{k} \times \vec{E} = \frac{\omega}{c}\vec{H}, \\ &\vec{k} \cdot \vec{H} = 0, \\ &\vec{k} \times \vec{H} = -\frac{\omega\varepsilon}{c}\left(\vec{E} + i\vec{E} \times \vec{Q}\right). \end{aligned} \tag{3.16}$$

While $\vec{D}$, $\vec{H}$ and $\vec{k}$ are perpendicular to each other, $\vec{E}$ has a component parallel to the wave vector $\vec{k}$. In the local coordinate system the electric field can be written as

$$\vec{E} = E_p\vec{e}_p + E_s\vec{e}_s + i(-E_pQ_s + E_sQ_p)\vec{e}_k, \tag{3.17}$$

where $\vec{e}_p$, $\vec{e}_s$ and $\vec{e}_k$ are unit vectors along the p, s and k directions (see Figure 3.1). For the s and p components of the electric field the equations of motion are

$$\begin{aligned} \left(\frac{\omega^2\varepsilon}{c^2} - k^2\right)E_p + i\frac{\omega^2\varepsilon}{c^2}\left(\vec{Q} \cdot \vec{e}_k\right)E_s = 0, \\ -i\frac{\omega^2\varepsilon}{c^2}\left(\vec{Q} \cdot \vec{e}_k\right)E_p + \left(\frac{\omega^2\varepsilon}{c^2} - k^2\right)E_s = 0. \end{aligned} \tag{3.18}$$

To the first order in Q, the normal modes are right (R) and left (L) circularly polarized modes with

$$k_{R,L} = k\left(1 \pm \frac{1}{2}\vec{Q}\cdot\vec{e}_k\right), \text{ and } n_{R,L} = n\left(1 \pm \frac{1}{2}\vec{Q}\cdot\vec{e}_k\right), \tag{3.19}$$

where $k = (\omega/c)\sqrt{\varepsilon}$ and $n = \sqrt{\varepsilon}$ are the wave vector and refractive index without magnetization. In the local coordinate the relations between the s and p components of the R and L modes are

$$E_p^R = iE_s^R, \quad E_p^L = -iE_s^L. \tag{3.20}$$

P-polarized light can be expressed as a superposition of the R and L modes. Upon the reflection from a magnetic material the difference between refractive indices of the right and left circularly polarized components give rise to the in-phase S-polarized component which leads to the rotation of the polarization, and the out-of-phase S-polarized component which leads to the ellipticity.

To simulate reflection and transmission of a multilayer system we use an approach based on the medium boundary and propagation matrices [27, 28].

The medium boundary matrix describes the relation between the x and y components of $\vec{E}$ and $\vec{H}$ with p and s components of the electric field:

$$\begin{pmatrix} E_x \\ E_y \\ H_x \\ H_y \end{pmatrix} = A \begin{pmatrix} E_p^+ \\ E_s^+ \\ E_p^- \\ E_s^- \end{pmatrix}, \tag{3.21}$$

where A is the medium boundary matrix:

$$A = \begin{pmatrix} \cos\theta - iQ_y\sin\theta & \frac{i}{2}\left[\tan\theta(1+\cos^2\theta)Q_x - Q_z\sin^2\theta\right] & -\cos\theta - iQ_y\sin\theta & \frac{i}{2}\left[-\tan\theta(1+\cos^2\theta)Q_x - Q_z\sin^2\theta\right] \\ 0 & 1 & 0 & 1 \\ \frac{in}{2}(Q_x\tan\theta + Q_z) & -n\cos\theta & \frac{in}{2}(-Q_x\tan\theta + Q_z) & n\cos\theta \\ n & \frac{in}{2}(Q_x\sin\theta + Q_z\cos\theta) & n & \frac{in}{2}(Q_x\sin\theta - Q_z\cos\theta) \end{pmatrix}. \tag{3.22}$$

'+' and '-' denote the waves propagating in the positive and negative directions with respect to the $\hat{z}$ axis.

The medium propagation matrix describes the relations between E_p and E_s at the boundaries z and $z + d$ of the layer with thickness d:

$$\begin{pmatrix} E_p^+ \\ E_s^+ \\ E_p^- \\ E_s^- \end{pmatrix}_z = \overline{D} \begin{pmatrix} E_p^+ \\ E_s^+ \\ E_p^- \\ E_s^- \end{pmatrix}_{z+d}, \tag{3.23}$$

where $\overline{D}$ is the medium propagation matrix:

$$\overline{D} = S^{-1}DS \tag{3.24}$$

with the matrix S expressing the relations between the y components of the R and L modes and the p and s components of the electric field

$$\begin{pmatrix} E_y^{+,R} \\ E_y^{+,L} \\ E_y^{-,R} \\ E_y^{-,L} \end{pmatrix} = S \begin{pmatrix} E_p^{+} \\ E_s^{+} \\ E_p^{-} \\ E_s^{-} \end{pmatrix} = \frac{1}{2} \begin{pmatrix} -i & 1 & 0 & 0 \\ i & 1 & 0 & 0 \\ 0 & 0 & -i & 1 \\ 0 & 0 & i & 1 \end{pmatrix} \begin{pmatrix} E_p^{+} \\ E_s^{+} \\ E_p^{-} \\ E_s^{-} \end{pmatrix}, \tag{3.25}$$

and the matrix D expressing the relations between the y components of the R and L modes at the boundaries z and $z+d$

$$\begin{pmatrix} E_y^{+,R} \\ E_y^{+,L} \\ E_y^{-,R} \\ E_y^{-,L} \end{pmatrix}_z = D \begin{pmatrix} E_y^{+,R} \\ E_y^{+,L} \\ E_y^{-,R} \\ E_y^{-,L} \end{pmatrix}_{z+d}, \tag{3.26}$$

$$D = \begin{pmatrix} \exp(-ik_R^+ d\cos\theta_R^+) & 0 & 0 & 0 \\ 0 & \exp(-ik_L^+ d\cos\theta_L^+) & 0 & 0 \\ 0 & 0 & \exp(-ik_R^- d\cos\theta_R^-) & 0 \\ 0 & 0 & 0 & \exp(-ik_L^- d\cos\theta_L^-) \end{pmatrix}. \tag{3.27}$$

Knowing the A and D matrices allows to calculate the magneto-optical response of a multilayer structure, which consists of N layers. If we consider a beam of light incoming from the initial medium i, a beam reflected back to the initial medium i and a beam transmitted into the final medium f will be a result of multiple reflections.

The electric fields in the media i and f can be expressed as

$$\begin{pmatrix} E_p^{+} \\ E_s^{+} \\ E_p^{-} \\ E_s^{-} \end{pmatrix}_i = \begin{pmatrix} E_p^{+} \\ E_s^{+} \\ r_{pp}E_p^{+} + r_{ps}E_s^{+} \\ r_{sp}E_p^{+} + r_{ss}E_s^{+} \end{pmatrix} \text{ and } \begin{pmatrix} E_p^{+} \\ E_s^{+} \\ 0 \\ 0 \end{pmatrix}_f = \begin{pmatrix} t_{pp}E_p^{+} + t_{ps}E_s^{+} \\ t_{sp}E_p^{+} + t_{ss}E_s^{+} \\ 0 \\ 0 \end{pmatrix} \tag{3.28}$$

Here r and t are the reflection and transmission coefficients for p- and s-polarized components. Since E_x, E_y, H_x and H_y are continuous at each interface, the relation between the electric fields in the media i and f can be derived as

$$A_i \begin{pmatrix} E_p^{+} \\ E_s^{+} \\ E_p^{-} \\ E_s^{-} \end{pmatrix}_i = \prod_{m=1}^{N} \left(A_m D_m A_m^{-1}\right) A_f \begin{pmatrix} E_p^{+} \\ E_s^{+} \\ E_p^{-} \\ E_s^{-} \end{pmatrix}_f \tag{3.29}$$

$$\begin{pmatrix} E_p^{+} \\ E_s^{+} \\ E_p^{-} \\ E_s^{-} \end{pmatrix}_i = A_i^{-1} \prod_{m=1}^{N} \left(A_m D_m A_m^{-1}\right) A_f \begin{pmatrix} E_p^{+} \\ E_s^{+} \\ E_p^{-} \\ E_s^{-} \end{pmatrix}_f \tag{3.30}$$

To simplify the expressions, we introduce the layer matrix C_m:

$$C_m = A_m D_m A_m^{-1}. \tag{3.31}$$

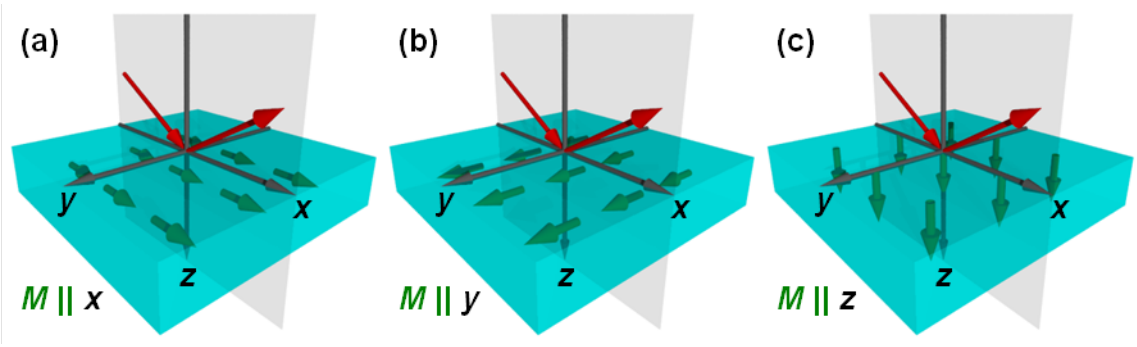

Figure 3.2: Three magneto-optical configurations: (a) longitudinal, (b) transversal, and (c) transversal.

So the expression can rewritten as

$$\begin{pmatrix} E_p^+ \\ E_s^+ \\ E_p^- \\ E_s^- \end{pmatrix}_i = A_i^{-1} \prod_{m=1}^{N} C_m A_f \begin{pmatrix} E_p^+ \\ E_s^+ \\ E_p^- \\ E_s^- \end{pmatrix}_f \tag{3.32}$$

Finally the matrix T

$$T = A_i^{-1} \prod_{m=1}^{N} (C_m)\, A_f = \begin{pmatrix} G & H \\ I & J \end{pmatrix} \tag{3.33}$$

The 2×2 matrices G and I can be used to obtain the reflection and transmission coefficients:

$$G^{-1} = \begin{pmatrix} t_{pp} & t_{ps} \\ t_{sp} & t_{ss} \end{pmatrix} \text{ and } IG^{-1} = \begin{pmatrix} r_{pp} & r_{ps} \\ r_{sp} & r_{ss} \end{pmatrix} \tag{3.34}$$

The Kerr rotation ψ'_K and ellipticity ψ''_K for s- and p-polarized light are given by

$$\psi_{K,p} = \psi'_{K,p} + i\psi''_{K,p} = \frac{r_{sp}}{r_{pp}} \text{ and } \psi_{K,s} = \psi'_{K,s} + i\psi''_{K,s} = \frac{r_{ps}}{r_{ss}} \tag{3.35}$$

Depending on the direction of the magnetization, there are three configurations of the magneto-optical Kerr effect: longitudinal ($\vec{M}\|\hat{x}$), transversal ($\vec{M}\|\hat{y}$) and polar ($\vec{M}\|\hat{z}$) configurations (see Figure 3.2). The transversal MOKE depends on the second order terms in Q and results in a change of reflectivity. The polar MOKE is usually an order of magnitude larger than the longitudinal one, because in the final expression for the Kerr angle Q_z appears with an n^2 enhancement factor [46]. Another important difference between the polar (POL) and longitudinal (LON) MOKE is a relation between the polarization changes of the initially p- and s-polarized waves [27]:

$$r_{ps}^{POL} = r_{sp}^{POL}, \quad r_{ps}^{LON} = -r_{sp}^{LON}. \tag{3.36}$$

Thus using p- and s-polarized probe pulses, it is possible to disentangle the polar and longitudinal contributions to the MOKE signal.

3.2.2 Microscopic formalism

In 1955 Argyres showed that the Kerr effect is caused by the combined action of the exchange interaction and spin-orbit coupling [113]. The spin-orbit coupling acts on the electrons like an external magnetic field, which results in the rotation of the polarization of the linearly polarized light. However, if clockwise and counterclockwise rotations are equally probable, they will cancel each other, meaning that the spin-orbit interaction alone is not enough. In paramagnetic materials in the absence of the external magnetic field, there is no MOKE signal. In ferromagnets the exchange interaction splits the electronic band structure into the majority and minority sub-bands. The densities of states at the fixed energy are different in these sub-bands, therefore the Kerr rotations for majority and minority electrons no longer cancel each other, and a non-zero MOKE signal can be observed. Thus it can be deduced that qualitatively the MOKE is proportional to the difference in the optical transition rates in the majority and minority sub-bands [114].

Following the self-consistent-field approach suggested by Ehrenreich and Cohen [115], one can obtain the expression for the off-diagonal terms of the linear susceptibility [114]:

$$\begin{aligned}&\chi_{xy}^{(1)}(q,\omega,M_z) = -\chi_{yx}^{(1)}(q,\omega,M_z)\\ &= \frac{4\pi e^2}{V}\frac{\lambda_{s.o.}}{\hbar\omega}\sum_{k,l,l',\sigma}\left(\langle k+q,l',\sigma|y|kl\sigma\rangle\langle kl\sigma|x|k+q,l'\sigma\rangle\frac{f(E_{k+q,l'\sigma})-f(E_{kl\sigma})}{E_{k+q,l'\sigma}-E_{kl\sigma}-\hbar\omega+i\hbar\alpha_1}\right),\end{aligned} \tag{3.37}$$

where $\lambda_{s.o.}$ is the spin-orbit coupling constant. Majority and minority energy sub-bands $E_{kl\sigma}$ are denoted with σ. $|kl\sigma\rangle = \frac{1}{V}u_{kl\sigma}e^{ik\cdot r}$ are the Block states of the wave-vector $\vec{k}$ and spin σ in the l-th band, V is the volume, $\vec{q}$ is the photon wave-vector, and α_1 is the experimental resolution. The off-diagonal term $\chi_{xy}^{(1)}$ is responsible for the polar Kerr rotation [114]:

$$\psi_K^{POL} = \psi_K' + i\psi_K'' = -\frac{\chi_{xy}^{(1)}}{\chi_{xx}^{(1)}\sqrt{1+4\pi\chi_{xx}^{(1)}}}. \tag{3.38}$$

If $\vec{M}\|\hat{z}$, all other off-diagonal elements vanish because of the selection rules.

3.3 Magneto-induced Second Harmonic Generation

In addition to the linear MOKE, one can also use non-linear magneto-optical techniques as magnetization-induced Second Harmonic Generation (mSHG) to monitor magnetization dynamics. Initially sensitivity of the surface/interface SHG to magnetization was theoretically predicted by Pan et al. in 1989 [116]. Then in 1991 it was experimentally demonstrated on a Fe(110) surface by Reif et al. [117].

3.3.1 Macroscopic formalism

SHG arises from the nonlinear polarization $P(2\omega)$ induced by the incident laser field $E(\omega)$. In the electric dipole approximation the polarization $P(2\omega)$ can be written as

$$\vec{P}(2\omega) = \chi^{(2,D)}\vec{E}(\omega)\vec{E}(\omega). \tag{3.39}$$

The susceptibility tensor $\chi^{(2)}$ has 27 components. Since $\chi^{(2)}_{ijk} \equiv \chi^{(2)}_{ikj}$, the number of the independent components can be reduced to 18, and the expression (3.39) can be rewritten in the following matrix form:

$$\begin{pmatrix} P_x \\ P_y \\ P_z \end{pmatrix} = \begin{pmatrix} \chi_{xxx} & \chi_{xyy} & \chi_{xzz} & \chi_{xzy} & \chi_{xzx} & \chi_{xxy} \\ \chi_{yxx} & \chi_{yyy} & \chi_{yzz} & \chi_{yzy} & \chi_{yzx} & \chi_{yxy} \\ \chi_{zxx} & \chi_{zyy} & \chi_{zzz} & \chi_{zzy} & \chi_{zzx} & \chi_{zxy} \end{pmatrix} \begin{pmatrix} E_xE_x \\ E_yE_y \\ E_zE_z \\ 2E_yE_z \\ 2E_xE_z \\ 2E_xE_y \end{pmatrix}. \tag{3.40}$$

Symmetry considerations show that the dipole contribution is zero in the bulk of a centrosymmetric medium, thereby limiting the electric dipole radiation to the surfaces and interfaces where the inversion symmetry is broken. The HC and spin transport may give rise to the bulk contributions which will be addressed in the last section of this chapter.

Metallic multilayer structures studied in the present work consist of the epitaxial Fe(001) and Au(001) films grown on the MgO substrate on the top of each other. Without magnetization the (001) surface has 4mm symmetry (C_{4v}). Because magnetization $\vec{M}$ is an axial vector which conserves its orientation under the spatial inversion operation, its presence will not affect the inversion symmetry. Nevertheless, $\vec{M}$ does lower the symmetry of the film surface, introducing more non-zero tensor components than in the case of the non-magnetic surfaces and interfaces [116]. The non-zero elements of $\chi^{(2)}(M)$ can be obtained from the invariance of $\chi^{(2)}(M)$ under the symmetry operations. Thus if the xz is the plane of incidence, for the (001) surface we find [116, 118]

$$\chi^{(2)} = \begin{pmatrix} \chi^{odd}_{xxx}(M_y) & \chi^{odd}_{xyy}(M_y) & \chi^{odd}_{xzz}(M_y) & \chi^{odd}_{xzy}(M_z) & \chi^{even}_{xzx} & \chi^{odd}_{xxy}(M_x) \\ \chi^{odd}_{yxx}(M_x) & \chi^{odd}_{yyy}(M_x) & \chi^{odd}_{yzz}(M_x) & \chi^{even}_{yzy} & \chi^{odd}_{yzx}(M_z) & \chi^{odd}_{yxy}(M_y) \\ \chi^{even}_{zxx} & \chi^{even}_{zyy} & \chi^{even}_{zzz} & \chi^{odd}_{zzy}(M_x) & \chi^{odd}_{zzx}(M_y) & \chi^{odd}_{zxy}(M_z) \end{pmatrix}, \tag{3.41}$$

where the even terms always contribute to the mSHG signal, while the odd terms depends on the corresponding projection of the magnetization vector $\vec{M}$. For the analysis it is useful to separate the even and odd terms:

$$\hat{\chi}^{(2)} = \hat{\chi}^{(2),even} + \hat{\chi}^{(2),odd}. \tag{3.42}$$

In the first approximation, the even term $\chi^{(2),even}$ is independent of the magnetization, and the odd term $\chi^{(2),odd}$ is linearly proportional to the magnetization $\vec{M}$ and can be expressed as [118]:

$$\chi^{(2),odd}_{ijk} = \chi^{(3)}_{ijk,l}M_l, \tag{3.43}$$

where $\chi^{(3)}_{ijk,l}$ is the fourth-rank tensor independent of $\vec{M}$.

In an optical experiment the mSHG intensity is measured for opposite directions of the magnetization:

$$I^{\uparrow\downarrow}_{2\omega} = |\vec{E}^{even}_{2\omega}|^2 + |\vec{E}^{odd}_{2\omega}|^2 \pm 2|\vec{E}^{even}_{2\omega}| \cdot |\vec{E}^{odd}_{2\omega}| \cos\phi_{2\omega}, \tag{3.44}$$

where $\phi_{2\omega}$ is the optical phase shift between the even $\vec{E}^{even}_{2\omega}$ and odd $\vec{E}^{odd}_{2\omega}$ SH fields. It should be noted that in a lossless medium, the time-reversal properties of $\chi^{(2)}(M)$ dictate that the real part of $\chi^{(2)}(M)$ is an even function of M, while the imaginary part is an odd function of M. It means that in this case the even $\vec{E}^{even}_{2\omega}$ and odd $\vec{E}^{odd}_{2\omega}$ SH fields has a $\phi_{2\omega} = 90°$ phase shift.

Nonlinear optical response of a multilayer structure

Calculation of the mSHG response of a multilayer structure is a stepwise procedure and similar to the calculation of the linear magneto-optical response. First of all, one has to find distribution of the fundamental field, which can be done using the self-consistent 4×4 matrix method described in the previous section [1]. Since the mSHG is the second order effect, the liner MOKE rotation can be neglected, as well as the depletion of the fundamental wave by the mSHG. Further we assume that there are only electric dipole sources of the SH field at the interfaces. The following consideration can also be performed in a more general case.

Following the ideas of Bloembergen and Pershan [119], at each interface we introduce an infinitely thin nonlinear sheet with thickness $2\delta_2$ inside an infinitely thin vacuum sheet with thickness $2\delta_1$ (see Figure 3.3). This sheet has a refractive index n^i_j, the refractive index of the interface. The xz plane is the plane of incidence ($k_y = 0$), therefore the induced polarization in the sheet is:

$$\vec{P}^{sh}_{2\omega}(\vec{r}_j, t) = \vec{P}^{sh}_{2\omega,j} \exp^{i[2k_x(\omega)x - 2\omega t]}, \tag{3.45}$$

where $\vec{r}_j$ corresponds to the points in the plane of the interface j.

$$P^{sh}_{2\omega,k,j} = \chi^{(2)}_{klm,j}(2\omega) E_{\omega,l,j} E_{\omega,m,j}, \tag{3.46}$$

where $k, l, m = x, y, z$, and $\chi^{(2)}_{klm}(2\omega)$ is the nonlinear susceptibility tensor of the interface j. The presence of the source $P^{sh}_{2\omega,j}$ causes a discontinuity of the SH fields at the interface j [46]. Discontinuity of the electric $\Delta E_{2\omega}, x, j$ and magnetic $\Delta H_{2\omega,y,j}$ fields can be derived from the boundary conditions, where the presence of the SH source polarization is taken into account [120, 121]:

$$\Delta E_{2\omega,x,j} = -\frac{ik_x(2\omega)}{\left[n^i_j(2\omega)\right]^2} 4\pi P^{sh}_{2\omega,z,j}, \tag{3.47}$$

$$\Delta H_{2\omega,y,j} = \frac{i2\omega}{c} 4\pi P^{sh}_{2\omega,x,j}. \tag{3.48}$$

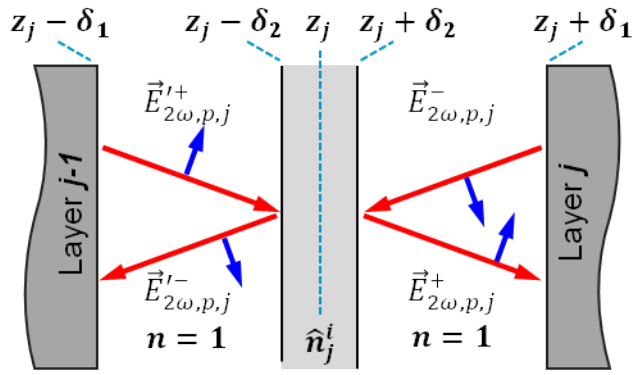

Figure 3.3: Infinitely thin nonlinear sheet with thickness $2\delta_2$ inside infinitely thin vacuum sheet with thickness $2\delta_1$ at the interface j between layers j and $j-1$. $\vec{E}'^{,\pm}_{2\omega,p,j}$ are the p-polarized forward and backward SH waves in the vacuum sheet $(z_j-\delta_1; z_j-\delta_2)$, respectively. $\vec{E}^{\pm}_{2\omega,p,j}$ are the p-polarized forward and backward SH waves in the vacuum sheet $(z_j+\delta_2; z_j+\delta_1)$. $\hat{n}^i_j$ is the refractive index of the nonlinear sheet. The figure was redrawn after [46]

.

The equations (3.47), (3.48) determine the difference between the field components in the vacuum sheets on both sides of the nonlinear sheet j:

$$\Delta E_{2\omega,x,j} = E_{2\omega,x,j} - E'_{2\omega,x,j}, \tag{3.49}$$

$$\Delta H_{2\omega,y,j} = H_{2\omega,y,j} - H'_{2\omega,y,j}, \tag{3.50}$$

where $E'_{2\omega,j}$ and $H'_{2\omega,j}$ are the electric and magnetic field in the vacuum sheet with $z_j - \delta_1 < z < z_j - \delta_2$, and $E_{2\omega,j}$ and $H_{2\omega,j}$ are the fields in the vacuum sheet with $z_j+\delta_2 < z < z_j+\delta_1$. These field components can be expressed with the field components of the forward and backward waves:

$$\Delta E_{2\omega,x,j} = \left[\left(E^{+}_{2\omega,p,j} - E^{-}_{2\omega,p,j}\right) - \left(E'^{+}_{2\omega,p,j} - E'^{-}_{2\omega,p,j}\right)\right] \cdot \cos\theta_{\omega,0}, \tag{3.51}$$

$$\Delta H_{2\omega,y,j} = \left(E^{+}_{2\omega,p,j} + E^{-}_{2\omega,p,j}\right) - \left(E'^{+}_{2\omega,p,j} + E'^{-}_{2\omega,p,j}\right). \tag{3.52}$$

. In vacuum there is no dispersion, and $\theta_{2\omega,0} = \theta_{\omega,0}$.

Using the medium boundary and propagation matrices (3.22), (3.27), and the layer matrix (3.31), for the SH field in the final medium f we can write:

$$A_0 \begin{pmatrix} E^{+}_{2\omega,p,j} \\ 0 \\ E^{-}_{2\omega,p,j} \\ 0 \end{pmatrix} = \left(\prod_{m=j}^{N} C_m\right) A_f \begin{pmatrix} E^{+}_{2\omega,p,f} \\ 0 \\ 0 \\ 0 \end{pmatrix}. \tag{3.53}$$

[1]If both fundamental and SH waves are p-polarized, we can swith to a 2×2matrix method, as it was done in [46].

If we define

$$T = A_0^{-1} \left(\prod_{m=j}^{N} C_m \right) A_f, \tag{3.54}$$

then

$$E^+_{2\omega,p,j} = T_{11} \cdot E^+_{2\omega,p,f}, \quad E^-_{2\omega,p,j} = T_{31} \cdot E^+_{2\omega,p,f} \Rightarrow E^-_{2\omega,p,j} = \frac{T_{31}}{T_{11}} \cdot E^+_{2\omega,p,j}. \tag{3.55}$$

For SH field in the initial medium i:

$$A_i \begin{pmatrix} 0 \\ 0 \\ E^-_{2\omega,p,j} \\ 0 \end{pmatrix} = \prod_{m=1}^{j-1} C_m^{2\omega} A_0 \begin{pmatrix} E'^+_{2\omega,p,f} \\ 0 \\ E'^-_{2\omega,p,f} \\ 0 \end{pmatrix}. \tag{3.56}$$

If we define

$$T = A_i^{-1} \prod_{m=1}^{j-1} (C_m) A_0, \tag{3.57}$$

then

$$T_{11} \cdot E'^+_{2\omega,p,j} + T_{13} \cdot E'^-_{2\omega,p,j} = 0. \tag{3.58}$$

Thus we demonstrated how to calculate the outgoing SH waves generated at the interface j. Since the SH fields originating at the surfaces and interfaces are so small, we can neglect interaction between them, and the total SH response is just a sum of the SH waves calculated separately for each interface.

3.3.2 Microscopic formalism

The odd components of the SH susceptibility tensor $\chi^{(2)}_{ijm}$ can be obtained in a similar way as the off-diagonal components of the linear susceptibility (3.37) [114]:

$$\begin{aligned} &\chi^{(2)}_{ijm}\left(2q_\parallel, 2\omega, M\right) = 4\pi \frac{e^3 q_\parallel a}{V} \frac{\lambda_{s.o.}}{\hbar\omega} \\ &\times \sum_\sigma \sum_{k,l,l',l''} \langle k+2q_\parallel, l''\sigma|i|kl\sigma\rangle \langle kl\sigma|j|k+q_\parallel, l'\sigma\rangle \langle k+q_\parallel, l'\sigma|m|k+2q_\parallel, l''\sigma\rangle \\ &\times \frac{\frac{f(E_{k+2q_\parallel,l''\sigma}) - f(E_{k+q_\parallel,l'\sigma})}{E_{k+2q_\parallel,l''\sigma} - E_{k+q_\parallel,l'\sigma} - \hbar\omega + i\hbar\alpha_1} - \frac{f(E_{k+q_\parallel,l'\sigma}) - f(E_{kl\sigma})}{E_{k+q_\parallel,l'\sigma} - E_{kl\sigma} - \hbar\omega + i\hbar\alpha_1}}{E_{k+2q_\parallel,l''\sigma} - E_{kl\sigma} - 2\hbar\omega + i2\hbar\alpha_1}, \end{aligned} \tag{3.59}$$

where $\langle kl\sigma|j|k+2q_\parallel, l'\sigma\rangle$ are the transition matrix elements which determine the symmetry and consequently the interface sensitivity. In some cases the matrix elements can be treated as constants, but one has to introduce a cut-off to guarantee the surface sensitivity. The odd components of $\hat{\chi}^{(2)}$ are also linearly proportional to the constant of the spin-orbit coupling $\lambda_{s.o.}$. So it is one of the key parameter for linear and nonlinear magneto-optics.

3.4 Hot carrier dynamics probed by the MOKE and the mSHG

Considerations of the MOKE and mSHG signals in two previous section are mostly related to the steady state in the absence of the optical excitation or applied electric field. It was demonstrated that both MOKE and mSHG are sensitive to the magnetization. This section is devoted to the challenges in the interpretation of the pump-induced variations of the magneto-optical signals.

3.4.1 Variation of the magneto-optical constants

In the second section of this chapter it was shown that both MOKE rotation and ellipticity are linearly proportional to the bulk magnetization, therefore their variations should reflect real magnetization dynamics. However, it was found that on a femtosecond time scale after the optical excitation both MOKE rotation and ellipticity can be affected not only by the magnetization dynamics, but also by the state-filling effect, or so-called the optical bleaching [82]. The reason is that absorption of a strong pump laser pulse leads to the generation of the non-equilibrium (NEQ) electrons above the Fermi level and NEQ holes below the Fermi level, which populate final states and depopulate initial states of the linear optical transitions, respectively. Thus the pump pulse may partially block the optical transitions available for the probe pulse, or open new ones. The state-filling effect decays together with the NEQ electron distribution during the electron-electron thermalization. At the same time, an increase of the electron and lattice temperatures changes the magneto-optical constant of a ferromagnet, which also causes the difference between the MOKE rotation and ellipticity. It should be noted that because of the different depth sensitivities of the MOKE rotation and ellipticity [122], the difference between their variations may occur even in the absence of the optical artefacts, which should be also taken into account in the interpretation of the experimental data. In more detail this problem and its possible solution are discussed in **Chapters 5 and 6**

3.4.2 Current- and spin-current-induced contributions to the mSHG

On top of the surface/interface (bulk in non-centrosymmetric media) non-magnetic and magneto-induced contributions, the mSHG response contains bulk terms proportional to the charge current and spin current (SC). Both current- [123] and SC [124]-induced contributions have been observed in GaAs with relatively large light penetration depth. The current-induced SHG has been also demonstrated in graphene [125]. In spite of small light penetration depth, such contributions can be also expected in metals, especially in Au owing to a large inelastic mean free path, which facilitates high currents, and large spin-orbit coupling which is required for the magneto-optical effects. In **Chapters 7 and 8** it is demonstrated that the laser-induced SC pulse gives rise to the SH field originating in the bulk of Au.

Chapter 4

Experimental details

To study ultrafast HC driven magnetization dynamics experimental setup (see figure 4.1) for time-resolved MOKE and mSHG spectroscopy has been built in the Fritz Haber Institute of the Max Planck Society. It is based on a pump-probe technique, employing an intense laser pulse to excite the system and a weak probe pulse to measure its response. The setup is driven by 14-fs, 40 nJ pulses with 820 nm central wavelength at 1-MHz repetition rate and allows to switch easily between back-pump-front-probe and standard front-pump-front-probe schemes. Implementation of the motorized stages in the crucial parts of the setup and development of the LabView program to control them made it possible to perform experiments in different magneto-optical and polarization geometries simultaneously in a reliable and controlled manner. In the following, the experimental setup is described.

4.1 Ti:sapphire Oscillator with Cavity dumper

The Coherent Mantis laser system used in this work is a mode-locked Ti:sapphire (Ti:Sa) oscillator extended with a cavity dumper (see figure 4.2). The design incorporates an Optically Pumped Semiconductor (OPS) laser. It pumps a Ti:Sa crystal with 532-nm light, which serves as a gain medium with an extremely broad emission band ranging from 700 to 900 nm [126, 127]. An optical cavity of length l restricts the radiation to the longitudinal modes of index m which satisfy the criterion:

$$\frac{m\lambda_m}{2} = l \text{ or } \nu_m = \frac{mc}{2l}, \tag{4.1}$$

where λ_m and ν_m are the wavelength and the frequency of the longitudinal mode $m \in \mathbb{N}$. The mode spacing $\Delta\nu = \nu_{m+1} - \nu_m = c/(2l)$ is related to the cavity round-trip time $\tau_{RT} = 1/\Delta\nu$. Forcing all the modes to have an equal phase (mode-locking) implies in the time domain that all the waves of different frequencies will add constructively at one point, resulting in an intense and short burst of light (see Figure 4.3(b)). Ti:Sa permits

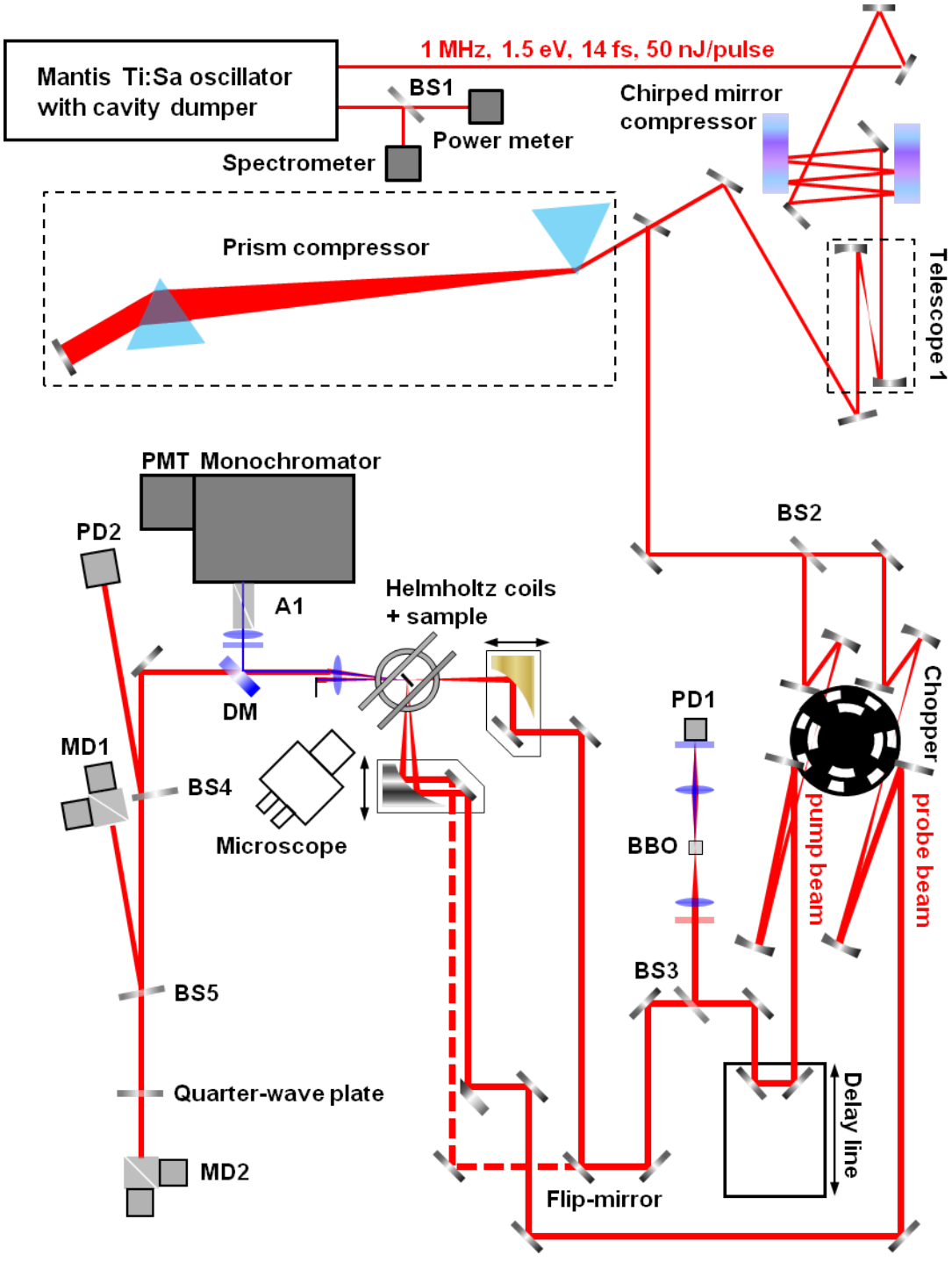

Figure 4.1: Experimental setup. Abbreviations: BS – beam splitter, PD – photodiode, MD – MOKE detector, DM – dichroic mirror, PMT – photomultiplier tube, A – analyzer.

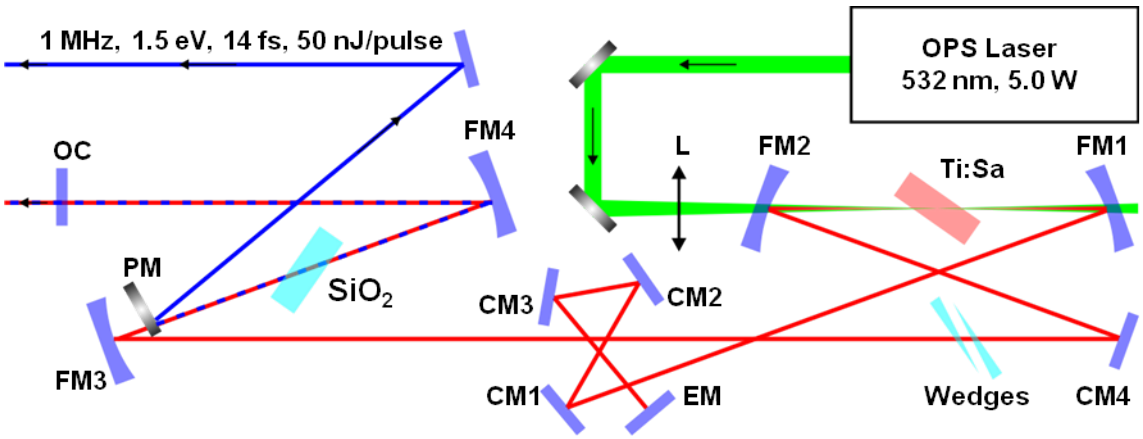

Figure 4.2: Simplified scheme of the Coherent Mantis laser system extended with the cavity dumper. The Ti:Sa crystal is pumped by a continuous-wave OPS laser with output power 5 W via a focusing lens L. The oscillator cavity is formed by the end mirror EM and the 3% output coupler OC. The focusing mirrors FM1 and FM2 are responsible for a high power density in the Ti:Sa crystal, enhancing the Kerr effect. Chirped mirrors CM1, CM2, CM3, CM4 introduce negative dispersion with each reflection. The cavity is designed in such way that the aggregate round-trip dispersion results in stable mode-locked operation. Glass wedges (SiO_2) introduce positive dispersion. They are used to achieve the desired bandwidth and spectral shape. Spherical mirror FM3 focuses the beam into an acoustooptic Bragg cell (a SiO_2 crystal), where a part of the beam is deflected upon applying an acoustic signal. Spherical mirror FM4 collimates the beam. Pick-up mirror (PM) reflects the diffracted pulses to the output of the cavity dumper. Total extracted pulse from the cavity is a sum of the diffracted pulses on the way to the output coupler OC and back to the end mirror EM. It is possible to switch to a smaller cavity, if one put an output coupler before the focusing mirror FM3. The Bragg cell and the wedges are made from the same material, therefore to switch between small and extended cavity, one needs just to change the position of the output coupler OC and slide the wedges compensating dispersion introduced by the Bragg cell. In order to reduce reflection losses, the glass wedges, the SiO_2 crystal, and the Ti:Sa crystal are aligned to be at the Brewster angle to the laser beam.

passive mode-locking through the optical Kerr effect. This third-order nonlinear effect causes a change in the refractive index of the Ti:Sa crystal, which is proportional to the light intensity. The laser beam with a Gaussian profile induces such spatial profile of the refractive index that it acts as a transient lens (self-focusing) and modulates loss and gain of the optical cavity, synchronizing all longitudinal modes in the certain spectral range. In the case of M oscillating modes with equal amplitudes and frequencies $\omega_j = 2\pi\nu_j = \omega_l + 2\pi j\Delta\nu$ the total electric field is

$$E(t) = \frac{1}{2}\tilde{E}(t)e^{i\omega_l t} = \frac{1}{2}E_0 e^{i\omega_l t}\sum_{j=-\frac{M-1}{2}}^{(M-1)/2} e^{i(2j\pi\Delta\nu t+\phi_0)} = \frac{1}{2}E_0 e^{i\omega_l t}\frac{\sin(M\pi\Delta\nu t)}{\sin(\pi\Delta\nu t)}, \qquad (4.2)$$

where ω_l is a center of the mode spectrum. For large M this corresponds to a train of single pulses spaced by τ_{RT}. From (4.2) the duration of one pulse is

$$\tau_p = \frac{1}{M\Delta\nu} = \frac{\tau_{RT}}{M}. \qquad (4.3)$$

Thus to produce a train of 14-fs pulses in the Mantis laser system with the round-trip time $\tau_{RT} = 18.5$ ns, about 10^6 modes are required.

Group velocity dispersion (GVD) of the optical components inside the cavity leads to a temporal broadening of the single pulses, which would eventually switch off the Kerr lens and break the mode-locking. In order to prevent this, a set of the chirped mirrors is used. Their optical coating introduces a small amount of negative dispersion [1] with each reflection. The cavity is designed so that the aggregate round-trip dispersion results in a stable mode-locked operation.

18.5-ns round-trip time of the Mantis oscillator corresponds to a pulse repetition rate of 54 MHz. In pump-probe experiments it is desirable to use a lower repetition rate and be able to vary it. For this purpose a cavity dumper was chosen as an intracavity technique which allows not only to change the repetition rate, but also increase the pulse energy up to 50 nJ.

Function of the cavity dumper is based on the acoustooptic effect. In a fused silica crystal (SiO_2) a modulation of density and consequently of refractive index is introduced by applying an acoustic signal with high frequency, and results in a Bragg diffraction. The acoustic wave inside the crystal is generated by applying an electrical signal to a piezoelectric transducer cemented on the crystal. By using short radio-frequency (RF) pulses, single laser pulses can be selected out of the pulse train and deflected from the initial direction. So they are separated from the other pulses and available for usage in the experiment.

In order to describe the dumping process, the optical pulse is assumed to be given by:

$$E(t) = E_0(t)\cos(\omega t), \qquad (4.4)$$

where $E_0(t)$ denotes the time dependent envelope and ω the laser carrier frequency. Scattering of the light on the acoustic wave in the SiO_2 crystal causes a frequency shift of the pulse by an amount equal the frequency Ω of the electric signal.

[1] 'Positive dispersion' ('negative dispersion') corresponds to the situation when larger (smaller) frequencies propagate slower than smaller (larger) frequencies.

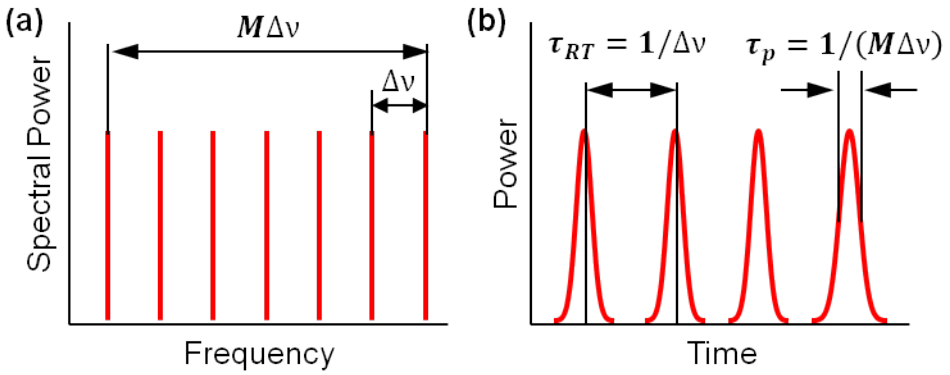

Figure 4.3: Spectral amplitude of a set of equally spaced cavity modes (a), and field amplitude in the time domain, when all modes are 'locked' to the same phase (b) [128].

When the cavity laser pulse propagate through the Bragg cell on the way to the output coupler, scattered pulse E_s and depleted cavity pulse E_d are given by [129]:

$$\begin{aligned} E_s &= \sqrt{\eta} E_0 \cos(\omega t + \Omega t + \Phi), \\ E_d &= \sqrt{1-\eta} E_0 \cos(\omega t), \end{aligned} \tag{4.5}$$

where η is the diffraction efficiency, and Φ is the adjustable phase of the electric signal inducing the acoustic wave. On the way from the output coupler to the end mirror the cavity laser pulse undergoes scattering for the second time and both scattered pulses are extracted by the pick-up mirror. The total output of the cavity dumper is given by the sum of the two scattering contributions as:

$$E_{extr} = \sqrt{1-\eta}\sqrt{\eta} E_0 \left[cos(\omega t + \Omega t + \Phi) + cos(\omega t - \Omega t - \Phi)\right]. \tag{4.6}$$

Thus the resulting intensity of the dumped output of the laser is:

$$I_{cd} = 4\eta(1-\eta)|E_0|^2 \cos^2(\Omega t + \Phi). \tag{4.7}$$

The dumping efficiency can be enhanced, if the interference is constructive, or decreased, if the interference is destructive, depending on the phase of the RF signal.

4.2 Temporal pulse compression

Due to GVD, propagation of the short laser pulse with broad spectrum through air and different optical components (beam splitters, wave plates, lenses etc.) leads to temporal pulse broadening. In order to maintain time resolution in the pump-probe experiment, an external dispersion control outside the laser cavity is required. In the experimental scheme presented in Figure 4.1 a combination of a chirped mirror compressor and a prism compressor is used. These two compressors compensate GVD

in such a way that the laser pulse has the shortest length of about 14 fs at the sample position.

The chirped mirror compressor is a pair of parallel chirped mirrors which introduce certain amount of the negative dispersion, depending on the number of reflections. Moving a pick-up mirror (PM) along the chirped mirrors, one can change the number of reflections and consequently the amount of the negative dispersion in a stepwise manner. Two drawbacks of the chirped mirror compressor are an additional divergence of the beam caused by a single reflection from a chirped mirror and an increase of the beam path with the number of reflections, which in turn increases the beam size after the chirped mirror compressor. For this reason, a pair of spherical mirrors (telescope 1: the first mirror is fixed, the second one is placed on a manual linear translator along the beam) is used to recollimate the beam for the prism compressor.

The prism compressor introduces both positive and negative dispersion. The amount of the positive dispersion depends on the amount of glass (fused silica/prism material) introduced into the beam. As for the negative dispersion, the part of the spectrum with smaller wavelengths undergoes larger deflection in the first prism and consequently propagates through smaller thickness of glass at the second prism. Thus due to the angular dispersion of the prisms, different parts of the laser spectrum have different optical path in the prism compressor, which results in the negative contribution to GVD.

Since the SH intensity is proportional to the square of the intensity of the fundamental pulse, it is a good reference to adjust duration of the laser pulse: the shorter laser pulse at the sample surface, the larger the SH signal from the sample surface. One way to determine the pulse duration is to measure SH cross-correlation signal, originating between pump and probe signal beams, when two pulses overlap in space and time. The 20-fs SH cross-correlation signal shown in Figure 4.9(a) corresponds to 14 fs duration of the pump and probe laser pulses. A beam splitter BS3 reflects small portion of the pump beam for the reference channel, where it is focused into the BBO crystal (see Figure 4.1). The blue filter in front of the photodiode PD1 transmits only SH beam generated in the BBO crystal, which makes its signal sensitive not only to changes of the average power of the laser output, but also to the pulse duration. A red filter before the first lens focusing fundamental beam into the BBO crystal is used to suppress SH beam going back to the main scheme.

The distance between two prisms in the prism compressor is so large, that when the pump and probe beams are focused with the parabolic mirrors, only the prism compressor is sufficient to achieve the smallest pulse duration [2]. However, when lenses or thick filters are used, both compressors are required to maintain 20-fs time resolution.

4.3 Data acquisition

After the prism compressor the laser pulse is splitted with a beam splitter BS2 (80%) into the pump and probe pulses. Then both beams go through their own telescopes, constructed with pairs of spherical mirrors. These telescopes have three functions:

[2] In this case the pick-up mirror in the chirped mirror compressor is set to zero reflections.

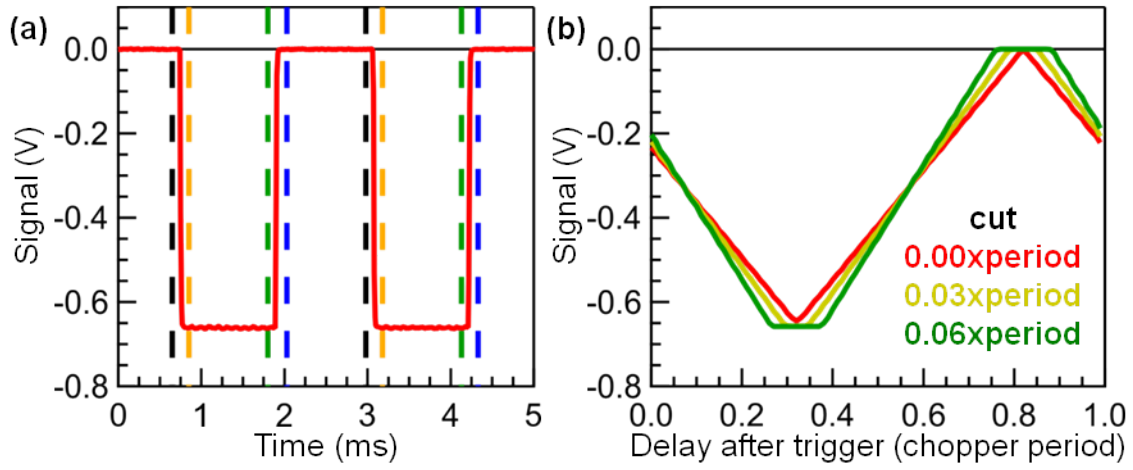

Figure 4.4: (a) Signal at the photodiode PD2 (see Figure 4.1) measuring linear reflectivity versus real time. Orange and green dash lines depict start and end of the open-phases of the chopper, and blue and black dash lines depict start and end of the closed-phases of the chopper, respectively. (b) Photodiod signal averaged over the chopper-half-period time interval versus the delay between the trigger signal and the first sample of the time interval. Different colours correspond to different values of the parameter 'cut' determining the portion of the ignored samples.

- correct divergence of each beam separately from the other one;
- increase the beam sizes for tighter focusing on the sample: x2.3 for the probe beam and x2 for the pump beam;
- decrease the beam sizes at the chopper.

In order to be able to measure background signal, probe signal in the absence or in the presence of the pump pulse, the double-row chopper was used. Its typical operation frequency is approximately 430 Hz, which corresponds to the modulation frequency of the probe beam with the outer blades of the chopper (see Figure 4.4(a)), while the pump beam was chopped with the inner blades at 246 Hz [3]. In pump-probe experiments people usually use a lock-in amplifier which allows to improve signal-to-noise ratio by selecting only certain region in the frequency domain related to the chopper frequencies. However, in our experiment we use a photomultiplier tube (PMT) in a photon-counting mode, which excludes the usage of a lock-in amplifier. Also in the pump-probe experiments, discussed in this thesis, the number of the collected signals varied from 5 to 7, which would require several lock-in amplifiers. For this reason, a data acquisition (DAQ) card BNC2090A from National Instruments was used to acquire signals from all detectors simultaneously. It has 2 analog output channels,

[3]The ratio between the modulation frequencies of the pump and probe beams is determined by the number of windows in the inner and outer rows of the chopper.

which were used to set certain current through the Helmholtz coils, 2 channels for digital or timing signal, and 8 analog input channels. Only 6 of these channels were in constant use:

- first two channels were connected to the two outputs of the chopper, sending the rectangular signals generated by the optocouplers;
- the third channel was connected to the photodiode PD1 (reference signal), controlling the energy of the laser pulse;
- the fourth channel was connected to the photodiode PD2, measuring linear reflectivity;
- other two channels were connected to two identical MOKE detectors MD1 and MD2.

The PMT was connected to the amplifier forming TTL pulses which were sent to the channel for timing signal to count the number of the rising edges corresponding to the number of photoelectrons. The DAQ card can acquire all input signal simultaneously with the sampling rate 100 kHz. Figure 4.4(a) shows the acquired signal from the photodiode PD2 measuring linear reflectivity (see Figure 4.1). Using one of the chopper signals as a trigger for the acquisition process and analyzing all signals, it is possible to determine the chopper frequency and which samples correspond to the open or closed states of the chopper. Averaging the signal over the chopper-half-period time intervals, one can obtain the dependence of the averaged signal on the delay between the trigger and the first sample of the time interval, shown in Figure 4.4(b). When the first sample of the time interval corresponds to the first sample of the closed phase, the averaged signal is almost zero, but when the first sample of the time interval becomes closer to the the first sample of the open phase, the averaged signal linearly increases. However, there are samples which correspond to the moments, when the laser beam was partially blocked with the chopper blade. Removing some samples at the beginning and at the end of the half-period time interval from the averaging process results in the appearance of two plateaus: one corresponds to the open phase, another to the closed phase. Total duration of the ignored samples is determined by the parameter 'cut' as a portion of the chopper period. From the dependences of the averaged signal on the delay between the trigger and the first sample, obtained separately for the pump (the inner blades of the chopper) and probe (the outer blades of the chopper) beams, one can set the delay between the trigger signal and the first sample of the open phase and the parameter 'cut' in a such way that they determine samples corresponding to one of five phases:

- both beams are open $S_{\mathrm{oo}} = S^*_{\mathrm{pump}} + S^*_{\mathrm{probe}} + S_{\mathrm{background}}$ [4];
- pump beam is open, and probe beam is closed $S_{\mathrm{oc}} = S_{\mathrm{pump}} + S_{\mathrm{background}}$;

[4] S^*_{pump} is the pump signal in the presence of the probe pulse, S^*_{probe} is the probe signal in the presence of the pump pulse

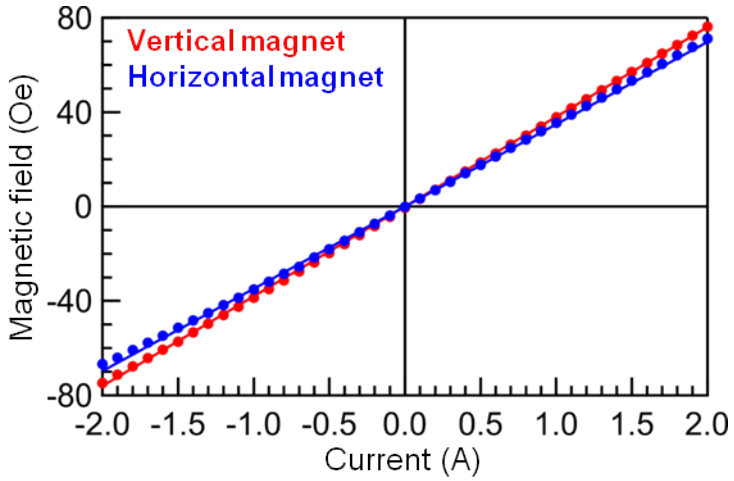

Figure 4.5: Calibration of the magnets. Dots represent experimental data measured with a Hall detector, and solid lines were obtained with linear fit $H = k \cdot I$: $k_{vert.} = (38.00 \pm 0.07)$ Oe/A, $k_{horiz.} = (34.83 \pm 0.14)$ Oe/A. Red and blue colours correspond to the vertical and horizontal magnets, respectively.

- pump beam is closed, probe beam is open $S_{\text{co}} = S_{\text{probe}} + S_{\text{background}}$;
- both beams are closed $S_{\text{cc}} = S_{\text{background}}$;
- at least one of the beams is partially blocked, therefore the corresponding sample is ignored.

In the experiments the pump beam and the cross-correlator (see Section 4.7) are blocked with the knife, therefore the static probe signal and its pump-induced variations are given by:

$$S_{\text{probe}} = S_{\text{co}} - S_{\text{cc}}, \tag{4.8}$$

$$\Delta_S = \frac{S^*_{\text{probe}}}{S_{\text{probe}}} = \frac{S_{\text{oo}} - S_{\text{oc}}}{S_{\text{co}} - S_{\text{cc}}}. \tag{4.9}$$

4.4 Calibration of the magnet

In order to apply external magnetic field in transversal and longitudinal directions, two crossed pairs of the Helmholtz coils were used in this work. They were held in a single construction which was designed and built by Adrian Glaubitz at the Free University of Berlin. Complete sketch of this construction can be found in his diploma thesis [130]. To be able to apply higher currents and achieve larger magnetic fields, old wires were replaced with new ones with larger cross section 1mm^2, therefore new calibration was required (see Figure 4.5).

4.5 Samples

Samples studied in this work are epitaxial Fe/Au/Fe/MgO(001) and Au/Fe/MgO(001) structures. They have several significant advantages concerning the investigation of the optically induced HC transport and ultrafast spin dynamics.

First, optically transparent MgO(001) substrate makes it possible to realize either back-pump-front-probe or front-pump-front-probe schemes (see Figure 4.6(d)).

Secondly, the remarkable feature of the epitaxial MLs is a well-defined structure which makes it suitable for ab initio analysis and suppresses inelastic HC scattering on lattice inhomogeneities [49]. Thin Fe(001) and Au(001) films were grown in ultra high vacuum (UHV, $\sim 10^{-9}$ Torr) following [131, 132] and analyzed with microscopy techniques. Preparation technique is usually referred to as Molecular Beam Epitaxy (MBE). All Au/Fe/MgO(001) and Au(cap layer)/Fe/Au/Fe/MgO(001) samples have been prepared by Damian Bürstel and Jan Meyburg, PhD students in the group of Dr. Detlef Diesing at the University of Duisburg-Essen in the department of Physical Chemistry. Their MBE setup is very typical and reflects the common setup described in [133].

The iron and gold films grow epitaxially with $[001]_{Au}||[001]_{Fe}||[001]_{MgO}$ and $[010]_{Au}||[110]_{Fe}||[010]_{MgO}$ (see Figure 4.6(a)). As it was discussed in **Chapter 2**, directions [100] and [010] in bcc-Fe correspond to the magnetization easy axes (see Figure 4.6(c)). In the optical pump-probe experiments samples were mounted in the sample holder presented in Figure 4.6(b), so one of the easy axes was parallel to the plane of incidence, and the other one is perpendicular to it. It allows to perform measurements in the transversal and longitudinal magneto-optical geometries either in remanence or in saturating magnetic field.

Usually each sample was divided into 9 regions with different Fe and Au thicknesses. Perfomance of the back-pump-front-probe requires an 'alignment area' (see Figure 4.6(c)), a region with one Fe layer capped with thin Au layer, so the SHG cross-correlation signal, used to adjust the overlap between the back pump and probe beams and determine pump-probe zero delay, could be observed (see Figure 4.9). When the alignment procedure was done, sample was moved parallel to its plane with the motorized stages to the region of interest. Experimental setup allows to align all three beams (probe, back and front pump) at the same spot on the sample, so the switching between back-pump-front-probe and front-pump-front-probe schemes can be done just by a flip of a mirror (see Figure 4.1). However, for reliability pump-probe overlap was checked and corrected (if necessary) before each measurement.

Varying thicknesses and evaporation conditions, one can obtain two Fe films with different coercivities. It makes possible to realize different mutual orientations of the magnetizations in the spin-emitter and the spin-collector. Collecting reflected back-pump and probe mSHG and MOKE signals, all magnetic configurations can be correctly identified (see Figure 8.2).

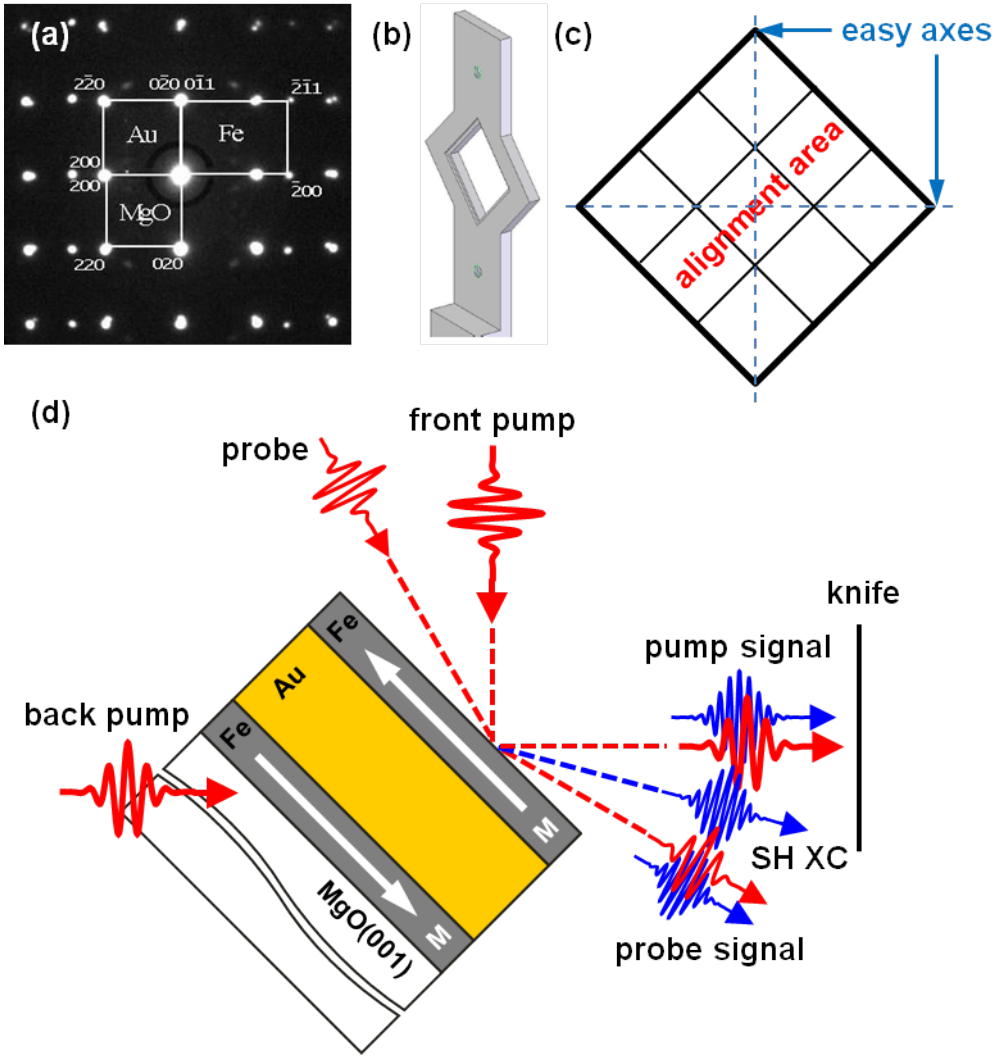

Figure 4.6: (a) Electron diffraction pattern of Fe/Au/Fe/MgO(001), provided by Dr. Vladimir Roddatis, (b) sample holder, (c) typical sample sketch, (d) experimental scheme. Samples mounted in a such way that one of the substrate diagonals is parallel to the optical table, and the other one is perpendicular. Vertical and horizontal dash lines depict magnetization easy axes of the Fe film along the [100] and [010] directions.

4.6 MOKE measurements

For complete characterization of the linear magneto-optical response, two identical MOKE detectors MD1 and MD2 were designed and constructed to measure MOKE rotation and ellipticity. Each detector consists of a Glan-Laser polarizer, which transmits P polarized beam (e-ray) and reflects S polarized beam (o-ray), and a pair of photodiodes PD1 and PD2 mounted on the exit windows of the Glan-laser polarizer (see Fig. 4.7(a)). Usually one uses a wollaston prism, but in this case the photodiodes should be placed on the sufficient distance from the prism due to relatively small angle between e- and o-beams, which makes the detector more bulky.

Assuming that the probe pulse is P-polarized and magnetization of the sample is parallel to the plane of incidence, the S-polarized component of the electric field caused by the MOKE is given by:

$$E_s = E_p \cdot (\psi'_K + i\psi''_K), \tag{4.10}$$

where ψ'_K is the MOKE rotation, and ψ''_K is the MOKE ellipticity. According to Figure 4.7(b), the intensities on each photodiode are

$$I_{PD1} = |E_p|^2 \cdot |\cos\alpha_A + \psi'_K \sin\alpha_A + i\psi''_K \sin\alpha_A|^2, \tag{4.11}$$

$$I_{PD2} = |E_p|^2 \cdot |-\sin\alpha_A + \psi'_K \cos\alpha_A + i\psi''_K \cos\alpha_A|^2, \tag{4.12}$$

where α_A is an angle between the optical axis of the Glan-laser analyzer and the direction corresponding to the P-polarization. Thus generating the difference signal from two photodiodes by a differential amplifier yields

$$\begin{aligned} S_{MOKE} &= I_{PD1} - I_{PD2} \\ &= |E_p|^2 \cdot \left[4\psi'_K \sin\alpha_A \cos\alpha_A - (\psi'^2_K + \psi''^2_K - 1) \cdot (\cos^2\alpha_A - \sin^2\alpha_A)\right] \\ &= R \cdot \left[2\psi'_K \sin 2\alpha_A + (1 - \psi'^2_K - \psi''^2_K)\cos 2\alpha_A\right], \end{aligned} \tag{4.13}$$

where R is the linear reflectivity.

In (4.13) there is a term linearly proportional to the MOKE rotation ψ'_K which changes its sign upon the reversal of the magnetization. If there is a quarter-wave plate in front of the MOKE detector, the linear term will be proportional to the MOKE ellipticity ψ''_K. Figure 4.8(a) shows the hysteresis loop in the MOKE ellipticity signal: the external magnetic field was applied parallel to the plane of incidence and the film surface. Measuring the dependence of the MOKE signals in horizontal saturating magnetic field of the opposite polarities on the rotation angle of the MOKE detector, it is easy to find a calibration coefficient between the signal (in Volts) from the MOKE detector and the rotation of polarization (in degrees) (see Figure 4.8(b)), and a position of the rotation stage at which $\cos 2\alpha_A = 0$ and the transient MOKE signal is

$$S_{MOKE}(t) = 2 \cdot R(t) \cdot \psi'_K(t). \tag{4.14}$$

Usually $\delta R = \Delta R(t)/R_0 \ll \Delta\theta(t)/\theta_0$, but for complete separation of magnetic and non-magnetic contributions variation $\Delta_{MOKE}(t) = (R(t)\psi'_K(t) - R_0\psi'_{K,0})/R_0\psi'_{K,0}$ of the MOKE should be normalized on the reflectivity variation $\delta R(t)$:

$$\delta\psi'_K(t) = \frac{1 + \Delta_{MOKE}(t)}{1 + \delta R(t)} - 1. \tag{4.15}$$

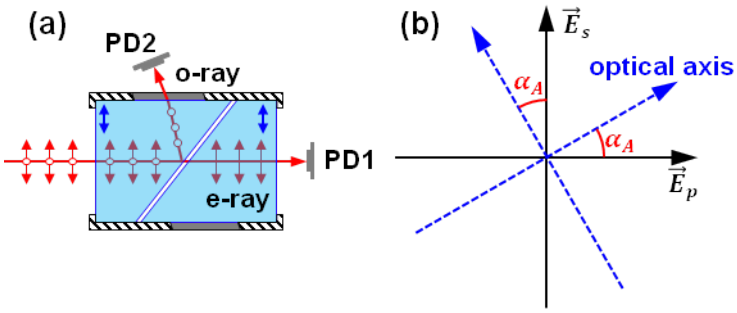

Figure 4.7: (a) MOKE detectors based on a Glan-laser prism. (b) Mutual orientation of the p- and s-polarized electric fields and an optical axis.

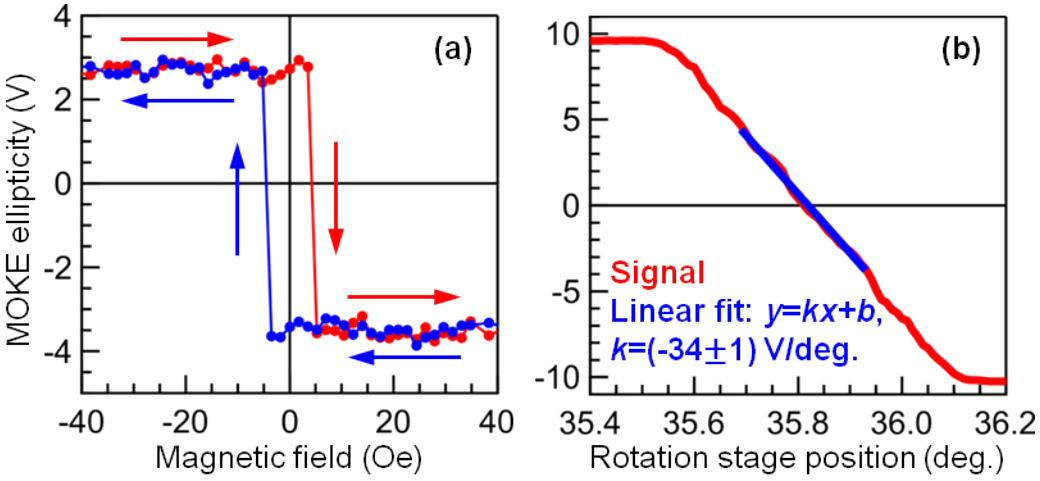

Figure 4.8: Hysteresis loop in the MOKE ellipticity signal (a) and dependence of the MOKE ellipticity signal on the position of the rotation stage (b), measured probing the Fe side of the Au/Fe/MgO(001) structure with 130 nm of Au and 15.5 nm of Fe.

4.7 mSHG measurements

The mSHG signal was separated from the fundamental pulse with a dichroic mirror and analyzed with a Glan-Thompson prism (A1 in Figure 4.1), mounted into a motorized rotation stage. Depending on certain magneto-optical geometry, the analyzer A1 was set to transmit p-polarization, s-polarization or mixed-polarization. To suppress portion of the fundamental pulse reflected from the dichroic mirror, additional filter was placed in front of the analyzer A1. Then for the reduction of the background signal, the mSHG beam went through a monochromator to the PMT.

Introducing half-wave or quarter-wave plates into pump and probe beams before

the sample, it is possible to realize different polarization geometries. Since in the most cases pump and probe beams were p-polarized, only p-in geometry will be considered here.

4.7.1 Data analysis

The mSHG electric field consists of the even and odd terms with respect to the reversal of the magnetization $\vec{M}$:

$$\vec{E}_{2\omega}^{total} = \vec{E}_{2\omega}^{even} + \vec{E}_{2\omega}^{odd} = \vec{\beta} + \hat{\alpha}\vec{M}. \tag{4.16}$$

In the transversal magneto-optical geometry ($\vec{M}\|y$) both even and odd components are p-polarized, therefore measured mSHG intensity is given by

$$I_{2\omega}^{\uparrow\downarrow} = |\vec{E}_{2\omega}^{even}|^2 \pm 2 \cdot |\vec{E}_{2\omega}^{even} \cdot \vec{E}_{2\omega}^{odd}| \cdot \cos\phi + |\vec{E}_{2\omega}^{odd}|^2, \tag{4.17}$$

where ϕ is a phase shift between the even $E_{2\omega}^{even}$ and odd $E_{2\omega}^{odd}$ SH fields, '$\pm$' corresponds to opposite directions of the magnetization $\vec{M}$. In the longitudinal magneto-optical geometry ($\vec{M}\|x$) for p-polarized probe pulse $\vec{E}_{2\omega}^{even}$ is p-polarized, and $\vec{E}_{2\omega}^{odd}$ is s-polarized. If the axis of the analyzer A1 is parallel to the p-polarization, $I_{2\omega}^{\rightarrow} = I_{2\omega}^{\leftarrow}$ and the variation of the even SH field is given by

$$\delta E_{2\omega}^{even}(t) = \frac{E_{2\omega}^{even}(t) - E_{2\omega,0}^{even}}{E_{2\omega,0}^{even}} = \sqrt{\frac{I_{2\omega}^{\rightarrow}(t) + I_{2\omega}^{\leftarrow}(t)}{I_{2\omega,0}^{\rightarrow} + I_{2\omega,0}^{\leftarrow}}} - 1, \tag{4.18}$$

where $I_{0,2\omega}^{\rightarrow}$, $I_{0,2\omega}^{\leftarrow}$ are the intensities measured without excitation. Using the intensities $I_{2\omega}^{\uparrow}$, $I_{2\omega}^{\downarrow}$ measured in the transversal magneto-optical geometry, it is possible to evaluate variation of the odd SH field:

$$\delta E_{2\omega}^{odd,T}(t) = \sqrt{\frac{(I_{2\omega}^{\uparrow} + I_{2\omega}^{\downarrow}) - (I_{2\omega}^{\rightarrow} + I_{2\omega}^{\leftarrow})}{(I_{2\omega,0}^{\uparrow} + I_{2\omega,0}^{\downarrow}) - (I_{2\omega,0}^{\rightarrow} + I_{2\omega,0}^{\leftarrow})}} - 1. \tag{4.19}$$

The cosine of the phase shift $\phi_{2\omega}^{T}$ between the even $E_{2\omega}^{even}$ and odd $E_{2\omega}^{odd,T}$ SH fields is given by

$$\cos\phi_{2\omega}^{T}(t) = \frac{I_{2\omega}^{\uparrow} - I_{2\omega}^{\downarrow}}{2\sqrt{(I_{2\omega}^{\rightarrow} + I_{2\omega}^{\leftarrow})[(I_{2\omega}^{\uparrow} + I_{2\omega}^{\downarrow}) - (I_{2\omega}^{\rightarrow} + I_{2\omega}^{\leftarrow})]}}. \tag{4.20}$$

If $|\vec{E}_{2\omega}^{odd}| \ll |\vec{E}_{2\omega}^{even}|$ and $\phi_{2\omega} = const$, one can neglect the last term in the expression (4.17) for the mSHG intensity in the transversal magneto-optical configuration. Thus to evaluate variation of the even mSHG field $\Delta E_{2\omega}$, one can use (4.18) with SH intensities measured in the transversal magneto-optical configuration. In this case the variation of the odd SH field $\Delta E_{2\omega}^{odd,T}$ will be given by

$$\delta E_{2\omega}^{odd,T}(t) = \frac{I_{2\omega}^{\uparrow}(t) - I_{2\omega}^{\uparrow}(t)}{I_{2\omega,0}^{\uparrow} - I_{2\omega,0}^{\uparrow}} \cdot \sqrt{\frac{I_{2\omega,0}^{\uparrow} + I_{2\omega,0}^{\uparrow}}{I_{2\omega}^{\uparrow}(t) + I_{2\omega}^{\uparrow}(t)}} - 1. \tag{4.21}$$

In the experiments, where the probe pulse is applied to the Au side of the two-layer Au/Fe/MgO(001) structures, there is no magnetization ($E^{odd}_{2\omega,0} = 0$) in the absence of the optical excitation, as expected for the surface of a paramagnetic material. In this case magnetization dynamics should be monitored by the SH contrast $\rho_{2\omega}$:

$$\rho^T_{2\omega}(t) = \frac{I^{\uparrow}_{2\omega}(t) - I^{\downarrow}_{2\omega}(t)}{I^{\uparrow}_{2\omega}(t) + I^{\downarrow}_{2\omega}(t)} \approx 2 \cdot \frac{E^{odd}_{2\omega}(t)}{E^{even}_{2\omega}(t)} \cdot \cos\phi_{2\omega}. \tag{4.22}$$

4.7.2 SH cross-correlation and time resolution

In a pump-probe experiment the weak probe pulse is an analogue of the snapshot photograph, aimed at detecting a change of an optical property ΔS, induced by the strong pump pulse. Varying the position of the delay-line stage (see Figure 4.1), one changes the length of the beam path for the pump pulse with respect to the probe pulse, providing certain temporal delay τ_d between two pulses at the sample. In the most of time-resolved experiments a signal $S(t_d)$ is measured as a function of delay τ_d. Since the detection electronics has no fs resolution, the measured signal is a time intergral:

$$S(\tau_d) = \int_{-\infty}^{\infty} I_g(t - \tau_d) f(t) dt, \tag{4.23}$$

where $f(t)$ is a physical quantity, and I_g is a gating function.

Temporal limitation of the pump-probe technique is the duration of the laser pulses. The SHG offers a possibility to measure cross-correlation (XC) function of the pump and probe pulses (or one can call it autocorrelation function of the laser pulse). When the pump and probe pulses overlap in space and time, total SHG signal reflected from the sample is given by

$$I^{total}_{2\omega} = I^{pump}_{2\omega} + I^{probe}_{2\omega} + 2 \cdot \alpha \sqrt{I^{pump}_{2\omega} \cdot I^{probe}_{2\omega}}, \tag{4.24}$$

where $I^{pump}_{2\omega}$, $I^{probe}_{2\omega}$ are the SHG signals only from the pump and probe pulses, respectively [5], and the last term is the mSHG XC-signal which can be obtained by the subtraction of the pump and probe signals from the total SHG signal (see Figure 4.9). Parameter α characterizes interference efficiency between two pulses. In the noncollinear scheme the mSHG XC appears between the pump and probe signals, so pump and probe signals can be cut out by a diafragm or a knife. Assuming a Gaussian shape of the laser pulses, the SHG XC-signal can be written as

$$\begin{aligned} I_{XC}(\tau_d) &\sim \int_{-\inf}^{+\inf} I^{pump}_{\omega}(t - \tau_d) \cdot I^{probe}_{\omega}(t) dt \\ &\sim \int_{-\infty}^{+\infty} e^{-2\cdot[(t-\tau_d)/t_G]^2} \cdot e^{-2\cdot[t/t_G]^2} dt \sim e^{-(\tau_d/t_G)^2}, \end{aligned} \tag{4.25}$$

where pulse duration $t_p = t_G\sqrt{2\ln 2}$, therefore temporal width of the SHG XC is $\sqrt{2}$ times larger than the pulse duration: 20-fs width of the SHG XC corresponds to the

[5] If both pump and probe pulse are present, $I^{pump}_{2\omega}$ and $I^{probe}_{2\omega}$ depend on the pump-probe delay τ_d.

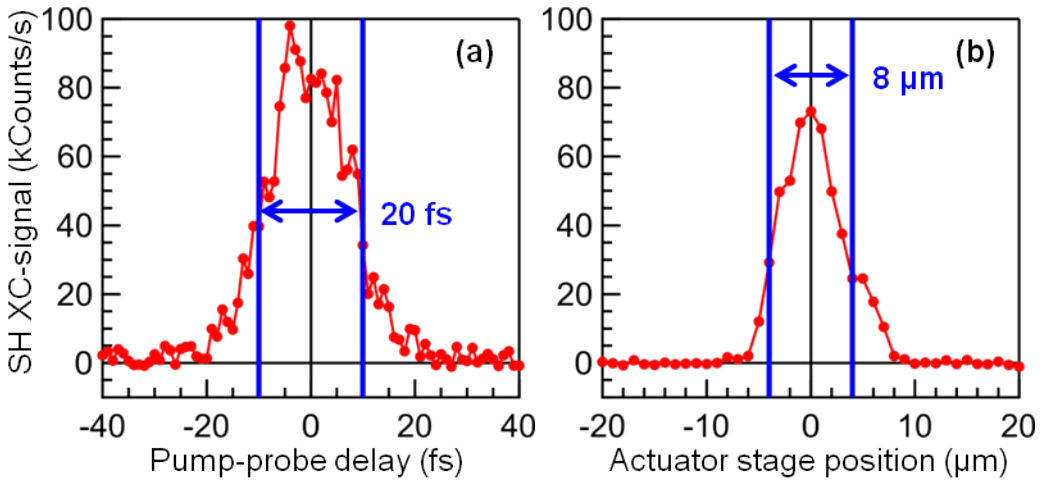

Figure 4.9: SH cross-correlation (XC) signal measured on the 5nm-Au/11nm-Fe/MgO(001) structure in back-pump(Fe)-front-probe(Au) scheme. Maximum of the SH XC-signal determines (a) zero delay between pump and probe pulses and (b) their optimal spatial overlap. According to the left figure, temporal width of the SH XC-signal is 20 fs, and according to the rigt figure, spot sizes are about 8-10μm: $1-\mu m$ step of the mirror-actuator roughly corresponds to $1-\mu m$ step of th laser spot on the sample.

pulse duration of 14 fs. Moreover, optimization of the SHG XC-signal determines the time zero delay $t = 0$ and maximum spatial overlap of the two beams. From Figure 4.9(b) the spot sizes can be estimated to be about 10 μm which was confirmed with a beam-profiler.

Chapter 5

Ultrafast demagnetization of Fe in the absence of hot carrier transport

One of the main goals of this work is to study ultrafast laser-induced demagnetization of ferromagnetic films and understand the role of the hot carrier (HC) transport in this process. Since it is not possible to exclude all other mechanisms contributing to the magnetization dynamics and the HC relaxation, it has been decided to consider two situations: (i) homogeneous optical excitation of a thin ferromagnetic film on a nonconducting substrate, and (ii) a ferromagnetic film in contact with a non-magnetic metal. In the first case homogeneous laser absorption leads to a uniform HC spatial distribution which in turn ensures the absence of the HC transport and its influence on the magneto-optical response. Thus magnetization dynamics during first several picoseconds is governed by spin-flip processes. Subsequent relaxation of magnetization occurs due to the slow heat diffusion away from the excited area. In the second case a non-magnetic metal serves as a sink of spin-polarized HCs, thereby leading to ultrafast demagnetization of the ferromagnetic film [22–24].

This chapter presents the experimental results obtained on a 8-nm polycrystalline Fe film grown on the MgO(001) substrate and capped with 3 nm of MgO (see Figure 5.1(a)). The sample was pumped and probed through the MgO substrate with 14-fs laser pulses under ambient conditions. Laser-induced magnetization dynamics was monitored with the linear (MOKE) and nonlinear (mSHG) magneto-optical responses. In all-optical pump-probe experiments pump- and probe-induced optical transitions may involve the same electronic states, which results in the appearance of the state-filling effect (or so-called optical bleaching) in the measured signals. It complicates an interpretation of the experimental data, but on the other hand, it provides information about relaxation of the non-equilibrium (NEQ) HCs. In order to enhance sensitivity to the NEQ HC dynamics, we used pump and probe pulses with the same photon energies $\hbar\omega_{pump} = \hbar\omega_{probe} = 1.5$ eV. In this chapter, it is demonstrated that the analysis of both MOKE rotation and ellipticity makes it possible to disentangle contributions of the transient magnetization and the optical bleaching using only few reasonable assumptions.

Figures 5.1(b) and (c) show that relative variations of the linear reflectivity $\delta R(t)$, MOKE rotation $\delta\psi'_K(t)$ and ellipticity $\delta\psi''_K(t)$ undergo drastic changes at the time zero

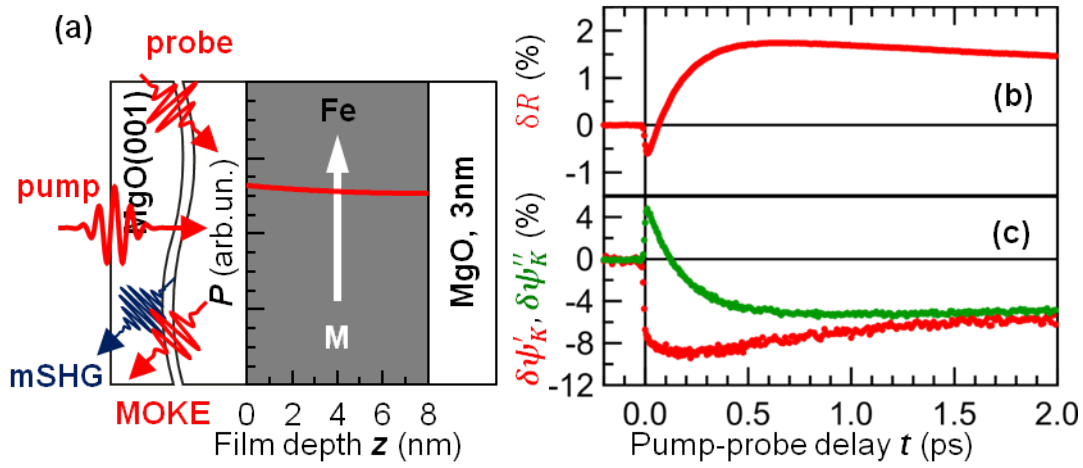

Figure 5.1: (a) Experimental scheme and laser absorption profile calculated for a 8-nm Fe film, using the 4x4 matrix method described in Chapter 3. Angles of incidence for the pump and probe pulses were about 45° and 50°, respectively. Pump-induced relative variations of the (b) linear reflectivity δR (red), (c) MOKE rotation $\delta\psi'_K$ (red) and ellipticity $\delta\psi''_K$ (green).

$t = 0$. Experimental 20-fs time resolution allows us to deduce that this effect is much faster than the electron thermalization which takes several hundreds femtoseconds [76]. Therefore it should be attributed to the optical bleaching which decays together with the NEQ HCs. Difference between $\delta\psi'_K$ and $\delta\psi''_K$ on a picosecond time scale is related to the variation of the magneto-optical constants following changes of the electron and lattice temperatures. In order to obtain characteristic time constants, measured signals were fitted with a simple phenomenological model similar to that one suggested in [70]. Then the experimental data were analyzed within the M3TM suggested by Koopmans et al. [86] and our 'microscopic' model supplemented with the dynamics of the NEQ HCs. The M3TM does fit the magnetization dynamics, but it is not capable to describe the linear reflectivity $\delta R(t)$. Besides that, in the derivation of the magnetization change rate dM/dt, the M3TM refers to the spin temperature T_s [1], as the 3TM [25]. The concept of the spin temperature T_S is very arguable at least on a short time scale, when the relaxation processes are dominated by the NEQ HCs. For this reason, our microscopic model describes the magnetization dynamics in terms of the energy flow and the transfer of the angular momentum without referring to the spin temperature T_S. Consideration of phenomenological and microscopic models revealed that ultrafast demagnetization occurs mostly due to the NEQ HCs, while subsequent relaxation of the magnetization is governed by the equilibrium (EQ) or thermalized HCs.

[1] However, we admit that T_s is not present in the final rate equations (2.27) of the M3TM.

5.1 Separation of magnetism and optics

Figures 5.1(b), (c) present dynamics observed for the 8-nm polycrystalline Fe film in the linear reflectivity R, MOKE rotation ψ'_K and ellipticity ψ''_K signals at $\hbar\omega_{probe} = 1.5$ eV with 20-fs time resolution. After the optical excitation $\hbar\omega_{pump} = 1.5$ eV, relative variations of the MOKE rotation $\delta\psi'_K(t)$ and ellipticity $\delta\psi''_K(t)$ have opposite signs, but they merge within first several picoseconds, meaning that on later pump-probe delays both $\delta\psi'_K(t)$ and $\delta\psi''_K(t)$ reflect real magnetization dynamics. In the case of the homogeneous magnetization profile and HC distribution, transient complex Kerr angle $\psi_K(t)$ can be expressed as

$$\psi_K(t) = \psi'_K(t) + i\psi''_K(t) = [a'(t) + ia''(t)] \cdot M(t), \tag{5.1}$$

where $a = a' + ia''$ is the magneto-optical constant depending on the Voigt constant q_{Fe} and the refractive index n_{Fe} of iron. Then $\delta\psi'_K(t)$ and $\delta\psi''_K(t)$ are given by

$$\delta\psi'_K(t) = \frac{a'(t) \cdot M(t) - a'_0 M_0}{a'_0 M_0} \approx \frac{\Delta M(t)}{M_0} + \frac{\Delta a'(t)}{a'_0} = \delta M(t) + \delta a'(t) \tag{5.2}$$

and

$$\delta\psi''_K(t) = \frac{a''(t) \cdot M(t) - a''_0 M_0}{a''_0 M_0} \approx \frac{\Delta M(t)}{M_0} + \frac{\Delta a''(t)}{a''_0} = \delta M(t) + \delta a''(t), \tag{5.3}$$

respectively. So the difference $\delta\psi''_K(t) - \delta\psi'_K(t) = \delta a''(t) - \delta a'(t)$ is purely non-magnetic.

In the further data analysis three crucial assumptions are made. First, we assume that the spin is conserved in the optical transitions and in the absence of the HC transport demagnetization of the Fe film occurs only due to the phonon-mediated spin-flip processes accompanied with the transfer of the angular momentum to the lattice. For this reason, we exclude any instantaneous (below 20 fs) changes of the magnetization upon laser excitation, i.e. $\delta M(t = 0) = 0$. Secondly, relaxation of the majority and minority NEQ HCs can be characterized with a common characteristic time of the electron-electron thermalization τ_{ee} due to the energy exchange between them. There are also data demonstrating minor difference between the lifetimes of the majority and minority electrons in 3d ferromagnets [71, 79]. The third assumption is the most questionable, but we believe that the real and imaginary parts of the magneto-optical constant $a'(t)$ and $a''(t)$ relax simultaneously to their static values:

$$\frac{\delta a'(t)}{\delta a'(t = 0)} = \frac{\delta a''(t)}{\delta a''(t = 0)} = f(t), \tag{5.4}$$

where $f(t)$ is a normalized difference between relative variations of the MOKE ellipticity and rotation:

$$f(t) = \frac{\delta\psi''_K(t) - \delta\psi'_K(t)}{\delta\psi''_K(t = 0) - \delta\psi'_K(t = 0)}. \tag{5.5}$$

The reason behind this is that the same optical transitions determine the MOKE rotation $\psi'_K(t)$ and ellipticity $\psi''_K(t)$. In the recent work performed by Carpene et al. [134],

it was reported that that the real and imaginary parts of the off-diagonal term of the conductivity tensor behave differently. However, these data were obtained on a 50-nm Fe film. It does simplifies the expression for the static Kerr angle, but such thick ferromagnetic film has a non-uniform laser absorption profile and does not exclude the influence of the HC transport. According to [19], the ballistic velocity of the majority electrons in Fe is about 0.6 nm/fs for the energy range between 0.5 and 1.5 eV, therefore within 20 fs (our time resolution) the HC transport can induce significant demagnetization of the probed region ($\sim$ 17 nm) and provide a inhomogeneous magnetization profile. In this case, the MOKE rotation ψ'_K and ellipticity ψ''_K behave differently because of their different depth sensitivities [122]. In any case our data obtained on a 8-nm Fe film with a uniform laser absorption profile do not make us suspect large deviations from the assumption (5.4).

Equations (5.2),(5.3) and (5.4) allow us to separate real magnetization dynamics $\delta M(t)$ (Figure 5.2(b), black dots) and a non-magnetic optical contribution $B(t)$ (Figure 5.2(d), black dots):

$$\delta M(t) = \frac{\delta\psi'_K(t) \cdot \delta a''(t=0) - \delta\psi''_K(t) \cdot \delta a'(t=0)}{\delta a''(t=0) - \delta a'_K(t=0)}, \tag{5.6}$$

$$B(t) = \delta\psi''_K(t) - \delta\psi'_K(t). \tag{5.7}$$

It should be noted that $\delta|\psi_K|$ (Figure 5.2(b), blue dots) also undergoes an instantaneous break-down, therefore both MOKE rotation $\delta\psi'_K(t)$ and ellipticity $\delta\psi''_K(t)$ are required for the evaluation of the real magnetization dynamics $\delta M(t)$.

5.2 Phenomenological description

Regarding non-magnetic dynamics, there are only few typical time scales which should be observed in the variation of the linear reflectivity $\delta R(t)$ and the MOKE difference $B(t)$:

- optical excitation of the NEQ HCs;
- thermalization of the NEQ HCs;
- electron-lattice thermalization;
- heat diffusion from the Fe film into the MgO substrate.

After the electron-lattice thermalization, the static value of the linear reflectivity R_0 is not reestablished within 600 ps, and the relaxation of $\delta R(t)$ gives characteristic time of the heat diffusion larger than 100 ps, which was also reported by Carpene et al. [87]. This characteristic time is also consistent with typical values of the thermal interface conductance [135]. MgO is a nonconducting material, and the heat flux from the Fe film into the substrate occurs through phonons and reaches its maximum, when the lattice temperature T_p does [2], i.e. after the electron-lattice thermalization. Performing

[2]The heat flux is proportional to the temperature difference between the Fe film and the region of the MgO substrate close to the Fe/MgO interface.

simulations of the optical excitation of the Fe film and subsequent relaxation processes, it has been found that the heat flux into the substrate can be neglected during first several picoseconds. As a result, we can conclude that the temporal width of the instantaneous break-down of $\delta R(t)$ (Figure 5.2(a), red dots) is determined by our 20-fs time resolution, while other time scales correspond to the electron-electron and electron-phonon thermalization. In the previous studies [86, 87, 134], the temporal resolution was comparable to the electron thermalization time constant ($\sim$ 200 fs) found by Rhie et. al in the time-resolved photoemission experiments [76], which led to the wrong assignment of the observed time scales: the time scale of 200 fs was referred to the electron-phonon thermalization.

In order to obtain the characteristic time constants of the electron-electron τ_{ee} and the electron-lattice τ_{ep} thermalization, $\delta R(t)$ and $B(t)$ were analyzed with a simple phenomenological fit functions similar to those presented in [70]:

$$\delta R(t) = b_0^R \cdot e^{-t/\tau_{ee}} + r_0 \cdot \left(1 - e^{-t/\tau_{ee}}\right) \cdot e^{-t/\tau_{ep}} + r_1 \cdot \left(1 - e^{-t/\tau_{ep}}\right), \tag{5.8}$$

$$B(t) = b_0^{\psi_K} \cdot [e^{-t/\tau_{ee}} + b_1^{\psi_K} \cdot \left(1 - e^{-t/\tau_{ee}}\right) \cdot e^{-t/\tau_{ep}}], \tag{5.9}$$

where the term $e^{-t/\tau_{ee}}$ describes relaxation of the optical bleaching, and other two terms $(1 - e^{-t/\tau_{ee}})e^{-t/\tau_{ep}}$ and $(1 - e^{-t/\tau_{ep}})$ correspond to the variation of the electron T_e and lattice T_p temperatures. The difference between the MOKE signals vanishes after few picoseconds, therefore the latter term is absent in the expression (5.9) for $B(t)$. The joint fitting procedure with the functions (5.8), (5.9) convolved with 20-fs Gaussian pulse gives $\tau_{ee} = 0.23 \pm 0.01$ ps, $\tau_{ep} = 1.2 \pm 0.1$ps. Time constants τ_{ee} and τ_{ep} are in agreement with earlier photoemission studies performed on 3d ferromagnetic metals [76, 88, 136].

After the analysis of the non-magnetic effects, the $\delta M(t)$ curve was fitted with a following bi-exponential function

$$\delta M(t) = m_0 \cdot \left(1 - e^{-t/\tau_M}\right) \cdot e^{-t/\tau_R} + m_1 \cdot \left(1 - e^{-t/\tau_R}\right), \tag{5.10}$$

where the time constants τ_M, τ_R correspond to the demagnetization and the recovery of the magnetization, respectively. It turned out that $\tau_M = 0.22 \pm 0.02$ ps and $\tau_R = 0.9 \pm 0.2$ ps. Since $\tau_M \approx \tau_{ee}$ and $\tau_R \approx \tau_{ep}$, it means that the ultrafast demagnetization of the Fe film is dominated by the NEQ HCs, while the recovery of the magnetization is governed by the EQ HCs. This conclusion allows us to fit the experimental data ($\delta R(t)$, $\delta\psi'_K(t)$ and $\delta\psi''_K(t)$) using only two time constants τ_{ee} and τ_{ep} (see Figures 5.2(a) and (b)). Functions reproducing the MOKE rotation $\Delta\psi'_K(t)$ and ellipticity $\Delta\psi''_K(t)$ are the sums of (5.9) and (5.10):

$$\begin{aligned}\delta\psi'_K(t) = b'_0 \cdot [e^{-t/\tau_{ee}} + b_1^{\psi_K} \cdot \left(1 - e^{-t/\tau_{ee}}\right) \cdot e^{-t/\tau_{ep}}] \\ + m_0 \cdot \left(1 - e^{-t/\tau_{ee}}\right) \cdot e^{-t/\tau_{ep}} + m_1 \cdot \left(1 - e^{-t/\tau_{ep}}\right),\end{aligned} \tag{5.11}$$

$$\begin{aligned}\delta\psi''_K(t) = b''_0 \cdot [e^{-t/\tau_{ee}} + b_1^{\psi_K} \cdot \left(1 - e^{-t/\tau_{ee}}\right) \cdot e^{-t/\tau_{ep}}] \\ + m_0 \cdot \left(1 - e^{-t/\tau_{ee}}\right) \cdot e^{-t/\tau_{ep}} + m_1 \cdot \left(1 - e^{-t/\tau_{ep}}\right),\end{aligned} \tag{5.12}$$

while $\delta R(t)$ is given by (5.8).

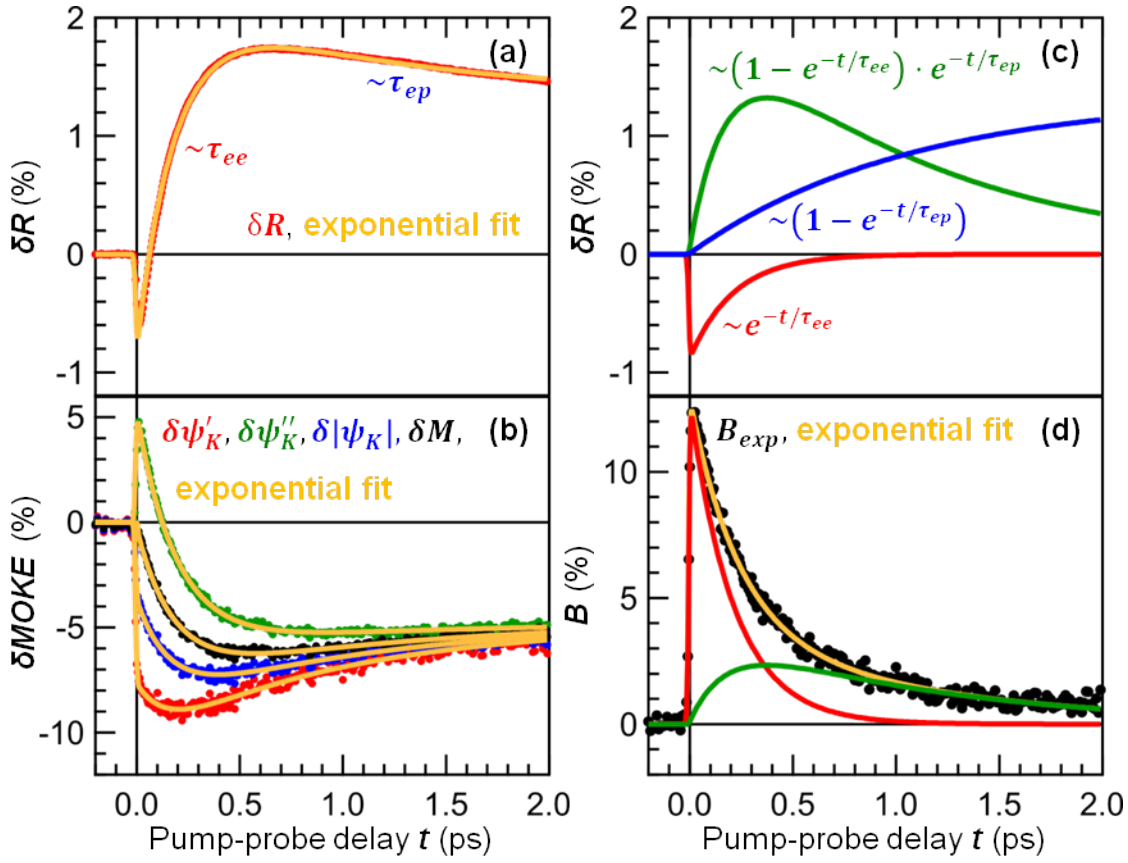

Figure 5.2: Relative variations of the linear magneto-optical response measured on a 8-nm polycrystalline Fe film: (a) linear reflectivity $\delta R(t)$ (red dots), (b) MOKE rotation $\delta\psi'_K(t)$ (red dots), ellipticity $\delta\psi''_K(t)$ (green dots), absolute value of the Kerr angle $\delta|\psi_K|(t)$ (blue dots) and the bulk magnetization $\delta M(t)$ (black dots) evaluated using (5.6). Orange lines reproduce the experimental data according to the phenomenological model (5.8), (5.11), (5.12). (c) Different contributions to the variation of the linear reflectivity: $\sim e^{-t/\tau_{ee}}$ (red line), $\sim (1-e^{-t/\tau_{ee}})\cdot e^{-t/\tau_{ep}}$ (green line) and $\sim (1-e^{-t/\tau_{ee}})\cdot e^{-t/\tau_{ep}}$ (blue line). (d) Difference between the relative variations of the MOKE ellipticity and rotation $B(t) = \delta\psi''_K(t) - \delta\psi'_K(t)$ (black dots - experiment, orange line - phenomenological model). Red and green lines in (d) indicate contributions to $B(t)$, which are similar to those in (c).

MOKE difference	$b_0' = -7.58 \pm 0.06$ [%] $b_0'' = 5.57 \pm 0.06$ [%] $b_1^{\psi_K} = 0.31 \pm 0.01$
Reflectivity	$b_0^R = -0.91 \pm 0.05$ [%] $r_0 = 2.27 \pm 0.05$ [%] $r_1 = 1.34 \pm 0.03$ [%]
Magnetization	$m_0 = -7.81 \pm 0.05$ [%] $m_1 = -4.79 \pm 0.05$ [%]
Time constants	$\tau_{ee} = \tau_M = 0.21 \pm 0.01$ [ps] $\tau_{ep} = \tau_R = 1.06 \pm 0.03$ [ps]

Table 5.1: Parameters used in the phenomenological model to reproduce the experimental data. Presented values were obtained after the joint fitting procedure of the data shown in Figure 5.2.

All parameters obtained in the joint fitting procedure are summarized in Table 5.1 [3]. The total number of the independent parameters in the phenomenological model is 10 for 3 experimental curves. Figures 5.2(c), (d) demonstrate different contributions to $\delta R(t)$ and $B(t)$. Comparing our results with the data presented in [87], it should be noted that the variations of the linear reflectivity induced by the changes of the electron and lattice temperatures can have opposite signs depending on the wavelength of the probe pulse. From (5.8) and (5.10) it is clear that r_1 and m_1 correspond to the linear reflectivity and magnetization established during the electron-lattice thermalization ($\tau_{ep} \approx \tau_R$). Thus m_1 should be determined by the equilibrium magnetization [137]:

$$m_1 = \frac{M_{eq}}{M_0} - 1, \text{ where } M_{eq} = M(T_{eq}) = \left[1 - s\left(\frac{T_{eq}}{T_C}\right)^{3/2} - (1-s)\left(\frac{T_{eq}}{T_C}\right)^4\right]^{1/3}, \tag{5.13}$$

where T_{eq} is the temperature of the probed area after the electron-lattice thermalization, $T_C = 1043$ K is the Curie temperature of Fe [102], and s is a microscopic parameter which can be calculated ab initio ($s = 0.41$), but in the analysis the empirical value $s = 0.35$ was used. Function (5.13) reproduces the experimental dependence of the equilibrium magnetization of the Fe film on its temperature T_{eq} [137]. Using the initial temperature $T_0 = 300$ K and $m_1 = -4.79\%$ one can estimate the equilibrium temperature $T_{eq} = 554$ K and consequently the absorbed energy of the laser pulse

$$P_{abs} = 0.5\gamma_e \cdot [T_{eq}^2 - T_0^2] + \int_{T_0}^{T_{eq}} C_p(T)dT + I_M[M_0^2 - M_{eq}^2] \approx 926\ J/cm^3. \tag{5.14}$$

[3] The time zero was determined by the SHG cross-correlation signal which can be seen in Figure 5.7

Here $\gamma_e \approx 0.7\ mJ \cdot cm^{-3} \cdot K^{-2}$ is the electronic specific heat, C_p is the lattice heat capacity calculated within the Debye model (The Debye temperature of Fe $T_D = 470$ K) [102]. The last term in (5.14) describes the magnetic (exchange) energy in the approximation of the mean field [36]. $I_M \approx 1055\ J/cm^3$ is the exchange parameter obtained from the temperature dependence of the total heat capacity of Fe [102].

5.3 Microscopic models

Using simple phenomenological model, it has been shown that upon homogeneous optical excitation of the Fe film, demagnetization occurs on the time scale of the HC thermalization, while the time scale of the magnetization recovery corresponds to the electron-phonon thermalization. This observation sustains the results of the ab-initio calculations performed by Carva et al. for 3d ferromagnets [96]. They reported that the NEQ HCs provide a stronger demagnetization rate than thermalized ones, meaning that NEQ HCs are essential for ultrafast spin dynamics. This conclusion emphasizes necessity to consider finite electron thermalization time.

In this section we try go beyond the phenomenological description. As a starting point, we consider the M3TM [86]. Although the M3TM can separately reproduce the magnetization dynamics $\delta M(t)$, it fails to describe the linear reflectivity $\delta R(t)$. This problem is related to the assumption about an instantaneous electron thermalization, which has been proven to be wrong in the previous section. In order to provide more adequate description of the experimental data, we introduce a microscopic model complemented with the NEQ HC dynamics.

5.3.1 Microscopic three-temperature model

The M3TM has already been discussed in **Chapter 2**. Its detailed derivation and description can be found in [86, 95]. For more clarity we rewrite the set of the M3TM rate equations (2.27):

$$\begin{aligned} C_e\frac{dT_e}{dt} &= \alpha \exp\left[-\frac{2(t-t_0)^2}{t_G^2}\right] + g_{ep}(T_p - T_e), \\ C_p\frac{dT_p}{dt} &= g_{ep}(T_e - T_p), \\ \frac{dM}{dt} &= \Gamma_M M T_p \left[1 - M\coth\left(\frac{MT_c}{T_e}\right)\right]. \end{aligned} \tag{5.15}$$

Because of the uniform HC distribution and magnetization profile, the term responsible for the electron heat conductivity is omitted here. $\alpha \exp\left[-2(t-t_0)^2/t_G^2\right]$ is the source term, where α is the absorption coefficient, t_0 is the time zero, and t_G is a time constant related to the duration of the laser pulse $t_{pulse} = 0.014$ ps:

$$t_G = \frac{t_{pulse}}{\sqrt{2\ln 2}} \approx 0.017 \text{ ps}. \tag{5.16}$$

This value corresponds to the Gaussian pulse with a 20-fs width [4]. Koopmans et al. [86] considered that the electron system is heated instantly to the certain electron temperature at the time zero, which is then used as the initial condition. Consideration of the source term does not make any difference, but more clearly incorporates the experimental time resolution.

Special form of the magnetization change rate in (5.15) dictates that the equilibrium magnetization M_{eq} should be determined by

$$M_{eq} = \tanh\left(\frac{M_{eq}T_c}{T}\right). \tag{5.17}$$

The rate equations (5.15) explicitly determine the magnetization dynamics. However, Koopmans et al. [86] did not try to reproduce $\delta R(t)$ within the M3TM. For this reason, some assumptions have to be made regarding the linear reflectivity $\delta R(t)$ and the MOKE difference $B(t)$. In earlier works it was suggested that the change of the linear reflectivity $\delta R(t)$ of the 3d ferromagnetic metals is linearly proportional to the electron T_e [51] and lattice T_p [138] temperatures:

$$\delta R(t) = r_e[T_e(t) - T_0] + r_p[T_p(t) - T_0]. \tag{5.18}$$

Since both $\delta R(t)$ and $B(t)$ are attributed to the variations of the magneto-optical constants, $B(t)$ should also depend linearly on the electron T_e and lattice T_p temperatures, therefore the MOKE rotation $\delta\psi'_K(t)$ and ellipticity $\delta\psi''_K(t)$ are given by:

$$\begin{aligned} \delta\psi'_K(t) &= \delta M(t) + b'_e[T_e(t) - T_0] + b'_p[T_p(t) - T_0], \\ \delta\psi''_K(t) &= \delta M(t) + b''_e[T_e(t) - T_0] + b''_p[T_p(t) - T_0], \end{aligned} \tag{5.19}$$

where $b'_p/b'_e = b''_p/b''_e$. Thus the equations (5.15), (5.18) and (5.19) completely define the linear magneto-optical response of the Fe film. In general the electron-phonon coupling g_{ep} is not a constant and depends on the electron temperature T_e [139]. However, according to the data presented in [139], up to 2000 K the dependence of the electron-phonon coupling g_{ep} in Fe on T_e can be neglected.

Figures 5.3(a) and (b) demonstrate the results of the joint fitting procedure within the M3TM. Values of the adjustable parameters are summarized in Table 5.2. Even before the fitting procedure, it could be noted that the only parameter which characterizes a non-magnetic dynamics in the M3TM during first several picoseconds after the optical excitation is the electron-phonon coupling g_{ep}, which is not enough to describe $\delta R(t)$ within the M3TM. For this reason, one may consider the heat flux into the MgO substrate. But we have already concluded that the characteristic time constant ~ 1 ps is too small for this process, and it can be neglected on small pump-probe delays. As for the magnetization dynamics, there are two parameters Γ_M and g_{ep} which determine the magnetization change rate. When $\delta M(t)$ is analyzed separately from $\delta R(t)$, it can be perfectly reproduced within the M3TM (not shown here).

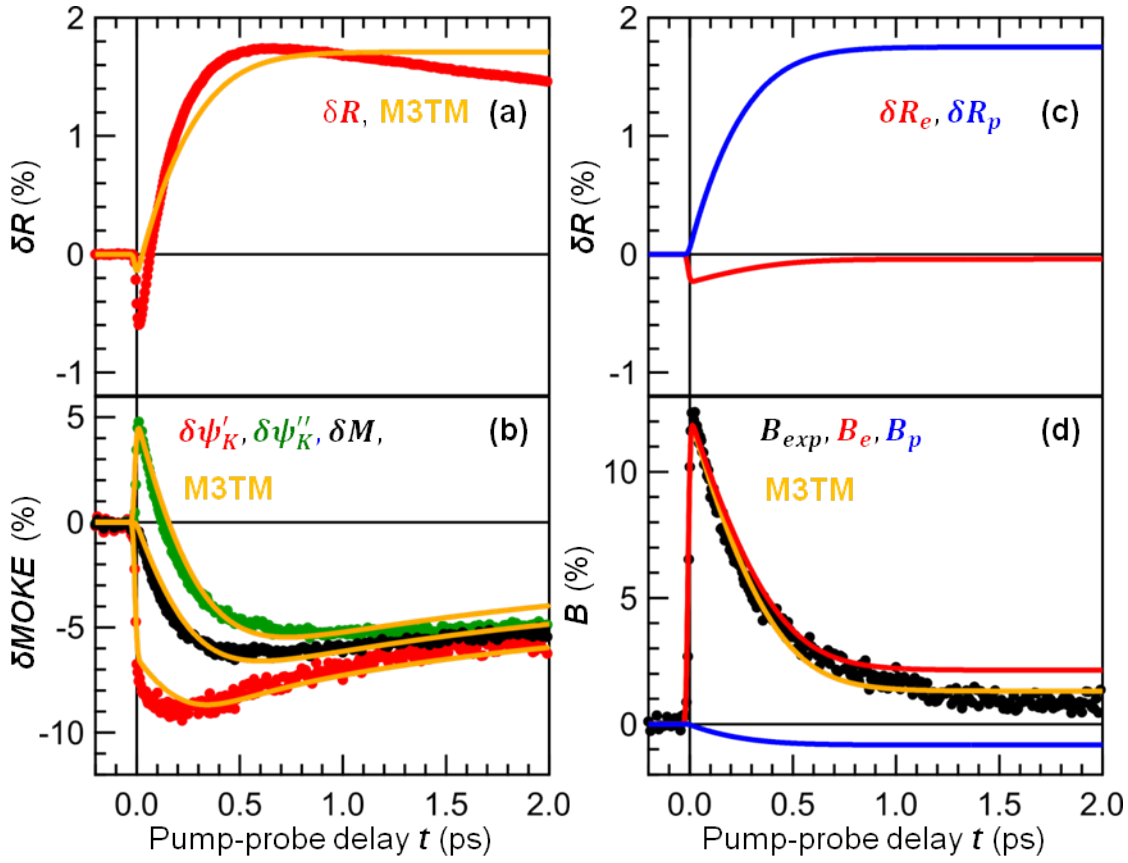

Figure 5.3: Relative variations of the linear magneto-optical response measured on a 8-nm polycrystalline Fe film: (a) linear reflectivity $\delta R(t)$ (red dots), (b) MOKE rotation $\delta\psi'_K(t)$ (red dots), ellipticity $\delta\psi''_K(t)$ (green dots), and the bulk magnetization $\delta M(t)$ (black dots) evaluated using (5.6). Orange lines reproduce the experimental data within the M3TM (5.15), (5.18) and (5.19) (c) Contributions $\delta R_e(t)$ (red line) and $\delta R_p(t)$ (blue line) to the variation of the linear reflectivity $\delta R(t)$, corresponding to the influence of the electron T_e and lattice T_p temperatures, respectively. (d) Difference between the relative variations of the MOKE ellipticity and rotation $B(t) = \delta\psi''_K(t) - \delta\psi'_K(t)$ (black dots - experiment, orange line - M3TM fit). As in (d), red and blue lines in (d) indicate contributions $B_e(t)$ and $B_p(t)$ due to the variations of the electron T_e and lattice T_p temperatures, respectively.

Laser absorption	$\alpha t_G \sqrt{\pi/2} \approx (6.80 \pm 0.02) \cdot 10^8$ $[J/m^3]$
MOKE difference	$b'_e = -(5.62 \pm 0.02) \cdot 10^{-5}$ $[K^{-1}]$ $b''_e = (4.47 \pm 0.02) \cdot 10^{-5}$ $[K^{-1}]$ $b'_p/b'_e = b''_e/b''_p = -0.39 \pm 0.01$
Reflectivity	$r_e = -(2.1 \pm 0.1) \cdot 10^{-6}$ $[K^{-1}]$ $r_p = (8.92 \pm 0.02) \cdot 10^{-5}$ $[K^{-1}]$
Magnetization	$\Gamma_M = (0.14 \pm 0.02) \cdot 10^{-2}$ $[ps^{-1}K^{-1}]$
Electron-phonon coupling	$g_{ep} = (2.05 \pm 0.03) \cdot 10^{18}$ $[W \cdot m^{-3} \cdot K^{-1}]$

Table 5.2: Adjustable parameters in the M3TM. Presented values were obtained after the joint fitting procedure of the data shown in Figures 5.3(a) and (b).

Another disadvantage of the M3TM is that it neglects the fact that upon demagnetization of a ferromagnetic sample some energy has to be transferred to the spin system [36], which in turn leads to the underestimation of the absorbed energy. It is more evident, when the sample temperature approaches the Curie point, where the magnetic contribution to the total heat capacity of a ferromagnet becomes comparable or even larger than the lattice heat capacity [102].

5.3.2 Model with the non-equilibrium hot carriers

In order to describe not only the magnetization dynamics $\delta M(t)$, but also $\delta R(t)$, we introduce a microscopic model complemented with the NEQ electron dynamics. General idea of this model is presented in Figure 5.4(a). It considers four energy reservoirs: NEQ HCs, EQ HCs, phonons (P) and magnetic system (M). The last two are also reservoirs for the angular momentum. The magnetic system can be considered as a spin system, because the orbital momentum of the electrons in 3d ferromagnets is known to be quenched by the strong crystal field [36]. Since we are interested in ultrafast spin dynamics, we do not consider the direct phonon-magnon interaction occurring on a time scale of several tens of picoseconds [26, 94], meaning that the energetic coupling between phonons and the magnetic system is neglected. When the magnetization changes, it affects primarily the energy of the EQ electrons. However, according to previous theoretical and experimental works discussed in **Chapter 2**, ultrafast demagnetization has to be accompanied with the transfer of the angular momentum to the lattice. In the following, we will discuss laser-induced HC and magnetization dynamics in more detail and eventually come to the set of the rate equations (5.28) describing the energy flux and the transfer of the angular momentum between different reservoirs.

[4]Since product αt_G determines the total amount of the absorbed energy and the number of the optically excited HCs, the 20-fs experimental time resolution can be taken into account already in (5.15), otherwise all transient dependencies have to be convolved afterwards with the 14-fs probe laser pulse.

Non-equilibrium hot carriers

Initially the absorption of the pump laser pulse leads to the generation of the majority $h^{\uparrow}$ and minority $h^{\downarrow}$ holes below E_F, majority $e^{\uparrow}$ and minority $e^{\downarrow}$ electrons above E_F (see Figure 5.4(b)), which lose their energy interacting with other carriers and phonons. For the sake of simplicity, it is assumed that the NEQ HCs maintain their energy until they become thermalized, therefore the energy stored in the NEQ HCs is proportional to their density:

$$U_{neq} = n_{neq}\hbar\omega_{pump}, \tag{5.20}$$

and its relaxation is described by the following rate equation:

$$\frac{dn_{neq}}{dt} = \alpha \exp\left[-\frac{2(t-t_0)^2}{t_G^2}\right] - \frac{n_{neq}}{\tau_{ee}^{neq}} - \frac{n_{neq}}{\tau_{ep}^{neq}}, \tag{5.21}$$

where the factor $\hbar\omega_{pump}$ is omitted. The first term in (5.21) is a source term with the absorption coefficient α measured in the number of the NEQ HCs excited per a unit volume per a unit of time. The second and third terms describe the NEQ HC relaxation and are referred to the energy flux $W_{neq\to eq} = n_{neq}\hbar\omega_{pump}/\tau_{ee}^{neq}$ to the EQ HCs and the energy flux $W_{neq\to p} = n_{neq}\hbar\omega_{pump}/\tau_{ep}^{neq}$ to the lattice, respectively. Here τ_{ee}^{neq} and τ_{ep}^{neq} are characteristic time constants of these processes. In the first approximation the influence of the magnetization dynamics on the energy of the NEQ HCs can be neglected. Thus the change of the magnetization affects first the EQ HCs, and then they equilibrate with the lattice, as depicted in Figure 5.4(a). The energy flow between the magnetic system and the EQ HCs will be considered later.

In [95] it was shown that the number of the electron-phonon scattering processes is proportional to the energy flux from the electrons to the lattice. Some part of these processes are followed by spin-flips. Since the phonon energy is limited by the Debye energy 40 meV, one can neglect a change of the NEQ electron energy upon a spin-flip (see Figure 5.4(b)). The spin-flip probability is proportional to the product of the number of the filled initial states in one sub-band and the number of the empty states in another sub-band with the opposite spin. Ignoring the dependence of the spin-flip matrix elements on the electron binding energy, in Figure 5.4(b) it can be seen that the number of the spin decreasing processes exceeds the number of the spin increasing processes. From this consideration, the demagnetization rate due to the NEQ HCs can be written as:

$$\left(\frac{dM}{dt}\right)_{neq} = -\Gamma_{neq}(M_0, M)\frac{n_{neq}\hbar\omega_{pump}}{\tau_{ep}^{neq}}. \tag{5.22}$$

The dependence of $\Gamma_{neq}(M_0, M)$ on the initial M_0 and transient M magnetizations can be explained by the fact that when $M_0 = 0$, there is no exchange splitting and the number of the spin-increasing and spin-decreasing processes are equal to each other. Also it was observed experimentally that if one approaches high demagnetization level due to larger pump fluence [86] or higher initial sample temperature [89], further demagnetization tends to slow down.

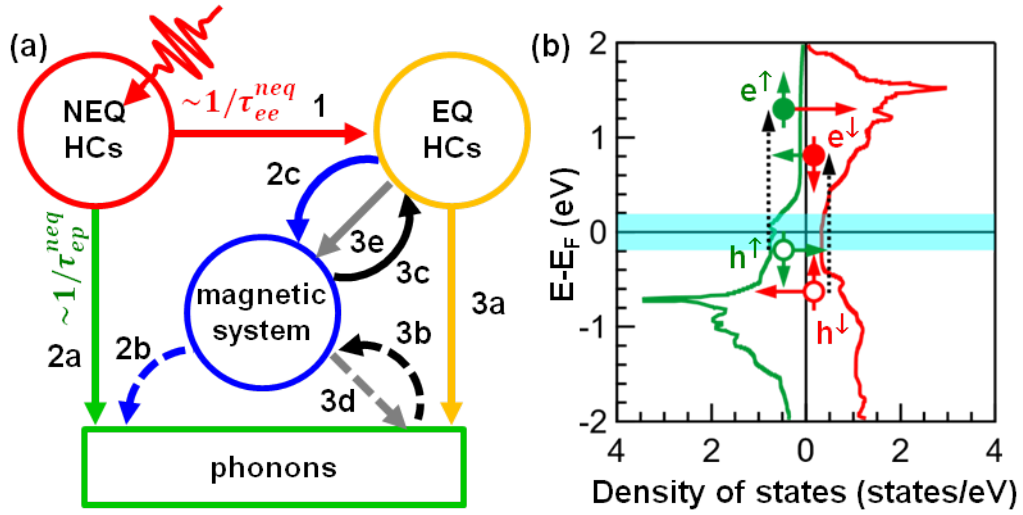

Figure 5.4: (a) Microscopic model for the energy and angular momentum transfer. Solid arrows depict energy flows, and dash arrows depict flows of the angular momentum. Initially pump laser pulse excites nonequilibrium (NEQ) HCs. Their population decreases due to scattering on equilibrium (EQ) HCs and phonons. As a result, part of the energy stored by the NEQ HCs is transferred to the EQ HCs (1) with a characteristic time τ_{ee}^{neq}, and the other part is transferred to the lattice (2a) with a characteristic time τ_{ep}^{neq}. Demagnetization rate due to the NEQ HCs is proportional to the energy flow (2a) and must be accompanied with the transfer of the angular momentum to the lattice (2b). The magnetization dynamics leads primarily to the change of the total energy of the EQ HCs, therefore demagnetization due to the NEQ HCs results in the energy flow from the EQ HCs to the magnetic system (2c). In general, interaction of the EQ HCs with the phonon system can lead to either recovery of the magnetization, corresponding to the angular momentum transfer (3b) and the energy flow (3c), or demagnetization, corresponding to opposite processes (3e) and (3d). However, as long as $T_e > T_p$, energy flows from the EQ HCs to the lattice (3a), which in turn leads to the recovery of the magnetization (3b), (3c). (b) Electronic density of states (DOS) of Fe in the majority (green) and minority (red) sub-bands redrawn after [45]. Dash arrows depict absorption of the pump pulse $\hbar\omega_{pump} = 1.5$ eV leading to the generation of the majority $h^{\uparrow}$ and minority $h^{\downarrow}$ holes below the Fermi energy E_F, and the majority $e^{\uparrow}$ and minority $e^{\downarrow}$ electrons above the Fermi energy E_F. After the optical excitation, HCs in the majority and minority sub-bands have different binding energies. Then due to the electron-electron, electron-phonon and electron-magnon scattering, HCs lose their energy and become EQ HCs. For comparison energy range of the EQ HCs with the electron temperature $T_e = 5000$ K is marked with a cyan colour. Red and green solid arrows depict phonon-mediated spin-decreasing and spin-increasing processes, respectively.

Equilibrium hot carriers

After the electron thermalization, the energy distributions of the majority and minority HCs are described by the same Fermi-Dirac function with the electron temperature T_e:

$$f^{\uparrow}(E_e, T_e) = f^{\downarrow}(E_e, T_e) = \frac{1}{e^{E_e/k_B T_e} + 1}. \tag{5.23}$$

The energy flux $W_{eq\to p}$ from the EQ HCs to the lattice is described as it is done in the 2TM [93]:

$$W_{eq\to p} = g_{ep}(T_e - T_p). \tag{5.24}$$

In spite of the phenomenological character of (5.24), it can be also derived from the microscopic theory [95]. The expression for the magnetization change rate due to $W_{eq\to p}$ is similar to (5.22):

$$\left(\frac{dM}{dt}\right)_{eq} = \Gamma_{eq}(M_0, M) W_{eq\to p} = \Gamma_{eq}(M_0, M) g_{ep}(T_e - T_p), \tag{5.25}$$

where Γ_{eq} characterizes the spin-flip probability for the EQ HCs and depends on the initial M_0 and transient M magnetizations, as Γ_{neq}. Because of the small variations of the magnetization $\delta M(t)$ observed in the experiment, we consider $\Gamma_{neq} = const$ and $\Gamma_{eq} = const$. Since the NEQ HC dynamics leads to the demagnetization, and the EQ HC dynamics occurs together with the recovery of the magnetization, the total magnetization change rate is

$$\frac{dM}{dt} = -\Gamma_{neq} \frac{n_{neq} \hbar \omega_{pump}}{\tau_{ep}^{neq}} + \Gamma_{eq} W_{eq\to p}, \tag{5.26}$$

where $\Gamma_{neq} > 0$ and $\Gamma_{eq} > 0$.

Earlier it was mentioned that the change of the magnetization should be accompanied with the energy flow between the EQ HCs and the magnetic system. The total energy of these two systems is the sum of the kinetic energy of the conduction electrons $U_e = \gamma_e T_e^2/2$ and the magnetic (exchange) energy which in the mean field approximation can be written as $U_M = -I_M M^2$ [36]. Since the direct energy flow between the magnetic and phonon systems is neglected, in the absence of the energy flow $W_{eq\to p}$ (see Figure 5.4) $U_e + U_M$ is conserved, which allows us to derive a partial change rate of the electron temperature $(dT_e/dt)_M$ due to the magnetization dynamics:

$$\left(C_e \frac{dT_e}{dt}\right)_M = 2 I_M M \frac{dM}{dt}. \tag{5.27}$$

Hot carrier and magnetization dynamics

All above consideration of the energy flow and the transfer of the angular momentum due to the NEQ and EQ HCs can be summarized by a set of the differential equations:

$$\begin{aligned}
\frac{dn_{neq}}{dt} &= \alpha \exp\left[-\frac{2(t-t_0)^2}{t_G^2}\right] - \frac{n_{neq}}{\tau_{ee}^{neq}} - \frac{n_{neq}}{\tau_{ep}^{neq}}, \\
C_e\frac{dT_e}{dt} &= \frac{n_{neq}\cdot\hbar\omega_{pump}}{\tau_{ee}^{neq}} - g_{ep}\cdot(T_e - T_p) + 2I_M M\frac{dM}{dt}, \\
C_p\frac{dT_p}{dt} &= \frac{n_{neq}\cdot\hbar\omega_{pump}}{\tau_{ep}^{neq}} + g_{ep}\cdot(T_e - T_p)\,, \\
\frac{dM}{dt} &= -\Gamma_{neq}\frac{n_{neq}\hbar\omega_{pump}}{\tau_{ep}^{neq}} + \Gamma_{eq}g_{ep}(T_e - T_p).
\end{aligned} \tag{5.28}$$

In the simple phenomenological model it has been shown that the generation of the NEQ HCs leads to the drastic changes of the measured signals at the time zero, i.e. the state-filling effect. In [87] Carpene et al. demonstrated that the initial break-down of the MOKE rotation signal is linearly proportional to the absorbed energy, which was also confirmed in our experiments. For this reason, we introduce additional terms to (5.18), (5.19) proportional to the density of the NEQ HCs n_{neq}:

$$\delta R(t) = r_{neq}n_{neq}(t) + r_{eq}(T_e(t) - T_0) + r_p(T_p(t) - T_0), \tag{5.29}$$

$$\begin{aligned}
\delta\psi'_K(t) &= \delta M(t) + b'_{neq}n_{neq}(t) + b'_{eq}[T_e(t) - T_0] + b'_p[T_p(t) - T_0], \\
\delta\psi''_K(t) &= \delta M(t) + b''_{neq}n_{neq}(t) + b''_{eq}[T_e(t) - T_0] + b''_p[T_p(t) - T_0].
\end{aligned} \tag{5.30}$$

The results of the joint fitting procedure are presented in Figure 5.5 and corresponding values of the adjustable parameters are shown in Table 5.3. The microscopic model perfectly reproduces both the magnetization $\delta M(t)$ and the linear reflectivity $\delta R(t)$. One of the drawbacks in our model is that the equations (5.28) do not explicitly define the magnetization established after the electron-phonon thermalization. Probably we need to consider an additional term describing the phonon-magnon coupling and providing the equilibrium magnetization M_{eq}.

Comparing the results of the phenomenological and microscopic models (see Tables 5.1 and 5.3), one can note that

$$\tau_{ee}^{phen} \approx \frac{\tau_{ee}^{neq}\tau_{ep}^{neq}}{\tau_{ee}^{neq} + \tau_{ep}^{neq}} \approx 0.20 \pm 0.01 \text{ ps}. \tag{5.31}$$

Thus the phenomenological model gives the total relaxation time of the NEQ HCs.

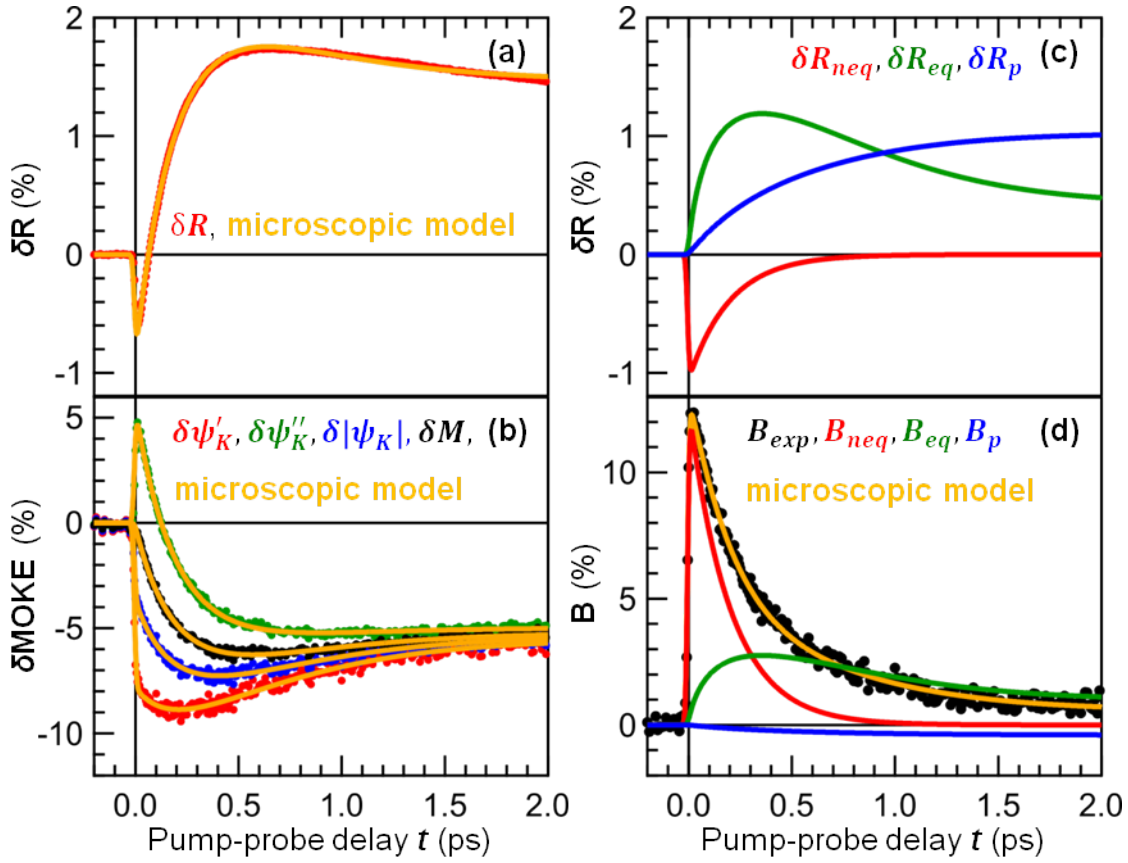

Figure 5.5: Pump-induced relative variations of the linear magneto-optical response measured on a 8-nm polycrystalline Fe film and reproduced within the microscopic model: (a) linear reflectivity $\Delta R(t)$ (red dots), (b) MOKE rotation $\delta\psi'_K(t)$ (red dots), ellipticity $\delta\psi''_K(t)$ (green dots), absolute value of the Kerr angle $\delta|\psi_K|(t)$ (blue dots) and the bulk magnetization $\delta M(t)$ (black dots) evaluated using (5.6). Orange lines reproduce the experimental data according to the microscopic model (5.28), (5.30) and (5.29). (c) Variations of the linear reflectivity induced by the NEQ HCs $\delta R_{neq}(t)$ (red line), heating of the EQ HCs $\delta R_{eq}(t)$ (green line) and the lattice $\delta R_p(t)$ (blue line). (d) Difference between the MOKE ellipticity and rotation $B(t) = \delta\psi''_K(t) - \delta\psi'_K(t)$ (black dots - experiment, orange line - microscopic model). Red, green and blue lines in (d) correspond to the contributions induced by the NEQ HCs ($B_{neq}(t)$), the changes of the electron T_e ($B_{eq}(t)$) and lattice T_p ($B_p(t)$) temperatures, respectively.

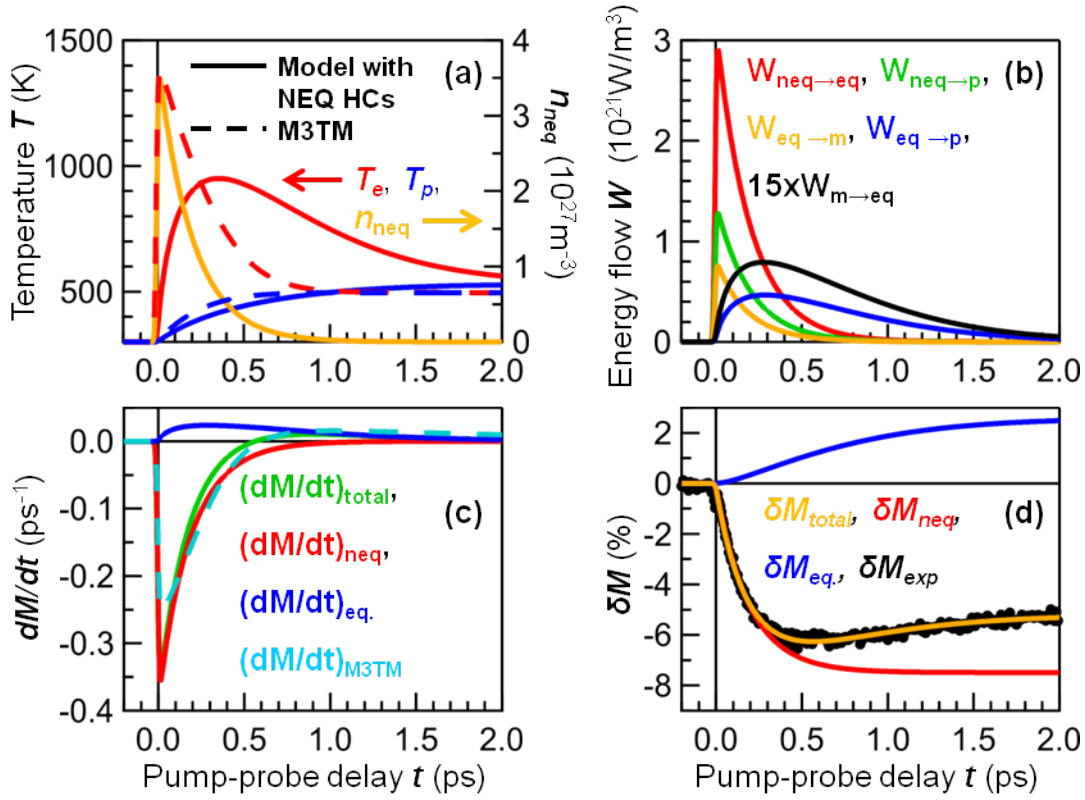

Figure 5.6: (a) Density of the NEQ HCs n_{neq} (orange), electron T_e (red) and lattice T_p (blue) temperatures upon laser excitation of the Fe film. Solid lines correspond to the model with NEQ HCs, and dash lines were obtained in the fitting procedure within the M3TM. (b) Power flow from the NEQ HCs to the EQ HCs $W_{neq\rightarrow eq}$(red), to the lattice $W_{neq\rightarrow p}$(green), power flow from the electronic system to the magnetic system due to the demagnetization $W_{eq\rightarrow m}$ (orange) and power flow back to the electronic system due to the remagnetization $W_{m\rightarrow eq}$ (black), and power flow from EQ HCs to the lattice $W_{eq\rightarrow p}$ (blue). (c) Total rate of the magnetization dynamics $(dM/dt)_{total}$ (green) and partial rates due to the NEQ $(dM/dt)_{neq}$ (red) and EQ $(dM/dt)_{eq}$ (blue) HCs. Magnetization change rate $(dM/dt)_{M3TM}$ obtained in the fitting procedure within the M3TM is depicted with a cyan dash line. (d) Total variation of the magnetization δM (black - the experimental data, orange - the microscopic model) and partial variations δM_{neq} and δM_{eq} due to the NEQ (red) and EQ (blue) HCs, respectively.

Laser absorption	$\alpha t_G \hbar\omega_{pump}\sqrt{\pi/2} \approx 9.3 \cdot 10^8\ [J/m^3]$
MOKE difference	$b'_{neq} = -(1.93 \pm 0.01) \cdot 10^{-29}\ [m^3]$ $b''_{neq} = (1.42 \pm 0.01) \cdot 10^{-29}\ [m^3]$ $b'_{eq}/b'_{neq} = b''_{eq}/b''_{neq} = (1.27 \pm 0.02) \cdot 10^{24}\ [K^{-1} \cdot m^{-3}]$ $b'_{p}/b'_{neq} = b''_{p}/b''_{neq} = -(0.52 \pm 0.02) \cdot 10^{24}\ [K^{-1} \cdot m^{-3}]$
Reflectivity	$r^R_{neq} = -(0.28 \pm 0.02) \cdot 10^{-29}\ [m^3]$ $r_{eq} = (1.83 \pm 0.02) \cdot 10^{-5}\ [K^{-1}]$ $r_{p} = (4.45 \pm 0.04) \cdot 10^{-5}\ [K^{-1}]$
Magnetization	$\Gamma_{neq} = (2.95 \pm 0.01) \cdot 10^{-10}\ [m^3 \cdot ps/J]$ $\Gamma_{eq} = (5.79 \pm 0.01) \cdot 10^{-11}\ [m^3 \cdot ps/J]$
Time constants	$\tau^{neq}_{ee} = 0.29 \pm 0.01\ [ps]$ $\tau^{neq}_{ep} = 0.65 \pm 0.02\ [ps]$
Electron-phonon coupling	$g_{ep} = (8.61 \pm 0.01) \cdot 10^{17}\ [W \cdot m^{-3} \cdot K^{-1}]$

Table 5.3: Adjustable parameters in the microscopic model. Presented values were obtained after the joint fitting procedure of the data shown in Figures 5.5(a) and (b).

Parameter Γ_{neq} is larger than Γ_{eq}, meaning that the NEQ HCs provide faster magnetization dynamics than the EQ HCs. This conclusion is in an agreement with the results of the ab-initio calculations performed by Carva et al. [96]. However, in contrast to [96], we showed that demagnetization of the Fe film is dominated by the NEQ HCs, while the EQ HCs contribute mostly to the recovery of the magnetization.

Figure 5.6(a) presents temporal profiles of the NEQ HC density n_{neq}, the electron T_e and lattice T_p temperatures. The electron T_e and lattice T_p temperatures calculated in the M3TM are shown for comparison. Predictions for the temperature established after the electron-phonon thermalization are close to each other. The difference between them are related to the difference between the equations (5.13) and (5.17) describing the experimental and theoretical temperature dependences of the equilibrium magnetization, respectively. The electron temperature T_e reaches its maximum at about 360 fs. At this time there is still a considerable amount of the NEQ HCs, so $|(dM/dt)_{neq}| > |(dM/dt)_{eq}|$ and the recovery of the magnetization starts only in 500 fs after the optical excitation (Figures 5.6(c) and (d)). In Figure 5.6(b) it can be seen that there is a significant energy flow to the magnetic system $W_{eq\to m}$, comparable to others. It means that in the estimation of the absorbed energy $W_{eq\to m}$ and $W_{m\to m}$ cannot be neglected as it was done in [86], especially for large demagnetization values or high initial temperatures approaching the Curie temperature T_C, when the magnetic heat capacity becomes larger than the lattice heat capacity.

5.4 Nonlinear magneto-optical response

In addition to the linear magneto-optical signals, the mSHG response of the Fe film has been measured. Small SH yield and interference of the SH fields originating at two Fe/MgO interfaces results in small, but measurable SH intensity. Large scattering of the mSHG data (see Figure 5.7) makes it worthless to use them in the joint fitting pro-

cedure together with the linear magneto-optical signals. However, upon homogeneous optical excitation, magnetization and HC dynamics at the interfaces should exhibit the same behaviour as in the bulk of the Fe film, therefore the linear magneto-optical response might be used to reproduce the mSHG data.

The SH field can be expressed as the sum of the even and odd terms with respect to the reversal of the magnetization:

$$\vec{E}_{2\omega} = \vec{E}^{even}_{2\omega} + \vec{E}^{odd}_{2\omega} = \vec{\xi}_{even} + \vec{\xi}_{odd} M. \tag{5.32}$$

In the first approximation, the even term is independent of and the odd term is linearly proportional to the magnetization. Applying p-polarized probe pulse in the transversal magneto-optical geometry results in p-polarized even $E^{even}_{2\omega}$ and odd $E^{odd}_{2\omega}$ SH fields. The SH intensity is given by

$$I^{\uparrow\downarrow}_{2\omega} = |E^{even}_{2\omega}|^2 \pm 2 \cdot |E^{even}_{2\omega} \cdot E^{odd}_{2\omega}| \cdot \cos\phi + |E^{odd}_{2\omega}|^2, \tag{5.33}$$

where $\uparrow\downarrow$ and $\pm$ correspond to the opposite directions of the magnetization. $\Delta^T_{even}(t)$ and Δ^T_{odd} shown in Figure 5.7(a) were calculated using the following expressions:

$$\Delta^T_{even} = \sqrt{\frac{I^{\uparrow}_{2\omega} + I^{\downarrow}_{2\omega}}{I^{\uparrow}_{0,2\omega} + I^{\downarrow}_{0,2\omega}}} - 1 = \sqrt{\frac{|E^{even}_{2\omega}|^2 + |E^{odd}_{2\omega}|^2}{|E^{even}_{0,2\omega}|^2 + |E^{odd}_{0,2\omega}|^2}} - 1, \tag{5.34}$$

$$\begin{aligned} \Delta^T_{odd} &= \frac{I^{\uparrow}_{2\omega} - I^{\downarrow}_{2\omega}}{I^{\uparrow}_{0,2\omega} - I^{\downarrow}_{0,2\omega}} \cdot \sqrt{\frac{I^{\uparrow}_{0,2\omega} + I^{\downarrow}_{0,2\omega}}{I^{\uparrow}_{2\omega} + I^{\downarrow}_{2\omega}}} - 1 \\ &= \frac{|E^{even}_{2\omega}| \cdot |E^{odd}_{2\omega}| \cos\phi}{|E^{even}_{0,2\omega}| \cdot |E^{odd}_{0,2\omega}| \cos\phi_0} \sqrt{\frac{|E^{even}_{0,2\omega}|^2 + |E^{odd}_{0,2\omega}|^2}{|E^{even}_{2\omega}|^2 + |E^{odd}_{2\omega}|^2}} - 1. \end{aligned} \tag{5.35}$$

Unlike the linear magneto-optical signals, Δ^T_{even} and Δ^T_{odd} do not undergo drastic variations at the time zero: a 20-fs width peak in Δ^T_{even} at the time-zero is the SH cross-correlation signal which presents while there is an overlap of the pump and probe pulses. Static mSHG contrast $\rho^T_{2\omega,0} = (I^{\uparrow}_{2\omega,0} - I^{\downarrow}_{2\omega,0})/(I^{\uparrow}_{2\omega,0} + I^{\downarrow}_{2\omega,0}) = (-82 \pm 1)\%$, so $|E^{odd}_{2\omega}|^2$ cannot be neglected. However, applying the external magnetic field in the longitudinal direction and measuring only p-polarized SH component, it is possible to derive the even $E^{even}_{2\omega}$, odd $E^{T,odd}_{2\omega}$ mSHG fields and the phase difference ϕ^T between them [5]. It turned out that both even $\delta E^{even}_{2\omega}$ and odd $\delta E^{odd}_{2\omega}$ SH fields are influenced by the state-filling effect as the linear magneto-optical response (see Figure 5.7(a)). Absence of the drastic changes in Δ^T_{even} and Δ^T_{odd} brings us to the conclusion that contributions of the state-filling effect to $\delta E^{even}_{2\omega}$ and $\delta E^{odd}_{2\omega}$ are equal to each other. It allows us to evaluate these contributions (see Figure 5.7(b)):

$$B_{2\omega} = 0.5(\delta E^{even}_{2\omega} - \delta E^{odd}_{2\omega}). \tag{5.36}$$

[5] According to (3.41), for p-polarized probe pulse only the transversal component of the magnetization gives rise to the p-polarized odd SH field $E^{odd}_{2\omega}$.

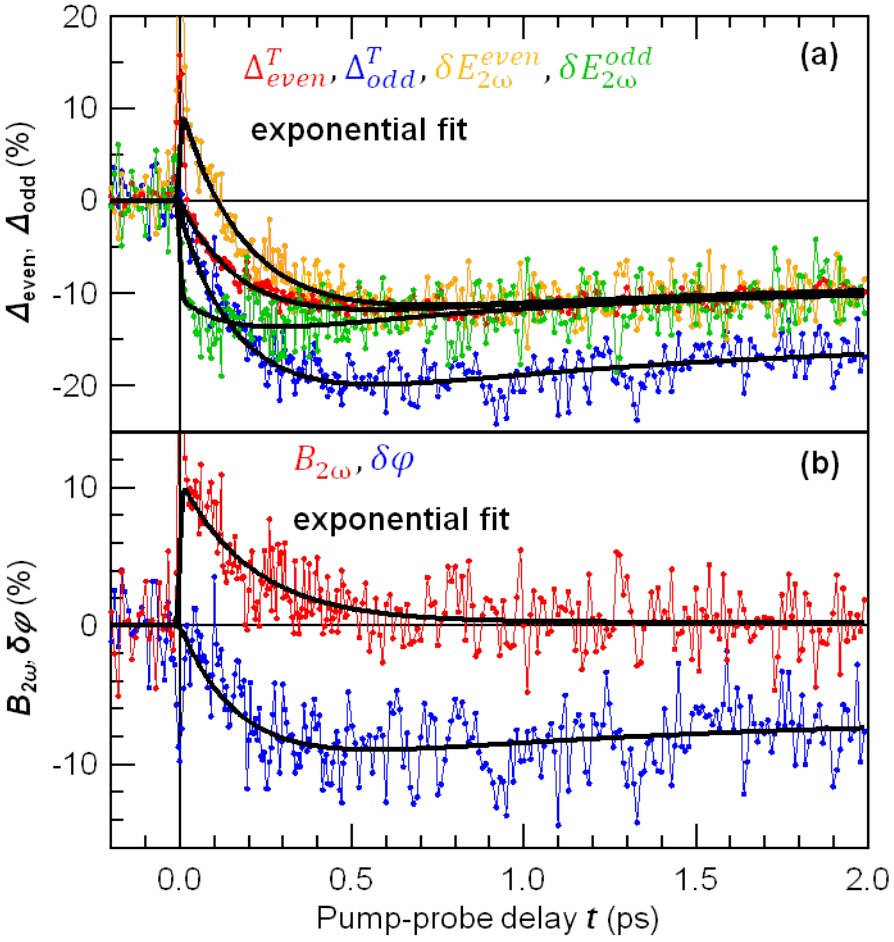

Figure 5.7: Pump-induced relative variations of the mSHG response: (a) red colour - Δ^T_{even}, blue colour - Δ^T_{odd}, orange and green colours - variations of the even $\delta E^{2\omega}_{even}$and odd $\delta E^{2\omega}_{odd}$ SH fields, respectively; (b) red colour - contribution of the optical bleaching to the variation of the SH fields $0.5 \cdot (\delta E^{2\omega}_{even} - \delta E^{2\omega}_{odd})$, blue colour - variation of the phase difference $\delta\phi$ between the even $\vec{E}^{2\omega}_{even}$ and odd $\vec{E}^{2\omega}_{odd}$ SH fields. Black lines were obtained in the joint fitting procedure of $\delta E^{2\omega}_{even}$, $\delta E^{2\omega}_{odd}$ and $\delta\phi$ using the results of the analysis of the linear magneto-optical response.

Because of the homogeneous optical excitation, HC and magnetization dynamics in the bulk of the Fe film and at the Fe/MgO interfaces should be identical, therefore linear magneto-optical response can be used to describe the mSHG signals.:

$$\delta E_{2\omega}^{even}(t) = b_{2\omega} \cdot e^{-t/\tau_{ee}} + \kappa_{2\omega}^{even} \cdot [r_0 \cdot (1 - e^{-t/\tau_{ee}}) \cdot e^{-t/\tau_{ep}} + r_1 \cdot (1 - e^{-t/\tau_{ep}})], \quad (5.37)$$

$$\begin{aligned}\delta E_{2\omega}^{odd}(t) = &-b_{2\omega} \cdot e^{-t/\tau_{ee}} + \kappa_{2\omega}^{odd} \cdot [r_0 \cdot (1 - e^{-t/\tau_{ee}}) \cdot e^{-t/\tau_{ep}} + r_1 \cdot (1 - e^{-t/\tau_{ep}})] \\ &+ [m_0 \cdot (1 - e^{-t/\tau_M}) \cdot e^{-t/\tau_R} + m_1 \cdot (1 - e^{-t/\tau_R})],\end{aligned} \quad (5.38)$$

$$\delta\phi(t) = \kappa_{2\omega}^{\phi} \cdot [r_0 \cdot (1 - e^{-t/\tau_{ee}}) \cdot e^{-t/\tau_{ep}} + r_1 \cdot (1 - e^{-t/\tau_{ep}})], \quad (5.39)$$

where r_0, r_1, m_0, m_1, $\tau_{ee} = \tau_M$, $\tau_{ep} = \tau_M$ are the fitting parameters obtained in the phenomenological model for the linear magneto-optical response. Here it is assumed that in the absence of the state-filling effect variations of $|\vec{\xi}_{even}|$ and $|\vec{\xi}_{odd}|$ are linearly proportional to the variation of the linear reflectivity induced by the heating of the electronic system and the lattice. Black solid lines in Figure 5.7 represent the result of the joint fitting procedure with only four parameters $b_{2\omega} = 10.5 \pm 0.4\%$, $\kappa_{2\omega}^{even} = -6.6 \pm 0.1$, $\kappa_{2\omega}^{odd} = -3.3 \pm 0.1$, $\kappa_{2\omega}^{\phi} = -4.98 \pm 0.09$. In spite of the small signal-to-noise ratio in the mSHG signals, there is a good agreement between the linear and nonlinear magneto-optical responses. Also good fit quality supports our assumption about the relation between variations of $|\vec{\xi}_{even}|$, $|\vec{\xi}_{odd}|$ and ΔR.

5.5 Conclusions

Ultrafast demagnetization of Fe in the absence of the HC transport has been studied using time-resolved MOKE and mSHG techniques. In order to be more sensitive to the generation of the NEQ HCs and their decay, we have utilized single-colour pump-probe experiments with the identical photon energies of the pump and probe pulses $\hbar\omega_{pump} = \hbar\omega_{probe} = 1.5$ eV. Owing to that, the state-filling effect [82] contributes to the reflectivity $\delta R(t)$, MOKE rotation $\delta\psi'_K(t)$ and ellipticity $\delta\psi''_K(t)$ signals. The difference between variations of the MOKE ellipticity and rotation $B(t) = \delta\psi''_K(t) - \delta\psi'_K(t)$ can appear not only due to the variation of the magneto-optical constants, but also in the case of the inhomogeneous magnetization profile as a result of the different depth sensitivities [122]. However, by choosing 8-nm (i.e. homogeneously pumped) Fe film on the non-conducting MgO substrate, we can exclude the HC transport (homogeneous magnetization profile) and treat $B(t)$ as a purely non-magnetic signal. In order to evaluate and characterize magnetization and HC dynamics, three main assumptions have been made. (i) In the absence of the HC transport demagnetization is governed by the spin-flip processes accompanied with the transfer of the angular momentum to the lattice. Assuming that the characteristic time of this demagnetization mechanism is considerably longer than the experimental 20-fs time resolution, one can neglect instantaneous changes of the magnetization at the time zero $\Delta M(t = 0) = 0$. (ii) The relaxation dynamics of the majority and minority NEQ HCs has been described with a single characteristic time τ_{ee}. The NEQ HC population decays into the thermalized (EQ HC) one which subsequently relaxes with a characteristic time τ_{ep} due to the

electron-phonon interaction. (iii) These processes induce modifications of the MOKE signals with the same temporal profile $B(t)$. Thus one can evaluate real magnetization dynamics, using the expression (5.6).

In order to obtain τ_{ee}, τ_{ep}, we have performed the joint fitting procedure for $B(t)$, $\delta R(t)$ curves with a sum of $e^{-t/\tau_{ee}}$ corresponding to the state-filling effect produced by the NEQ HCs, $(1-e^{-t/\tau_{ee}})e^{-t/\tau_{ep}}$ and $(1-e^{-t/\tau_{ep}})$ terms referred to the influence of the electron T_e and lattice T_p temperatures. At the same time $\delta M(t)$ curve has been fitted using the similar expression (5.10) with the time constants τ_M and τ_R characterizing the demagnetization and remagnetization time scales, respectively. Initially these time constants were independent from τ_{ee} and τ_{ep}, but it turned out that $\tau_M \approx \tau_{ee}$ and $\tau_R \approx \tau_{ep}$, which means that the demagnetization is dominated by the NEQ HCs, while the recovery of the magnetization is governed by the EQ HCs. Subsequently from the joint fitting procedure performed for $\delta R(t)$, $\delta\psi'_K(t)$ and $\delta\psi''_K(t)$ with just two characteristic time constants, we have obtained $\tau_M = \tau_{ee} = 0.21 \pm 0.01$ ps, $\tau_R = \tau_{ep} = 1.06 \pm 0.03$ ps. Here it should be noted that the experimental 20-fs time resolution excludes other possible assignments of the time constants τ_{ee} and τ_{ep}, which were suggested in the previous works performed on thin Fe [87, 134], Ni and Co films [86], where the smallest time constant ~ 100 fs was determined by the duration of the pump and probe pulses rather than the electron thermalization.

In addition to the phenomenological description, we have developed a microscopic model based on the 2TM complemented with the NEQ HCs which have not been considered neither in the 3TM [25] nor the M3TM [86]. In the microscopic model, the HC and magnetization dynamics has been described through the consideration of the energy flux and the transfer of the angular momentum. It has been suggested that the magnetization change rate is proportional to the energy flow from the NEQ and EQ HCs to the phonon system. The first process leads to the demagnetization, while the second one provides the recovery of the magnetization. In spite of certain assumptions, the microscopic model can reproduce the experimental data, including the transient reflectivity $\delta R(t)$, with the same fit quality as the phenomenological description.

Summarizing, it has been demonstrated how the magnetization dynamics and the optical effects can be disentangled from a complete set of the magneto-optical data. Both phenomenological and microscopic models reveal the dominant role of the NEQ HCs in the ultrafast spin dynamics, as it was suggested in [96]. However, it has been found that the demagnetization occurs on the time scale of the HC thermalization ~ 200 fs due to the NEQ HCs, while the EQ HCs contribute mostly to the recovery of the magnetization.

Chapter 6

Hot carrier injection from the Fe film into the Au layer

This chapter is devoted to laser-induced hot carrier (HC) transport from a ferromagnet into a noble metal. Experimental results presented here were obtained on Au/Fe/MgO(001) structures. In contrast to an isolated homogeneously pumped 8-nm Fe film discussed in **Chapter 5**, optical excitation of Fe is followed by the efficient HC emission into the Au film. Thus Au serves as a sink of heat and spin polarization (SP), and the HC transport contributes considerably to ultrafast spin dynamics in the Fe film.

Pumping and probing the Fe side of Au/Fe/Mgo(001) structures, transient MOKE gives information on the average magnetization in the bulk of the Fe and Au layers, and transient mSHG signal monitors variation of SP at the Fe/MgO and the Fe/Au interfaces. Comparison of the transient MOKE data with those presented in **Chapter 5** reveals a considerable role of the HC transport in ultrafast demagnetization of the Fe film. In **Chapter 6** it is demonstrated the injection of the spin-polarized HCs into Au gives rise to the magneto-optical response from the non-magnetic layer, thereby proving that the HC-driven spin transfer is really present.

Due to the exchange-split energy band structure of a ferromagnet, majority and minority carriers are excited in different areas of the Brillouine zone to the states with different wave vectors and binding energies. As a result, they have different velocities v^{HC}, lifetimes τ^{HC}, ballistic lengthes λ^{HC} in Fe and Au, and different transmission probabilities through the Fe/Au interface. All these quantities determine magnetization profile in the Fe film and accumulation of spin-polarized HCs in the Au layer in the vicinity of the Fe/Au interface during first 100 fs after laser excitation (see Figure 6.1). Because of the different depth sensitivity of the MOKE rotation and ellipticity, a non-uniform magnetization profile causes the difference between them in addition to the optical bleaching and the variation of the magneto-optical constants, discussed in **Chapter 5**. Using the ballistic HC profiles, it is nevertheless possible to disentangle all contributions to the MOKE signals and reproduce the experimental data.

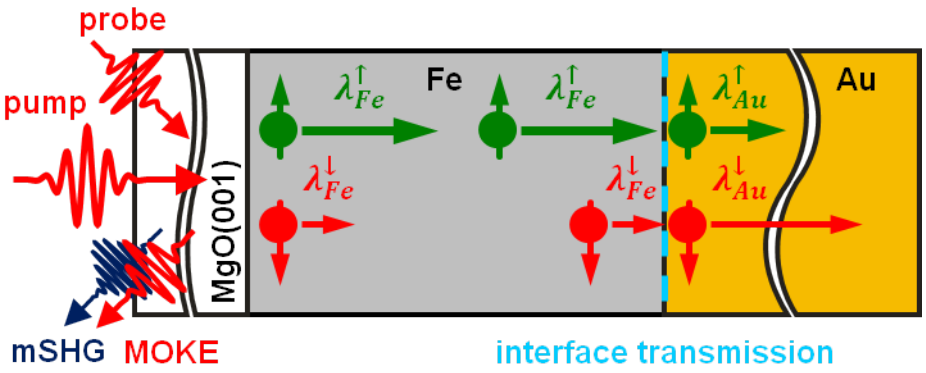

Figure 6.1: Experimental scheme to study spin dynamics induced in the Fe film by optical pumping. Arrows depict propagation of majority (green) and minority (red) carriers in the Fe and Au layers with ballistic lengthes $\lambda^{\uparrow}_{Fe}$, $\lambda^{\uparrow}_{Au}$, $\lambda^{\downarrow}_{Fe}$ and $\lambda^{\downarrow}_{Au}$.

6.1 Static magneto-optical response of the Fe film

For correct interpretation of spin dynamics induced in the Fe film, static linear and nonlinear magneto-optical responses of the Au/Fe/MgO(001) structure should be understood in detail. In **Chapter 2** it was discussed that the linear optical properties of Fe in the near-infrared region are determined by the interband transitions, while for Au the free-carrier contribution dominates. Regarding the SHG response of Au for $\hbar\omega_{probe} = 1.5$ eV, it includes the interband transitions from the initial states in the d-band with the top edge at about -1.8 eV below the Fermi energy E_F [46]. Owing to the free-carrier contribution, Au has larger SHG yield than Fe. Besides that there is no SP in Au in the absence of the pump pulse. All these factors lead to strong dependence of the magneto-optical response on the iron d_{Fe} and gold d_{Au} thicknesses.

In Figure 6.2 three maps of the linear reflectivity R (a), SH intensity $I^T_{2\omega} = (I^{\uparrow}_{2\omega} + I^{\downarrow}_{2\omega})/2$ (b) and SH contrast $\rho^T_{2\omega} = (I^{\uparrow}_{2\omega} - I^{\downarrow}_{2\omega})/(I^{\uparrow}_{2\omega} + I^{\downarrow}_{2\omega})$ (c) measured on the Au/Fe/MgO(001) sample with six different regions are presented. For each Fe thickness ($d_{Fe} = 2, 5,$ and 8 nm) there are two regions with thin ($d_{Au} = 5$ nm) and thick ($d_{Au} = 47$ nm) Au layer. Due to higher reflectivity and nonlinearity of Au, the linear reflectivity R and SH yield $I^T_{2\omega}$ increase with the reduction of d_{Fe}. Total mSHG signal in the absence of the optical excitation is a result of the interference of the SH fields originating at the Fe/MgO, Fe/Au interfaces and the Au surface. The amplitudes of these SH fields and the phase differences between them depend on d_{Fe} and d_{Au} leading to either negative or positive values of the SH contrast $\rho^T_{2\omega}$ (see Figure 6.2(c)). Thus these maps make it much easier to identify all regions and borders between them. Moreover, sometimes it is impossible to distinguish neighbouring regions using only the optical microscope (see Figure 4.1). But on such maps of the magneto-optical signals even small differences can be seen.

From Figure 6.2 one can see that in spite of small light penetration depths in Fe and Au (for $\hbar\omega_{probe} = 1.5$ eV 17 and 13 nm, respectively), much deeper parts of the iron and gold films contribute considerably to the linear and nonlinear magneto-optical

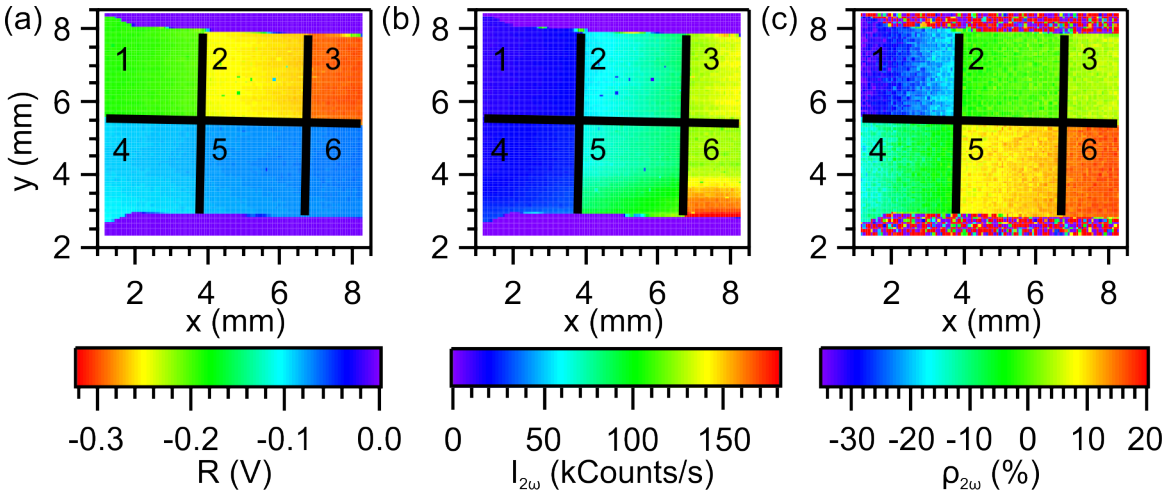

Figure 6.2: Maps of the linear reflectivity R(a), SH intensity $I_{2\omega}$(b) and SH contrast $\rho_{2\omega}$ measured probing through the MgO substrate a two-layer Au/Fe/MgO(001) sample with six different regions: (1) $d_{Fe} = 8$ nm, $d_{Au} = 47$ nm; (2) $d_{Fe} = 5$ nm, $d_{Au} = 47$ nm; (3) $d_{Fe} = 2$ nm, $d_{Au} = 47$ nm; (4) $d_{Fe} = 8$ nm, $d_{Au} = 5$ nm; (5) $d_{Fe} = 5$ nm, $d_{Au} = 5$ nm; (6) $d_{Fe} = 2$ nm, $d_{Au} = 5$ nm.

responses. Since this chapter is devoted to the HC injection from the Fe film into the Au layer, our attention will be focused on the results obtained on the Au/Fe/MgO(001) structures with 130 nm of Au. Considering small pump-probe delays $\sim 40 - 60$ fs, it allows us to simplify the interpretation of the experimental data, because for such thick Au film the presence of the Au surface does not affect the magneto-optical signals and it takes more time for the HCs to propagate back and forth across the sample.

Figure 6.3(a) shows the dependencies of the static linear reflectivity R_0, MOKE rotation $\psi'_{K,0}$, ellipticity $\psi''_{K,0}$, and the MOKE magnitude $|\psi_{K,0}| = \sqrt{\psi'^2_{K,0} + \psi''^2_{K,0}}$ on d_{Fe} for Au/Fe/MgO(001) structure with 130 nm of Au. The reflectivity signal R_0 was scaled to fit the theoretical values for thick Fe films, where the reflectivity dependence on d_{Fe} is more or less flat. At the same time, no fitting procedure was used for the MOKE signals. Theoretical curves were calculated for the 130nm-Au/Xnm-Fe/0.5mm-MgO(001) structure probed with the laser pulse $\hbar\omega_{probe} = 1.5$ eV at 50° angle of incidence, according to the self-consistent 4x4 matrix method described in **Chapter 3**. The MgO substrate is 0.5 mm thick, so it takes about 5.8 ps for the laser pulse to go back and forth through it. Thus for 14-fs laser pulses no interference effects caused by the MgO substrate should be observed. For this reason, in the calculations $d_{MgO} = 0$. It gives the same result as the calculations performed for $d_{MgO} = 0.5$ mm and a 14-fs probe pulse with central wavelength 1.5 eV. Consideration of all frequency components consumes more computational time than the consideration of only one single component with $\hbar\omega = 1.5$ eV, therefore for the analysis of the transient signals measured in the pump-probe experiments all calculations were done for single wavelength $\hbar\omega = 1.5$ eV.

In order to calculate the magneto-optical response of the Au/Fe/MgO(001) structures with a non-uniform magnetization profiles, the Fe and Au films were splitted into the sublayers with thicknesses $\Delta z = 0.1$ nm, so the magnetization within one sublayer is nearly constant. Figure 6.3(b) presents the depth sensitivities of the longitudinal MOKE rotation $w'_K(z)$ and ellipticity $w''_K(z)$ calculated for the Au/Fe/MgO(001) structure with 15 nm of Fe and 130 nm of Au. They correspond to the contributions of the sublayer at the depth z in the Fe film to the MOKE signals. The total MOKE rotation ψ'_K and ellipticity ψ''_K signals are simply given by the sums of the contributions from all the sublayers in the Fe and Au films:

$$\psi'_K = \sum_j w'_K(z_j)M(z_j),\ \psi''_K = \sum_j w''_K(z_j)M(z_j). \tag{6.1}$$

The depth sensitivities $w'_K(z)$, $w''_K(z)$ changes with d_{Fe}, but Figure 6.3(b) reflects the general tendency that $w''_K(z)$ has its maximum at the Fe/MgO interface and decreases with the film depth z, while $w'_K(z)$ is small at the Fe/MgO interface and increases towards the Fe/Au interface. Later in the analysis of the pump-probe experiments it will be demonstrated that a non-uniform magnetization profile leads to the different behaviour of the MOKE rotation $\psi_K(t)$ and ellipticity $\psi''_K(t)$ even in the absence of the optical artefacts.

For the linear magneto-optical signal there is a good agreement between theoretical and experimental results, but with the mSHG response situation is rather complicated. For the samples with 130 nm of Au, the total mSHG response presented in the Figure 6.3(b) is the result of the interference of the SH fields $\vec{E}_{2\omega}^{Fe/MgO}$ and $\vec{E}_{2\omega}^{Fe/Au}$ originating at the Fe/MgO and Fe/Au interfaces. For the p-polarized probe pulse, the even SH component $\vec{E}_{2\omega}^{even}$ is p-polarized, while the odd SH component $\vec{E}_{2\omega}^{odd}$ is p-polarized in the transversal magneto-optical configuration ($\vec{M}||\hat{y}$:$\uparrow$ and $\downarrow$) and s-polarized in the longitudinal magneto-optical configuration ($\vec{M}||\hat{x}$:$\rightarrow$ and $\leftarrow$) [116]. Using the analyzer set to transmit only the p-polarized component and measuring SH intensities in both magneto-optical geometries, it is possible to evaluate the amplitudes of the even $|\vec{E}_{2\omega}^{even}|$ and odd $|\vec{E}_{2\omega}^{odd,T}|$ SH fields[1], and the optical phase $\phi_{2\omega}^T$ between them (see Figure 6.3(c)):

$$|\vec{E}_{2\omega}^{even}| = \sqrt{\frac{I_{2\omega}^{\rightarrow} + I_{2\omega}^{\leftarrow}}{2}}, \tag{6.2}$$

$$|\vec{E}_{2\omega}^{odd,T}| = \sqrt{\frac{I_{2\omega}^{\uparrow} + I_{2\omega}^{\downarrow}}{2} - \frac{I_{2\omega}^{\rightarrow} + I_{2\omega}^{\leftarrow}}{2}}, \tag{6.3}$$

$$\cos\phi_{2\omega}^T(t) = \frac{I_{2\omega}^{\uparrow} - I_{2\omega}^{\downarrow}}{2\sqrt{(I_{2\omega}^{\rightarrow} + I_{2\omega}^{\leftarrow})[(I_{2\omega}^{\uparrow} + I_{2\omega}^{\downarrow}) - (I_{2\omega}^{\rightarrow} + I_{2\omega}^{\leftarrow})]}}. \tag{6.4}$$

[1]The mark 'T' means that $\vec{E}_{2\omega}^{odd,T}$ arises only from the transversal magnetization component or the spin current with the spin polarization $\vec{\sigma}||\hat{y}$, formed by the hot carriers propagating across the sample $\vec{v}_{HC}||\hat{z}$.

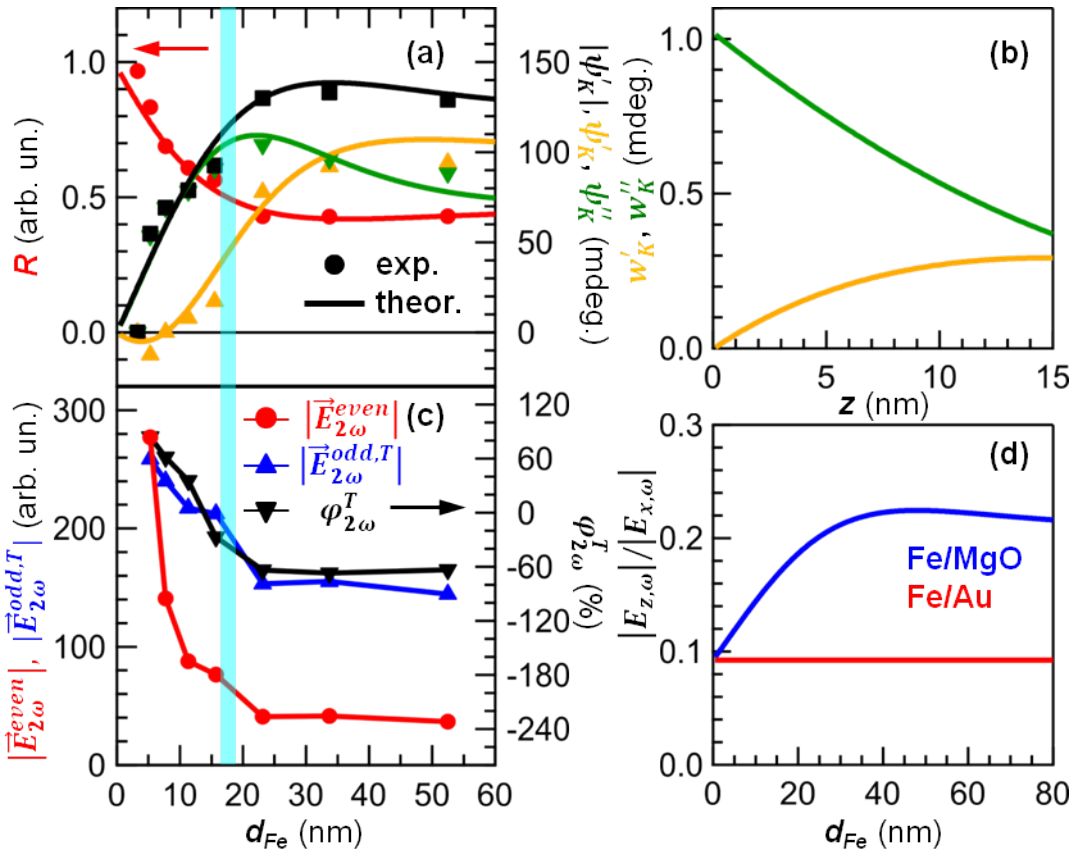

Figure 6.3: (a) Static reflectivity R_0 (red dots), MOKE rotation $\psi'_{K,0}$ (orange up-trianlges), ellipticity $\psi''_{K,0}$ (green down-trianlges) and absolute value of the Kerr angle $|\psi_{K,0}| = \sqrt{\psi'^2_{K,0} + \psi''^2_{K,0}}$ (black squares) measured for 130 nm of Au and different Fe thicknesses. Marks represent experimental values, solid lines are the theoretical dependences ($\hbar\omega = 1.5$ eV, $\theta_{probe} = 50°$, $n^{\omega}_{MgO} = 1.7271$ [140], $n^{\omega}_{Au} = 0.08 + 5.0i$ [48], $n^{\omega}_{Fe} = 3.05 + 3.77i$, $q^{\omega}_{Fe} = 0.0588 - 0.0099i$ [141]) calculated according to the method described in the chapter 3. (b) Depth sensitivities of the longitudinal MOKE rotation $w'_K(z)$ and ellipticity $w''_K(z)$. $w'_K(z)$, $w''_K(z)$ are contributions to the MOKE signals from the sublayer ($\Delta z = 0.1$ nm) with the magnetization $\vec{M} \| \hat{x}$ ($|\vec{M}| = 1$) at the distance z from the Fe/MgO interface in the Fe film, calculated for Au/Fe/MgO(001) structure with 15 nm of Fe and 130 nm of Au. (c) Dependences of the static amplitudes of the even $|\vec{E}^{even}_{2\omega}|$ and odd $|\vec{E}^{odd,T}_{2\omega}|$ SH fields, and the optical phase $\phi^T_{2\omega}$ between them, derived from the SH intensities using the expressions (6.2), (6.3), (6.4). (d) Ratio between the amplitudes of the z- and x-components of the fundamental field $\vec{E}_{\omega}$ at the Fe/MgO (blue) and Fe/Au (red) interfaces, calculated for Au/Fe/MgO(001) structure with 130 nm of Au and different Fe thicknesses. Cyan vertical line in (a) and (c) depicts the light penetration depth of Fe 17 nm.

Because of the absorption of the fundamental and signal waves, the even $E_{2\omega}^{Fe/Au,even}$ and odd $E_{2\omega}^{Fe/Au,odd}$ SH fields from the Fe/Au interface are negligibly small for thick Fe films, but they rise with the reduction of d_{Fe}, increasing the amplitudes of the total even $|\vec{E}_{2\omega}^{even}|$ and odd $|\vec{E}_{2\omega}^{odd,T}|$ SH fields, and changing the optical phase $\phi_{2\omega}^{T}$.

One can also calculate the SH response of the Au/Fe/MgO(001) structure using the 4x4 matrix method [2], but in this case we have to deal with lots of unknown parameters. According to (3.41), in the transversal magneto-optical geometry ($\vec{M}||y$) components χ_{zxx}, χ_{zzz}, χ_{xzx} contribute to $\vec{E}_{2\omega}^{even}$ and $\chi_{xxx}(M_y)$, $\chi_{xzz}(M_y)$, $\chi_{zzx}(M_y)$ contribute to $\vec{E}_{2\omega}^{odd}$ [116]. It could be possible to replace these components of the $\hat{\chi}^{(2)}$ tensor with only two even and odd effective susceptibilities for each interface. However, because of the multiple reflections of the fundamental pulse in the Fe film and complex refractive indices of Fe and Au, the ratio between the z- and x-components of the fundamental electric field $\vec{E}_{\omega}^{Fe/MgO}$ at the Fe/MgO interface changes with the Fe thickness d_{Fe} (see Figure 6.3(d)), therefore the effective susceptibilities of the Fe/MgO interface also depends on d_{Fe}. The ratio between the z- and x-components of the fundamental field $\vec{E}_{\omega}^{Fe/Au}$ at the Fe/Au interface is nearly constant, meaning that the initially transmitted wave is much stronger than the waves reflected from the Fe/Au and Fe/MgO interfaces.

In the following sections of this chapter we concentrate on the analysis of the transient MOKE signals. As for the transient mSHG response of the Fe film, it is better to analyse it considering the experiments performed on the three-layer Fe/Au/Fe/MgO(001) structures with the pump pulse applied either from the same side of the samples as the probe pulse, or from the opposite side. All these experiments are discussed in **Chapter 8**.

6.2 Laser-induced demagnetization of the Fe film

Figure 6.4 presents pump-induced variations of the MOKE signals measured on the Au/Fe/MgO(001) structures with 130 nm of Au and different Fe thicknesses. Non-uniform laser absorption profile (see Figure 6.7(a)) and the presence of Au enhance the efficiency of the HC transport. For thick Fe films $d_{Fe} > 20$ nm the MOKE rotation $\delta\psi'_K(t)$ (see Figure 6.4(a)) undergoes instantaneous break-down, while the MOKE ellipticity $\delta\psi''_K(t)$ (Figure 6.4(c)) decreases on a longer time scale. The reason is that the state-filling effect results in the negative variation of $\delta\psi'_K(t)$ and the positive variation of $\delta\psi''_K(t)$, as well as for the MgO/8nm-Fe/MgO sample discussed in **Chapter 5**. At the same time optically excited HCs propagate into the bulk of the Fe film, leading to demagnetization of the region close to the Fe/MgO interface and, consequently, to the negative variations of $\delta\psi'_K(t)$ and $\delta\psi''_K(t)$. So the contributions of the demagnetization and the state-filling effect to $\delta\psi''_K(t)$ partially compensate each other.

All the curves presented in Figure 6.4 have been measured under the same incident pump fluence. For thick films the influence of the Fe/Au interface on the laser

[2] Linear MOKE can be neglected for the calculations of the distribution of the fundamental electric field $\vec{E}_{\omega}$. Moreover, in the transversal magneto-optical geometry for p-polarized probe pulse both even $E_{2\omega}^{even}$ and odd $E_{2\omega}^{odd}$ SH fields are p-polarized, meaning that it is possible to switch to the 2x2 matrices.

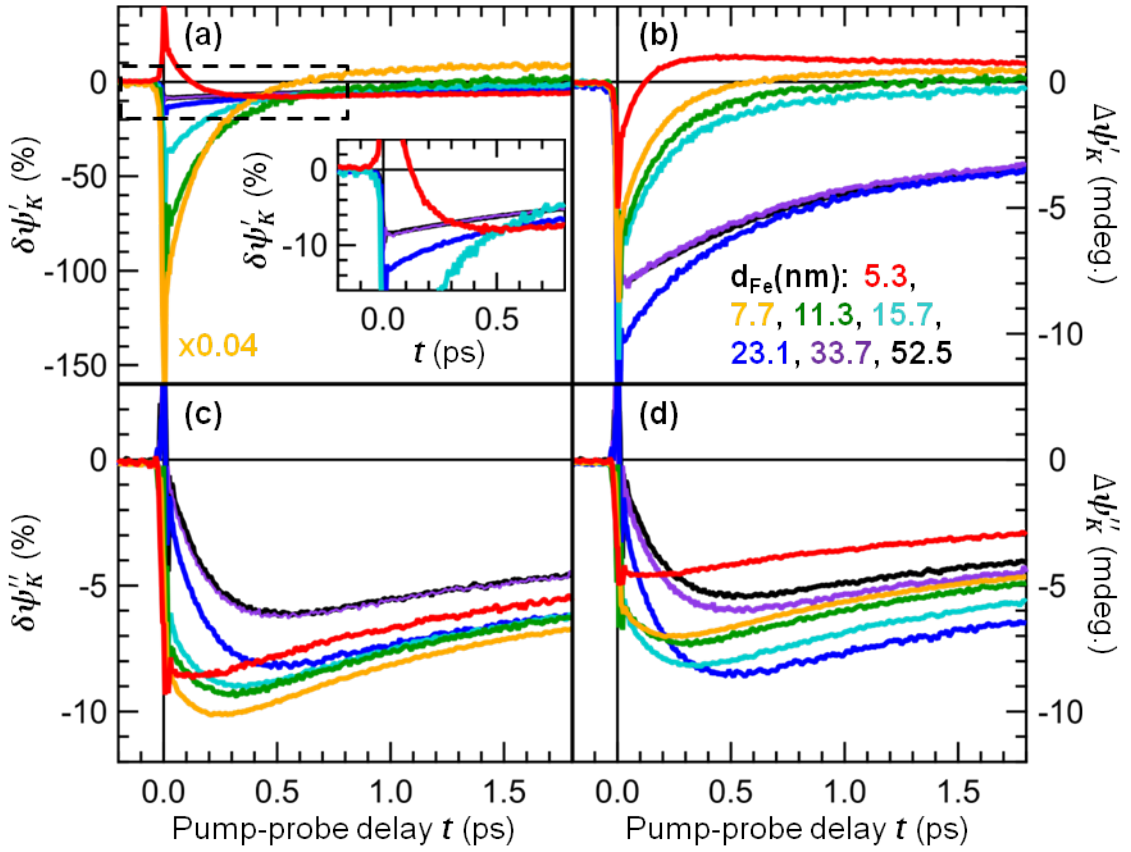

Figure 6.4: Pump-induced variations of the MOKE signals measured on Au/Fe/MgO(001) structures with 130 nm of Au and different thicknesses of the Fe layer at 10 mJ/cm^2 incident pump fluence: (a) relative $\delta\psi'_K(t)$ and (b) absolute $\Delta\psi'_K(t)$ variations of the MOKE rotation, (c) relative $\delta\psi''_K(t)$ and (d) absolute $\Delta\psi''_K$ variations of the MOKE ellipticity. The inset shows the expansion of the region inside the dashed rectangle. For the demonstration of $\delta\psi'_K(t)$ measured for the samples with $d_{Fe} > 20$ nm, some curves for smaller Fe thicknesses were removed from the inset.

absorption profile and the magneto-optical response is negligibly small, therefore the curves $\delta\psi'_K(t)$, $\delta\psi'_K(t)$ obtained for 33.7 and 52.5 nm of Fe are almost identical and reproduce each other. With further reduction of d_{Fe} the HC injection into the Au layer becomes more effective. As a result, for 23.1 nm of Fe we observed larger demagnetization established during first several hundreds femtoseconds, which corresponds to the time scale of the electron thermalization (see **Chapter 5**). The region close to the Fe/Au interface still does not contribute much to the measured signals, and just after the optical excitation $\delta\psi''_K(t)$ for $d_{Fe} = 23.1$ nm starts together with the curves $\delta\psi''_K(t)$ obtained for the samples with thicker Fe films, but then owing to more efficient HC emission into the Au layer, it decreases faster and reflects larger demagnetization values.

For $d_{Fe} < 20$ nm the linear magneto-optical response becomes more sensitive to the Fe/Au interface, and both MOKE rotation $\delta\psi'_K(t)$ and ellipticity $\delta\psi''_K$ break down immediately after the pump pulse. Velocity of the ballistic HCs v_{HC} is about 1 nm/fs and corresponds to a 20-nm travel path within 20 fs (experimental time resolution), therefore the observed variations of the MOKE signals $\delta\psi'_K(t)$ and $\delta\psi''_K(t)$ are consistent with ultrafast demagnetization induced by the ballistic HC transport.

Certainly not all optically excited HCs leave the Fe film in the ballistic regime. Some of them scatter and produce secondary HCs, so the HC transport evolves from the ballistic regime to the diffusive regime. According to the previous experimental and theoretical works performed on Fe and other ferromagnets [29], majority electrons with the positive SP are more mobile than other HCs. It also agrees with our results for thick Fe films, otherwise we would have observed an increase of the magnetization in the region close to the Fe/MgO interface: more mobile HCs propagate faster into the bulk of the Fe film, leaving behind other HCs with opposite SP. When d_{Fe} becomes comparable to the ballistic length of the majority electrons $\lambda_{e\uparrow} \sim 3-5$ nm, a significant amount of the positive SP is already injected into the Au layer during first 100 fs, and later we observe only the recovery of the magnetization (see the red curve in Figure 6.4(c)).

6.3 Model of the ballistic hot carrier transport

Since the static MOKE rotation $\psi'_{K,0}$ changes its sign at about $d_{Fe} = 8nm$ (see Figure 6.3(a)), it is more appropriate to compare the absolute variations of the MOKE rotation $\Delta\psi'_K(t)$ and $\Delta\psi''_K(t)$ (see Figures 6.4(b) and (d)). As a result of different depth sensitivities and the influence of the optical artefacts, $\Delta\psi'_K(t)$ and $\Delta\psi''_K(t)$ behave differently with the reduction of d_{Fe}. It is also should be taken into account that the injection of the spin-polarized HCs gives rise to the MOKE signal from Au, which is demonstrated in **Chapter 7**. In order to disentangle all contributions, one has to calculate spatial HC and magnetization profiles. Complete description of the superdiffusive transport of the spin-polarized HCs, leading to the redistribution of the magnetization in Fe and Au, requires an advanced model similar to those developed in [22, 24, 142–144]. Here we focus on the fastest time scale account only for the ballistic HC transport.

6.3.1 Calculation of the ballistic hot carrier profile

Efficiency of the ballistic HC transport is defined by lifetimes and velocities of different HCs excited in Fe by the pump laser pulse. T.O. Wehling and A. Lichtenstein have performed calculation [106] of the energy and momentum distribution of HCs excited in Fe, based on the density functional theory as implemented in the WIEN2K package [145] using the linearized augmented plane wave method and a generalized gradient approximation [146] to the exchange and correlation potential. It was obtained that HCs are excited to relatively small regions in the k-space (see Figure 6.5): one-third of majority HCs has the wave vectors $\vec{k}$ parallel to the Fe/Au interface, and other

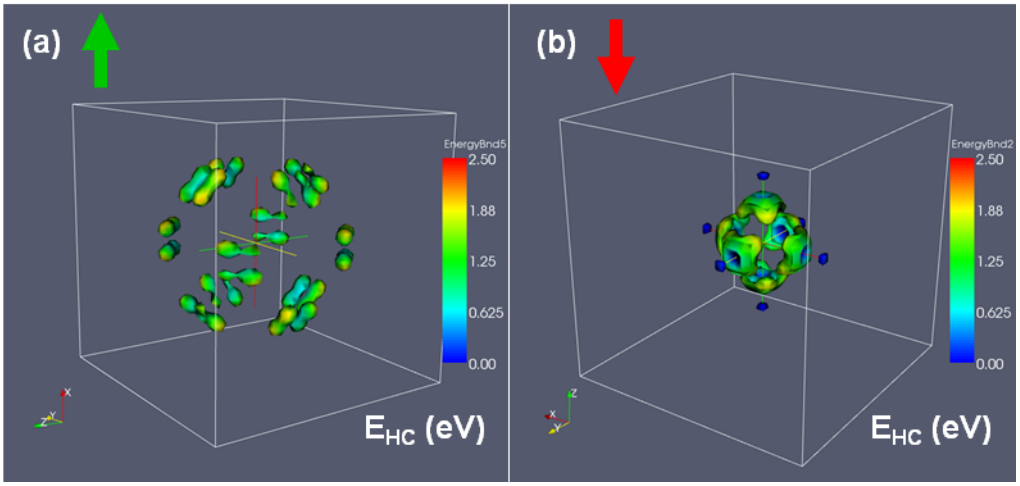

Figure 6.5: Distribution of the optically excited majority (a) and minority (b) electrons ($\hbar\omega = 1.5$ eV) in the first Brillouin zone of Fe, calculated by T.O. Wehling and A. Lichtenstein using joint density of states.

two-thirds have the k-vectors with non-zero projection on the normal to the Fe/Au interface; one-third of minority HCs starts to propagate perpendicular to the Fe/Au interface, and the k-vectors of other two-thirds have zero projection on the normal to the Fe/Au interface.

In the model of the HC transport four types of HCs are considered: majority electrons $e^{\uparrow}$ and minority holes $h^{\downarrow}$ with positive SP, minority electrons $e^{\downarrow}$ and majority holes $h^{\uparrow}$ with negative SP. Figure 6.6(a) shows energy spectra of the optically excited HCs ($\hbar\omega = 1.5$ eV) after momentum averaging [106]. So in addition to well-directed k-vectors, HCs have relatively narrow energy distributions. When HCs pass through the Fe/Au interface, their energies and momentum components parallel to the interface are conserved.

The known band structure of Au allows to calculate the normal-to-interface momentum component of the injected HCs and corresponding ballistic velocity v_{Au}^{HC} (see Table 6.1). The velocities were calculated based on the density functional theory using the band structures of bulk Au obtained within the Vienna Ab Initio simulation package (VASP) with the projector augmented waves basis sets. Using HC velocities v_{Fe}^{HC} in Fe and lifetimes τ_{Fe}^{HC}, τ_{Au}^{HC} in Fe and Au estimated from ref. [19, 78], one can estimate ballistic lengths in Fe and Au for different types of HCs: $\lambda_{Fe} = v_{Fe}\tau_{Fe}$ and $\lambda_{Au} = v_{Au}\tau_{Au}$. Here we have to admit difficulty of a theoretical treatment of 3d ferromagnets, discussed in **Chapter 2**. Lifetimes of the minority carriers in Fe, reported recently by Kalteborn et al. [79], differ much from those presented in [19, 78], but the predictions for the lifetime of the majority electrons are very close. It is known that the majority electrons in Fe are excited mostly to the sp-band, while other HCs are in the d-band. It means that the majority electrons are more mobile and have larger ballistic lengths than other

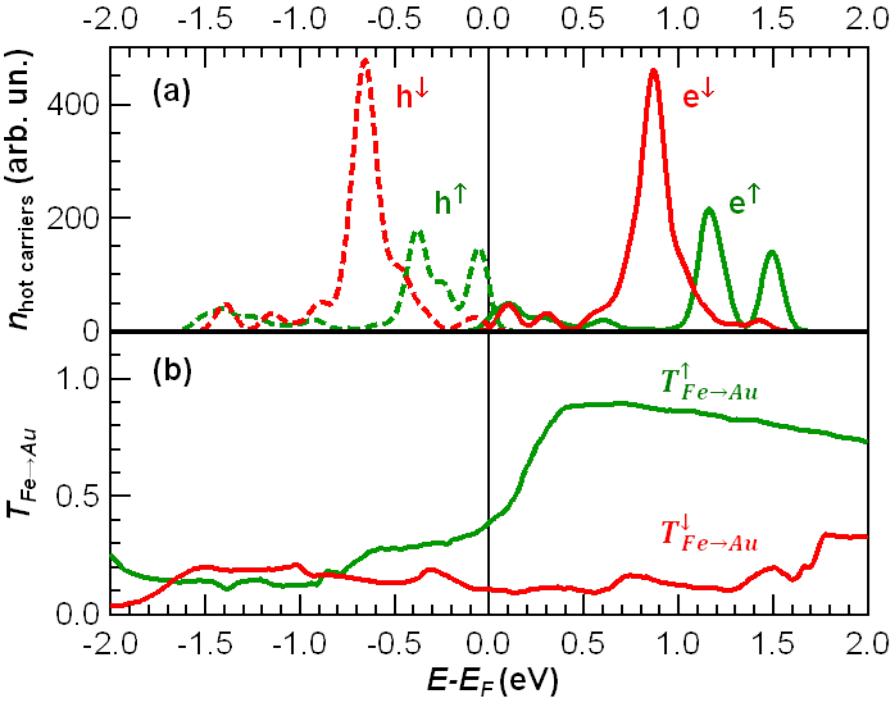

Figure 6.6: (a) Hot carrier excitation spectra reproduced from [106]: majority electrons $e^{\uparrow}$ (solid green line), majority holes $h^{\uparrow}$ (dash green line), minority electrons $e^{\downarrow}$ (solid red line), minority holes $h^{\downarrow}$ (dash red line). (b) Transmission of the Fe/Au interface for majority (green line) and minority (red line) carriers, calculated by I. Rungger, M. Stamenova, and S. Sanvito.

HCs. Thus considering the time scale of the ballistic transport, we assume that only the majority electrons contribute to the HC transport, while other HCs stay where they are excited.

Another parameter required for the description of the ballistic HC transport is the transmission of the Fe/Au interface. First principles quantum transport calculations for the Fe(100)/Au(100) interface were performed by I. Rungger, M. Stamenova, and S. Sanvito using the non-equilibrium Green's function technique implemented in the Smeagol code [147, 148] at the level of the local density approximation. The system consists of two semi-infinite and periodic in the transverse direction leads: a bcc Fe lead with a lattice constant $a_{Fe} = 2.87$ Å and a commensurate fcc Au lead with $a_{Au} = \sqrt{2}a_{Fe} = 4.08$ Å. The scattering region treated self-consistenly consists of 12 atomic layers of Fe and 12 atomic layers of Au forming a (100) interface. The full spin-dependent transmission matrix between all incoming states from Fe and outgoing states in Au has been calculated [149]. Figure 6.6(b) shows the averaged over

HC	v_{Fe}(nm/fs)	τ_{Fe}(fs)	λ_{Fe}(nm)	v_{Au}(nm/fs)	τ_{Au}(fs)	λ_{Au}(nm)	$T_{Fe\to Au}$
$e^{\uparrow}$	0.43	8	3.4	0.95	15	14	0.83
$h^{\uparrow}$	0.08	< 8	< 0.64	0.77	200	154	0.32
$e^{\downarrow}$	0.30	2	0.6	1.17	40	47	0.15
$h^{\downarrow}$	0.21	~ 2	~ 0.4	0.94	80	75	0.15

Table 6.1: Velocities, lifetimes, ballistic lengths and transmission of the Fe/Au interface for different types of HCs. Values for v_{Au}^{HC} were taken from [106], and v_{Fe}^{HC}, τ_{Au}^{HC}, τ_{Fe}^{HC} were estimated from [19, 78].

all incoming channels transmission probability of the majority and minority carriers. The transmission values $T_{Fe\to Au}$ of the Fe/Au interface averaged over the energy range of particularly excited HCs are given in Table 6.1. The most striking result of these calculations is that the values of the Fe/Au interface transmission for hot electrons and holes in the minority sub-band do not differ significantly from the transmission value at the Fermi level, while in the majority sub-band transmission of the hot holes is slightly smaller than the value at the Fermi level, and that of the hot electrons is about two times larger.

When all parameters are known, one can calculate changes of the HC profile due to the HC transport. Initially at the time zero spatial densities of the optically excited HCs are proportional to the absorbed energy of the pump laser pulse:

$$\begin{aligned} P_{e^{\uparrow}}^{tot}(z, t=0) &= P_{h^{\uparrow}}^{tot}(z, t=0) = \alpha\eta_{\uparrow} P_{pump}(z), \\ P_{e^{\downarrow}}^{tot}(z, t=0) &= P_{h^{\downarrow}}^{tot}(z, t=0) = \alpha\eta_{\downarrow} P_{pump}(z), \end{aligned} \tag{6.5}$$

where $P_{pump}(z)$ is the laser absorption profile, α is a factor between the absorbed energy and the total HC density, $\eta_{\uparrow} \approx 0.373$, $\eta_{\downarrow} \approx 0.637$ are portions of the majority and minority carriers in the total number of the excited HCs, calculated from the energy spectra of majority and minority electrons (see Figure 6.6(a)). Figure 6.7(a) shows laser absorption profile in the Fe/Au structure calculated for 15 nm of Fe and 130 nm of Au. Since light absorption at 1.5 eV is much more efficient in Fe than in Au, HCs generated in the Au layer by the pump laser pulse can be neglected in this consideration. Spin redistribution in the Fe/Au structure is determined as a difference between transient spatial densities of HCs carrying opposite spins:

$$\Delta M(z,t) = P_{e^{\uparrow}}^{tot}(z,t) - P_{h^{\uparrow}}^{tot}(z,t) - P_{e^{\downarrow}}^{tot}(z,t) + P_{h^{\downarrow}}^{tot}(z,t). \tag{6.6}$$

Since we neglect transport of the majority $h^{\uparrow}$, minority $h^{\downarrow}$ holes, and minority electrons $e^{\downarrow}$, their spatial distributions $P_{h^{\uparrow}}(z,t)$, $P_{h^{\downarrow}}(z,t)$ and $P_{e^{\downarrow}}(z,t)$ do not change with time. As for the majority electrons $e^{\uparrow}$, it should be taken into account that HCs with ballistic velocities parallel to the Fe/Au interface do not contribute to the spin redistribution. So the two-thirds of the optically excited majority electrons $e^{\uparrow}$ propagate across the sample, leaving behind the two-thirds of the corresponding majority holes $h^{\uparrow}$ with negative SP, therefore

$$\Delta M(z,t) = P_{e^{\uparrow}}^{\perp}(z,t) - \frac{2}{3}\alpha\eta_{\uparrow} P_{pump}(z), \tag{6.7}$$

where

$$P^{\perp}_{e^{\uparrow}}(z,t) = f\left(\frac{2}{3}\alpha\eta_{\uparrow}P_{pump}(z), t, v^{e^{\uparrow}}_{Fe}, \tau^{e^{\uparrow}}_{Fe}, v^{e^{\uparrow}}_{Au}, \tau^{e^{\uparrow}}_{Au}, T^{e^{\uparrow}}_{Fe\to Au}, T^{e^{\uparrow}}_{Au\to Fe}\right) \tag{6.8}$$

is a spatial distribution profile of the majority electrons with a non-zero velocity component perpendicular to the Fe/Au interface at time t, and f is a function, which determines $P^{\perp}_{e^{\uparrow}}(z,t)$, using the initial HC distribution profile $\frac{2}{3}\alpha\eta_{\uparrow}P_{pump}(z)$, ballistic velocities $v^{e^{\uparrow}}_{Fe}$, $v^{e^{\uparrow}}_{Au}$ and lifetimes $\tau^{e^{\uparrow}}_{Fe}$, $\tau^{e^{\uparrow}}_{Au}$ in Fe and Au.

Figure 6.7(b) describes numerical calculation of the spatial HC distribution $P^{\perp}_{e^{\uparrow}}(z, t+\Delta t)$ at time $t+\Delta t$ using the spatial HC distribution $P^{\perp}_{e^{\uparrow}}(z,t)$ at time t. Fe and Au layers are divided into the sublayers in such way that it takes the majority electrons a single time step Δt to pass from one sublayer to the next one. Since HCs have different velocities in Fe and Au, sublayers have different thicknesses $v_{Fe}\Delta t$ and $v_{Au}\Delta t$. Spatial HC density at the pump-probe zero delay $t = 0$ have to be recalculated into the numbers $n^{b}_{BC}(z_i, t=0)$ and $n^{f}_{BC}(z_i, t=0)$ of the ballistic HCs moving backward and forward in each sublayer:

$$n^{b}_{BC}(z_i, t=0) = n^{f}_{BC}(z_i, t=0) = \frac{1}{2}\cdot P^{\perp}_{HC}(z_i, t=0)\cdot S\cdot v_{Fe}\Delta t \text{ for } 1 \leqslant i \leqslant N_{Fe}, \tag{6.9}$$

where S is a square of the film, i is the sublayer index, and z_i is its position. Then following the procedure of the numerical calculation, total number of scattered $n_{SC}(z_i,t)$ and ballistic $n^{b}_{BC}(z_i,t) + n^{f}_{BC}(z_i,t)$ HCs in each sublayer at time t can be evaluated and recalculated back to the spatial HC density:

$$\begin{aligned} P^{\perp}_{HC}(z_i,t) &= \frac{n_{SC}(z_i,t) + n^{b}_{BC}(z_i,t) + n^{f}_{BC}(z_i,t)}{S\cdot v_{Fe}\Delta t} \text{ for } 1 \leqslant i \leqslant N_{Fe}, \\ P^{\perp}_{HC}(z_i,t) &= \frac{n_{SC}(z_i,t) + n^{b}_{BC}(z_i,t) + n^{f}_{BC}(z_i,t)}{S\cdot v_{Au}\Delta t} \text{ for } N_{Fe}+1 \leqslant i \leqslant N_{Fe}+N_{Au}. \end{aligned} \tag{6.10}$$

It is assumed that the Fe/MgO interface and the Au surface reflect all incident HCs. As for the Fe/Au interface, these relations have been used:

$$\begin{aligned} n^{b}_{BC}(z_{N_{Fe}}, t+\Delta t) = (1 - T_{Fe\to Au})\cdot n^{f}_{BC}(z_{N_{Fe}}, t)\cdot e^{-\Delta t/\tau_{Fe}} \\ + T_{Au\to Fe}\cdot n^{b}_{BC}(z_{N_{Fe}+1}, t)\cdot e^{-\Delta t/\tau_{Au}}, \end{aligned} \tag{6.11}$$

$$n^{f}_{BC}(z_{N_{Fe}}, t+\Delta t) = n^{f}_{BC}(z_{N_{Fe}-1}, t)\cdot e^{-\Delta t/\tau_{Fe}}, \tag{6.12}$$

$$\begin{aligned} n_{SC}(z_{N_{Fe}}, t+\Delta t) = n_{SC}(z_{N_{Fe}}, t) + (1 - e^{-\Delta t/\tau_{Fe}})\cdot n^{f}_{BC}(z_{N_{Fe}-1}, t) \\ + (1 - e^{-\Delta t/\tau_{Au}})\cdot T_{Au\to Fe}\cdot n^{b}_{BC}(z_{N_{Fe}+1}, t), \end{aligned} \tag{6.13}$$

$$n^{b}_{BC}(z_{N_{Fe}+1}, t+\Delta t) = n^{b}_{BC}(z_{N_{Fe}+2}, t)\cdot e^{-\Delta t/\tau_{Au}}, \tag{6.14}$$

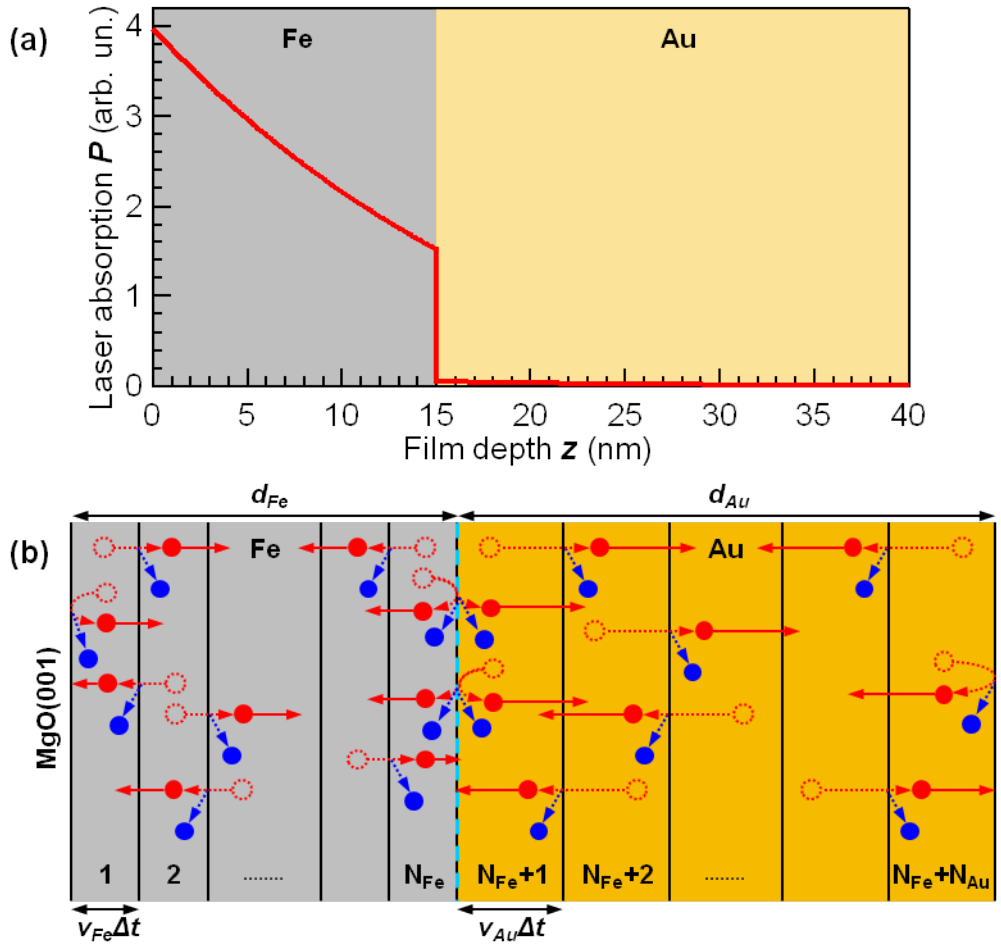

Figure 6.7: (a) Laser absorption profile calculated for Au/Fe/MgO(001) structure with 15 nm of Fe and 130 nm of Au. Spatial density of the excited hot carriers is proportional to the absorbed energy of the pump laser pulse: $P_{HC}^{tot}(z, t = 0) = \alpha P_{pump}(z)$. (b) Model for numerical calculations of the ballistic HC transport. For specified type of HCs Fe and Au layers can be divided into N_{Fe} sublayers with thicknesses $v_{Fe}\Delta t$ and N_{Au} sublayers with thicknesses $v_{Au}\Delta t$, respectively. v_{Fe}, v_{Au} are ballistic velocities in Fe and Au (see table 6.1), and Δt is a time step small enough to calculate HC spatial distribution with certain accuracy and neglect the differences $|N_{Fe}v_{Fe}\Delta t - d_{Fe}|$ and $|N_{Au}v_{Au}\Delta t - d_{Au}|$. Dashed red circles depict HCs propagating in ballistic regime at time t, and full blue and red circles depict scattered HCs and ballistic HCs at time $t + \Delta t$, respectively. At time $t + \Delta t$ one part ($e^{-\Delta t/\tau_{Fe}}$ in Fe and $e^{-\Delta t/\tau_{Au}}$) in Au) of HCs transmitted into the next sublayer gets scattered and becomes 'frozen', the other part ($(1-e^{-\Delta t/\tau_{Fe}})$ in Fe and $(1-e^{-\Delta t/\tau_{Au}})$ in Au) proceeds to the next sublayers. The same happens with HCs reflected from the Fe/MgO interface in the sublayer '1', HCs reflected from the Fe/Au interface in the sublayers 'N_{Fe}' and '$N_{Fe}+1$', HCs reflected from the Au surface in the sublayer '$N_{Fe}+N_{Au}$', but unlike other HCs, they only change velocity direction and remain in the current sublayer.

$$n^f_{BC}(z_{N_{Fe}+1}, t+\Delta t) = T_{Fe\to Au}\cdot n^f_{BC}(z_{N_{Fe}}, t)\cdot e^{-\Delta t/\tau_{Fe}} + (1-T_{Au\to Fe})\cdot n^b_{BC}(z_{N_{Fe}+1}, t)\cdot e^{-\Delta t/\tau_{Au}}, \tag{6.15}$$

$$n_{SC}(z_{N_{Fe}+1}, t+\Delta t) = n_{SC}(z_{N_{Fe}+1}, t) + (1-e^{-\Delta t/\tau_{Fe}})\cdot T_{Fe\to Au}\cdot n^f_{BC}(z_{N_{Fe}}, t) + (1-e^{-\Delta t/\tau_{Au}})\cdot n^b_{BC}(z_{N_{Fe}+2}, t). \tag{6.16}$$

Thus we have demonstrated the procedure for the calculation of the HC redistribution due to the ballistic HC transport.

6.3.2 Analysis of the experimental data

Now we will use the model of the ballistic transport to reproduce the absolute variations of the MOKE rotation $\Delta\psi'_K(t)$ and ellipticity $\Delta\psi''_K(t)$ at 40 fs pump-probe delay. At this time the pump pulse is over, and the diffusive HC transport does not contribute considerably yet. According to **Chapter 5**, the characteristic of the phonon-mediated spin-flip processes $\tau_M = 210 \pm 10$ fs, therefore their influence on the magnetization dynamics can be also neglected.

In **Chapter 7** we discuss the experiments where the Au/Fe/MgO(001) was pumped from the Fe side and probed from the Au side. It is demonstrated that the injection of the spin-polarized HCs into the Au layer give rise to a measurable MOKE signal from Au. The MOKE rotation and ellipticity data allowed us to estimate the ratio between the real and imaginary parts of the Voigt constant of Au $q'_{Au}/q''_{Au} = 2.7 \pm 0.1$ (for more details see **Chapter 7**). In the experiments discussed here, both pump and probe pulses were applied from the Fe side of the Au/Fe/MgO(001) structures, meaning that the contributions of the SP injected into the Au layer to $\Delta\psi'_K(t)$ and $\Delta\psi''_K(t)$ should be even larger. They grow with the reduction d_{Fe}, because it increases the MOKE sensitivity to the bulk of the Au layer and HCs have to propagate smaller distance to leave the Fe film. However, because of the large reflectivity of Au at 1.5 eV, the portion of the absorbed energy decreases for small Fe thickness (see Figure 6.3(a)), which affects the amplitudes of the demagnetization and the Au contributions to the MOKE signals. In order to reduce the number of the fitting parameters, we set the ratio q'_{Au}/q''_{Au} and used only the absolute value $|q_{Au}| = \sqrt{q'^2_{Au} + q''^2_{Au}}$ as an adjustable parameter.

According to the data presented in **Chapter 5**, the variations of the real and imaginary parts of the Voigt constant of iron q_{Fe} are proportional to the density of the optically excited HCs, i.e. the total energy of the non-equilibrium HCs:

$$\Delta q'_{Fe}(z,t) = b'_{neq}\frac{E_{e\uparrow}P_{e\uparrow}(z,t) + E_{h\uparrow}P_{h\uparrow}(z,t) + E_{e\downarrow}P_{e\downarrow}(z,t) + E_{h\downarrow}P_{h\downarrow}(z,t)}{1.5}, \tag{6.17}$$

$$\Delta q''_{Fe}(z,t) = b''_{neq}\frac{E_{e\uparrow}P_{e\uparrow}(z,t) + E_{h\uparrow}P_{h\uparrow}(z,t) + E_{e\downarrow}P_{e\downarrow}(z,t) + E_{h\downarrow}P_{h\downarrow}(z,t)}{1.5}, \tag{6.18}$$

where $E_{e\uparrow} = 1.3$ eV, $E_{h\uparrow} = 0.2$ eV, $E_{e\downarrow} = 0.87$ eV, $E_{h\downarrow} = 0.63$ eV are the energies of the optically excited HCs (see Figure 6.6). In contrast to the experiments on a 8-nm Fe film discussed in **Chapter 5**, the spatial HC distributions are neither uniform nor identical. In order to reduce further the number of the adjustable parameters, we set

Laser absorption Magnetization profile	${}^{*}\alpha = 1.00 \pm 0.02$
State-filling effect	${}^{*}b'_{neq} = -(1.52 \pm 0.02) \cdot 10^{-4}$ ${}^{*}b''_{neq} = -(1.40 \pm 0.02) \cdot 10^{-4}$
The Voigt constant of Au	${}^{**}q'_{Au}/q''_{Au} = 2.7 \pm 0.1$ $\lvert q_{Au} \rvert = \sqrt{q'^2_{Au} + q''^2_{Au}} = 0.10 \pm 0.02$

Table 6.2: Adjustable parameters used in the model of the ballistic transport to reproduce the experimental data. Presented values were obtained after the joint fitting procedure of the data shown in Figure 6.9. *Marked parameters were rescaled for the laser absorption profiles $P_{abs.}(z)$ in Figure 6.8(a). ** q'_{Au}/q''_{Au} has been estimated from the data presented in **Chapter 7**.

the ratio b'_{neq}/b''_{neq} to the value obtained in **Chapter 5** and used the common factor b_0:

$$b'_{neq} = b_0\tilde{b}'_{neq},\ b''_{neq} = b_0\tilde{b}''_{neq}, \tag{6.19}$$

where $\tilde{b}'_{neq}$, $\tilde{b}''_{neq}$ corresponds to the relative variations of the MOKE rotation $\delta\psi'_K(t = 0) = -7.58$ % and ellipticity $\delta\psi'_K(t = 0) = -7.58$ % observed on a 8-nm Fe film at the time zero (parameters b'_0 and b''_0 in Table 5.1). Even if the ratio b'_{neq}/b''_{neq} is not hold, the fitting procedure gives a value close to the value obtain in **Chapter 5**.

Initially the HC and magnetization profiles were calculated in the arbitrary units, using velocities $v^{e\uparrow}_{Fe}$, v_{Au} and lifetime τ_{Au} of the majority electrons shown in Table 6.1. For the lifetime of the majority electrons in Fe we used $\tau_{Fe} = 12$ fs from [79], but also close to the predictions in [19]. α in (6.7) was used as an adjustable parameter to calibrate the absorption profiles $P_{abs}(z)$ in the number of the optically excited electrons per atom (see Figure 6.8(a)), and the magnetization profiles $\Delta M(z,t)$ in the Au/Fe/MgO(001) structures in the units of the saturation magnetization of Fe M_{Fe} (see Figure 6.8(b)).

The results of the joint fitting procedure for the absolute variations of the MOKE rotation $\Delta\psi'_K(t = 40\text{ fs}, d_{Fe})$ and ellipticity $\Delta\psi''_K(t = 40\text{ fs}, d_{Fe})$ are presented in Figure 6.9 and corresponding parameters are shown in Table 6.2. In spite of that the model of the ballistic transport reproduces the experimental dependences and gives reasonable demagnetization value, it obviously **overestimates** the number of the optically excited electrons per atom. The reason is that the model of the ballistic transport does not consider secondary electrons which can contribute significantly to the HC transport at 40 fs after the pump pulse. Consequently, it may also underestimate the amount of the SP injected into the Au layer and the corresponding contributions to $\Delta\psi'_K$ and $\Delta\psi''_K$. As a result, the differences between the red solid and dash lines in Figures 6.9(b) and (d) are not so big, and the model of the ballistic transport provides very rough estimation for the Voigt constant q_{Au}, because the MOKE originates mostly in Fe. Nevertheless, consideration of the ballistic regime of the HC transport revealed its contribution to the magnetization dynamics. Although the state-filling

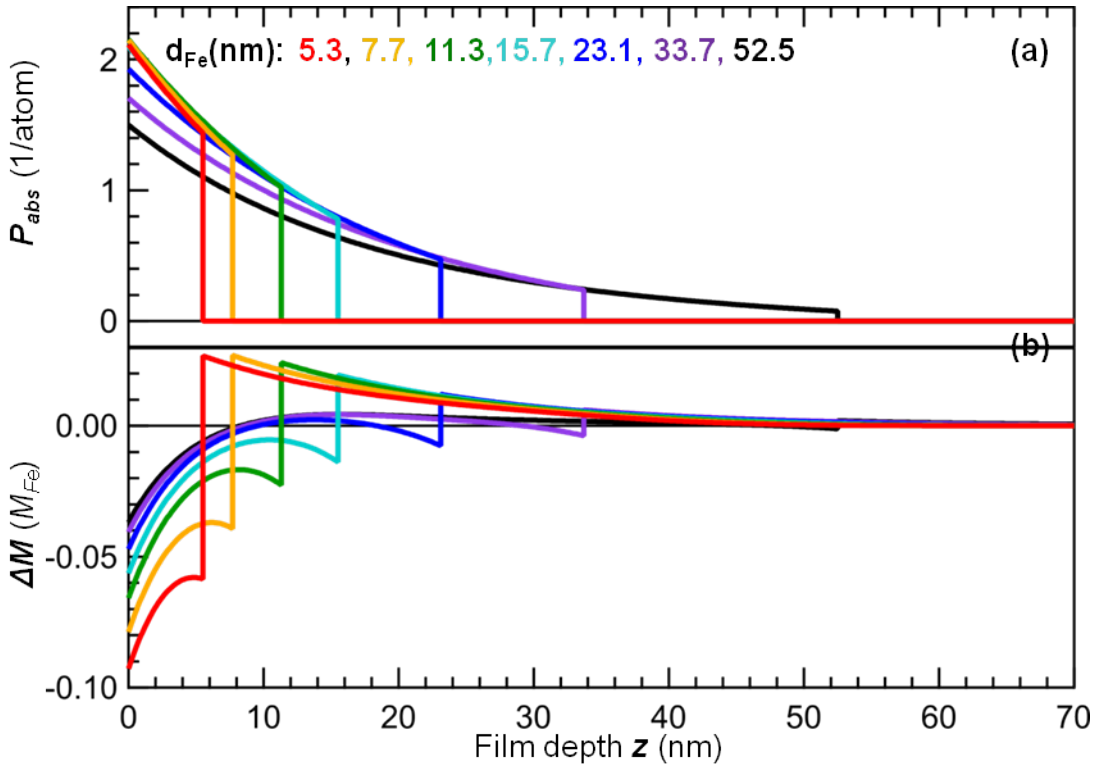

Figure 6.8: (a) Laser absorption $P_{abs.}(z)$ profiles. (b) Magnetization $\Delta M(z)$ spatial profiles established in 40 fs after the optical excitation of the Fe film. $P_{abs.}(z)$ and $\Delta M(z)$ were calibrated using the fitting procedure for the absolute variations of the MOKE rotation $\Delta\psi'_K$ and ellipticty $\Delta\psi''_K$ at 40-fs pump-probe delay (see Figure 6.9). The film depth z is the distance from the Fe/MgO interface, and the abrupt changes in $P_{abs.}(z)$ and $\Delta M(z)$ correspond to the position of the Fe/Au interface.

effect induces large variations of the MOKE rotation and ellipticity and can reproduce $\Delta\psi'_K(t = 40 \text{ fs}, d_F e)$ (green line in Figure 6.9(b)) alone, the absence of the HC transport does not allow us to describe $\Delta\psi'_K(t = 40 \text{ fs}, d_F e)$. The curves in Figure 6.9 are the simulations performed with the parameters obtained in the complete fitting procedure (see Table 6.2). If we exclude the HC transport, the only adjustable parameter is b_0, therefore in this case the fitting procedure is limited to simple stretching of the green curves along the vertical axis. Different influence of the ultrafast demagnetization and the optical bleaching on $\Delta\psi'_K$ and $\Delta\psi''_K$ is related to their depth sensitivities. The region of the Fe film close to the Fe/MgO interface contributes more to the MOKE ellipticity ψ''_K than to the MOKE rotation ψ'_K, as it was shown for $d_{Fe} = 15$ nm in Figure 6.3(b). For this reason, the HC transport affects more $\Delta\psi''_K$ than $\Delta\psi'_K$.

Summarizing, our model demonstrates that the HC transport plays an important role in ultrafast laser-induced demagnetization of the Fe film. In spite of all simplifications and assumptions, our model provides a realistic estimation for the amount of the

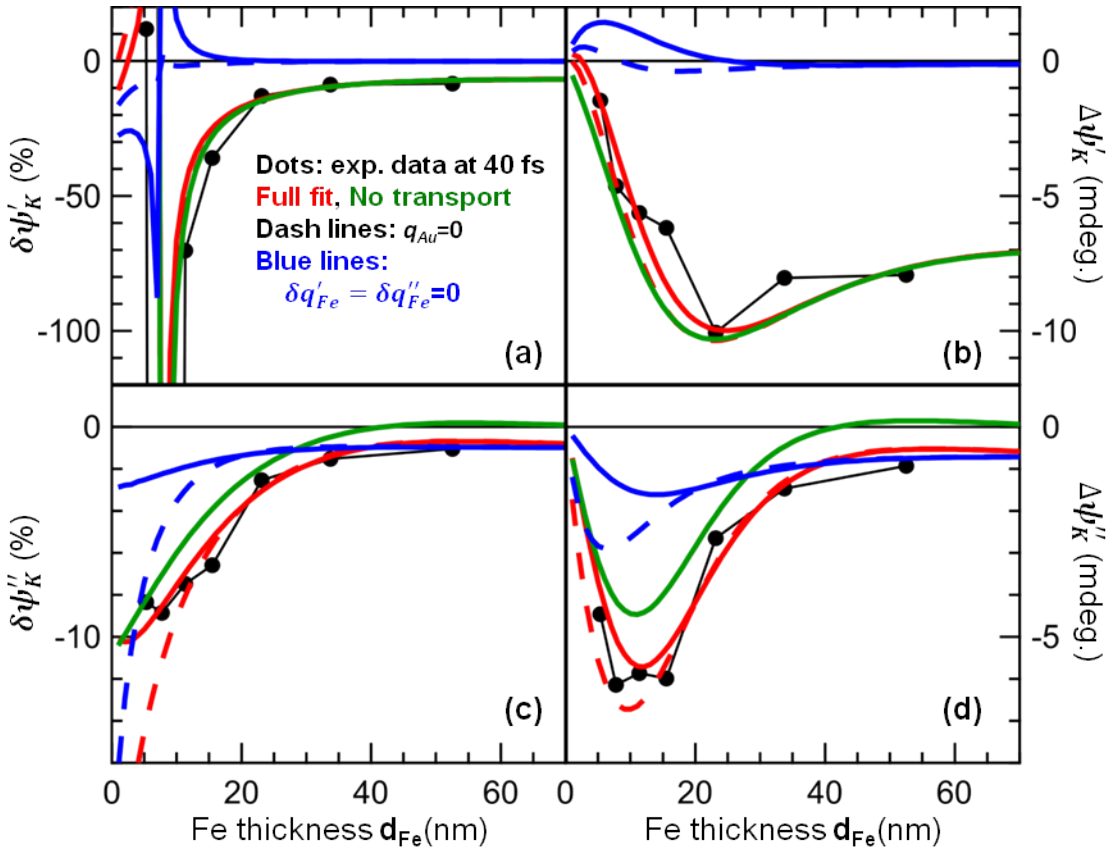

Figure 6.9: Absolute (a-$\delta\psi'_K$, c-$\delta\psi''_K$) and relative (b-$\Delta\psi'_K$, d-$\Delta\psi''_K$) variations of the MOKE rotation ψ'_K and ellipticity ψ''_K, induced in the 130nm-Au/x-Fe/MgO(001) structures at 40-fs pump-probe delay with 20 mJ/cm^2 incident pump fluence.

positive SP injected into the Au layer during first several tens of femtoseconds after the pump pulse. Description of the measured MOKE signals for later pump-probe delays requires more sophisticated model similar to that presented in [22–24].

6.4 Conclusions

Laser-induced injection of the spin-polarized HCs from the Fe film into the Au layer has been studied using the time-resolve MOKE and mSHG techniques. Comparison of the transient variations of the MOKE rotation and ellipticity with those presented in **Chapter 5** revealed the HC transport contributes considerably to ultrafast demagnetization of the Fe film and confirmed the results reported in [22–24].

According to the data obtained in the ab initio calculations, the emission of the majority electrons with the positive SP from the Fe film into Au is much more efficient than the emission of other HCs. Unlike the phonon-mediated spin-flip processes with the characteristic time $\tau_M \sim 200$ fs, ultrafast injection of the positive SP into the Au

layer via the HC transport results in a fast drop of the magnetization within first 20 fs after the optical excitation of the Fe film. Modelling the HC and magnetization spatial profiles established on the time scale of the ballistic HC transport, it is possible to disentangle all contributions to the MOKE signals. Because of the different depth sensitivities, the HC transport affects more the MOKE ellipticity $\Delta\psi''_K(t)$ than the MOKE rotation $\Delta\psi'_K(t)$. The latter is mostly determined by the state-filling effect during first 100 fs.

The Voigt constant of gold $q_{Au} = 0.094 + 0.035i$, obtained in the analysis of the MOKE data, is consistent with the experimental results, concerning the HC transport in Au (see **Chapter 7**), as well as the estimation for the SP injected into the Au layer on the time scale of the ballistic HC transport.

Chapter 7

Transport of spin-polarized hot carriers in Au

In **Chapter 6** the initial stage of the hot carrier (HC) transport was discussed, i.e. the injection of spin-polarized HCs from a ferromagnetic film into a non-magnetic metal. The analysis of the transient MOKE rotation $\Delta\psi'_K(t)$ and ellipticity $\Delta\psi''_K(t)$ revealed that the HC transport plays a considerable role in ultrafast demagnetization of the Fe film. Comparison of the ballistic lengths λ_{Fe}^{HC} and the transmission through the Fe/Au interface $T_{Fe\rightarrow Au}$, obtained for different HCs from the ab-initio calculations, clearly indicates that the spin current (SC) pulse injected from the Fe film into the Au layer is dominated by the majority electrons carrying positive spin polarization (SP), which is consistent with our experimental results. Owing to a large inelastic mean free path in Au, the injected spin-polarized HCs propagate further into the bulk of the non-magnetic layer without losing their initial SP. For the reasons mentioned above, it can be assumed that the SC pulse in Au is formed only by the majority electrons with the positive SP. In order to study temporal evolution of the HC packet and the SC pulse, pump-probe experiments have been performed on epitaxial bilayer Au/Fe/MgO(001) structures with different thicknesses of the Fe and Au films. In contrast to the experiments presented in **Chapter 6**, the probe pulse $\hbar\omega_{probe} = 1.5$ eV has been applied from the Au side (see Figure 7.1(a)).

Performing pump-probe experiments in the transversal and longitudinal magneto-optical geometries, it has been found that the total odd SH field $\vec{E}_{2\omega}^{odd}$ is the sum of the SP-induced SH field $\vec{E}_{2\omega}^{SP}$, originating at the Au surface, and the SC-induced SH field $\vec{E}_{2\omega}^{SC}$, originating in the bulk of Au. Analyzing the mSHG and MOKE signals, it is demonstrated that the injected majority electrons propagate in Au in a quasi-ballistic regime. The steep front of the SC pulse consists of the optically excited electrons which leave the Fe film in the ballistic regime, while the shallow trailing part of the SC pulse is formed by the secondary electrons.

7.1 Transient magneto-optical response of Au

Since there is no initial SP in paramagnets, in the absence of the pump pulse the Au layer does not contribute to the MOKE rotation and ellipticity:

$$\psi'_{Au,K}(t<0)=0,\ \psi''_{Au,K}(t<0)=0. \tag{7.1}$$

Also in the static regime there is neither HC current nor SC, and the measured SH intensity is the result of the interference of the SH fields $\vec{E}_{2\omega}^{Fe/MgO}$, $\vec{E}_{2\omega}^{Fe/Au}$ and $\vec{E}_{2\omega}^{Au\ surf.}$ originating at the Fe/MgO, Fe/Au interfaces and the Au surface, respectively. Here we neglect the bulk quadrupole contribution. For Au it was shown to be small with respect to the surface dipole one [150]. When the Au thickness d_{Au} is large enough ($>$ 40 nm, see Figure 7.3(b)) the Au surface can be considered as the only source of the SH field. In the first approximation, the surface dipole polarization $\vec{P}_{2\omega}^{Au\ surf.}$ can be expressed as a sum of the even term independent of the magnetization $\vec{M}$ and the odd term linearly proportional to it:

$$P_{2\omega,i}^{Au\ surf.}=\chi_{ijk}^{(2)}E_{\omega,j}E_{\omega,k}+\chi_{ijk,l}^{(3,SP)}E_{\omega,j}E_{\omega,k}M_l, \tag{7.2}$$

where $i,\ j,\ k=x,\ y,\ z$, and $\chi_{ijk,l}^{(3,SP)}$ is a pseudo-tensor with respect to the last index. This expression is also valid for the SH dipole polarizations $\vec{P}_{2\omega}^{Fe/MgO}$ and $\vec{P}_{2\omega}^{Fe/Au}$ at the Fe/MgO and Fe/Au interfaces. At the negative pump-probe delays $t<0$, there is no odd SH field originating at the Au surface. For this reason, spin dynamics in the bulk of the Au layer and at the Au surface has been monitored by the absolute variations of the MOKE rotation $\psi'_K(t)$, ellipticity $\psi''_K(t)$ and the SH contrast $\rho_{2\omega}(t)$:

$$\Delta\psi'_K(t)=\psi'_K(t)-\psi'_{K,0},\ \Delta\psi''_K(t)=\psi''_K(t)-\psi''_{K,0}, \tag{7.3}$$

$$\rho_{2\omega}(t)=\frac{I_{2\omega}^{\uparrow}(t)-I_{2\omega}^{\downarrow}(t)}{I_{2\omega}^{\uparrow}(t)+I_{2\omega}^{\downarrow}(t)}, \tag{7.4}$$

where $I_{2\omega}^{\uparrow}(t)$, $I_{2\omega}^{\downarrow}(t)$ are the SH intensities measured for the opposite directions the saturating magnetic field.

After the optical excitation of the Fe film, the HC current[1], flowing in Au, breaks the spatial inversion symmetry and hence gives rise to the bulk SH contribution:

$$P_{2\omega,i}^{HC\ cur.}=\chi_{ijkz}^{(3)}E_{\omega,j}E_{\omega,k}j_z, \tag{7.5}$$

where the tensor $\chi_{ijkz}^{(3)}j_z$ has exactly the same symmetry and non-zero components as the tensor $\chi_{ijk}^{(2)}$ corresponding to the surface non-magnetic SH field. The surface magnetic SH term $\chi_{ijk,l}^{(3,SP)}M_l$ has its bulk SC-induced 'twin' as well:

$$P_{2\omega,i}^{SC}=\chi_{ijkz,l}^{(4,SC)}E_{\omega,j}E_{\omega,k}j_{z,l}^{S}. \tag{7.6}$$

[1]Charge current is expected to be partially compensated by the displacement of the 'cold' electrons [151].

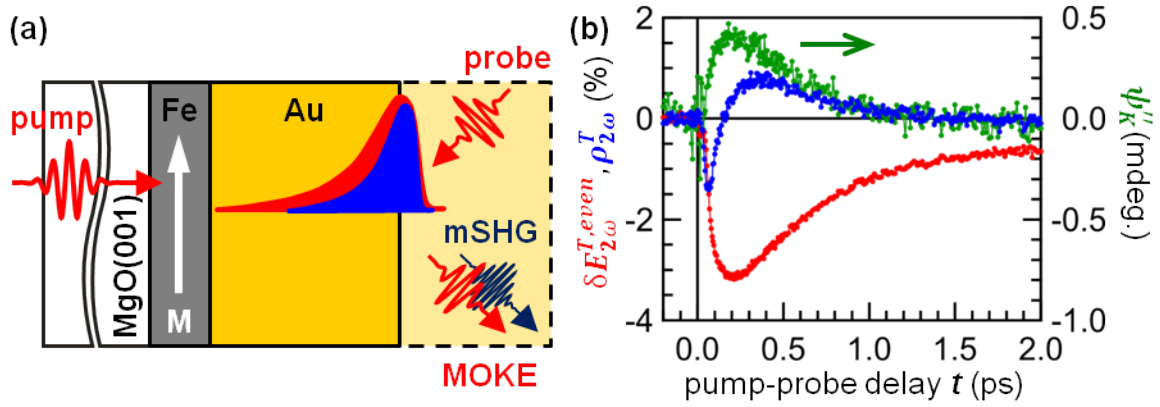

Figure 7.1: (a) Experimental scheme to study transport of the spin-polarized HCs in Au. Considering elastic HC scattering from the Au surface, measurements performed on the Au/Fe/MgO(001) structures with different Au thicknesses make it possible to track the evolution of the HC and spin current pulses propagating in a infinitely thick Au layer. (b) Transient pump-induced variations of the even SH field $\delta E_{2\omega}^{T,even}$ (red), SH contrast $\rho_{2\omega}^{T}$ (blue) and MOKE ellipticity ψ_K'' (green) obtained for the Au/Fe/MgO(001) structure with 8 nm of Fe and 75 nm of Au. $\delta E_{2\omega}^{T,even}$ and $\rho_{2\omega}^{T}$ were measured in the transversal magneto-optical geometry $\vec{M}||\hat{y}$, while ψ_K'' was measured in the longitudinal magneto-optical geometry $\vec{M}||\hat{x}$.

Here $\chi_{ijkz,l}^{(4,SC)}$ is again a pseudo-tensor with respect to the last index, and $j_{z,l}^{S}$ is the SC component with the HC velocity $\vec{v}_{HC}$ along $\hat{z}$ and spin $\vec{s}_{HC}$:

$$\vec{j}^{S} \sim \vec{v}_{HC} \otimes \vec{s}_{HC}, \; j_{z,l}^{S} \sim v_z s_l \tag{7.7}$$

The product $\chi_{ijkz,l}^{(4,SC)} j_{z,l}^{S}$ is identical to $\chi_{ijk,l}^{(3,SP)} M_l$ in terms of the symmetry and non-zero components.

As for the non-magnetic effects, they were monitored by the relative variations of the linear reflectivity $R(t)$ and the even SH field $E_{2\omega}^{even}$:

$$\delta R(t) = \frac{R(t) - R_0}{R_0}, \tag{7.8}$$

$$\delta E_{2\omega}^{even}(t) = \frac{E_{2\omega}^{even}(t) - E_{2\omega,0}^{even}}{E_{2\omega,0}^{even}}, \tag{7.9}$$

where R_0 and $E_{2\omega,0}^{even}$ are the linear reflectivity and the even SH field in the absence of the pump pulse, respectively.

In contrast to the experiments where the probe pulse was applied to the Fe film, the magneto-induced SH field originating in Au can be considered to be small in comparison

to the total SH response[2]:

$$|E_{2\omega}^{even}| \gg |E_{2\omega}^{odd}|. \tag{7.10}$$

Neglecting $|E_{2\omega}^{odd}|^2$ in the expression (4.17) for the SH intensity, the even SH field $E_{2\omega}^{even}$ is given by

$$E_{2\omega}(t) \approx \sqrt{\frac{I_{2\omega}^{\uparrow}(t) + I_{2\omega}^{\downarrow}(t)}{2}}, \tag{7.11}$$

and the SH contrast $\rho_{2\omega}$ is

$$\rho_{2\omega}(t) \approx 2\frac{E_{2\omega}^{odd}}{E_{2\omega}^{even}} \cos\phi_{2\omega}, \tag{7.12}$$

where $\phi_{2\omega}$ is the relative phase difference between $\vec{E}_{2\omega}^{even}$ and $\vec{E}_{2\omega}^{odd}$.

Figure 7.1(b) shows the experimental results measured on the Au/Fe/MgO(001) structure with 8 nm of Fe and 75 nm of Au using 14-fs p-polarized pump and probe laser pulses in the transversal magneto-optical geometry $\vec{M}||\hat{y}$ (xz is a plane of incidence). Pump-induced variations of the even SH field $\delta E_{2\omega}^{even}(t)$ undergoes a fast drop during first 200 fs and then recovers on a picosecond time scale. At the same time the SH contrast $\rho_{2\omega}^{T}(t)$ goes down, reaches its negative peak at about 63 fs, changes its sign at about 150 fs and finally vanishes within first 2 ps after the optical excitation. The MOKE ellipticity signal $\psi_K''(t)$ also decays on a picosecond time scale, but exhibits no negative variations[3]. The curves $\delta E_{2\omega}^{even}(t)$ and $\rho_{2\omega}^{T}(t)$ are similar to those obtained by Melnikov et al. using 35-fs laser pulses [106]. In [106] the mSHG was considered as a purely surface-sensitive technique, therefore the negative peak of $\rho_{2\omega}^{T}(t)$ was assigned to the ballistic HCs with negative SP, while the positive peak of $\rho_{2\omega}^{T}(t)$ was referred to the contribution of the majority electrons $e^{\uparrow}$. It does not contradict with the absence of the negative variations of $\psi_K''(t)$. Since the MOKE gives information on the average magnetization in the Au layer, the contribution of the majority electrons $e^{\uparrow}$ to the MOKE ellipticity $\psi_K''(t)$ dominates even when the negative peak of the SH contrast $\rho_{2\omega}^{T}(t)$ appears. Nevertheless, in the following it will be shown that $\rho_{2\omega}^{T}(t)$ does possess the SC-induced contribution, and a well-accepted interpretation of the mSHG data in [106] has to be reconsidered.

According to (3.41), for a p-polarized probe pulse in the longitudinal magneto-optical configuration $\vec{M}||\hat{x}$ the odd SH field $\vec{E}_{2\omega}^{L,odd}$ is s-polarized. In order to observe interference between $\vec{E}_{2\omega}^{even}$ and $\vec{E}_{2\omega}^{L,odd}$, leading to a non-zero SH contrast $\rho_{2\omega}^{L}(t)$, one has to use an analyzer with the optical axis set between the p- and s-polarizations. Although both $\rho_{2\omega}^{T}(t)$ and $\rho_{2\omega}^{T}(t)$ reach their extremum at about 63 fs, $\rho_{2\omega}^{L}(t)$ does not change its sign (see Figure 7.2(a)). In 500 fs after the optical excitation of the Fe film $\rho_{2\omega}^{T}(t)$ and $\rho_{2\omega}^{L}(t)$ merge together. Considering the mSHG as a purely surface/interface sensitive technique and following the concept suggested in [106], one can assume that the components of the $\hat{\chi}^{(2)}$ tensor responsible for the appearance of the odd SH field

[2]The SH contrast $\rho_{2\omega}^{T}(t)$ measured with the p-polarized probe pulse in the transversal magneto-optical configuration did not exceeded 10%

[3]Fast variations of $\psi_K''(t)$ at the time zero are related to the temporal overlap of the pump and probe pulses.

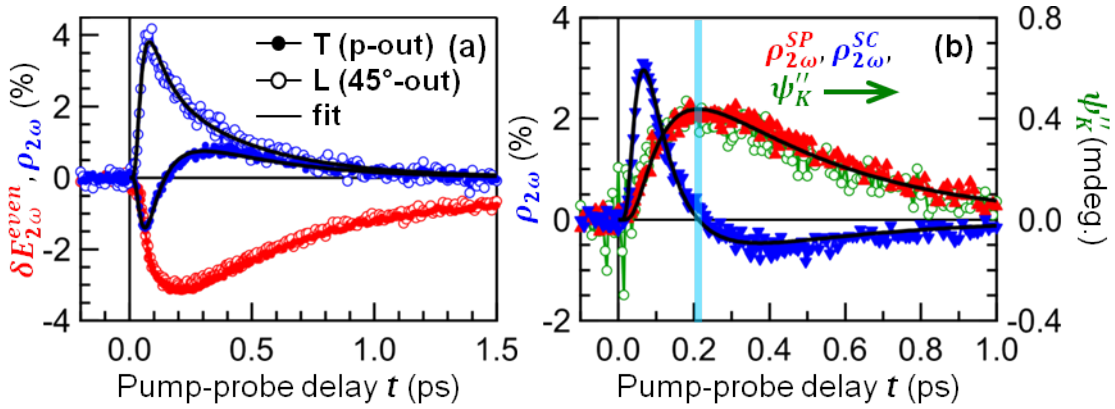

Figure 7.2: (a) Pump-induced relative variations of the even SH field $\delta E_{2\omega}^{even}(t)$ (red) and the SH contrast $\rho_{2\omega}(t)$ (blue) measured on a Au/Fe/MgO(001) structure with 8 nm of Fe and 75 nm of Au in the transversal (filled dots) and longitudinal (empty dots) magneto-optical configurations. For the transversal magneto-optical geometry the analyzer was set to transmit only p-polarized light, while for the longitudinal magneto-optical geometry the optical axis of the analyzer was aligned at 45° with respect to the direction of the p-polarization. (b) Dynamics of the spin-current- and spin-polarization-induced contributions $\rho_{2\omega}^{SC}(t)$ (blue down-triangles), $\rho_{2\omega}^{SP}(t)$ (red up-triangles) to the SH contrast $\rho_{2\omega}$, and the MOKE ellipticity ψ_K'' (green empty circles) measured on a Au/Fe/MgO(001) structure with 8 nm of Fe and 75 nm of Au. Cyan line denotes the pump-probe delay $t^* \approx 210$ fs, when $\rho_{2\omega}^{SC}(t)$ becomes negative, and $\rho_{2\omega}^{SP}(t)$ reaches its maximum. Solid black lines are the results of the joint fitting procedure of the curves $\rho_{2\omega}^{T}(t)$ and $\rho_{2\omega}^{L}(t)$ with the sum of the functions (7.17) and (7.18).

$\vec{E}_{2\omega}^{odd}$ may behave differently upon the arrival of the HCs with different binding energies. However, thanks to the pump-probe experiments performed on three-layer Fe/Au/Fe/MgO(001) structures, which are discussed in **Chapter 8**, we can conclude that in addition to the accumulation of the SP at the Au surface, the laser-induced SC flowing from the Fe film leads to the generation of the odd SH field $\vec{E}_{2\omega}^{odd}$ in the bulk of Au:

$$\vec{E}_{2\omega}^{odd} = \vec{E}_{2\omega}^{SP} + \vec{E}_{2\omega}^{SC}. \tag{7.13}$$

In order to explain the measured $\rho_{2\omega}^{T}(t)$ and $\rho_{2\omega}^{L}(t)$ curves, we suggest that one of the terms in (7.13) changes its sign, when we switch between the transversal and longitudinal magneto-optical geometries. Since the SC-induced odd SH field originates in the bulk of the Au layer, its contribution to the SH contrast $\rho_{2\omega}(t)$ builds up earlier than the other one provided by the SP at the Au surface. From Figure 7.2(a) one can deduce that the SP-induced contribution is positive for $\rho_{2\omega}^{T}(t)$ and $\rho_{2\omega}^{L}(t)$, while the SC-induced one has opposite signs[4].

[4]Actually it depends on the orientation of the analyzer. If the analyzer is rotated in the opposite direction with respect to the position, where it transmits only the p-polarized component, $\rho_{2\omega}^{L}(t)$ becomes negative.

It should be noted that different components of $\chi^{(4,SC)}_{ijkz,l} j^S_{z,l}$ and $\chi^{(3,SP)}_{ijk,l} M_l$ are responsible for the appearance of the odd SH field in the transversal and longitudinal magneto-optical geometries, therefore $\rho^L_{2\omega}(t)$ and $\rho^T_{2\omega}(t)$ can be expressed as

$$\rho^L_{2\omega}(t) = \rho^{SC}_{2\omega}(t) + \rho^{SP}_{2\omega}(t), \quad \rho^T_{2\omega}(t) = -\alpha\rho^{SC}_{2\omega}(t) + \beta\rho^{SP}_{2\omega}(t), \tag{7.14}$$

where $\rho^{SC}_{2\omega}(t)$, $\rho^{SP}_{2\omega}(t)$ are the temporal profiles of the SC- and SP-induced contributions, respectively. The coefficients α and β are account for different amplitudes of these terms in two magneto-optical geometries. According to the theoretical predictions for the transmission through the Fe/Au interface (see Figure 6.6(b)) and the ballistic lengths in Fe (see Table 6.1), it is reasonable to assume that the SC pulse in Au is formed only by the majority electrons with the positive SP determined by the magnetization $\vec{M}_{Fe}$ of the Fe film. When the front of the SC pulse reaches the Au surface, reflected majority electrons propagate back to the bulk of Au. As a result, they compensate the SC flowing from the Fe film, providing sharp peaks in the $\rho^T_{2\omega}(t)$, $\rho^L_{2\omega}(t)$ signals at about 63 fs. From the mSHG data obtained on three-layer Fe/Au/Fe/MgO(001) structures it is evident that the SC reverses, because of the electrons reflected from the Fe/Au interface (see **Chapter 8**). In a two-layer Au/Fe/MgO(001) structure all HCs approaching the Au surface undergo spin-independent scattering, and the reversed SC should have larger amplitude than in the case of a three-layer Fe/Au/Fe/MgO(001) structure with the same thickness of the Au spacer, where some portion of the spin-polarized HCs is transmitted into the spin-collector. When $\rho^{SC}_{2\omega}(t)$ changes its sign, the reversed SC becomes larger than the direct one, and the amount of the positive SP, accumulated at the Au surface, is maximal. Thus

$$\rho^{SC}_{2\omega}(t^*) = 0 \;\Rightarrow\; \left(\frac{d\rho^{SP}_{2\omega}(t)}{dt}\right)_{t=t^*} = 0. \tag{7.15}$$

Using (7.15), it is possible to determine α and β in (7.14), and evaluate temporal profiles of the SC- and SP-induced contributions $\rho^{SC}_{2\omega}(t)$ and $\rho^{SP}_{2\omega}(t)$:

$$\rho^{SC}_{2\omega}(t) = \frac{\beta\rho^L_{2\omega}(t) - \rho^T_{2\omega}(t)}{\alpha+\beta}, \quad \rho^{SP}_{2\omega}(t) = \frac{\alpha\rho^L_{2\omega}(t) + \rho^T_{2\omega}(t)}{\alpha+\beta}. \tag{7.16}$$

In spite of that $\rho^{SC}_{2\omega}(t)$ is proportional to the convolution of the spatial profile of the SC $\vec{j}^S(z,t)$ with the depth sensitivity of the mSHG, it turned out that $\rho^{SC}_{2\omega}(t)$ resembles the time derivative of the SP at the Au surface, i.e. $d\rho^{SP}_{2\omega}(t)/dt$, while $\rho^{SP}_{2\omega}(t)$ reproduces the MOKE ellipticity signal $\psi''_K(t)$ (see Figure 7.2(b)). In order to derive characteristic time constants, $\rho^{SP}_{2\omega}(t)$ was described with the following function

$$\rho^{SP}_{2\omega}(t) = \frac{A}{2\sqrt{\pi(b_0 + b_1(t-t_0))}} \exp\left(-\frac{(t-t_0)^2}{4(b_0+b_1(t-t_0))}\right). \tag{7.17}$$

The derivative of this function corresponds to the SC-induced contribution:

$$\begin{aligned}\rho^{SC}_{2\omega}(t) = &-\frac{B}{8\sqrt{\pi(b_0+b_1(t-t_0))}}\left[\frac{2b_1}{b_0+b_1(t-t_0)} + \frac{2b_0(t-t_0)+b_1(t-t_0)^2}{(b_0+b_1(t-t_0))^2}\right] \\ &\times \exp\left(-\frac{(t-t_0)^2}{4(b_0+b_1(t-t_0))}\right).\end{aligned} \tag{7.18}$$

In Figure 7.2(a) it is demonstrated that the sum of the functions (7.17) and (7.18) approximately reproduces the measured curves $\rho^T_{2\omega}(t)$ and $\rho^L_{2\omega}(t)$. The corresponding adjustable parameters are shown in Table 7.1. Function (7.17) and its derivative (7.18) do not imply any specific model of the laser-induced HC generation in Fe and HC emission into the Au layer, but they exhibit two features which (should) present in $\rho^{SP}_{2\omega}(t)$ and $\rho^{SC}_{2\omega}(t)$. (i) When $\rho^{SC}_{2\omega}(t)$ changes the sign, $\rho^{SP}_{2\omega}(t)$ reaches its maximum. (ii) There are also one maximum and one minimum of $\rho^{SC}_{2\omega}(t)$, where $\rho^{SP}_{2\omega}(t)$ changes its convexity.

In the next subsection it will be shown that HCs propagate in Au mostly in a quasi-ballistic regime, and the temporal profiles of the SH contrast $\rho_{2\omega}$ and the MOKE ellipticity $\psi''_K(t)$ are determined by the emission of the majority electrons from the Fe film, which increases on the time scale of the electron-electron thermalization in Fe ~ 200 fs (see **Chapter 5**) due to the generation of the secondary HCs, and decreases on a larger time scale because of the relaxation processes.

7.1.1 Hot carrier transport: dependence on the Au thickness

Experimental data shown in Figure 7.2 were obtained on the Au/Fe/MgO(001) structure with 75 nm of Au. Absence of the static MOKE signals and the SH contrast allowed us to neglect all contributions from the Fe film and treat SP and SC flowing in the Au layer as the only source of the magneto-optical response. However, it is not always the case. For $d_{Au} = 23$ nm the static SH contrasts $\rho^T_{2\omega,0} = -(1.7 \pm 0.1)$ % and $\rho^L_{2\omega,0} = (1.0 \pm 0.2)$ % (see Figure 7.3(a)). During the first picosecond after the pump pulse, all injected majority electrons propagate to the Au surface and then return back into the Fe film. Some part may be reflected from the Fe/Au interface, but it is so small that it does not provide significant contribution to the dynamic SH contrasts $\rho^T_{2\omega}(t)$ and $\rho^L_{2\omega}(t)$. Thus on a larger time scale $\rho^T_{2\omega}(t)$ and $\rho^L_{2\omega}(t)$ monitor only the magnetization dynamics in the ferromagnetic film. Figure 7.3(b) presents the dependency of the ratio between the amplitudes of the SH fields $\vec{E}^{Au\ surf.}_{2\omega}$, $\vec{E}^{Fe/Au}_{2\omega}$ originating at the Au surface and the Fe/Au interface, respectively. Assuming identical efficiency of the SHG at the Au surface and the Fe/Au interface, the Fe/Au interface should contribute considerably to the mSHG response for the Au thicknesses up to 40 nm. As for the linear magneto-optical response, the absorption of the signal wave in Au at the fundamental frequency $\hbar\omega = 1.5$ eV is less efficient than the absorption of the SH wave (see Figure 2.5), therefore the contribution of the Fe film to the MOKE is considerable for the Au thicknesses up to 70 nm (see Figure 7.3(d)). In spite of the fact that the contributions from the Fe film to the magneto-optical signals complicates the analysis of the spin dynamics induced in the Au layer, they provide information about laser-induced demagnetization. Absolute variations of the MOKE ellipticity $\delta\psi''_K$ shown in Figure 7.3(c) indicate approximately 10 % demagnetization of the 8-nm Fe film at 2 ps after the optical excitation. Since both spin-flip processes and the HC transport contribute to the demagnetization of the ferromagnetic film, this value cannot be used for the estimation of the SP injected into the non-magnetic layer. We will come back to this problem later.

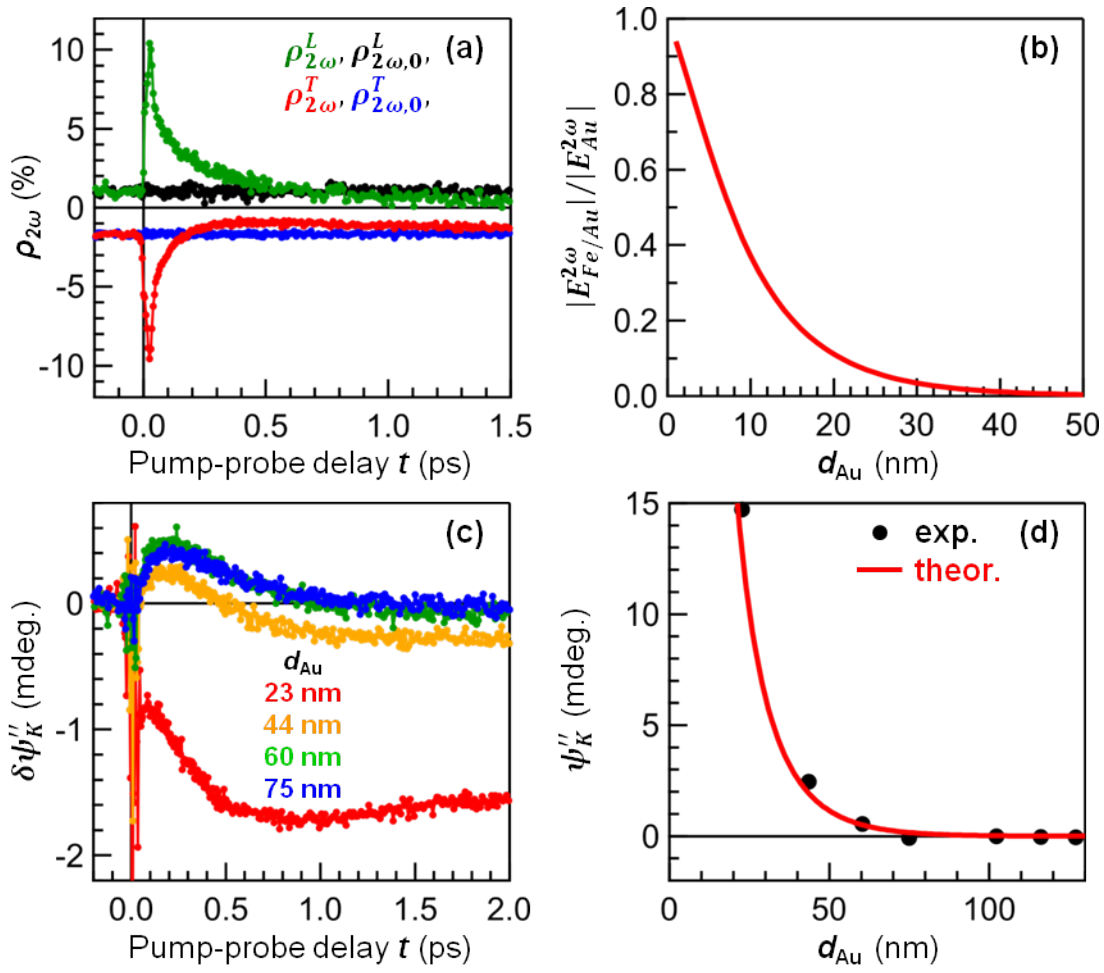

Figure 7.3: (a) Pump-induced variations of the SH contrasts $\rho^T_{2\omega}$ (red) and $\rho^L_{2\omega}$ (green) measured on the Au/Fe/MgO(001) structure with 23 nm of Au and 8 nm of Fe in the transversal (T) and longitudinal (L) magneto-optical geometries. $\rho^T_{2\omega,0}$ (blue) and $\rho^L_{2\omega,0}$ (black) are the static SH contrasts. (b) Ratio between the amplitudes of the reflected SH fields originating at the Fe/Au interface and the Au surface, calculated in the assumption that the SH sources are the current sheets in the Au layer with polarization $P^{sh}_{2\omega,p} = \chi^{(2)} \cdot E_{\omega,p}E_{\omega,p}$, where $\chi^{(2)}_{Ausurf.} = \chi^{(2)}_{Fe/Au} = 1$ and $\hbar\omega = 1.5$eV. (c) Pump-induced absolute variations of the MOKE ellipticity $\delta\psi''_K(t)$ measured on Au/Fe/MgO(001) structures with 8 nm of Fe and different Au thicknesses: 23 nm (red), 44 nm (orange), 60 nm (green), 75 nm (blue). (d) Dependence of the static MOKE ellipticity signal ψ''_K on the Au thickness d_{Au}. Black dots represent experimental values, and solid red line is calculated according to the method described in [27].

d_{Au} (nm)	A_T/A_L	B_T/B_L	b_0 (ps^2)	b_1 (ps)	t_0 (ps)
44	0.23 ± 0.02	-0.71 ± 0.06	0.034 ± 0.002	0.126 ± 0.006	0.254 ± 0.006
60	0.25 ± 0.01	-0.60 ± 0.02	0.036 ± 0.002	0.125 ± 0.003	0.285 ± 0.004
75	0.26 ± 0.01	-0.53 ± 0.03	0.034 ± 0.002	0.112 ± 0.004	0.304 ± 0.005
116	0.44 ± 0.02	-0.51 ± 0.03	0.039 ± 0.002	0.094 ± 0.004	0.40 ± 0.01
127	0.31 ± 0.02	-0.44 ± 0.04	0.041 ± 0.003	0.098 ± 0.006	0.42 ± 0.01

Table 7.1: Adjustable parameters obtained after the joint fitting procedure of the SH contrasts $\rho_{2\omega}^T(t)$ and $\rho_{2\omega}^L(t)$ measured in the transversal and longitudinal magneto-optical configurations, respectively. The fitting function is a sum of the functions (7.17) and (7.18).

In the experiments performed on the Au/Fe/MgO(001) structures with $d_{Au} > 40$ nm, the SH contrasts $\rho_{2\omega}^T(t)$ and $\rho_{2\omega}^L(t)$ are zero for $t < 0$, meaning that only Au contributes to the SH signal, and for $t > 0$ they look similar to the curves presented in Figure 7.2(a). Fitting the experimental data with the sum of the functions (7.17) and (7.18), we disentangled the SC- and SP-induced contributions $\rho_{2\omega}^{SC}(t)$ and $\rho_{2\omega}^{SP}(t)$ to the SH contrast. Figure 7.4 shows pump-induced variations of the even SH field $\delta E_{2\omega}^{even}(t)$, $\rho_{2\omega}^{SC}(t)$ and $\rho_{2\omega}^{SP}(t)$ measured on the samples with 44 (red), 60 (orange), 75 (green) and 116 nm (blue) of Au. The results of the fitting procedure are summarized in Table 7.1. Assuming that all majority electrons propagate back into the bulk of Au after the reflection from the Au surface, it is clear that the parameters b_0 and b_1 characterize the spatial shape of the SC pulse injected into the Au layer. Their values obtained for different Au thicknesses are close to each other. It allows us to conclude that the majority electrons propagate in Au in a quasi-ballistic regime and the temporal profiles of $\rho_{2\omega}^{SC}(t)$ and $\rho_{2\omega}^{SP}(t)$ are mostly determined by the HC flux through the Fe/Au interface. The temporal width of the front of the HC packet $\sqrt{b_0} \approx 0.2$ ps which corresponds to the time scale of the electron-electron thermalization (see **Chapter 5**). It is not surprising, because relaxation of the non-equilibrium electrons in Fe increases the number of the electrons above the Fermi level. Since the majority electrons have larger ballistic length in Fe and higher transmission probability through the Fe/Au interface than other HCs (see Figure 6.6(a)), it provides a net flux of the positive SP from the Fe film into the Au layer, which lasts as long as the electron temperature in Fe is larger than in Au. The temporal width of $\rho_{2\omega}^{SP}(t)$ gives the characteristic time of the electron equilibration between the Fe and Au films: 0.56 ± 0.03 ps.

For the perfect epitaxial Au/Fe/MgO(001) structures, the ratios A_T/A_L and B_T/B_L are expected to be the same for different d_{Au}. However, variation of the sample quality may enhance/reduce one contribution to the SH contrast $\rho_{2\omega}(t)$ with respect to another one, thereby affecting A_T/A_L and B_T/B_L.

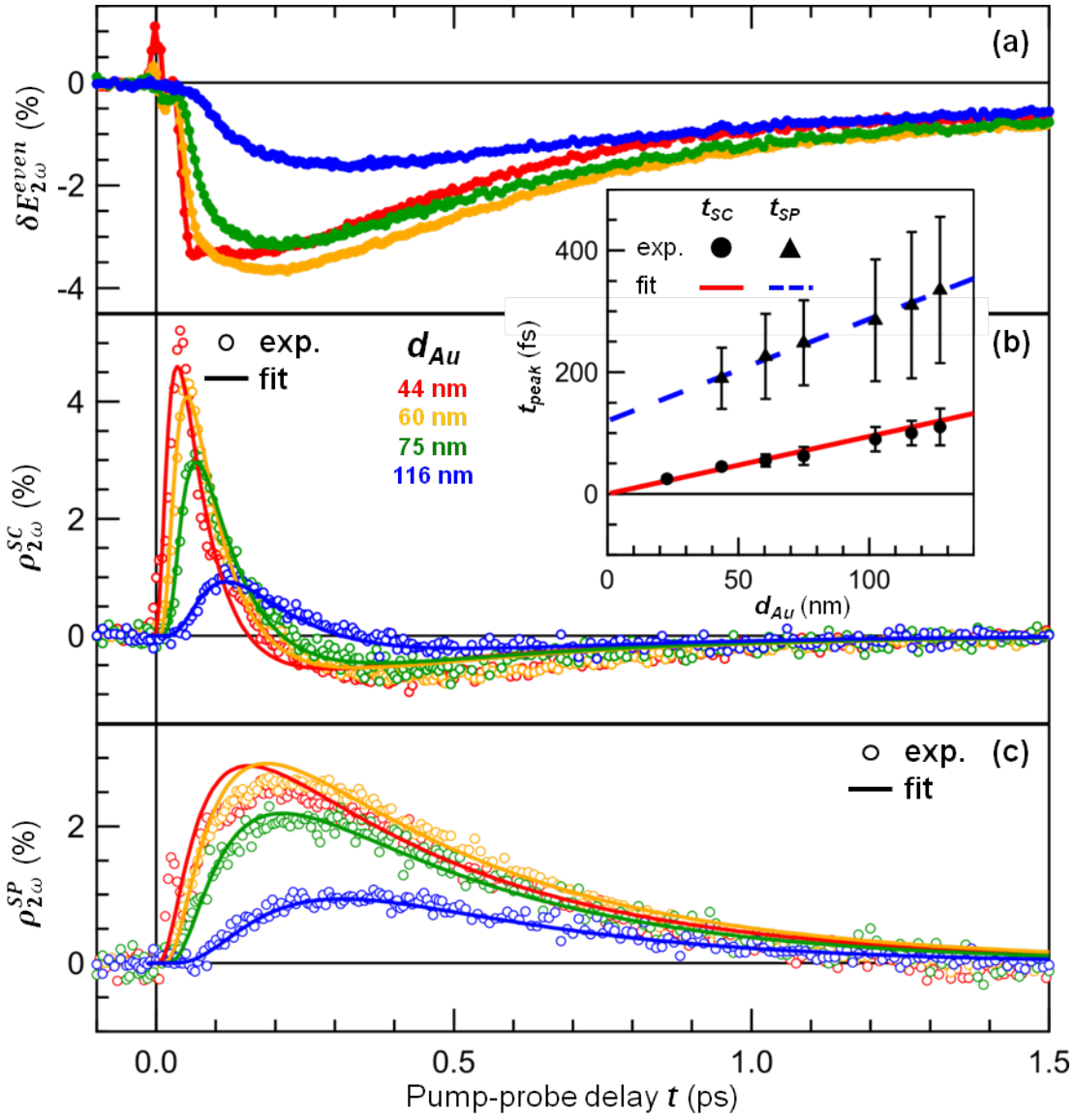

Figure 7.4: Pump-induced relative variations of the even SH field $\delta E_{2\omega}^{even}(t)$ (a), SC- and SP-induced contributions to the SH contrast $\rho_{2\omega}^{SC}(t)$ (b) and $\rho_{2\omega}^{SP}(t)$ (c), measured on the Au/Fe/MgO(001) structures with 8 nm of Fe and different Au thicknesses: 44 nm (red), 60 nm (orange), 75 nm (green), 116 nm (blue). In order to evaluate $\rho_{2\omega}^{SP}(t)$ and $\rho_{2\omega}^{SC}(t)$ for each Au thickness, the SH contrasts $\rho_{2\omega}^{T}$ and $\rho_{2\omega}^{L}$, measured in the transversal (p-out) and longitudinal (45°-out) magneto-optical configurations, were fitted with a sum of the functions (7.17) and (7.18). Using the ratios A_T/A_L, B_T/B_L obtained in the fitting procedure (see Table 7.1), it is possible to derive $\rho_{2\omega}^{SP}(t)$ and $\rho_{2\omega}^{SC}(t)$: the empty circles in (b) and (c) depict the experimental data, while the solid lines correspond to the fitting functions (7.17) for $\rho_{2\omega}^{SP}(t)$ and (7.18) for $\rho_{2\omega}^{SC}(t)$. The inset shows the dependencies of t_{SC} (circles) and t_{SP} (triangles) on d_{Au}. t_{SC} and t_{SP} are the peak positions of the SC- and SP-induced contributions $\rho_{2\omega}^{SC}(t)$ and $\rho_{2\omega}^{SP}(t)$, respectively.

In Figure 7.4 one can note that functions (7.17) and (7.18) describes the SC- and SP-induced contributions $\rho_{2\omega}^{SC}(t)$ and $\rho_{2\omega}^{SP}(t)$ for large Au thicknesses, and there are some deviations for small Au thicknesses. The reason is that there are two types of the majority electrons which contribute to the spin dynamics in Au: optically excited electrons that leave the Fe film in the ballistic regime, and secondary electrons. According to Figure 6.5, the optically excited electrons have well-directed velocity distribution in contrast to the secondary electrons. However, because of the higher binding energies the optically excited electrons have smaller lifetimes in Au. As a result, their contribution to the SH contrast decreases faster with d_{Au} than that of the secondary electrons. For $d_{Au} = 44$ nm $\delta E_{2\omega}^{even}(t)$ exhibits a double-peak structure which is smeared into a single broad peak for larger Au thicknesses. The sharp peak in $\delta E_{2\omega}^{even}(t)$, as well as that of $\rho_{2\omega}^{SC}(t)$, corresponds to the arrival of the optically excited electrons at the Au surface.

The inset in Figure 7.4 shows that the position t_{SC} of the positive peak of $\rho_{2\omega}^{SC}(t)$ is linearly proportional to d_{Au}, which is a true signature of the ballistic transport. The linear fit $d_{Au} = v_{Au1} t_{SC}$ (solid red line) gives the velocity of the majority electrons which leave the Fe film in the ballistic regime: $v_{Au1} = (1.06 \pm 0.07)$ nm/fs. The amplitude of the peak of $\rho_{2\omega}^{SC}(t)$ decays with an increase of d_{Au}. The exponential fit (not shown here) gives the ballistic length $\lambda_{Au1} = (25 \pm 3)$ nm. Then the lifetime is $\tau_{Au1} = \lambda_{Au1}/v_{Au1} = (24 \pm 4)$ fs. Both v_{Au1} and τ_{Au1} are close to the results of the ab initio calculations [19, 106]. Position t_{SP} of the peak of $\rho_{2\omega}^{SP}(t)$ is also linearly proportional to d_{Au}, which supports our conclusion that all injected majority electrons propagate in Au in quasi-ballistic regime. The linear fit $d_{Au} = v_{Au2}(t_{Au2} - t_0)$ (dash blue line) gives the velocity of the secondary majority electrons $v_{Au2} = (0.6 \pm 0.4)$ nm/fs and the time $t_0 = 120 \pm 84$ fs, when the flux of the secondary electrons through the Fe/Au interface is maximal. The secondary electrons has smaller binding energies and larger lifetimes than the optically excited electrons, therefore the amplitude of $\rho_{2\omega}^{SP}(t)$ decreases slower with d_{Au} than that of $\rho_{2\omega}^{SC}(t)$.

When $d_{Au} > 65$ nm, the MOKE signal reflects only spin dynamics in the Au layer. Figure 7.5 shows that in this case ratio between the MOKE ellipticity $\psi_K''(t)$ and rotation $\psi_K'(t)$ remains constant for $t > 100$ fs after the pump pulse. Moreover, this ratio is almost independent of the Au thickness. This allows us to conclude that the observed variations of the MOKE signals are not related to the variations of the Voigt constant of gold q_{Au} and occur only due to spin transfer in the Au layer. Fitting the MOKE ellipticity $\psi_K''(t)$ with the function 7.17, we demonstrate that for $d_{Au} > 65$ nm the SP-induced contribution to the SH contrast $\rho_{2\omega}^{SP}(t)$ resembles the MOKE ellipticity $\psi_K''(t)$ (see Tables 7.1 and 7.2). It means that the magnetization profile in the probed region of the Au layer is more or less homogeneous.

In order to obtain some information about the Voigt constant of gold q_{Au}, we calculated the depth sensitivities of the MOKE rotation $w'_{K,re}(z)$, $w'_{K,im}(z)$ and ellipticity $w''_{K,re}(z)$, $w''_{K,im}(z)$ (see Figure 7.5). Curves $w''_{K,re}(z)$, $w'_{K,re}(z)$, $w'_{K,im}(z)$ and $w''_{K,im}(z)$ represent the dependencies of the MOKE ellipticity and rotation on the depth z^* of the sublayer ($\Delta z = 0.1$ nm) with a unit magnetization $m(z^*) = 1$ and magneto-optical

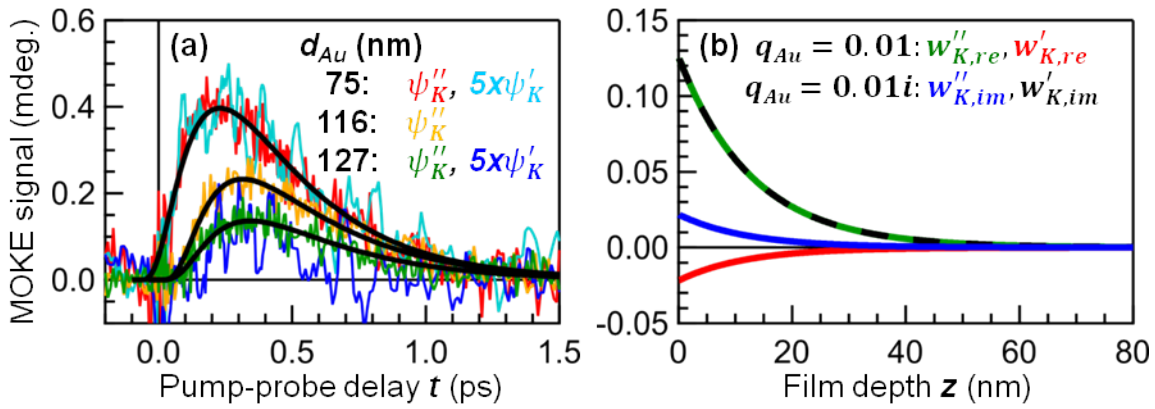

Figure 7.5: (a) MOKE ellipticity $\psi''_K(t)$ and rotation $\psi'_K(t)$, measured for 8 nm of Fe and different Au thicknesses: 75 nm (red and cyan), 116 nm (orange) and 127 nm (green and blue). The MOKE rotation curves $\psi'_K(t)$ were scaled and smoothed ($5\ pt. = 20\ fs$). Black lines represent the results of the fitting procedure of the MOKE ellipticity $\psi''_K(t)$ with the function (7.17). (b) Depth sensitivities of the longitudinal MOKE rotation $w'_{K,re}(z)$ (solid red line), $w'_{K,im}(z)$ (dash black line) and ellipticity $w''_{K,re}(z)$ (solid green line), $w''_{K,im}(z)$ (solid blue line). $w'_{K,re}(z)$, $w'_{K,im}(z)$, $w''_{K,re}(z)$, and $w''_{K,im}(z)$ are the contributions to the MOKE signals from the sublayer ($\Delta z = 0.1$ nm) with a unit magnetization $\vec{M} \| \hat{x}$ ($|\vec{M}| = 1$) at the distance z from the Au surface. $w''_{K,re}$, $w'_{K,re}$ correspond to $q_{Au} = 0.01$, and $w''_{K,im}$, $w'_{K,im}$ correspond to $q_{Au} = 0.01i$.

constant $q_{re} = 0.01$ and $q_{im} = 0.01i$, respectively. It turned out that

$$w''_{K,re}(z) \approx w'_{K,im}(z) = w_1(z) \geqslant 0, \tag{7.19}$$

$$w''_{K,im}(z) \approx -w'_{K,re}(z) = w_2(z) \geqslant 0. \tag{7.20}$$

If $q_{Au} = q'_{Au} + iq''_{Au}$ and $M(z)$ is the magnetization profile, the MOKE ellipticity ψ''_K and rotation ψ'_K are given by

$$\begin{aligned} \psi''_K &= \sum_j M(z_j) \cdot \frac{q'_{Au} w_1(z_j) + q''_{Au} w_2(z_j)}{0.01}, \\ \psi'_K &= \sum_j M(z_j) \cdot \frac{-q'_{Au} w_2(z_j) + q''_{Au} w_1(z_j)}{0.01}. \end{aligned} \tag{7.21}$$

We can also express $q_{Au} = |q_{Au}| \cdot e^{i\phi_{Au}}$, where $r = \tan^{-1} \phi_{Au} = q'_{Au}/q''_{Au}$:

$$\begin{aligned} \frac{\psi''_K}{\psi'_K} &= \frac{\sum_j M(z_j) \cdot (q'_{Au} w_1(z_j) + q''_{Au} w_2(z_j))}{\sum_j M(z_j) \cdot (-q'_{Au} w_2(z_j) + q''_{Au} w_1(z_j))} \\ &= \frac{\sum_j M(z_j) \cdot (r \cdot w_1(z_j) + w_2(z_j))}{\sum_j M(z_j) \cdot (-r \cdot w_2(z_j) + w_1(z_j))}. \end{aligned} \tag{7.22}$$

d_{Au} (nm)	A (mdeg · ps)	b_0 (ps^2)	b_1 (ps)	$^*t_0$ (ps)
75	0.246 ± 0.005	0.034 ± 0.002	0.082 ± 0.008	0.304 ± 0.004
116	0.152 ± 0.003	0.037 ± 0.002	0.089 ± 0.007	0.40 ± 0.01
127	0.091 ± 0.003	0.039 ± 0.003	0.084 ± 0.012	0.42 ± 0.01

Table 7.2: Adjustable parameters obtained after the fitting procedure of the MOKE ellipticity $\psi''_K(t)$ with the function (7.17). *Parameter t_0 was held at the value obtained in the joint fitting procedure of the SH contrasts $\rho^T_{2\omega}(t)$ and $\rho^L_{2\omega}(t)$.

Then

$$\frac{\partial}{\partial r}\left(\frac{\psi''_K}{\psi'_K}\right) = \frac{\left[\sum_j M(z_j)\cdot w_1(z_j)\right]^2 + \left[\sum_j M(z_j)\cdot w_2(z_j)\right]^2}{\left[\sum_j M(z_j)\cdot(-r\cdot w_2(z_j) + w_1(z_j))\right]^2} \geqslant 0. \tag{7.23}$$

It means that ψ''_K/ψ'_K is a monotone function of the ratio r. In Figure 7.5(a) it is shown that $\psi''_K(t)/\psi'_K(t)$ does not change much with the Au thickness. It is possible to show that this condition demands a small gradient of the magnetization within the probed region of the Au layer, as well as the identical dynamics observed in $\rho^{SP}_{2\omega}(t)$ and $\psi''_K(t)$. Considering uniform magnetization profile in a 75-nm Au film, for the amplitudes of the MOKE ellipticity $\psi''_K(t)$ and rotation $\psi'_K(t)$ we found $Q_{Au} = q_{Au}M_{Au} = (2.4 + 0.9i)\cdot 10^{-4}$ and $r = Q'_{Au}/Q''_{Au} = q'_{Au}/q''_{Au} = 2.7 \pm 0.1$. In **Chapter 6** we used the ratio q'_{Au}/q''_{Au} in the analysis of the pump-induced variations of the MOKE signals, monitoring the magnetization dynamics in the Au/Fe/MgO(001) structures from the Fe side, and obtained $|q_{Au}| = \sqrt{q'^2_{Au} + q''^2_{Au}} = 0.10 \pm 0.02$, i.e. $q_{Au} \approx 0.094 + 0.035i$. Then the average magnetization in the Au layer is $M_{Au} = Q_{Au}/q_{Au} \approx 0.0026\ [M_{Fe}] \approx 0.0082\ [\mu_B/atom]$ [5]. This estimation is consistent with the ballistic magnetization profiles shown in Figure 6.8(b).

7.1.2 Hot carrier transport: dependence on the Fe thickness

In order to verify the relevance of the Fe thickness, pump-probe experiments were performed on the Au/Fe/MgO(001) structures with 47 nm of Au and different thicknesses of the Fe film. Figure 7.6 shows pump-induced variations of the even SH field $\delta E^{even}_{2\omega}(t)$ and SH contrast $\rho^T_{2\omega}(t)$ measured for 2, 11 and 17 nm of Fe under the same incident pump fluence. With the reduction of the Fe thickness d_{Fe}, portion of the reflected pump pulse increases due to high reflectivity of Au. However, it leads to an increase of the number of the HCs excited in the vicinity of the Fe/Au interface and the HC emission into the Au layer. As a result, the amplitude of $\delta E^{even}_{2\omega}(t)$ increases with the decreasing d_{Fe}.

[5] Here $M_{Fe} = 2.2\ \mu_B/atom$ is the saturation magnetization of Fe. Also it is taken into account that one unit cell of bcc-Fe ($a_{Fe} = 0.287$ nm) contains 2 atoms, while one unit cell of fcc-Au ($a_{Au} = 0.408$ nm) contains 4 atoms.

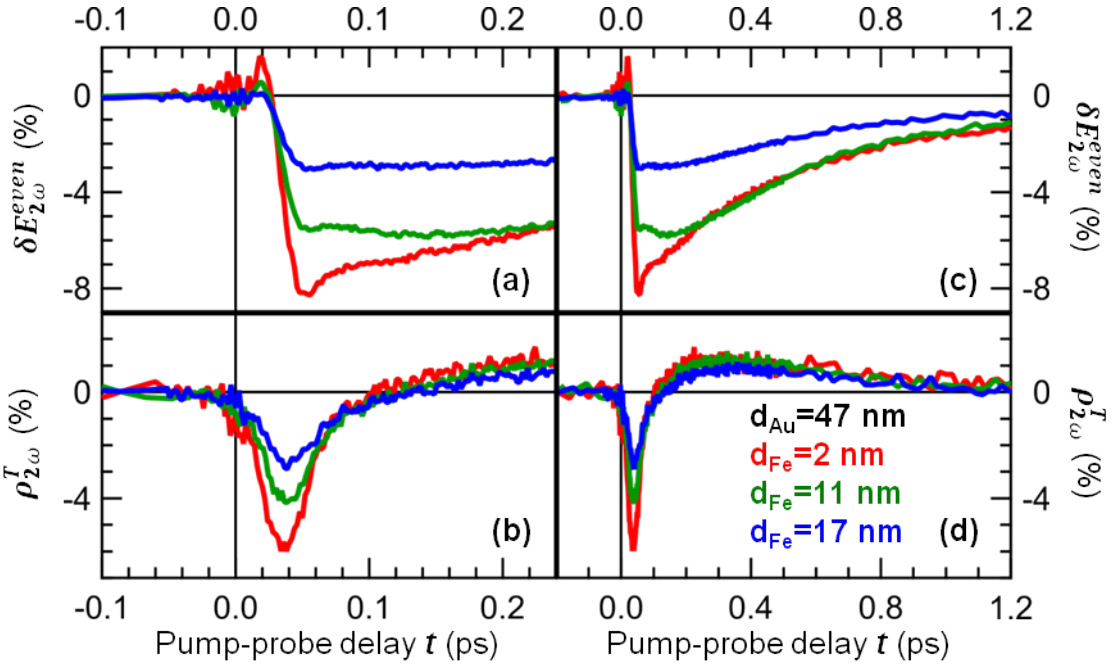

Figure 7.6: Pump-induced variations of the even SH field $\delta E_{2\omega}^{even}(t)$ (a) and SH contrast $\rho_{2\omega}^{T}(t)$ (b), measured in the transversal magneto-optical geometry for 47 nm of Au and 2, 11 and 17 nm of Fe.

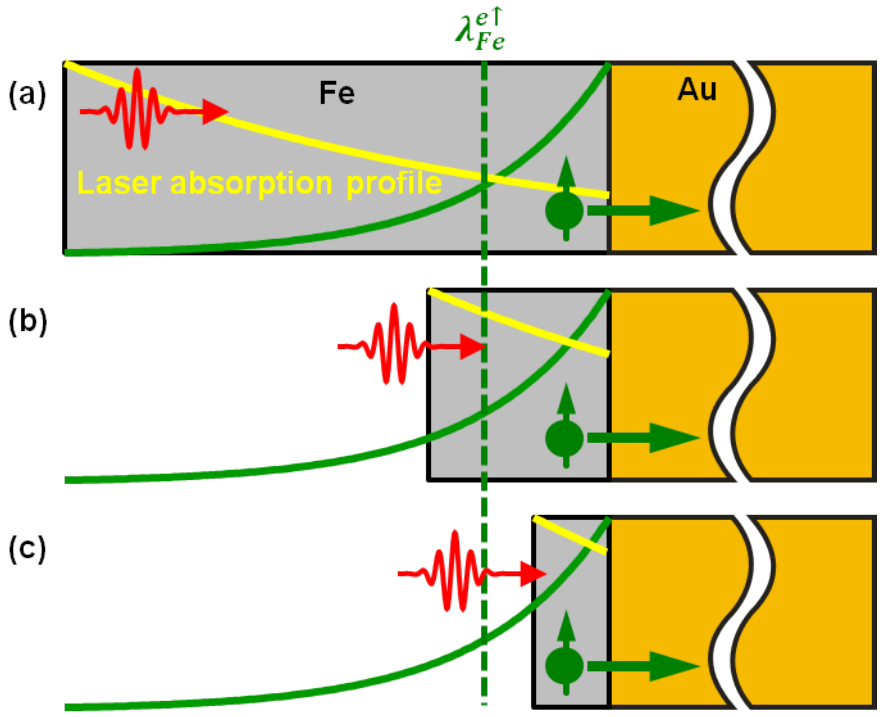

Figure 7.7: Emission of the majority electrons $e^{\uparrow}$ from the Fe film into the Au layer for different ratios between the Fe thickness d_{Fe} and the ballistic length $\lambda_{Fe}^{e\uparrow}$: (a) $d_{Fe} \gg \lambda_{Fe}^{e\uparrow}$, (b) $d_{Fe} \gtrsim \lambda_{Fe}^{e\uparrow}$, (c) $\lambda_{Fe}^{e\uparrow} > d_{Fe}$.

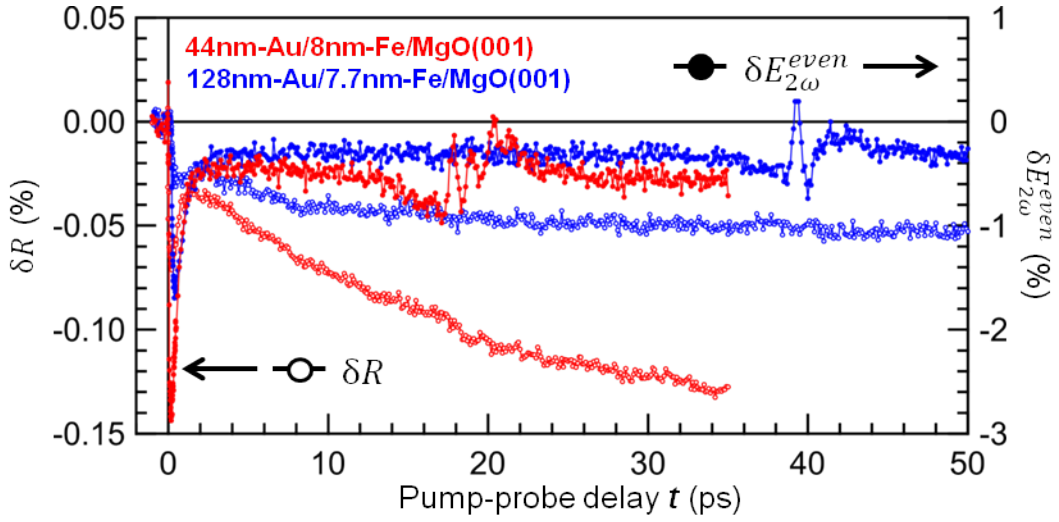

Figure 7.8: Variations of the even SH field $\delta E_{2\omega}^{even}(t)$ (filled circles) and the linear reflectivity $\delta R(t)$ (empty circles), measured on 60nm-Au/8nm-Fe/MgO(001) (red) and 128nm-Au/7.7nm-Fe/MgO(001) (blue) structures.

At the same time the position of the negative peak of the SH contrast $\rho_{2\omega}^{T}(t)$ does not vary with d_{Fe}, but its amplitude exhibits strong reduction with the increasing d_{Fe}. This observation supports our suggestion that an appearance of the negative peak of $\rho_{2\omega}^{T}(t)$ corresponds to the arrival of the optically excited majority electrons at the Au surface. For small d_{Fe} comparable or smaller than the ballistic length $\lambda_{Fe}^{e\uparrow}$ of the majority electrons in Fe, the portion of the optically excited electrons injected into the Au layer in the ballistic regime is large enough (see Figure 7.7), so that the corresponding sharp peak in $\delta E_{2\omega}^{even}(t)$ becomes more pronounced in comparison with the broad peak of the secondary electrons. Thus both Fe and Au thicknesses determine the portion of the optically excited electrons approaching the Au surface.

7.1.3 Acoustic response as a tool to measure Au thickness

According to Figure 7.1(b), contributions from the Au layer to the MOKE ellipticity $\psi_K''(t)$ and the SH contrast $\rho_{2\omega}(t)$ vanish within first 2 ps after the time zero. Despite of that the variations of the linear reflectivity $\delta R(t)$ and even SH field $\delta E_{2\omega}^{even}(t)$, measured on a larger time scale, offer us possibility to determine the Au thickness with sufficient accuracy directly in the pump-probe experiment. Optical excitation (see Figure 7.1(a)) heats the Fe film up resulting in its extension and a generation of an acoustic wave which then propagates in the Au layer. When the acoustic wave reaches the Au surface, the induced strain leads to an appearance of the peak in $\delta E_{2\omega}^{even}(t)$ (see Figure 7.8). However, because of the reflection of the acoustic wave from the free Au surface, there

is no pronounced peak in $\delta R(t)$. In **Chapter 8** we discuss the experiments performed on three-layer Fe/Au/Fe/MgO(001) structures, where reflection of the acoustic wave from the Fe/Au interface results in the drastic variations of both even SH field $\delta E_{2\omega}^{even}(t)$ and linear reflectivity $\delta R(t)$.

7.2 Conclusions

Transport of spin-polarized HCs in a non-magnetic Au film has been studied using the time-resolved MOKE and mSHG techniques. It has been demonstrated that the laser-induced SC is formed predominantly by the majority electrons injected from the Fe film into the Au layer. This result is consistent with the transmission of the Fe/Au interface, obtained in the first-principle quantum transport calculations for the Fe/Au structure (see Figure 6.6(b)). The steep front of the SC pulse consists of the optically excited electrons which leave the Fe film in the ballistic regime. Relaxation of the optically excited electrons in Fe leads to the generation of the secondary electrons. They provide a net flux of the positive SP through the Fe/Au interface, as long as the electron temperature in Fe is larger than in Au. Analysis of the SH contrast and MOKE signals give the characteristic time of the electron equilibration between the Fe and Au films: 0.56 ± 0.03 ps. Both optically excited and secondary majority electrons propagate in Au in a quasi-ballistic regime, maintaining their initial SP. From the analysis of the mSHG response we found the velocity of the optically excited majority electrons $v_{Au1} = (1.06 \pm 0.07)\ nm/fs$ and their lifetime $\tau_{Au1} = (24 \pm 4)\ fs$ in Au. The secondary electrons have smaller binding energies and hence longer lifetimes than the optically excited electrons. However, their velocity distribution is more uniform and provides smaller average velocity projection along $\hat{z}$: $v_{Au2} = (0.6 \pm 0.4)\ nm/fs$.

From the comparison of the SH contrasts $\rho_{2\omega}^{T}(t)$ and $\rho_{2\omega}^{L}(t)$ measured in the transversal and longitudinal magneto-optical geometries, it has been shown that in addition to the surface contribution, the SC gives rise to the odd SH field $\vec{E}_{2\omega}^{odd}$ originating in the bulk of Au. It has been confirmed in the experiments performed on three-layer Fe/Au/Fe/MgO(001) structures (see **Chapter 8**). The SP-induced surface contribution to the SH contrast $\rho_{2\omega}(t)$ resembles the dynamics of the MOKE ellipticity $\psi''_K(t)$, meaning that the magnetization profile within the probed region of the Au layer is more or less uniform. The same conclusion follows from the independence of the ratio $\psi''_K(t)/\psi'_K(t)$ from the Au thickness for $d_{Au} > 65$ nm, when contributions of the Fe film to the MOKE signals can be neglected. Assuming the uniform magnetization profile, from the amplitudes of $\psi''_K(t)$ and $\psi'_K(t)$, measured on the Au/Fe/MgO(001) structure with 8 nm of Fe and 75 nm of Au, we found $Q_{Au} = q_{Au}M_{Au} = (2.4 + 0.9i) \cdot 10^{-4}$ ($Q''_{Au}/Q'_{Au} = q''_{Au}/q'_{Au} = 2.7 \pm 0.1$). Using $q_{Au} = 0.094 + 0.035i$ (see **Chapter 6**), we estimated the average magnetization built up in the Au layer by the SC flowing from the Fe film: $M_{Au} = Q_{Au}/q_{Au} \approx 0.0026\ [M_{Fe}] \approx 0.0082\ [\mu_B/atom]$.

Chapter 8

Spin dynamics induced in the Fe film by hot carrier injection

In **Chapters 6** and **7** we considered the hot carrier (HC) injection from a ferromagnetic film into a non-magnetic layer and transport of the spin-polarized HCs in a noble metal. In this chapter we discuss the injection of the spin-polarized HCs into a ferromagnetic film. Pump-probe experiments have been performed on three-layer Fe/Au/Fe/MgO(001) structures capped with thin Au layer, where the back pump pulse excites one of the Fe layers, the spin-emitter (E), and the front probe pulse monitors spin dynamics in the second Fe layer which serves as the spin collector (C) (see Figure 8.1). Depending on the mutual orientation of the magnetizations $\vec{M}_E$ and $\vec{M}_C$, laser-induced spin current (SC) can lead to the absolute changes of the magnetization $\Delta|\vec{M}_C|$ (incoherent dynamics) or even drive its precessional motion via the spin transfer torque (STT) mechanism.

In the first section it will be demonstrated that it is possible to realize different mutual orientations of the magnetizations $\vec{M}_E$, $\vec{M}_C$ in the spin-emitter and the spin-collector. Then we will discuss the temporal profile of the SC flowing from the spin-emitter to the spin-collector. In **Chapter 7** it has been suggested that the mSHG is sensitive not only to the magnetization dynamics at the interfaces, but also to the SC flowing through the multilayer (ML) structure. Due to a more various set of possible magnetic configurations in three-layer Fe/Au/Fe/MgO(001) than in two-layer Au/Fe/MgO(001) structures, the measured mSHG response provides clear and doubtless evidence for the appearance of the SC-induced SH contribution.

In the final section of this chapter, different types of the magnetization dynamics, induced in the spin-collector, will be demonstrated upon the analysis of the MOKE data. Changing the direction of the external magnetic field $\vec{H}_{ext}$, we can disentangle coherent magnetization dynamics driven by the laser-induced heating and the STT. Owing to more inhomogeneous spatial profile of the STT, the laser-induced SC can excite higher spin wave modes than the laser-induced heating.

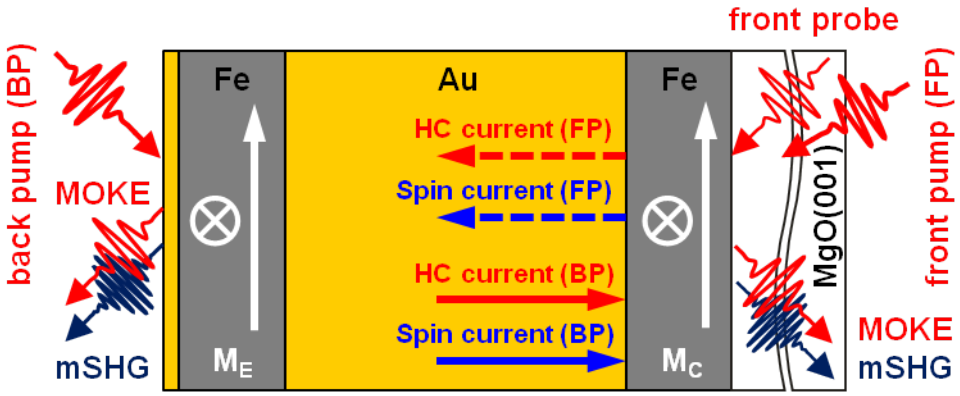

Figure 8.1: Experimental scheme for pump-probe measurements performed on three-layer Au/Fe/Au/Fe/MgO(001) structures. When two Fe films have different coercitivities, it is possible to align their magnetizations collinear or orthogonal to each other. In order to demonstrate the appearance of the HC-current- and SC-induced SH fields, experimental results obtained in the back-pump(BP)-front-probe scheme was compared with those obtained in the front-pump(FP)-front-probe scheme.

8.1 Magnetic configurations

Transparent MgO substrate and thin Au cap layer provide optical access from both sides of three-layer Fe/Au/Fe/MgO(001) structures. All experimental results presented in this chapter were obtained in the configuration shown in Figure 8.1: the back pump was applied from the side of the top Fe film (spin emitter) capped with a thin Au layer, and the front probe monitored HC and magnetization dynamics from the side of the bottom Fe film (spin collector) through the MgO substrate [1].

Measuring reflected pump and probe signals, it is possible to identify directions of the magnetizations $\vec{M}_E$, $\vec{M}_C$ in the spin emitter and the spin collector, respectively. Figure 8.2 shows hysteresis loops measured versus transversal magnetic field $\vec{H}_T||\hat{y}$ (The plane of incidence is set to (x,z)) simultaneously for both Fe layers by the mSHG and the MOKE, which are sensitive to M_y and M_x, respectively. Samples were oriented in a such way, that $\hat{x}$ and $\hat{y}$ directions correspond to the easy axes of the Fe films. In the absence of the bias magnetic field applied in the longitudinal direction $\vec{H}_L||\hat{y}$, $\vec{M}_E$ and $\vec{M}_C$ switch abruptly from the up-state to the down-state and back to the up-state, indicating single domain states of the ferromagnetic layers. For $H_L \neq 0$, $\vec{M}_E$ and $\vec{M}_C$ flip through the intermediate state corresponding to the horizontal easy axis, which results in plateaus. The sign of H_L determines the sign of the $y-$projections of $\vec{M}_E$ and $\vec{M}_C$, while the width of the plateaus depend on $|H_L|$. Values for H_L were chosen in a such way that it is possible to realize all 16 mutual orientations of $\vec{M}_E$ and $\vec{M}_C$.

[1] In the inverted sample orientation we observed similar laser-induced magnetization dynamics.

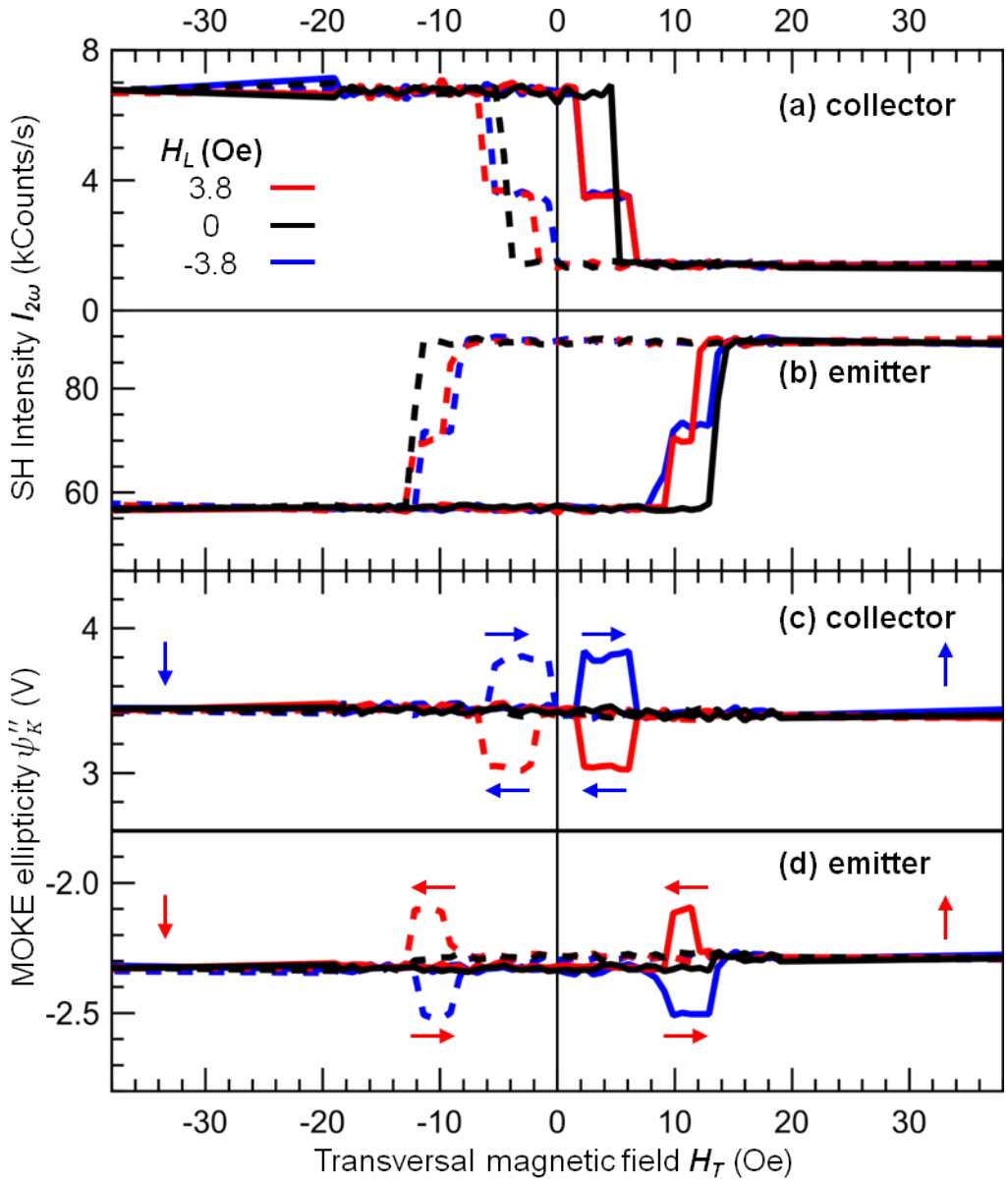

Figure 8.2: Hysteresis loops in the SH (a, b) and MOKE ellipticity (c, d) signals measured simultaneously on 5nm-Au/16nm-Fe/55nm-Au/15nm-Fe/MgO(001) structure. Hysteresis loops (a) and (c) were measured probing the 15-nm Fe layer through the MgO substrate, while hysteresis loops (b) and (d) were measured probing 16-nm Fe layer through the 5-nm Au cap layer. In the latter case the role of the 'probe' pulse was played by the back pump pulse. Different colours of the curves correspond to different bias fields H_L applied in the longitudinal direction and forward (- to +) and backward (+ to -) branches of the hysteresis loops. Red and blue arrows depict magnetization states of the 16-nm and 15-nm Fe layers at certain points on the hysteresis loops, respectively.

8.2 Spin current

Laser excitation of the Fe film leads to the HC current and SC flowing through the Au layer (see **Chapter 7**). It is similar to conventional spin Seebeck effect [152], but in our case the spin transfer is dominated by non-equilibrium HCs. Unlike the MOKE, the mSHG is sensitive not only to the transient magnetization, but also to the spin current. However, it requires some effort to disentangle these two contributions.

Probing sample with the p-polarized probe and measuring p-polarized SH component in the transversal (T:↑↓) and longitudinal (L:→←) magneto-optical geometries with respect to $\vec{M}_C$, we can evaluate the even (non-magnetic) $\vec{E}_{2\omega}^{even}$ and odd (magneto-induced) $\vec{E}_{2\omega}^{odd}$ SH fields, and the phase difference between them $\phi_{2\omega}$:

$$E_{2\omega}^{even} = \sqrt{\frac{I_{2\omega}^{\rightarrow} + I_{2\omega}^{\leftarrow}}{2}}, \tag{8.1}$$

$$E_{2\omega}^{odd} = \sqrt{\frac{I_{2\omega}^{\uparrow} + I_{2\omega}^{\downarrow}}{2} - \frac{I_{2\omega}^{\rightarrow} + I_{2\omega}^{\leftarrow}}{2}}, \tag{8.2}$$

$$\cos\phi_{2\omega} = \frac{I_{2\omega}^{\uparrow} - I_{2\omega}^{\downarrow}}{4 \cdot |E_{2\omega}^{even}| \cdot |E_{2\omega}^{odd}|}. \tag{8.3}$$

In the back-pump-front-probe experiments, we did not observe significant variations of the phase difference $\phi_{2\omega}$ and one can use its static value $\phi_{2\omega,0}$ to derive the odd SH field:

$$E_{2\omega}^{odd} = \frac{I_{2\omega}^{\uparrow} - I_{2\omega}^{\downarrow}}{\sqrt{8(I_{2\omega}^{\rightarrow} + I_{2\omega}^{\downarrow})}\cos\phi_{2\omega,0}}. \tag{8.4}$$

In the static regime, there is neither HC current nor SC, therefore $\vec{E}_{2\omega}^{even}$ and $\vec{E}_{2\omega}^{odd}$ originate from the interface dipole polarization [2]:

$$P_{i,2\omega} = \chi_{ijk}^{(2)} E_{j,\omega} E_{k,\omega} + \chi_{ijk,l}^{(3,m)} E_{j,\omega} E_{k,\omega} M_{C,l}, \tag{8.5}$$

where $i,\ j,\ k = x, z$, and $\chi_{ijk,l}^{(3,m)}$ is a pseudo-tensor with respect to the last index. In **Chapter 7** we discussed that after the laser excitation there are additional current-induced $\chi_{ijkz}^{(3)} E_{j,\omega} E_{k,\omega} j_z$ and SC-induced $\chi_{ijkz,l}^{(4,SC)} E_{\omega,j} E_{\omega,k} j_{z,l}^{S}$ contributions. The tensors $\chi_{ijkz}^{(3)} j_z$ and $\chi_{ijkz,l}^{(4,SC)} j_{z,l}^{S}$ have exactly the same symmetry and non-zero components as the interface terms $\chi_{ijk}^{(2)}$ and $\chi_{ijk,l}^{(3,m)} M_{C,l}$, respectively. Thus the mSHG gives us a direct access to the SC flowing through the metallic multilayer structure, which is demonstrated in the analysis of the pump-induced variations of the even $\delta E_{2\omega}^{even}(t)$ and odd $\delta E_{2\omega}^{odd}(t)$ SH fields, measured for different mutual alignments of the magnetizations $\vec{M}_E$ and $\vec{M}_C$ (see Figure 8.3).

[2] In [150] it was shown that in Au the bulk quadrupole contribution is small in comparison with the surface dipole one.

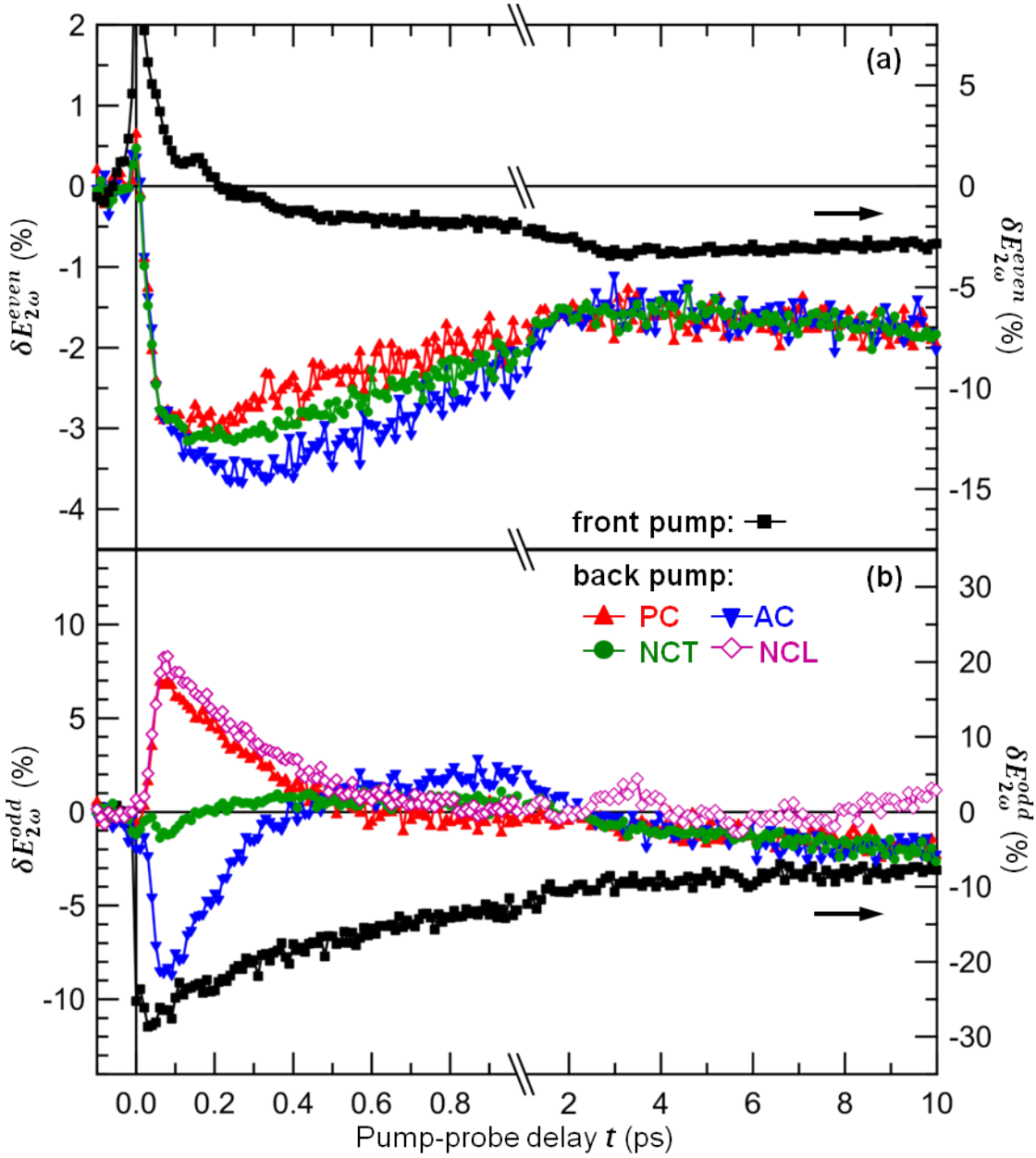

Figure 8.3: Relative variations of the (a) even $\delta E_{2\omega}^{even}$ and (b) odd $\delta E_{2\omega}^{odd}$ mSHG components, measured on the Fe/Au/Fe/MgO(001) structure with the 16-nm top Fe layer as the spin-emitter (E), the 15-nm bottom Fe layer as the spin-collector (C) and the 55-nm Au spacer. Front pump (black squares). Back pump: PC - parallel collinear alignment of the magnetizations $\vec{M}_E$ and $\vec{M}_C$ (red up-triangles), AC - antiparallel collinear alignment (blue down-triangles), NCT - non-collinear transversal alignment with the static $\vec{M}_{C,0} \| \hat{y}$ (green circles), NCL - non-collinear longitudinal alignment with the static $\vec{M}_{C,0} \| \hat{x}$ (empty violet diamonds).

In the front-pump-front-probe geometry, we observe rapid positive (negative) variations of the even SH field $E_{2\omega}^{even}$ (the odd SH field $E_{2\omega}^{odd}$). Switching to the back-pump-front-probe geometry with $\vec{M}_E$ parallel to $\vec{M}_C$, we reverse the velocity of the majority electrons $\vec{v}_{e\uparrow}$ thereby changing the sign of j_z and $j_{z,y}^S$. As a result, rapid variations of both $\delta E_{2\omega}^{even,PC}(t)$ and $\delta E_{2\omega}^{odd,PC}(t)$ have opposite signs with respect to the front-pump-front-probe scheme. If we reverse $\vec{M}_E$, it becomes anti-parallel to $\vec{M}_C$ and leads to the sign change of $j_{z,y}^S$, but not of j_z. In Figure 8.3 it can be seen that the rapid variations of the even SH field in the PC and AC geometries $\delta E_{2\omega}^{even,PC}(t)$ and $\delta E_{2\omega}^{even,AC}(t)$ are the same, while the rapid variations of the odd SH field $\delta E_{2\omega}^{odd,PC}(t)$ and $\delta E_{2\omega}^{odd,AC}(t)$ have opposite signs. If we set $j_{z,y}^S = 0$ by the alignment of $\vec{M}_E$ along $\hat{x}$ (NCT geometry in Figure 8.3), there are no strong variations of $\delta E_{2\omega}^{odd}(t)$, because the SC-induced contribution $E_{2\omega}^{SC} = 0$. It indicates the dominant role of $E_{2\omega}^{SC}$ at short pump-probe delays. Finally, if we align $\vec{M}_C$ along $\hat{x}$ and $\vec{M}_E$ along $\hat{y}$ (NCL geometry), the static odd SH field $E_{2\omega,0}^{odd,NCL} = 0$ [3], meaning that only the SC-induced term contributes to $\delta E_{2\omega}^{odd,NCL}(t)$ which in turn gives us the temporal profile of the SC pulse.

With the above qualitative consideration we demonstrate sensitivity of the mSHG to the HC flux and SC. In order to analyze the data in more details, we suggest the following structure of the mSHG response:

$$\delta E_{2\omega}^{even,g}(t) = -J_+(t) + \beta_{even}^g J_-(t) + \gamma_{even}^g Q(t) - \eta_{even}^g H_{even}(t), \tag{8.6}$$

$$\delta E_{2\omega}^{odd,g}(t) = \alpha_{odd}^g J_+^S(t) + \beta_{odd}^g J_-^S(t) + \gamma_{odd}^g S_g(t) - \eta_{odd}^g H_{odd}(t), \tag{8.7}$$

where $g = PC, AC, NCT, NCL$ denotes a geometry. The current- and SC-induced contributions from HC moving towards the collector are described by $J_+(t)$ and $J_+^S(t)$ which are given by the convolution of $j_z(z,t)$ and $j_z^S(z,t)$, respectively, with the effective depth sensitivity of the mSHG within the Au layer. Similarly, $J_-(t)$ and $J_-^S(t)$ correspond to the HC flux and SC reflected from the Au/Fe interface. HCs, which penetrate into the spin-collector, modify the effective interface contribution charging the Fe film behind the interface and altering $M_{C,y}$. Influence of these processes on $\delta E_{2\omega}^{even}(t)$ and $\delta E_{2\omega}^{odd}(t)$ is described by $Q(t)$ and $S_g(t)$, respectively. Since $J_+^S(t)$ is determined only by the HC emission from the spin-emitter into the Au layer and the orientation of $\vec{M}_E$, $\alpha_{odd}^{PC} = \alpha_{odd}^{NCL} = -\alpha_m^{AC} = -1$ and $\alpha_{odd}^{NCT} = 0$, while $\beta_{even/odd}^g$ and $\gamma_{even/odd}^g$ depend on the transmission $T_{Au\to Fe}$ through the Au/Fe interface (see Figure 8.4) and hence on the mutual orientation of $\vec{M}_E$ and $\vec{M}_C$. The Au/Fe interface heating by the HC impact (fast) and heat diffusion (slow) is described by $H_{even}(t)$, and $H_{odd}(t)$ corresponds to $\Delta M_{C,y}$ induced by this heating. We assume fast relaxation of $S_{g\neq L}(t)$ and $Q(t)$ and $\eta_{even/odd}^{PC} = \eta_{even/odd}^{AC} = \eta_{even/odd}^{NCT} = 1$, because the corresponding curves in Figure 8.3 merge together at $t > 2$ ps. At the same time $\eta_{odd}^{NCL} = 0$, because $E_{2\omega,0}^{NCL} = 0$.

[3] For the normalization we used the amplitude of the static odd SH field, obtained in the geometries with $\vec{M}_C \| \hat{y}$.

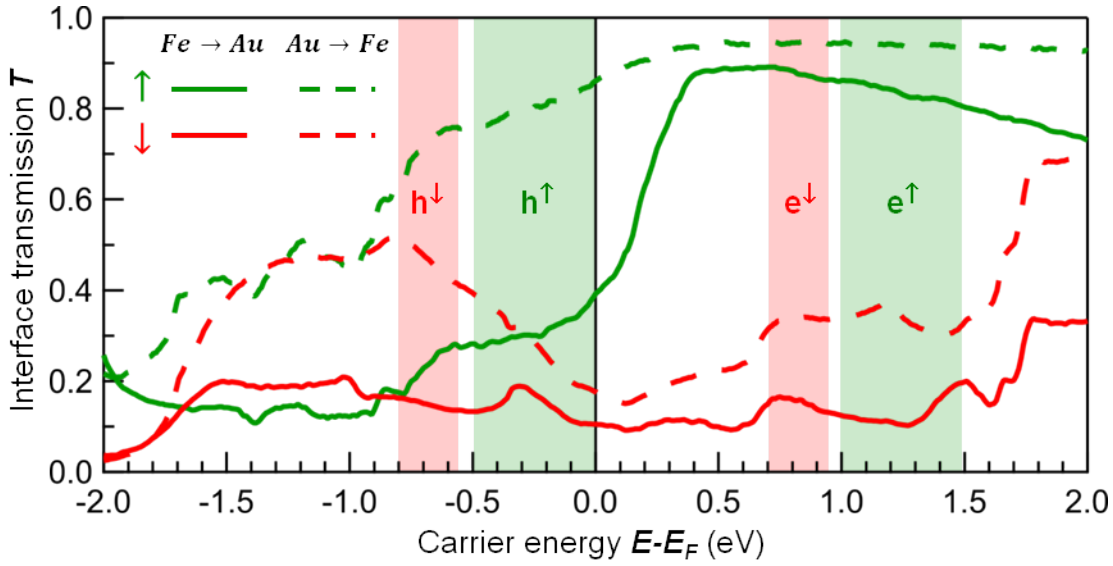

Figure 8.4: Energy-resolved k-averaged transmission of the Fe/Au interface calculated for majority (↑ - green lines) and minority (↓ - red lines) carriers moving from Fe to Au (solid lines) and from Au to Fe (dash lines). Shaded regions depict the energy ranges of the optically excited HCs in Fe [106]. First principle quantum transport calculations for the Fe/Au structure were performed by I. Rungger, M. Stamenova and S. Sanvito.

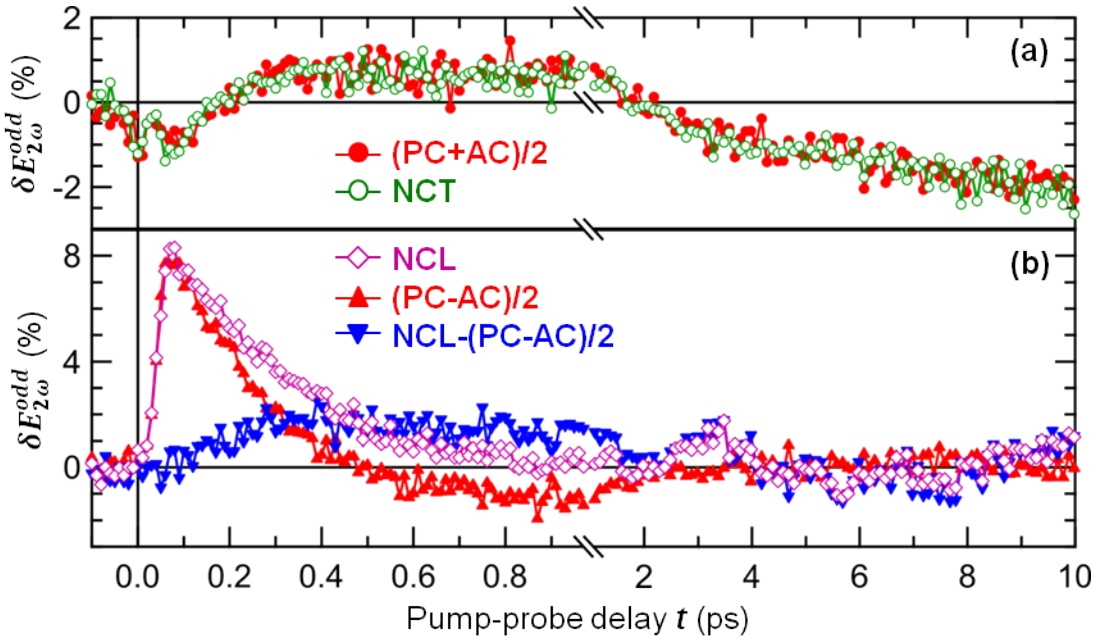

Figure 8.5: Relative variations of the odd SH field $\delta E_{2\omega}^{odd}(t)$: (b) $(PC + AC)/2$ (red circles), NCT (empty green circles), (c) NCL (empty violet diamonds), $(PC - AC)/2$ (red up-triangles), $NCL - (PC - AC)/2$ (blue down-triangles).

In the NCL geometry where $\vec{M}_{C,0} = (M_{C,x}, 0, 0)$, the laser-induced SC $j^S_{z,y}$ results in $\vec{M}_C = (M_{C,x}, \Delta M_{C,y}, 0)$ followed by a precession of $\vec{M}_C$ around $\hat{x}$ axis. This leads to an oscillatory behaviour of $S_L(t)$ observed in $\delta E^{NCL}_{2\omega}$ at larger pump-probe delays. This precessional dynamics of $\vec{M}_C$ is more clearly pronounced in the MOKE signals on a much longer time scale (up to 500 ps), which will be discussed in the next section. The STT produced by the SC pulse with the spin polarization (SP) $\vec{\sigma}_{SC} \perp \vec{M}_C$ leads to the excitation of several lowest standing spin wave modes in the spin-collector. The interference of these modes is quite complex at short delays where higher modes are strong and the precessional dynamics still develops. From the data shown in Figures 8.3(b) and 8.5, one can see that the amplitude $S_L(t)$ is on the order of 0.01 or $\Delta M_{C,y} \approx 0.01 M_{C,x}$.

Now let us focus on the HC reflection/transmission at the Au/Fe interface. In Figure 8.5 one can see that $\delta E^{even/odd,NCT}_{2\omega}(t) = (\delta E^{even/odd,PC}_{2\omega}(t) + \delta E^{even/odd,AC}_{2\omega}(t))/2$ within the scattering of the experimental data. Reflected HC flux $J_-(t)$ and SC $J^S_-(t)$ are proportional to the incoming HC flux, while $Q(t)$ and $S_g(t)$ are rather proportional to the integral of this flux convolved with some sort of decay. So $J_-(t) \neq Q(t)$ and $J^S_-(t) \neq S_g(t)$. This brings us to the relations:

$$\beta^{NCT}_{even/odd} = \frac{\beta^{PC}_{even/odd} + \beta^{AC}_{even/odd}}{2} \text{ and } \gamma^{NCT}_{even/odd} = \frac{\gamma^{PC}_{even/odd} + \gamma^{AC}_{even/odd}}{2}. \tag{8.8}$$

Regarding the current-induced SH components, (8.8) can be rewritten as

$$T^{\perp}_{Au\to Fe} = \frac{T^{\uparrow}_{Au\to Fe} + T^{\downarrow}_{Au\to Fe}}{2}, \tag{8.9}$$

where $T^{\uparrow}_{Au\to Fe}$, $T^{\downarrow}_{Au\to Fe}$ and $T^{\perp}_{Au\to Fe}$ are the interface transmissions for $\vec{\sigma}_e \uparrow\uparrow \vec{M}_C$, $\vec{\sigma}_e \downarrow\uparrow \vec{M}_C$, and $\vec{\sigma}_e \perp \vec{M}_C$ in the PC, AC, and NCT geometries, respectively. Regarding the SC-induced SH components the situation is more complex. In the PC and AC geometries $\vec{\sigma}_{SC}$ does not change upon the reflection/transmission. If this is also the case in the NCT geometry, where $\vec{M}_E = (M_{E,x}, 0, 0)$ and $\vec{M}_{C,0} = (0, M_{C,y}, 0)$, then for the reflected SC $j^S_{z,y}(t) = 0$ and the transmitted HCs do not affect $M_{C,y}$, i.e. $\beta^{NCT}_{odd} = 0$ and $\gamma^{NCT}_{odd} = 0$. From (8.8) we get that $\beta^{AC}_{odd} = -\beta^{PC}_{odd}$ and $\gamma^{AC}_{odd} = -\gamma^{PC}_{odd}$. This can be true only under the condition $T^{\uparrow}_{Au\to Fe} = T^{\downarrow}_{Au\to Fe}$, which contradicts with the results of the first principle quantum transport calculations (see Figure 8.4). In addition to that, demagnetization of the spin-collector alone cannot provide $\delta E^{odd,NCT}_{2\omega}(t) > 0$ at 0.2 ps $< t <$ 2 ps. Thus if $\vec{\sigma}_e \perp \vec{M}_C$ in the incoming HC packet, $\vec{\sigma}_e$ must change upon the reflection/transmission at the Au/Fe interface.

Let us consider the NCT geometry with $\vec{M}_E = (M_{E,x}, 0, 0)$ and $\vec{M}_{C,0} = (0, M_{C,y}, 0)$ in more detail. Upon the HC emission from the spin-emitter, the spin quantization axis is set by $\vec{M}_E$, which means that $\sigma_{e,x}$ is defined and $\sigma_{e,y}$ oscillates. As a result, hot electron reaches the spin-collector with random $\sigma_{e,y}$and in the incoming SC $j^S_{z,y} = 0$, because the average projection $< \sigma_{e,y} >= 0$. When an electron with defined $\sigma_{e,x}$ and random $\sigma_{e,y}$ penetrates into the Fe film which serves as a thermostat for σ, the new quantization axis is along $\hat{y}$. So $\sigma_{e,y}$ becomes defined and $\sigma_{e,x}$ becomes random within

the characteristic time of the quantum spin decoherence. The angular momentum is absorbed by the thermostat, which leads to $\vec{M}_C = (\Delta M_{C,x}, M_{C,y}, 0)$. In other words, HC spins orthogonal to $\vec{M}_C$ rotate with equal probability towards the up- and down-states with respect to $\vec{M}_C$ and are transmitted through and reflected from the interface in accordance with $T^{\uparrow\downarrow}_{Au\to Fe}$. This leads to $j^S_{z,y} \neq 0$ in the reflected SC and non-zero variation of $M_{C,y}$, and fulfils the relations (8.8). Both β^{NCT}_{odd}, $\gamma^{NCT}_{odd} > 0$ ($T^{\uparrow}_{Au\to Fe} > T^{\downarrow}_{Au\to Fe}$), which explains $\delta E^{NCT}_{odd}(t) > 0$ at 0.2 ps $< t <$ 2 ps.

In Figure 8.5 we reproduce $\delta E^{odd,NCL}_{2\omega}(t)$ together with

$$\delta E^{odd,PA}_{2\omega}(t) = \frac{\delta E^{odd,PC}_{2\omega}(t) - \delta E^{odd,AC}_{2\omega}(t)}{2} \tag{8.10}$$

and

$$\delta E^{odd,LPA}_{2\omega}(t) = \delta E^{odd,NCL}_{2\omega}(t) - \delta E^{odd,PA}_{2\omega}(t). \tag{8.11}$$

From the above considerations, $\beta^{NCL}_{odd} = 0$, $\eta^{NCL}_{odd} = 0$, $\alpha^{NCL}_{odd} = 1$, and $\gamma^{NCL}_{odd} = 1$, because $\sigma_{e,y}$ completely transfers into $\Delta M_{C,y}$. Thus

$$\delta E^{odd,NCL}_{2\omega}(t) = J^S_+(t) + S_{NCL}(t) \tag{8.12}$$

provides the temporal profile of the direct SC pulse, modulated by the oscillations of $S_{NCL}(t)$ with the amplitude ~ 1 %. The direct SC pulse has a sharp front with a maximum at about 70 fs after the pump pulse. It gives the HC velocity in gold $v_{Au} \approx 0.8\, nm/fs$, which is between the velocities of the optically excited and secondary electrons $v_{Au1} = (1.06 \pm 0.07)\ nm/fs$ and $v_{Au2} = (0.6 \pm 0.4)\ nm/fs$ (see **Chapter 7**). Then $\delta E^{odd,NCL}_{2\omega}(t)$ decays with the time constant $\tau_{SC} = (306 \pm 14)\ fs$, which is comparable to the characteristic time of the electron equilibration between the Fe and Au films 0.56 ± 0.03 ps, obtained in the experiments on two-layer Au/Fe/MgO(001) structures (see **Chapter 7**). Using $\alpha^{PC}_{odd} = 1$, $\alpha^{AC}_{odd} = -1$, and $\eta^{PC}_{odd} = \eta^{AC}_{odd}$, we derive

$$\delta E^{odd,PA}_{2\omega}(t) = J^S_+(t) + \frac{\beta^{PC}_{odd} - \beta^{AC}_{odd}}{2} J^S_-(t) + \frac{\gamma^{PC}_{odd} - \gamma^{AC}_{odd}}{2} S_{PC}(t), \tag{8.13}$$

where the heating-induced demagnetization of the spin-collector $H_{odd}(t)$ is subtracted, and only the influence of the SC pulse is left. Since $\beta^{AC}_{odd} > 0$, $\beta^{PC}_{odd} < 0$, $\gamma^{PC}_{odd} > 0$, $\gamma^{AC}_{odd} < 0$, and at short delays $S_{NCL}(t)$ should behave similar to $S_{PC}(t)$,

$$\delta E^{odd,LPA}_{2\omega}(t) = \frac{\beta^{PC}_{odd} - \beta^{AC}_{odd}}{2} J^S_-(t) + S_{NCL}(t) - \frac{\gamma^{PC}_{odd} - \gamma^{AC}_{odd}}{2} S_{PC}(t) \tag{8.14}$$

should resemble the temporal profile of the reflected SC pulse. Its front is not so sharp as that of the direct SC pulse, because some part of the incoming HCs are transmitted into the spin-collector and the reflected HCs have smaller velocity projection $|v_{e,z}|$ than the incoming ones.

Summarizing, it has been demonstrated that the mSHG is sensitive to the SC flowing through the metallic multilayer structure. The mSHG data obtained on three-layer Fe/Au/Fe/MgO(001) structures are consistent with those obtained on two-layer

Au/Fe/MgO(001) probing the Au surface (see **Chapter 7**). The temporal profile of the laser-induced SC is determined by the HC flux through the interface between the spin-emitter and the non-magnetic layer. The SC pulse consists of the optically excited electrons, leaving the Fe film in the ballistic regime, and the secondary electrons, which provide a net flux of the positive SP through the Fe/Au interface as long as the electron temperature in Fe is larger than in Au. The major difference between the experiments performed on Fe/Au/Fe/MgO(001) and Au/Fe/MgO(001) structures is that the HC reflection from the clean Au surface is spin-independent, while the Au/Fe interface transmits more effectively the majority electrons $e^{\uparrow}$ with respect to $\vec{M}_C$ than the minority ones (see Figure 8.4).

8.3 Magnetization dynamics

Unlike the mSHG, the MOKE is exclusively sensitive to the magnetization. Figure 8.6 presents the absolute variations of the MOKE rotation $\Delta\psi'_K$ and ellipticity $\Delta\psi''_K$ measured on a three-layer 5nm-Au/16nm-Fe(E)/55nm-Au/15nm-Fe(C)/MgO(001) structure for magnetic configurations, where the static magnetizations $\vec{M}_E||\hat{y}$ and $\vec{M}_C||\hat{x}$. Both $\Delta\psi'_K$ and $\Delta\psi''_K$ exhibit various dynamics, which includes precession of the magnetization $\vec{M}_C$ in the spin-collector, demagnetization induced by the HC injection and non-magnetic effects affecting the MOKE signals. In terms of the HC transport all orthogonal magnetic geometries are identical to each other, meaning that changes of the magnetization magnitude $\Delta|\vec{M}_C|$ are the same. Thus linear combinations of $\Delta\psi'_K$ and $\Delta\psi''_K$ measured in the orthogonal magnetic configurations $\vec{M}_E \perp \vec{M}_C$ allow us to disentangle coherent (precession) and incoherent (demagnetization) contributions to the magnetization dynamics, which will be discussed in the following subsections.

8.3.1 Incoherent dynamics

Figure 8.7 presents pump-induced relative variations of the MOKE rotation $\delta\psi'_K(t)$, ellipticity $\delta\psi''_K(t)$ and the linear reflectivity $\delta R(t)$ measured on the 5nm-Au/16nm-Fe(E)/55nm-Au/15nm-Fe(C)/MgO(001) structure for parallel collinear (PCL), antiparallel collinear (ACL) and non-collinear (NCL) magnetic configurations, where the static magnetization $\vec{M}_C\|\hat{x}$. In the PCL and ACL magnetic geometries the relative variations of the MOKE signals are given by:

$$\delta\psi'_{K,PCL}(t) = \frac{\Delta\psi'_{K,\leftleftarrows}(t) - \Delta\psi'_{K,\rightrightarrows}(t)}{\psi'_{K,0,\leftleftarrows} - \psi'_{K,0,\rightrightarrows}},\ \delta\psi''_{K,PCL}(t) = \frac{\Delta\psi''_{K,\leftleftarrows}(t) - \Delta\psi''_{K,\rightrightarrows}(t)}{\psi''_{K,0,\leftleftarrows} - \psi''_{K,0,\rightrightarrows}}, \quad (8.15)$$

$$\delta\psi'_{K,ACL}(t) = \frac{\Delta\psi'_{K,\rightleftarrows}(t) - \Delta\psi'_{K,\leftrightarrows}(t)}{\psi'_{K,0,\rightleftarrows} - \psi'_{K,0,\leftrightarrows}},\ \delta\psi''_{K,ACL}(t) = \frac{\Delta\psi''_{K,\rightleftarrows}(t) - \Delta\psi''_{K,\leftrightarrows}(t)}{\psi''_{K,0,\rightleftarrows} - \psi''_{K,0,\leftrightarrows}}, \quad (8.16)$$

where the upper arrow depicts the direction of $\vec{M}_E$, and the lower arrow depicts the direction of $\vec{M}_C$, if one looks at the sample from the side of the probe pulse (see

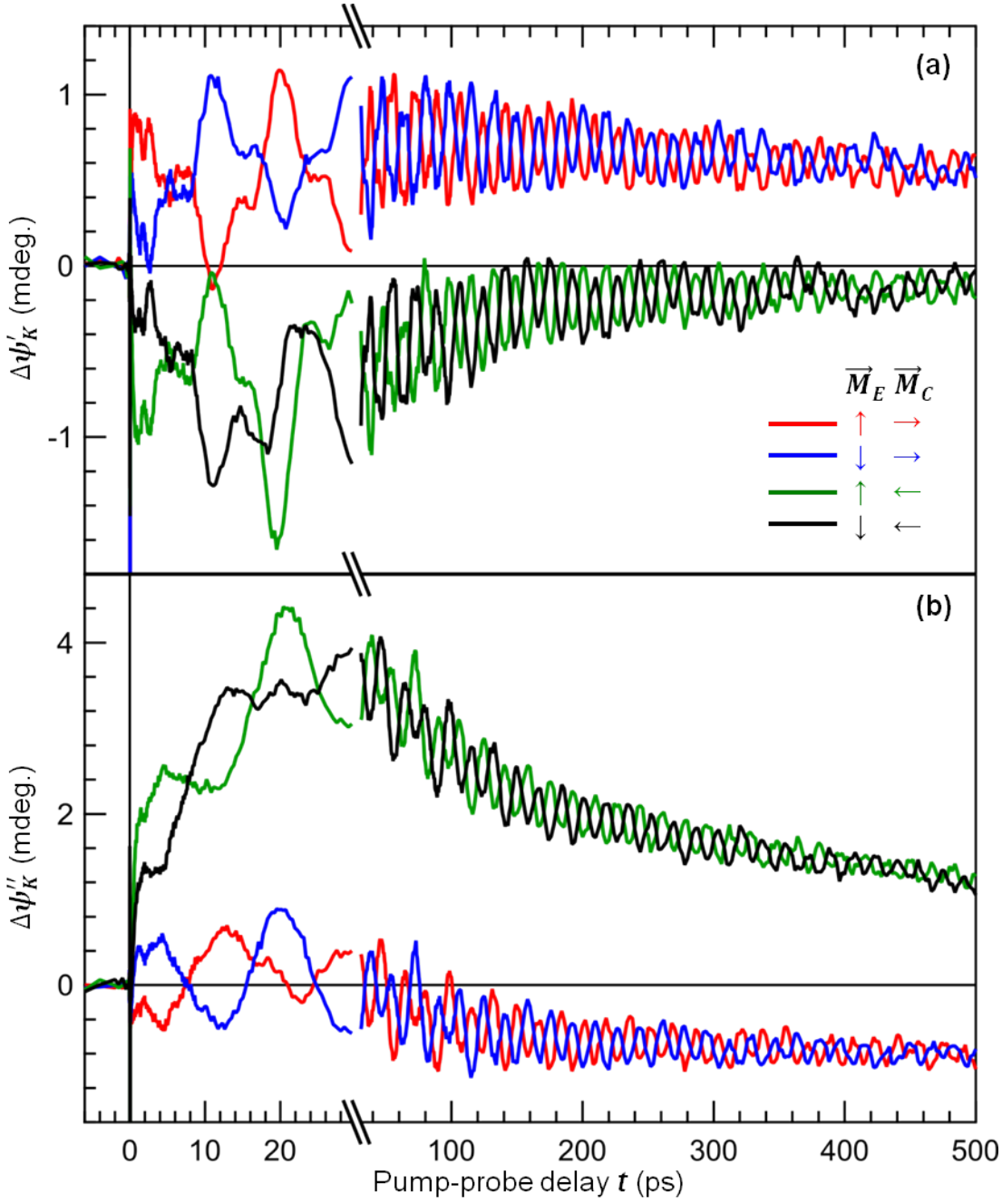

Figure 8.6: Absolute variations of the MOKE rotation $\Delta\psi'_K$ (a) and ellipticity $\Delta\psi''_K$ measured on 5nm-Au/16nm-Fe(E)/55nm-Au/15nm-Fe(C)/MgO(001) for magnetic configurations, where the static magnetization $\vec{M}_C$ of the spin-collector lies in the plane of incidence, and the static magnetization $\vec{M}_E$ of the spin-emitter is perpendicular to it. Arrows depict directions of the magnetizations, if one looks at the sample from the side of the probe pulse. Pump fluence was about 10 mJ/cm^2.

Figure 8.1). So '←' corresponds to the magnetic configuration, when the wave-vector of the incident probe pulse has positive projection on the magnetization vector. In the NCL magnetic geometry, demagnetization is given by:

$$\begin{aligned}\delta\psi'_{K,NCL}(t) &= \frac{\Delta\psi'_{K,\uparrow\leftarrow}(t) + \Delta\psi'_{K,\downarrow\leftarrow}(t) - \Delta\psi'_{K,\uparrow\rightarrow}(t) - \Delta\psi'_{K,\downarrow\rightarrow}(t)}{\psi'_{K,0,\uparrow\leftarrow}(t) + \psi'_{K,0,\downarrow\leftarrow} - \psi'_{K,0,\uparrow\rightarrow} - \psi'_{K,0,\downarrow\rightarrow}},\\ \delta\psi''_{K,NCL}(t) &= \frac{\Delta\psi''_{K,\uparrow\leftarrow}(t) + \Delta\psi''_{K,\downarrow\leftarrow}(t) - \Delta\psi''_{K,\uparrow\rightarrow}(t) - \Delta\psi''_{K,\downarrow\rightarrow}(t)}{\psi''_{K,0,\uparrow\leftarrow} + \psi''_{K,0,\downarrow\leftarrow} - \psi''_{K,0,\uparrow\rightarrow} - \psi''_{K,0,\downarrow\rightarrow}},\end{aligned} \tag{8.17}$$

where the first arrow depicts the direction of $\vec{M}_E$, and the second arrow depicts the direction of $\vec{M}_C$.

First of all, it should be noted that in contrast to the experiments performed on two-layer Au/Fe/MgO(001) structures, reflection of the acoustic wave, induced by the extension of the spin-emitter, at the interface between the Au spacer and the spin-collector provides a pronounced feature at about 20 ps not only in $\delta E_{2\omega}^{even}(t)$ (not shown here), but also in $\delta R(t)$ (for comparison see Figure 7.8). The same feature is also present in $\delta\psi'_K(t)$ and $\delta\psi''_K(t)$. Because of the different depth sensitivities of the MOKE rotation and ellipticity (see Figure 8.8(a)), the acoustic feature is more pronounced in $\delta\psi'_K(t)$ than in $\delta\psi''_K(t)$. On a large time scale the magnetization profile in the spin-collector is more or less uniform, and $\delta\psi'_K(t)$ and $\delta\psi''_K(t)$ relax simultaneously. In addition to the acoustic peaks present in $\delta R(t)$, $\delta\psi'_K(t)$ and $\delta\psi''_K(t)$ exhibit longitudinal oscillations of $\vec{M}_C$. Since we observe these oscillations in all geometries, they are probably related to the magneto-acoustic coupling. The main interest of the present work is the HC-driven magnetization dynamics, therefore in this subsection we will focus on small pump-probe delays, where we observe the difference between the MOKE signals measured in the PCL, ACL and NCL geometries.

For 0.04 ps $< t <$ 0.85 ps the curves in Figure 8.7(a) are arranged in the following order: $\delta\psi'^{ACL}_K(t) < \delta\psi'^{NCL}_K(t) < \delta\psi'^{PCL}_K(t) < 0$, while for $t >$ 0.85 ps the order is inverted: $\delta\psi'^{PCL}_K(t) < \delta\psi'^{NCL}_K(t) < \delta\psi'^{ACL}_K(t) < 0$. As for the MOKE ellipticity, there is a distinguishable difference between the PCL, ACL and NCL geometries for 0.04 ps $< t <$ 0.85 ps: $\delta\psi'^{ACL}_K(t) < \delta\psi'^{NCL}_K(t) < \delta\psi'^{PCL}_K(t) < 0$, but it vanishes on a larger time scale. Such behaviour cannot be explained only by a non-uniform magnetization profile, and it indicates an appearance of the contributions to the MOKE signals from the Au layer. When the probe pulse is applied from the Au side of the Au/Fe/MgO(001) structure, contribution from the Au layer to the longitudinal MOKE ellipticity $\psi''^L_K(t)$ is larger than to the longitudinal MOKE rotation $\psi'^L_K(t)$ (see Figure 7.5(a)). However, in agreement with the longitudinal MOKE depth sensitivities in Figure 8.8(a), when Au is probed through the Fe film, $|\psi'^L_{K,Au}| > |\psi''^L_{K,Au}|$. In the PCL geometry $\vec{\sigma}_e \uparrow\uparrow \vec{M}_C$ and $\delta\psi'^{PCL}_{K,Au}(t) > 0$, while in the ACL geometry $\vec{\sigma}_e \downarrow\uparrow \vec{M}_C$ and $\delta\psi'^{PCL}_{K,Au}(t) < 0$.

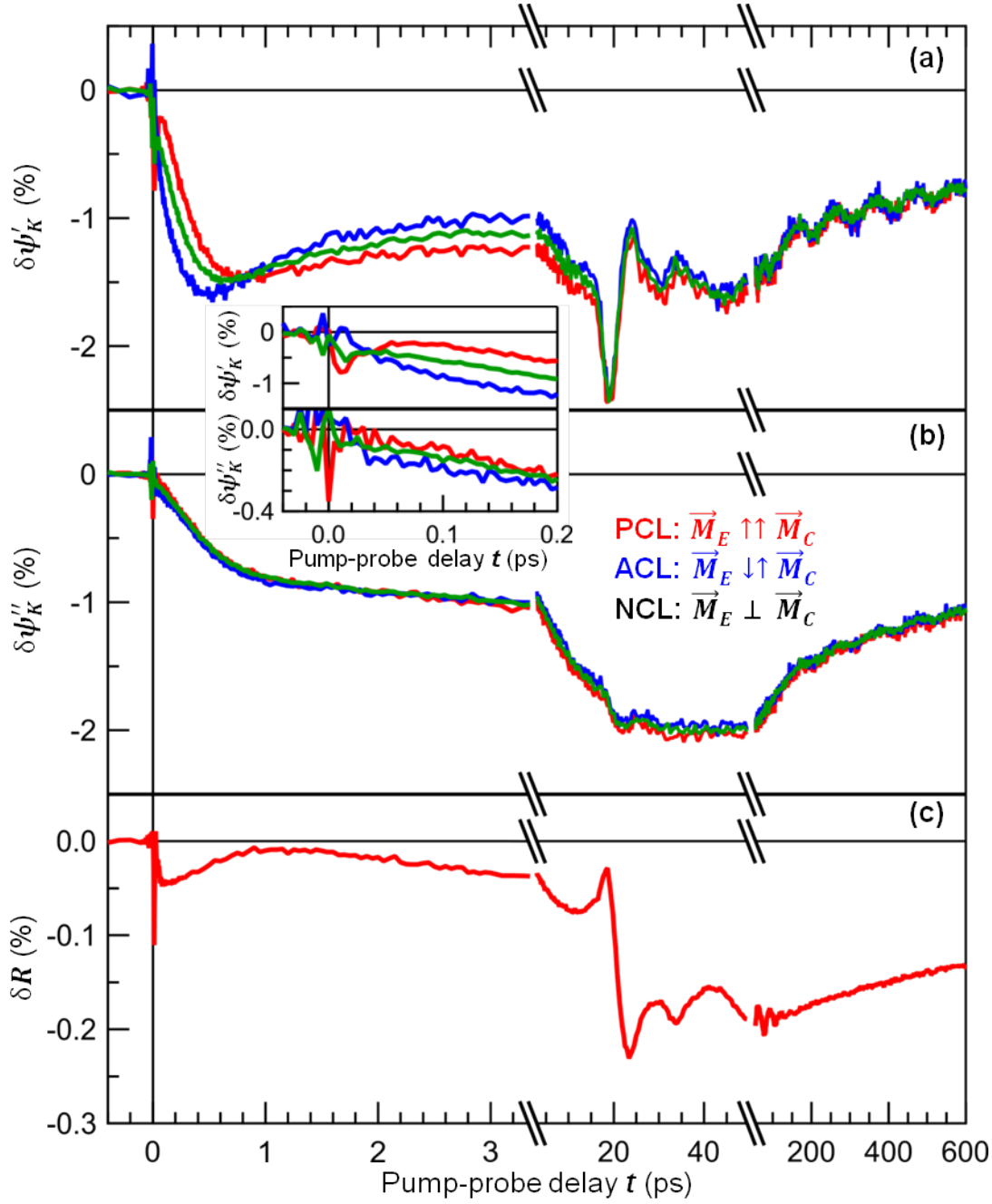

Figure 8.7: Relative variations of the MOKE rotation $\delta\psi'_K$ (a), ellipticity $\delta\psi''_K$ (b), and the linear reflectivity δR measured on 5nm-Au/16nm-Fe(E)/55nm-Au/15nm-Fe(C)/MgO(001) for parallel collinear (PCL-red), antiparallel collinear (ACL-blue), and non-collinear (NCL-green) magnetic configurations, where the static magnetization $\vec{M}_C$ of the spin collector is in the plane of incidence. Pump fluence was about 10 mJ/cm^2. The inset shows $\delta\psi'_K(t)$ and $\delta\psi''_K(t)$ in the vicinity of the time zero.

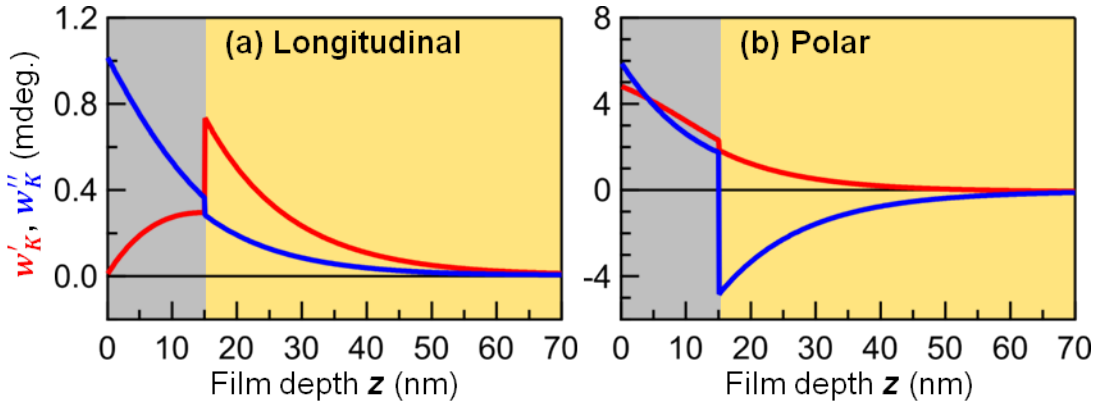

Figure 8.8: Depth sensitivities of the longitudinal (a) and polar (b) MOKE rotation $w'_K(z)$ (red) and ellipticity $w''_K(z)$ (blue), calculated for the 5nm-Au/16nm-Fe(E)/55nm-Au/15nm-Fe(C)/MgO(001) probed from the side of the bottom 15-nm Fe film. For the calculation of the MOKE response from Au, the Voigt constant of gold $q_{Au} \approx 0.094 + 0.035i$ was used (see **Chapters 6** and **7**).

In the ACL geometry majority electrons, injected into the Au layer from the spin-emitter, become minority for the spin-collector, therefore they have small transmission through the Au/Fe interface. Transmitted electrons accumulate in the vicinity of the Au/Fe interface, because of the small mobility of the minority electrons in Fe. Situation is the opposite in the PCL geometry. Majority electrons for the spin-emitter are also majority for the spin-collector: they penetrate into the Fe film much easier than in the ACL geometry and induce stronger demagnetization. As a result, when $\psi'_{K,Au}(t)$ vanishes, $|\delta\psi'_{K,PCL}(t)| > |\delta\psi'_{K,ACL}|$ for $t < 0.8$ ps. In the NCL geometry the SP of the incoming electrons $\vec{\sigma}_e \perp \vec{M}_C$, i.e. $\vec{\sigma}_e \| \hat{y}$. It means that the incoming electrons in Au do not contribute to the MOKE. Since $\delta\psi'_{K,NCL}(t) \approx (\delta\psi'_{K,PCL}(t) + \delta\psi'_{K,ACL}(t))/2$, spins orthogonal to $\vec{M}_C$, arriving at the Au/Fe interface, rotate with equal probabilities into the up- and down-states with respect to $\vec{M}_C$, as it was found in the analysis of the mSHG response. From the difference $(\delta\psi'_{K,PCL}(t) + \delta\psi'_{K,ACL}(t))/2$ we estimated the Au contributions at 0.34 % from the static longitudinal MOKE rotation $\psi'_{K,0} = 43$ *mdeg.* and ellipticity $\psi''_{K,0} = 90$ *mdeg.*, which corresponds to the average magnetization in the probed region of the Au layer $M_{Au} \approx 0.003\ [M_{Fe}] \approx 0.01\ [\mu_B/atom]$ [4]. This value is close to the estimation made in **Chapter 7**.

8.3.2 Coherent dynamics

Amplitude of the STT-induced magnetization precession is proportional to the component of the SC polarized in the perpendicular direction with respect to $\vec{M}_C$. Direction of the precession depends on the mutual orientation of the magnetizations $\vec{M}_E$ and

[4]Here $M_{Fe} = 2.2\ \mu_B/atom$ is the saturation magnetization of Fe. Also it is taken into account that one unit cell of bcc-Fe ($a_{Fe} = 0.287$ nm) contains 2 atoms, while one unit cell of fcc-Au ($a_{Au} = 0.408$ nm) contains 4 atoms.

Contributions	$\vec{M}_C$	$\vec{\sigma}$ ($\vec{M}_E$)	$\vec{H}_{eff}^{\perp}$
Heating-induced	odd	even	odd
STT-induced	even	odd	even
Demagnetization	odd	even	even
Non-magnetic dynamics	even	even	even

Table 8.1: Parity of different contributions to the MOKE signal with respect to the reversal of the magnetization $\vec{M}$, the spin current polarization $\vec{\sigma}$, and the component of the effective magnetic field $\vec{H}_{eff}$ orthogonal to the magnetization $\vec{M}_C$.

$\vec{M}_C$. It can be clearly seen from the Landau-Lifshitz-Gilbert (LLG) equation extended with the STT term:

$$\frac{d\vec{M}}{dt} = -\gamma\left[\vec{M}\times\vec{H}_{eff}\right] + \frac{\alpha}{|\vec{M}|}\left[\vec{M}\times\frac{d\vec{M}}{dt}\right] + \gamma\frac{J_S}{|\vec{M}|}\left[\vec{M}\times[\vec{\sigma}\times\vec{M}]\right], \tag{8.18}$$

Polar and longitudinal MOKE are much larger than the transversal one. For this reason, to study coherent magnetization dynamics, it is more convenient to perform measurements in the NCT magnetic geometry, where the static magnetization of the spin-collector $\vec{M}_C||\hat{y}$, and x (L-longitudinal), z (P-polar) components oscillate (see Figure 8.9):

$$\Delta\psi^{P}_{K,NCT}(t) = \left(\Delta\psi_{K,\leftarrow\uparrow}(t) + \Delta\psi_{K,\rightarrow\downarrow}(t) - \Delta\psi_{K,\rightarrow\uparrow}(t) - \Delta\psi_{K,\leftarrow\downarrow}(t)\right)/4, \tag{8.19}$$

$$\Delta\psi^{L}_{K,NCT}(t) = \left(\Delta\psi_{K,\leftarrow\uparrow}(t) + \Delta\psi_{K,\leftarrow\downarrow}(t) - \Delta\psi_{K,\rightarrow\uparrow}(t) - \Delta\psi_{K,\rightarrow\downarrow}(t)\right)/4. \tag{8.20}$$

When the NCT and NCL magnetic geometries are realized in a single measurement, $\Delta\psi^{P}_{K,NCT}$ almost reproduce $\Delta\psi^{P}_{K,NCL}$, which allow us to limit our consideration only to the NCT geometries.

Laser-induced heating vs Spin Transfer Torque

Before we proceed with the analysis of the STT-induced magnetization dynamics, we have to disentangle it from the dynamics induced by the laser heating, which is related to the change of the effective magnetic field $\vec{H}_{eff}$ (see **Chapter 2**). From (8.18), we can deduce that the heating-induced magnetization precession changes its direction, when the component $\vec{H}_{eff}^{\perp}$ of the effective field, perpendicular to $\vec{M}_C$, changes its sign. At the same time it does not affect the precession induced by the STT. Despite that the reversal of $\vec{H}_{eff}$ increases the total number of the magnetic geometries in a single measurement, it allows us to disentangle all contributions to the observed magnetization dynamics. In Table 8.1 it is summarized how different contributions behave upon the reversal of $\vec{M}_C$, $\vec{M}_E$, and $\vec{H}_{eff}^{\perp}$.

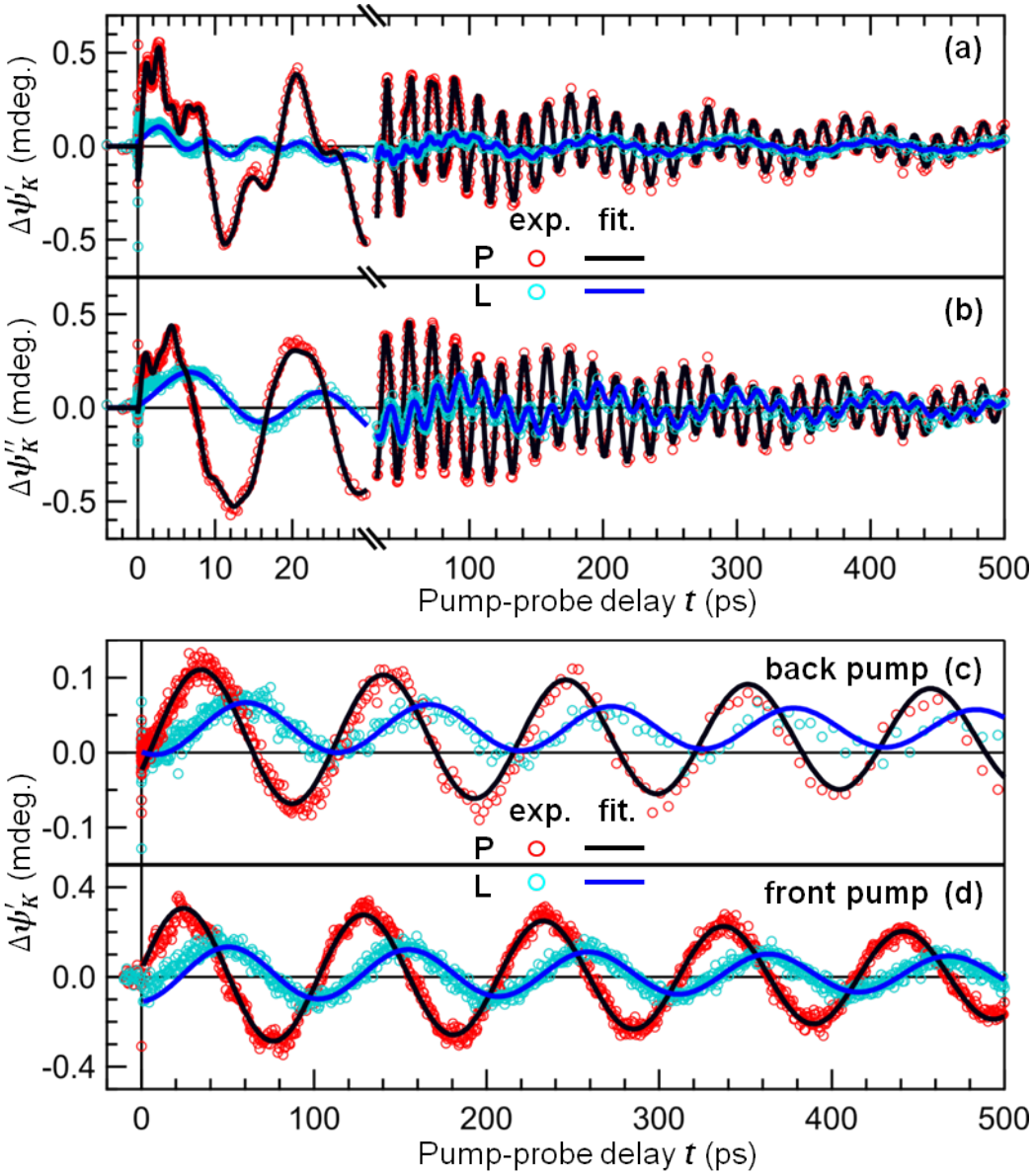

Figure 8.9: Absolute variations of the MOKE rotation $\Delta\psi'_K(t)$ (a, c) and ellipticity $\Delta\psi''_K(t)$ (b, d) due to the oscillations of the polar (P) and longitudinal (L) components of the magnetization $\vec{M}_C$ in the spin-collector, obtained on 5nm-Au/16nm-Fe/55nm-Au/15nm-Fe/MgO(001) structure. (a, b) correspond to the magnetization dynamics induced by the STT, observed in the back-pump-front-probe experiment. (c, d) correspond to the magnetization dynamics induced by the laser heating, observed in the schemes with the back and front pump, respectively.

Figure 8.9 presents the STT- and heating-induced contributions to the coherent magnetization dynamics. Even without any spectral analysis it can be clearly seen that the laser heating leads to the excitation of only the lowest fundamental mode $f_0 = (9.46 \pm 0.01)$ GHz, while the STT drives several modes. The reason is that the heat diffusion occurs on a longer time scale and relatively more homogeneous than the impact of the SC pulse which is absorbed in the spin-collector within several nanometers. Solid lines in Figures 8.9(c) represent the results of the joint fitting procedure, where the longitudinal and polar components are given by the following functions:

$$\Delta\psi_K^L(t) = a_{bg}^L + a_0^L \cdot e^{-t/\tau_0} \cos(2\pi f_0 t + \phi_0), \tag{8.21}$$

$$\Delta\psi_K^P(t) = a_{bg}^P + a_0^P \cdot e^{-t/\tau_0} \sin(2\pi f_0 t + \phi_0). \tag{8.22}$$

The values of the shared parameters $f_0 = 9.46 \pm 0.01$ GHz, $\tau_0 = 1307 \pm 180$ ps, $\phi_0 = -0.484 \pm 0.014$. When we switched to the front-pump-front-probe scheme and performed measurements in the same magnetic geometries, we observed only the heating-induced precession (see Figure 8.9(d)). Its amplitude is larger than for the back-pump-front-probe scheme, because the pump pulse is absorbed directly in the spin-collector. It also explains the phase shift between the precessional dynamics shown in Figures 8.9(c) and (d). Kampen et al. [18] demonstrated that the laser heating is capable to excite two lowest standing spin wave modes in 40-nm permalloy ($Ni_{80}Fe_{20}$) films. But in our case the spin-collector is much thinner (≈ 15.0 nm), and absorption of the pump pulse effectively excites only the lowest fundamental standing spin wave mode (see Figure 8.10(d)).

In the back-pump-front-probe scheme the STT-induced contribution is larger than the heating-induced one. In order to determine the observed frequencies, we have performed complex Fourier transformation of the curves shown in Figures 8.9(a) and (b), multiplied by the Gaussian window function $\exp(-(t-t_0)^2/\tau_w^2)$:

$$A(f, t_0, \tau_w) = \int_{-\infty}^{\infty} \Delta\psi_K(t) \cdot e^{-(t-t_0)^2/\tau_w^2} \cdot e^{-2\pi i f t} dt. \tag{8.23}$$

According to the Fourier spectra $|A(f, t_0, \tau_w)|$ of the polar and longitudinal contributions to the MOKE ellipticity $\Delta\psi_K''(t)$ and rotation $\Delta\psi_K'(t)$ in Figures8.10(a) and (b), the SC pulse, injected into the 15-nm spin-collector, drives at least five lowest spin wave modes. Different ratios between the amplitudes of the corresponding peaks in the spectra for $\Delta\psi_K''(t)$ and $\Delta\psi_K'(t)$ are again related to different depth sensitivities of the polar and longitudinal MOKE ellipticity and rotation (see Figure 8.8). In order to get more accurate values for the spin wave frequencies, the curves in Figures 8.9 were fitted simultaneously with the sums:

$$\Delta\psi_K(t) = a_{bg} + \sum_{l=0}^{4} a_l e^{-t/\tau_l} \cos(2\pi f_l t + \phi_l). \tag{8.24}$$

In the joint fitting procedure only the spin wave frequencies f_l and lifetimes τ_l were shared among all the curves. The magnitude of the external magnetic field, used in

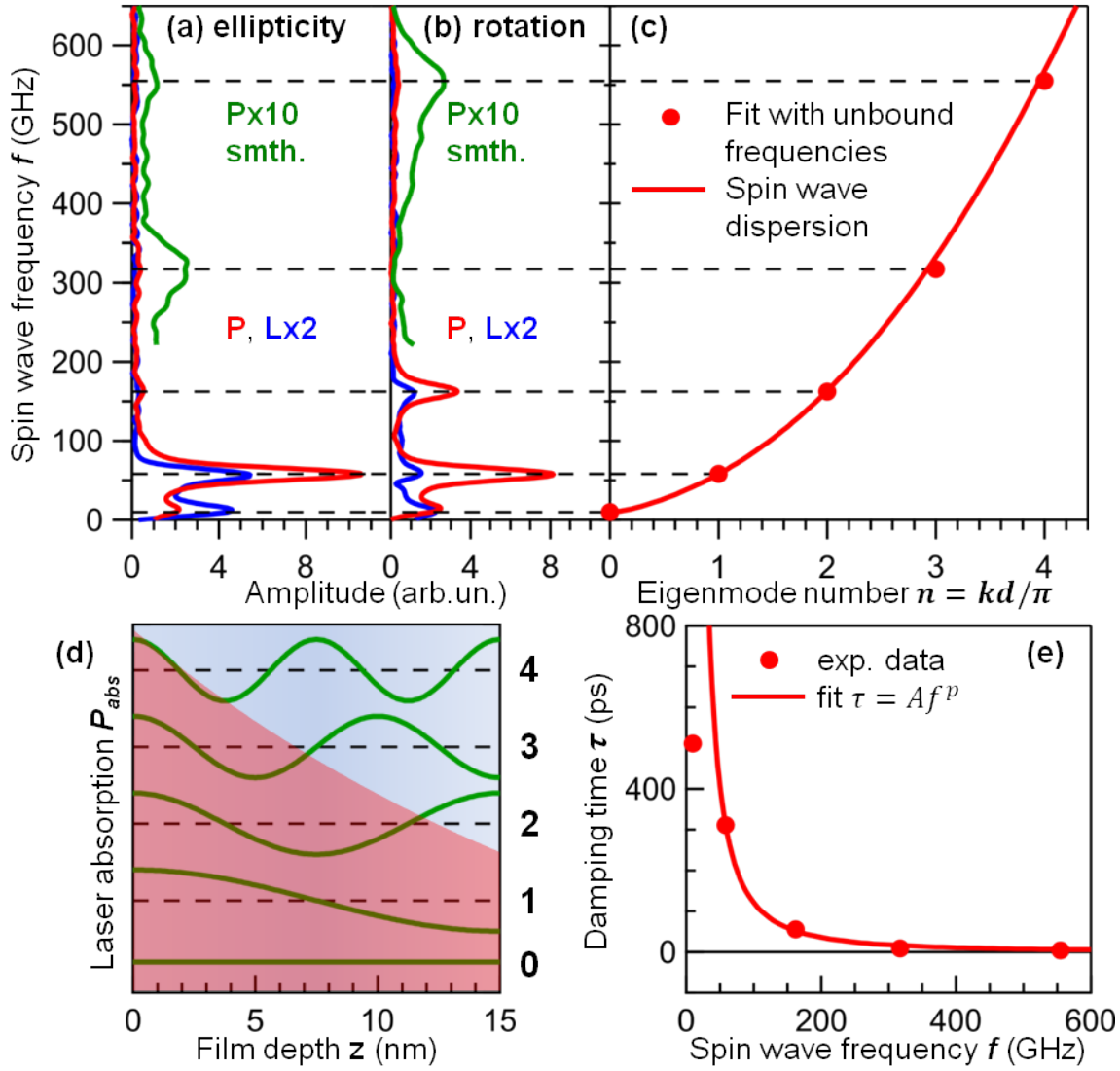

Figure 8.10: (a, b) Fourier spectra of the polar (P) and longitudinal (L) contributions to the MOKE ellipticity ψ''_K and rotation ψ'_K, shown in Figure 8.9. For the demonstration of the 3rd and 4th spin waves modes, the spectra corresponding to the polar contribution have been scaled as smoothed (5 pt. = 5 GHz). (c) Dispersion of the standing spin wave modes. Dots represent frequencies obtained in the joint fitting procedure of the curves shown in Figure 8.9. Solid line represents the fit of the experimental data with a theoretical spin wave dispersion relation (8.25). (d) Five lowest standing spin wave modes and laser absorption profile. (e) Spin wave damping time constants τ_d. Dots represent values obtained in the joint fitting procedure of the curves shown in Figure 8.9. Solid line is the fit of the experimental data with a power function $\tau_d = Af^p$ ($A = (3.9 \pm 1.7) \cdot 10^5$ $[ps \cdot GHz^{1.8}]$, $p = -1.8 \pm 0.1$. From the comparison of the STT- and heating-induced magnetization precession, the damping time of the 0th mode seems to be underestimated, therefore it was excluded from the fit.

the experiments, was negligibly small in comparison with the anisotropy field $H_{an} \approx$ 550 Oe [153] and $4\pi M_s \approx 2.2$ T, therefore the theoretical spin wave dispersion relation (2.47) can be rewritten as:

$$f(k) = \gamma\sqrt{(H_{anis} + Dk^2) \cdot (H_{anis} + 4\pi M_s + Dk^2)}, \tag{8.25}$$

where the absence of pinning at the Au/Fe and Fe/MgO interfaces dictates that for the standing spin waves $k = \pi n/d_{Fe}$. From the neutron scattering measurements [107] and spin-polarized electron energy loss spectroscopy [108], we know the exchange stiffness $D = 280$ Å$^2 \cdot meV$. Thus the only adjustable parameter is the Fe thickness d_{Fe}. For the experimental dependence of the spin wave frequency f on the spin wave mode number (see Figure 8.10(c)), we obtain $d_{Fe} = (14.3 \pm 0.1)$ nm, which is close to 14.7 nm, measured by Dr. Vladimir Roddatis with the transmission electron microscope.

Consideration of the LLG equation (8.18) with the damping parameter α independent of the spin wave frequency f leads to the spin wave lifetime $\tau_l \sim 1/f_l$ [104]. However, in the experiment $\tau_l \sim f_l^{-1.8}$ (see Figure 8.10(e)). Relaxation of the excited spin waves occurs via the interaction of the magnetic system with the electron and lattice systems. Detailed explanation of the observed dependence $\tau(f)$ requires further investigation.

The laser-induced STT has been already observed by Schellekens et al. [17] and Choi et al. [154]. In contrast to the present work, STT-induced magnetization dynamics in [17, 154] is limited to the fundamental mode with $k = 0$, corresponding to the homogeneous magnetization precession. The reason is that the thicknesses of the ferromagnetic layers were only few nm and comparable to the absorption length of the SC. In our experiments we demonstrate excitation of the fourth standing spin wave mode with the wavelength $\lambda_4 = d_{Fe}/2 \approx 7.5\ nm$ (see Figure 8.10(d)). From the consideration of the incoherent dynamics in the PCL, ACL and NCL geometries, we know approximate temporal profiles of the MOKE contributions from the Au layer to $\Delta\psi_K'^L(t)$ and $\Delta\psi_K''^L(t)$. Subtracting these contributions from $\Delta\psi_K'^L(t)$ and $\Delta\psi_K''^L(t)$, it is evident that the laser-induced SC tilts the magnetic moments of the spin-collector in the vicinity of the Au/Fe interface towards $\vec{M}_E$. This fact is consistent with that the HC packet, injected from the spin-emitter into the Au spacer, is dominated by the majority electrons (see **Chapter 7**). For this reason, there is no sign change of the spatial STT profile in the spin-collector. It brings us to the condition for the excitation of the inhomogeneous spin wave modes: the characteristic length λ_{SC} of the SC absorption in the spin-collector should be smaller or comparable to the quarter-wavelength of the highest spin wave mode, i.e. $\lambda_{SC} \sim \lambda_4/4 \approx 1.9\ nm$.

When $d_{Fe} \sim \lambda_{SC}$, the STT can be considered to be uniform within the spin-collector, and its modelling is rather simple. For large d_{Fe} it takes some time for the SC-induced perturbation of the magnetic order to propagate across the spin-collector. In other words, during first two picoseconds after the optical excitation of the spin-emitter, the standing spin waves in the spin-collector are not established yet. Assuming that the injection of the SC into the spin-collector during first picosecond leads to the tilt of the magnetization only in the 4-nm region close to the Au/Fe interface, we estimated the average magnetization component in this region, orthogonal to the

static magnetization $\vec{M}_C$, at about 0.006 $[M_{Fe}]$. This is very rough estimation, but it agrees with the amplitude of the standing spin waves established on a larger time scale 0.002 $[M_{Fe}]$ [5].

8.4 Conclusions

Spin dynamics, induced in a ferromagnetic film by the injection of the laser-induced SC, has been studied on pseudo spin valve Fe/Au/Fe/MgO(001) structures with the time-resolved MOKE and mSHG. Realizing different mutual orientations of the magnetizations $\vec{M}_E$ and $\vec{M}_C$ in the spin-emitter and the spin-collector, it has been proven that the mSHG is sensitive to the SC flowing across the metallic multilayer structure, while the MOKE is exclusively sensitive to the magnetization. Temporal profile of the SC-induced contribution to the mSHG agrees with the data, presented in **Chapter 7**, and the proposed scenario of the non-equilibrium spin Seebeck effect. The front of the SC pulse consists of the optically excited electrons, leaving the spin-emitter in the ballistic regime, while the trailing part is formed by the secondary electrons, providing a net flux of the positive SP as long as the electron temperature in Fe is large than in Au.

Since the STT exerted on $\vec{M}_C$ by the laser-induced SC is proportional to the SC component polarized in the orthogonal direction, in the magnetic geometries, where $\vec{M}_E \uparrow\uparrow \vec{M}_C$ or $\vec{M}_E \downarrow\uparrow \vec{M}_C$, we observed only variations of the magnitude of the magnetization vector $\vec{M}_C$. At the same time, when $\vec{M}_E \perp \vec{M}_C$, the MOKE rotation $\psi'_K(t)$ and ellipticity $\psi''_K(t)$ exhibited various dynamics, which includes precession of the magnetization $\vec{M}_C$ (coherent dynamics), demagnetization (incoherent dynamics) and non-magnetic effects affecting the MOKE signals. Owing to different parity of these contributions with respect to the reversal of $\vec{M}_E$ and $\vec{M}_C$, the coherent and incoherent dynamics can be easily disentangled. Moreover, applying the external magnetic field in different directions for each magnetic geometry, it is even possible to separate the heating- and STT-induced magnetization precession (see Table 8.1). The spatial profile of the STT is essentially non-uniform, which results in the excitation of the several standing spin wave modes in the 15-nm spin-collector (see Figures 8.9). The laser-induced heating drives only the fundamental mode, corresponding to the homogeneous magnetization precession. In **Chapter 7** it has been shown that the SC flowing from the spin-emitter is dominated by the majority electrons with $\vec{\sigma}_e \uparrow\uparrow \vec{M}_E$. From the MOKE data measured on the three-layer Fe/Au/Fe/MgO(001) structure, it is also evident that the injection of the laser-induced SC into the spin-collector tilts $\vec{M}_C$ towards $\vec{M}_E$. Assuming no sign change in the spatial profile of the STT, excitation of the fourth standing spin wave mode ($k_4 = 4\pi/d_{Fe}$) demands that the absorption length of the SC in the spin-collector λ_{SC} is comparable to the quarter-wavelength of the fourth mode $\lambda_4/4 \approx 1.9\ nm$.

All experimental data obtained on the Au/Fe/MgO(001) and Fe/Au/Fe/MgO(001)

[5] In the geometries, where $\vec{M}_C \| \hat{x}$, the static MOKE rotation and ellipticity are $\psi'_{K,0} = 43\ mdeg.$ and $\psi''_{K,0} = 90\ mdeg.$, respectively.

structures are consistent with each other, which sustains the proposed scenario of the HC transport and the HC-driven magnetization dynamics. Subsequently our data can be used to verify the results of the ab initio calculations and develop theoretical models which more accurately describe the observations.

Chapter 9

Conclusions

9.1 Summary and Conclusions

Ultrafast hot carrier (HC) driven magnetization dynamics in metallic multilayer structures have been studied using the time-resolved linear and nonlinear optical spectroscopy. The present work is focused on several aspects of the laser-induced magnetization dynamics:

- ultrafast laser-induced demagnetization of ferromagnetic films;
- transport of the spin-polarized HCs in a noble metal;
- magnetization dynamics induced in a ferromagnetic film by the injection of the spin-polarized HCs.

Each aspect has its special meaning and can be discussed separately from the others, but together they allow to develop a self-consistent model, describing all experimental results.

Ultrafast laser-induced demagnetization

Upon the laser excitation of a ferromagnetic film, both HC transport and spin-flip processes contribute to ultrafast demagnetization. The spin-flip processes, leading to the change of the magnetization, have to be accompanied with the transfer of the angular momentum to the lattice, which is so-called 'bottle neck', determining the spin-flip rate. At the same time, demagnetization, induced by the HC transport, depends only on the velocities and lifetimes of the majority and minority HCs carrying opposite spins. Since it is impossible to exclude the influence of the spin-flip processes, pump-probe experiments have been performed on a 8-nm Fe film grown on a nonconducting MgO substrate and capped with 3 nm of MgO. Due to a homogeneous laser absorption profile, the HC transport can be neglected and the magnetization dynamics is governed only by the spin-flip processes. In order to be more sensitive the generation of the non-equilibrium (NEQ) HCs, we have utilized the pump and probe pulses with identical photon energies $\hbar\omega_{probe} = \hbar\omega_{pump} = 1.5\ eV$. Spin is conserved in the optical

transitions, therefore there is no change of the magnetization at the time zero. Assuming that variation of the magneto-optical constants modifies the MOKE rotation $\delta\psi'_K(t)$ and ellipticity $\delta\psi''_K(t)$ with the same temporal profile, determined by the difference $B(t) = \delta\psi''_K(t) - \delta\psi'_K(t)$, it is possible to evaluate real magnetization dynamics $\delta M(t)$. Using simple phenomenological model to reproduce the relative variations of the linear reflectivity $\delta R(t)$, MOKE rotation $\delta\psi'_K(t)$ and ellipticity $\delta\psi''_K(t)$, it has been found that demagnetization of the Fe film occurs on the time scale of the electron-electron thermalization ($\tau_M = \tau_{ee} = 0.21 \pm 0.01\ ps$), meaning that it is dominated by the NEQ HCs. Subsequent recovery of the magnetization occurs on the time scale of the electron-phonon thermalization $\tau_R = \tau_{ep} = 1.06 \pm 0.03\ ps$. So it is mostly determined by the thermalized HCs. Owing to 20-fs experimental time resolution, we have excluded any other possible assignments of the observed time scales. Moreover, the characteristic time of the electron-electron thermalization τ_{ee} is in agreement with the photoemission studies performed on Fe [88] and Ni [76].

In order to go beyond the phenomenological description, we have tried to reproduce our data within the M3TM suggested by Koopmans et al. [86]. However, it is not capable to describe the complete set of the linear magneto-optical signals and considers an instantaneous electron thermalization, which contradicts with our experimental results. Describing the HC and magnetization dynamics in terms of the energy flux and the transfer of the angular momentum, we have developed a microscopic model. It has been suggested that the magnetization change rate is proportional to the energy flux from the NEQ and thermalized HCs to the lattice. In spite of the made assumptions, our microscopic model can perfectly reproduce all measured curves $\delta R(t)$, $\delta\psi'_K(t)$ and $\delta\psi''_K(t)$. It has revealed the dominant role of the NEQ HCs in ultrafast spin dynamics, as it was suggested by Carva et al. [96]. This result can be explained by the fact that for the NEQ HCs the phase space available for the spin-flip processes is larger than that for the thermalized HCs. However, in contrast to [96], we have found that the thermalized HCs contribute mostly to the recovery of the magnetization.

In order to understand the role of the HC transport, pump-probe experiments have been performed on two-layer Au/Fe/MgO(001) structures, where Au serves a sink of heat and spin polarization (SP). In this case the most important parameters are the ballistic lengths of the majority and minority HCs, and the transmission through the Fe/Au interface. Analyzing the MOKE data, measured on Au/Fe/MgO(001) with 130 nm of Au and different Fe thicknesses, and comparing them with those, obtained on the 8-nm Fe film, it has been revealed that the HC transport plays a considerable role in ultrafast demagnetization of the ferromagnetic film. Because of the different depth sensitivities, the MOKE rotation $\psi'_K(t)$ and ellipticity $\psi''_K(t)$ are affected differently by the non-uniform magnetization dynamics and the variation of the magneto-optical constants.

Transport of the spin-polarized hot carriers in a noble metal

Probing the Au side of the Au/Fe/MgO(001), it has been demonstrated that the optical excitation of the Fe film leads to the generation of the spin current (SC) flowing in the Au layer. This effect is an analog of the spin Seebeck effect [152], but in our

case it is dominated by the NEQ HCs. From the analysis of the mSHG and MOKE data, measured on the Au/Fe/MgO(001) structures with different Au thicknesses, it has been concluded that the front of the SC pulse consists of the optically excited majority electrons, leaving the Fe film in the ballistic regime, while the trailing part is formed by the secondary electrons, providing a net flux of the positive SP through the Fe/Au interface as long as the electron temperature in Fe is larger than in Au. Both optically excited and secondary majority electrons propagate in Au in a quasi-ballistic regime. It means that the shape of the SC pulse in Au is mostly determined by the HC flux through the Fe/Au interface. The characteristic time of the electron equilibration between the Fe and Au films has been estimated at $0.56 \pm 0.03\ ps$. In addition to that, we have found the velocity of the optically excited electrons $v_{Au1} = (1.06 \pm 0.06)\ nm/fs$ and their lifetimes $\tau_{Au1} = (24 \pm 4)\ fs$ in Au. Both values are close to the predictions made in the ab initio calculations [19, 106]. The secondary electrons have smaller binding energies and hence longer lifetimes than the primary ones. However, their velocity distribution is more uniform and results in a smaller velocity projection along the normal to the film plane: $v_{Au2} = (0.6 \pm 0.4)\ nm/fs$. The number of the electrons, optically excited in the vicinity of the Fe/Au interface, decreases with the Fe thickness. Thus changing the Fe thickness, one can control the ratio between the primary and secondary electrons, forming the SC pulse in Au.

Performing measurements in the transversal and longitudinal magneto-optical geometries, it has been shown that in addition to the contribution from the Au surface, the SC gives rise to the odd SH field $\vec{E}_{2\omega}^{SC}$ originating in the bulk of Au. For $d_{Au} > 65\ nm$, when there is no contribution from the Fe film neither to the MOKE nor to the mSHG, the SP-induced surface contribution to the SH contrast $\rho_{2\omega}^{SP}(t)$ resembles the temporal profile of the MOKE ellipticity $\psi_K''(t)$, indicating more or less uniform magnetization profile within the probed region of the Au layer. The same conclusion can be made from the independence of the ratio $\psi_K''(t)/\psi_K'(t)$ from time and the Au thickness. In the analysis of the experimental data, obtained probing either the Fe side or the Au side of the Au/Fe/MgO(001) structures, we have found the Voigt constant of gold $q_{Au} = 0.094 + 0.035i$ and estimated the average magnetization built up in the 75-nm Au layer by the SC flowing from the Fe film: $M_{Au} = Q_{Au}/q_{Au} \approx 0.0026\ [M_{Fe}] \approx 0.0082\ [\mu_B/atom]$.

Injection of the spin-polarized hot carriers into a ferromagnetic film

Epitaxial pseudo spin valve Fe/Au/Fe/MgO(001) structure is a good model system, where one Fe layer serves as the spin-emitter (E), and the other one serves as the spin-collector (C). Probing samples simultaneously from both sides with the MOKE and the mSHG, one can easily identify the directions of the magnetizations $\vec{M}_E$ and $\vec{M}_C$. Polarization of the direct SC is set by the magnetization $\vec{M}_E$. Depending on the mutual orientation of $\vec{M}_E$ and $\vec{M}_C$, hot electrons, propagating towards the spin-collector, can be effectively transmitted through the Au/Fe interface or reflected from it. It has been demonstrated that the laser-induced SC, polarized in the orthogonal direction with respect to $\vec{M}_C$, exerts a torque on $\vec{M}_C$ and drives its precessional motion. Unfortunately, the STT is not the only mechanism, which can excite coherent magnetization

dynamics. The laser-induced heating of the ferromagnetic film leads to the reduction of the anisotropy field $\vec{H}_{anis}$, thereby altering the direction of the effective magnetic field $\vec{H}_{eff}$. As a result, the magnetization starts to precess around new equilibrium direction determined by $\vec{H}_{eff}$. Eventually because of the heat diffusion away from the ferromagnetic film, the equilibrium direction of the magnetization recovers to its initial orientation. Typical thickness of the Au spacer is several tens of nanometers, therefore it suppresses the direct interaction of the back pump with the spin-collector and the amplitude of the heating-induced coherent dynamics is not expected to be large in comparison with the STT-induced one. Nevertheless, realizing different mutual orientations of $\vec{M}_E$, $\vec{M}_C$ and the external magnetic field $\vec{H}_{ext}$, it is possible to disentangle all contributions to the magnetization dynamics and analyze them separately from each other.

Since the SC, polarized in the orthogonal direction with respect to $\vec{M}_C$, is absorbed in the small region of the spin-collector close to the Au/Fe interface, the spatial profile of the STT is essentially non-uniform. In the experiments performed on the Fe/Au/Fe/MgO(001) structure, where the back pump was applied from the side of the 16-nm top Fe layer (spin-emitter) and the probe pulse was applied from the side of the 15-nm bottom Fe layer (spin-collector), the laser-induced SC pulse excited four lowest standing spin waves modes. It gives us the estimation for the SC absorption length: $\lambda_{SC} \approx \lambda_4/4 \approx 1.9\ nm$.

Regarding the mSHG response, a more various set of the magnetic geometries (in comparison with the experiments performed on the two-layer Au/Fe/MgO(001) structures) allowed us to prove that the mSHG signal possess the SC-induced contribution and derive its temporal profile.

9.2 Outlook

The present work shed light on laser-induced demagnetization of the ferromagnetic films and the HC-driven magnetization dynamics in metallic multilayers. In the most cases the dominant role was attributed to the NEQ HCs. Since the HC excitation and subsequent dynamics may vary with the spectrum of the pump laser pulse or depend on the studied materials, further investigation is required for complete understanding of the underlying elementary processes and development of the theoretical models tending to describe the experimental observations.

Comparing our experimental results concerning laser-induced demagnetization of the Fe film with other works performed on Ni [25, 76, 80–84, 86, 89] and Co [75, 85], there are certain similarities between them. For instance, the characteristic time of the electron thermalization should be about 200 fs. However, in terms of the magnetization dynamics, only for Ni two demagnetization time scales have been observed [86, 89]. In **Chapter 5** we demonstrated the magnetization change rate due to the NEQ and thermalized HCs are proportional to the energy flux to the lattice. In general the corresponding proportionality factors Γ_{neq} and Γ_{eq} depend on the initial and transient magnetizations M_0 and $M(t)$, but for the demagnetization values achieved in the experiment we did not notice it. Probably this dependence is more pronounced for Ni

than for Fe and Co. It may also explain the transition between two regimes, when one or two demagnetization time scales can be observed [86, 89].

On the example of the Au/Fe/MgO(001) structures, it was demonstrated that the laser-induced transport of the spin-polarized HCs leads to the accumulation of the SP in Au, which in turn gives rise to the measurable MOKE rotation and ellipticity. The HC injection from the ferromagnetic film into the non-magnetic layer is much more efficient than the usage of the external magnetic field [155], therefore this technique can be used to determine the magneto-optical constants of the non-magnetic materials. Also the observation of the SC-induced SH signal from Au should inspire reconsideration of the previous works like [106] and more wide application of the mSHG as the nonlinear-optical technique for direct monitoring of SC pulses.

In light of further development of the magnetic storage devices, investigation of the laser-induced SC pulses and SC-induced dynamics will continue to attract interest of many research groups. Eventually it may lead to a new breakthrough in spintronics.

Appendix A

Lists

A.1 Abbreviations

DAQ	Data acquisition
DOS	Density of states
EQ HCs	Equilibrium (thermalized) hot carriers
GVD	Group velocity dispersion
HC	Hot carrier
MRAM	Magnetic random access memory
mSHG	Magneto-induced Second Harmonic Generation
MOKE	Magneto-optical Kerr effect
M3TM	Microscopic three-temperature mode
ML	Multilayer
NEQ HCs	Non-equilibrium HCs
PMT	Photomultiplier tube
RF	Radio frequency
SH	Second Harmonic
SHG	Second Harmonic Generation
SC	Spin current
SP	Spin polarization
STT	Spin Transfer Torque
2PPE	Two-photon-photoemission
2TM	Two-temperature model
XMCD	X-ray magnetic circular dichroism

A.2 List of publications

Publication within this thesis

- A. Melnikov, A. Alekhin, D. Brstel, D. Diesing, T.O. Wehling, I. Rungger, M. Stamenova, S. Sanvito, and U. Bovensiepen: Ultrafast Non-local Spin Dynamics in Metallic Bi-Layers by Linear and Non-linear Magneto-Optics. In: J-Y. Bigot, W. Hbner, T. Rasing, R. Chantrell (eds.), Ultrafast Magnetism I Proceedings of Ultrafast Magnetism Conference, Strasbourg, October 2013, Springer Proceedings in Physics, 159, 3436 (2015) [2014]

- A. Alekhin, D. Bürstel, A. Melnikov, D. Diesing, and U. Bovensiepen: Ultrafast Laser-Excited Spin Transport in Au/Fe/MgO(001): Relevance of the Fe Layer Thickness. In: J-Y. Bigot, W. Hbner, T. Rasing, R. Chantrell (eds.), Ultrafast Magnetism I Proceedings of Ultrafast Magnetism Conference, Strasbourg, October 2013, Springer Proceedings in Physics, 159, 241143 (2015) [2014]

Publication concerning other topics

- A.I. Alekhin, S.V. Zabotnov, L.A. Golovan', P.A. Perminov, and P.K. Kashkarov "Dynamics of the pulsed picosecond laser ablation of silicon targets", J. Opt. Technol. **78**, 161 (2011).

In preparation

- A. Alekhin, I. Razdolski, M. Münzenberg, A. Melnikov "Role of non-equilibrium hot carriers in ultrasfast laser-induced demagnetization of Fe", in preparation for Physical Review B

- I. Razdolski, A. Alekhin, N. Ilin, J. Meyburg, D. Diesing, V. Roddatis, I. Rungger, M. Stamenova, S. Sanvito, T.O. Wehling, U. Bovensiepen, and A. Melnikov "Ultrafast transport of spin-polarized hot carriers in Fe/Au/Fe/MgO(001): non-equilibrium spin Seebeck effect and spin current reflection at interfaces", in preparation for Physical Review Letters

- I. Razdolski, A. Alekhin, and A. Melnikov "Strongly inhomogeneous ultrafast magnetization dynamics optically excited via spin transfer torque mechanism", in preparation for Nature Physics

A.3 Curriculum vitae

The curriculum vitae is omitted in the online version due to data privacy.

Appendix B

Acknowledgements

This research was supported by the Deutsche Forschungsgemeinschaft (ME 3570/1, Sfb 616), by the EU 7-th frame-work program (CRONOS) and by the Max-Planck-Gesellschaft (scholarship for doctoral students). This work would not have been possible without help and support of many people to whom I want to express my gratitude:

- Prof. Dr. Martin Wolf for giving me an opportunity to perform my PhD studies under his supervision and to work in the lab at the Fritz Haber Institute of the Max Planck Society on very exciting topic.
- Prof. Dr. Martin Weinelt for becoming my second referee and being a part of the thesis committee, for the fruitful discussions.
- Dr. Alexey Melnikov for cosupervising my work, for his expertise and knowledge in the nonlinear optics, solid state physics and time-resolved techniques, that he shared with me, for constructive criticism and useful advices.
- Dr. Detleft Diesing (University of Duisburg-Essen) and his PhD students Damian Bürstel and Jan Meyburg for the preparation of the two-layer Au/Fe/MgO(001) and the three-layer Fe/Au/Fe/MgO(001) structures; Dr. Markus Münzenberg (Ernst Moritz Arndt University of Greifswald) for the preparation of thin polycrystalline Fe films capped with the MgO.
- Prof. Dr. Uwe Bovensiepen (University of Duisburg-Essen), Dr. Tobias Kampfrath, Dr. Ilya Razdolski for fruitful discussions.
- Dr. Tim O. Wehling, Prof. Dr. Alexander Lichtenstein, Dr. Ivan Rungger, Dr. Stefano Sanvito and Dr. Maria Stamenova for collaboration and performance of the ab initio calculations.
- Dr. Vladimir Roddatis for the electron microscopy of the studied samples.
- Marcel Krenz for his expertise and knowledge in the laser physics and laser technology.
- Albrecht Ropers for technical support.

- Thomas Zehentbauer, Viktor Platschkowski for help in the construction of the MOKE detectors.

- Workshop department for fast and high quality production of different parts used in the experimental setup

- All current and former members of the Fritz-Haber-Institute for the good atmosphere and support: Dr. Alex Paarmann, Dr. Kramer Campen, Dr. Karsten Horn, Dr. Takashi Kumagai, Dr. Ralph Ernstorfer, Dr. Julia Stähler, Lukas Braun, Jan-Christoph Deinert, Dr. Daniel Wegkamp, Laura Foglia, Dr. Nikita Ilin, Dr. Marc Herzog, Sebastian Mährlein, Selene Mor, Christopher Nicholson, Dr. Stephan Böttcher, Dr. Hendrik Vita and many others.

- Last but not least, I would like to thank my family and friends for their understanding, support and encouragement.

Bibliography

[1] J. Kilby U.S. Patent 3.138.743 (Filed Feb. 1959).

[2] J. Kilby "Invention of the Integrated Circuit IEEE Transactions on Electron Devices", ED23 (7): 648-654 (1976).

[3] www.intel.com

[4] Martin Hilbert, López Priscila "The World's Technological Capacity to Store, Communicate, and Compute Information", Science **332**: 6065 (2011)

[5] . T. Kawahara, R. Takemura, K. Miura, J. Hayakawa, S. Ikeda, Y.M. Lee, R. Sasaki, Y. Gotot, K. Ito, T. Meguro, F. Matskura, H. Takahash, H. Matsuoka, and H. Ohno "2 Mb SPRAM (Spin-Transfer Torque RAM) with bit-by-bit bi-directional current write and parallelizing-direction current read", IEEE J Solid-State Circuits **43**, 109 (2008)

[6] J.C. Slonczewski "Current-driven excitation of magnetic multilayers", J. Magn. Magn. Mater. **159**, L1 (1996)

[7] L. Berger "Emission of spin waves by a magnetic multilayer traversed by a current", Phys. Rev. B **54**, 9353 (1996)

[8] J.C. Slonczewski "Excitation of spin waves by an electric current", J. Magn. Magn. Mater. **195**, L261 (1999).

[9] E.B. Myers, D.C. Ralph, J.A. Katine, R.N. Louie, R.A. Buhrman "Current-induced switching of domains in magnetic multilayer devices", Science **285**, 867 (1999).

[10] D.C. Ralph, M.D. Stiles "Spin transfer torques", J. Magn. Magn. Mater. **320**, 1190 (2008).

[11] I.N. Krivorotov, N.C. Emley, J.C. Sankey, S.I. Kiselev, D.C. Ralph, R.A. Buhrman "Time-domain measurements of nanomagnet dynamics driven by Spin-Transfer Torques", Science **307**, 228 (2005).

[12] S. Serrano-Guisan, K. Rott, G. Reiss, J. Langer, B. Ocker, and H.W. Schumacher "Biased Quasiballistic Spin Torque Magnetization Reversal", Phys. Rev. Lett. **101**, 087201 (2008).

[13] S. Garzon, L. Ye, R.A. Webb, T.M. Crawford, M. Covington, and S. Kaka "Coherent control of nanomagnet dynamics via ultrafast spin torques pulses", Phys. Rev. B **78**, 180401 (2008).

[14] Y. Acremann, J.P. Strachan, V. Chembrolu, S.D. Andrews, T. Tyliszczak, J.A. Katine, M.J. Carey, B.M. Clemens, H.C. Siegmann, and J. Stöhr "Time-resolved imaging of Spin Transfer Switching: beyond the macrospin concept", Phys. Rev. Lett. **96**, 217202 (2006).

[15] J.P. Strachan, V. Chembrolu, Y. Acremann, X.W. Yu, A.A. Tulapurkar, T. Tyliszczak, J.A. Katine, M.J. Carey, M.R. Scheinfein, H.C. Siegmann, and J. Stöhr "Direct observation of spin-torque driven magnetization reversal through nonuniform modes", Phys. Rev. Lett. **100**, 247201 (2008).

[16] G. Malinowski, F. Dalla Longa, J.H.H. Rietjens, P.V. Paluskar, R. Huijink, H.J.M. Swagten, and B. Koopmans "Control of speed and efficiency of ultrafast demagnetization by dirrect transfer of spin angular momentum", Nature Physics **4**, 855 (2008).

[17] A.J. Schellekens, K.C. Kuiper, R.R.J.C. de Wit, and B. Koopmans "Ultrafast spin-transfer torque driven by femtosecond pulsed-laser excitation", Nature Commun. **5**, 4333 (2014).

[18] M. van Kampen, C. Jozsa, J.T. Kohlhepp, P. LeClair, L. Lagae, W.J.M. de Jonge, and B. Koopmans "All-optical probe of coherent spin waves", Phys. Rev. Lett. **88**, 227201 (2002).

[19] V.P. Zhukov, E.V. Chulkov, and P.M. Echenique, "Lifetimes and inelastic mean free path of low-energy excited electrons in Fe, Ni, Pt, and Au: Ab initio GW+T calculations", Phys. Rev. B **73**, 125105 (2006).

[20] M.D. Stiles, A. Zangwill "Anatomy of spin transfer torque", Phys. Rev. B **66**, 014407 (2002).

[21] W. Kim, S.-W. Lee, and K.-J. Lee "Micromagnetic modelling on magnetization dynamics in nanopillars driven by spin-transfer torque", J. Phys. D: Appl. Phys. **44**, 384001 (2011).

[22] M. Battiato, K. Carva, and P.M. Oppeneer "Superdiffusive Spin Transport as a Mechanism of Ultrafast Demagnetization", Phys. Rev. Lett. **105**, 027203 (2010).

[23] M. Battiato, K. Carva, and P.M. Oppeneer "Theory of laser-induced ultrafast superdiffusive spin transport in layered heterostructures", Phys. Rev. B **86**, 024404 (2012).

[24] A. Eschenlohr, M. Battiato, P. Maldonado, N. Pontius, T. Kachel, K. Holldack, R. Mitzner, A. Fhlisch, P.M. Oppeneer, and C. Stamm "Ultrafast spin transport as key to femtosecond demagnetization", Nature Materials **12**, 332 (2013).

[25] E. Beaurepaire, J.-C. Merle, A. Daunois, and J.-Y. Bigot "Ultrafast Spin Dynamics in Ferromagnetic Nickel", Phys. Rev. Lett. **76**, 22, 4250 (1996).

[26] A. Kirilyuk, A.V. Kimel, and T. Rasing "Ultrafast optical manipulation of magnetic order", Rev. Mod. Phys. **82**, 2731-2784 (2010).

[27] J. Zak, E.R. Moog, C. Liu, and S.D. Bader "Universal approach to magnetooptics", JMMM **89**, 107 (1990).

[28] J. Zak, E.R. Moog, C. Liu, and S.D. Bader "Fundamental magnetooptics", J. Appl. Phys. **68**, 4203 (1990).

[29] J. Stöhr and H.C. Siegmann "Magnetism: From Fundamentals to Nanoscale Dynamics", Springer, Berlin (2006).

[30] L.D. Landau, E.M. Lifshitz "Quantum mechanics - Non relativistic theory", Course of theoretical physics, Volume 3, Institute of Physical Problems USSR, Academy of Science, Pergamon Press (1965).

[31] E.P. Wohlfarth, in Ferromagnetic Materials. A Handbook on the Properties of Magnetically Ordered Substances, ed. by E.P. Wohlfarth, North-Holland, Amsterdam (1980).

[32] S.P. Walch, W.A. Goddard III "Theoretical studies of the bonding of sulfur to models of the (100)suface of nickel", Surf. Sci. **72**, 645 (1978).

[33] H. Ibach, H. Lüth "Solid-State Physics: An Introduction to Principles of Materials Science", fourth edition, Springer (2009).

[34] R.M. Bozorth "Directional ferromagnetic properties of metals", J. Appl. Phys. **8**, 575 (1937).

[35] V.A. Bokov "Applied solid state physics. Physics of magnetic materials" (2002).

[36] V.Yu. Irkhin, Yu.P. Irkhin "Electronic configuration, physical properties and correlation'effects in d- and f-metals, and their compounds", monograph, Russian Academy of Science, Ural department, Institute for physics of metals (2004).

[37] N.F. Mott "A discussion of the transition metals on the basis of quantum mechanics.", Proc. Phys. Soc. (London) **47**, 571 (1935).

[38] J.C. Slater "The Ferromagnetism of Nickel", Phys. Rev. **49**, 537 (1936).

[39] J.C. Slater "The Ferromagnetism of Nickel. Temperature effects.", Phys. Rev. **49**, 931 (1936).

[40] E.C. Stoner "Collective electron specific heat and spin paramagnetism in metals", Proc. Roy. Soc. (London) A **154**, 656 (1936).

[41] E.C. Stoner "Collective electron ferromagnetism", Proc. Roy. Soc. (London) A **165**, 372 (1938).

[42] F.J. Himpsel, J.E. Ortega, G.J. Mankey, R.F.Willis "Magnetic nanostructures", Adv. Phys. **47**, 511 (1998).

[43] F.J. Himpsel, K.N. Altmann, in "Solid State Photoemission and Related Methods", ed. by W. Schattke, M.V. Hove, Wiley-VCH Verlag, Weinheim (2003).

[44] J. Schäfer, M. Hoinkis, Eli Rotenberg, P. Blaha, and R. Claessen "Fermi surface and electron correlation effects of ferromagnetic iron", Phys. Rev. B **72**, 155115 (2005).

[45] V.L. Moruzzi, J.F. Janak, A.R. Williams "Calculated electronic properties of metals", N.Y.: Pergamon Press (1978).

[46] K.H. Bennemann (ed.) "Nonlinear optics in metals", Clarendon Press, Oxford (1998).

[47] W. Greiner, L. Neise, and H. Stöcker "Thermodynamik and Statistische Mechanik", Verlag, Harri Deutsch (1987).

[48] J.H. Weaver and H.P.R. Frederikse "Optical properties of selected elements", Handbook of Chemistry and Physics, 95th edition, Section 12 (2014).

[49] T. Juhasz, H.E. Elsayed-Ali, G.O. Smith, C. Suárez, and W.E. Bron, "Direct measurements of the transport of nonequilibrium electrons in gold films with different crystal structures", Phys. Rev. B **48**, 15488 (1993).

[50] S.D. Brorson, J.G. Fujimoto, and E.P. Ippen "Femtosecond Electronic Heat-Transport Dynamics in Thin Gold Films", Phys. Rev. Lett. **59**, 1962 (1987).

[51] R.W. Schoenlein, W.Z. Lin, J.G. Fujimoto, and G.L. Eesley "Femtosecond studies of nonequilibrium electronic processes in metals", Phys. Rev. Lett. **58**, 1680 (1987).

[52] H.E. Elsayed-Ali, T.B. Norris, M.A. Pessot, and G.A. Mourou "Time-resolved observation of electron-phonon relaxation in copper", Phys. Rev. Lett. **58**, 1212 (1987).

[53] H.E. Elsayed-Ali, T. Juhasz, G.O. Smith, and W.E. Bron "Femtosecond thermoreflectivity and thermotransmissivity of polycrystalline and single-crystalline gold films", Phys. Rev. B **43** (1991).

[54] W.S. Fann, R. Storz, and H.W.K. Tom "Electron thermalization in gold", Phys. Rev. B **46**, 13592 (1992).

[55] W.S. Fann, R. Storz, H.W.K. Tom, and J. Bokor "Direct measurement of nonequilibrium electron-energy distributions in subpicosecond laser heated gold films", Phys. Rev. Lett. **68**, 2834 (1992).

[56] R.H.M. Groeneveld, R. Sprik, A. Lagendijk "Effect of a nonthermal electron distribution on the electron-phonon energy relaxation process in noble metals", Phys. Rev. B **45**, 5079 (1992).

[57] C.-K. Sun, F. Vallee, L.H. Acioli, E.P. Ippen, and J.G. Fujimoto "Femtosecond-tunable measurement of electron thermalization in gold", Phys. Rev. B **50**, 15337 (1994).

[58] X.Y. Wang, D.M. Riffe, Y.-S. Lee, and M.C. Downer "Time-resolved electron-temperature measurement in a highly excited gold target using femtosecond thermionic emission", Phys. Rev. B **50**, 8016 (1994).

[59] C.A. Schmuttenmaer, M. Aeschlimann, H.E. Elsayed-Ali, and R.J.D. Miller, D.A. Mantell, J. Cao and Y. Gao "Time-resolved two-photon photoemission from Cu(100): Energy dependence of electron relaxation", Phys. Rev. B **50**, 8957 (1994).

[60] R.H.M. Groeneveld, R. Sprik, A. Lagendijk "Femtosecond spectroscopy of electron-electron and electron-phonon energy relaxation in Ag and Au", Phys. Rev. B **51** (1995).

[61] C. Suárez, W.E. Bron, and T. Juhasz "Dynamics and transport of electronic carriers in thin gold films", Phys. Rev. Lett. **75**, 4536 (1995).

[62] T. Hertel, E. Knoesel, M. Wolf, and G. Ertl "Ultrafast electron dynamics at Cu(111): response of an electron gas to optical excitation", Phys. Rev. Lett. **76**, 535 (1996).

[63] M. Aeschlimann, M. Bauer, S. Pawlik "Competing nonradiative channels for hot electron induced surface photochemistry", Chem. Phys. **205**, 127 (1996).

[64] J. Hohlfeld, U. Conrad, E. Matthias "Does femtosecond time-resolved second-harmonic generation probe electron temperatures at surfaces", Appl. Phys. B **63**, 541 (1996).

[65] H. Petek and S. Ogawa "Femtosecond time-resolved two-photon photoemission studies of electron dynamics", Progress in Surf. Sci. **56** (1997).

[66] J. Cao, Y. Gao, H.E. Elsayed-Ali, R.J.D. Miller, D.A. Mantell "Femtosecond photoemission study of ultrafast electron dynamics in single-crystal Au(111) films", Phys. Rev. B **58**, 10948 (1998).

[67] K.L. Moore and T.D. Donnely "Probing nonequilibrium electron distributions in gold by use of second-harmonic generation", Opt. Lett. **24**, 990 (1999).

[68] M. Bonn, D.N. Denzler, S. Funk, and M. Wolf "Ultrafast electron dynamics at metal surfaces: Competition between electron-phonon coupling and hot-electron transport", Phys. Rev. B **61**, 1101 (2000).

[69] J. Hohlfeld, S.-S. Wellershoff, J. Güdde, U. Conrad, V. Jähnke, E. Matthias "Electron and lattice dynamics following optical excitation of metals", Chem. Phys. **251**, 237 (2000).

[70] N. Del Fatti, C. Voisin, M. Achermann, S. Tzortzakis, D. Christofilos, and F. Vallée "Nonequilibrium electron dynamics in noble metals", Phys. Rev. B **61**, 16956 (2000).

[71] M. Bauer, M. Aeschlimann "Dynamics of excited electrons in metals, thin films and nanostructures", J. Electron. Spectrosc. Relat. Phenom. **124**, 225 (2002).

[72] T. Kampfrath "Charge-carrier dynamics in solids and gases observed by time-resolved terahertz spectroscopy", PhD thesis at the Free University of Berlin (2005).

[73] J.J. Quinn "Range of excited electrons in metals", Phys. Rev. **126**, 1453 (1962).

[74] P. Noziéres, D. Pines "The theory of quantum liquids" Benjamin, New York, (1966).

[75] M. Aeschlimann, M. Bauer, S. Pawlik, W. Weber, R. Burgermeister, D. Oberli, and H.C. Siegman "Ultrafast spin-dependent electron dynamics in fcc Co", Phys. Rev. Lett. **79**, 5158 (1997).

[76] H.-S. Rhie, H.A. Dürr, and W. Eberhardt "Femtosecond electron and spin dynamics in Ni/W(110) films", Phys. Rev. Lett. **90**, 247201 (2003).

[77] A.B. Schmidt, M. Pickel, M. Donath, P. Buczek, A. Ernst, V.P. Zhukov, P.M. Echenique, L.M. Sandratskii, E.V. Chulkov, and M. Weinelt "Ultrafast magnon generation in an Fe film on Cu(100)", Phys. Rev. Lett. **105**, 197401 (2010).

[78] V.P. Zhukov, E.V. Chulkov, and P.M. Echenique "Lifetimes of Excited Electrons in Fe and Ni: First-Principles GW and the T-Matrix Theory", Phys. Rev. Lett. **93**, 096401 (2004).

[79] S. Kaltenborn and H.C. Schneider "Spin-orbit coupling effects on spin-dependent inelastic electronic lifetimes in ferromagnets", Phys. Rev. B **90**, 201104 (2014).

[80] J. Hohlfeld, E. Matthias, R. Knorren, and K.H. Bennemann "Nonequilibrium magnetization dynamics of nickel", Phys. Rev. Lett. **78**, 4861 (1997).

[81] H. Regensburger, R. Vollmer, and J. Kirschner "Time-resolved magnetization-induced second-harmonic generation from the Ni(110) surface", Phys. Rev. B **61**, 14716 (2000).

[82] B. Koopmans, M. van Kampen, J.T. Kohlhepp, and W.J.M. de Jonge "Ultrafast Magneto-Optics in Nickel: Magnetism or Optics?", Phys. Rev. Lett. **85**, 844 (2000).

[83] C. Stamm, T. Kachel, N. Pontius, R. Mitzner., T.Quast, K. Holldack, S. Khan, C. Lupulescu, E.F. Aziz, M. Wietstruk, H.A. Dürr, and W. Eberhardt "Femtosecond modification of electron localization and transfer of angular momentum in nickel", Nat. Mater. **6**, 740 (2007).

[84] C. Stamm, N. Pontius, T. Kachel, M. Wietstruk, and H.A.Dürr "Femtosecond x-ray absorption spectroscopy of spin and orbital angular momentum in photoexcited Ni films during ultrafast demagnetization", Phys. Rev. B **81**, 104425 (2010).

[85] A.B. Schmidt, M. Pickel, T. Allmers, M. Budke, J. Braun, M. Weinelt, and M. Donath "Surface electronic structure of fcc Co films: a combined spin-resolved one- and two-photon-photoemission study", J. Phys. D: Appl. Phys. **41**, 164003 (2008).

[86] B. Koopmans, G. Malinowski, F. Dalla Longa, D. Steiauf, M. Fähnle, T. Roth, M. Cinchetti, and M. Aeschlimann "Explaining the paradoxial diversity of ultrafast laser-induced demagnetization", Nature Materials **9**, 259 (2010).

[87] E. Carpene, E. Mancini, C. Dallera, M. Brenna, E. Puppin, and S. D. Silvestri "Dynamics of electron-magnon interaction and ultrafast demagnetization in thin iron films", Phys. Rev. B **78**, 174422 (2008).

[88] A. Weber, F. Pressacco, S. Günther, E. Mancini, P.M. Oppeneer, and C.H. Back "Ultrafast demagnetization dynamics of thin Fe/W(110) films: comparison of time- and spin-resolved photoemission with time-resolved magneto-optic experiments", Phys. Rev. B **84**, 132412 (2011).

[89] T. Roth, A.J. Schellekens, S. Alebrand, O. Schmitt, D. Steil, B. Koopmans, M. Cinchetti, and M. Aeschlimann "Temperature dependence of laser-induced demagnetization in Ni: a key for identifying the underlying mechanism", Phys. Rev. X **2**, 021006 (2012).

[90] M. Wietstruk, A. Melnikov, C. Stamm, T. Kachel, N. Pontius, M. Sultan, C. Gahl, M. Weinelt, H.A. Dürr, and U. Bovensiepen "Hot-electron-driven enhancement of spin-lattice coupling in Gd and Tb 4f ferromagnets observed by femtosecond X-ray magnetic circular dichroism", Phys. Rev. Lett. **106**, 127401 (2011).

[91] G.M. Müller, J. Walowski, M. Djordjevic, G.-X. Miao, A. Gupta, A.V. Ramos, K. Gehrke, V. Moshnyaga, K. Samwer, J. Schmalhorst, A. Thomas, A. Hütten, G. Reiss, J.S. Moodera, and M. Münzenberg "Spin polarization in half-metals probed by femtosecond spin excitation", Nat. Mater. **8**, 56 (2008).

[92] S.I. Anisimov, A.M. Bonch-Bruevich, M.A. El'yashevich, Y.A. Imas, N.A. Pavlenko, and G.S. Romanov "Deistvie moshchnykh svetovykh potokov na metally" Zh. tekhn. fiziki **36**, 1273 (1966) ["Effect of powerful light fluxes on metals", Sov. Phys. Tech. Phys. **11**, 945 (1967)].

[93] S.I. Anisimov, B.L. Kapeliovich, and T.L. Perel'man "Elektronnaya emissiya s poverkhnosti metallov pod deistviem ul'trakorotkikh lazernykh impul'sov" Zh. Eksp. Teor. Fiz. **66**, 776 (1974) ["Electron emission from metal surfaces exposed to ultrashort laser pulses" Sov. Phys. JETP **39**, 375 (1974)].

[94] A. Vaterlaus, T. Beutler, and F. Meier "Spin-lattice relaxation time of ferromagnetic gadolinium determined with time-resolved spin-polarized photoemission", Phys. Rev. Lett. **67**, 3314 (1991).

[95] A.J. Schellekens "Methods for controlling magnetization dynamics on the ultimate timescale", PhD thesis, Eindhoven University of Technology (2014).

[96] K. Carva, M. Battiato, D. Legut, and P.M. Oppeneer "Ab initio theory of electron-phonon mediated ultrafast spin relaxation of laser-excited hot electrons in transition-metal ferromagnets", Phys. Rev. B **87**, 184425 (2013).

[97] G.P. Zhang and W. Hübner "Laser-induced ultrafast demagnetization in ferromagnetic metals", Phys. Rev. Lett. **85**, 3025 (2000).

[98] D. Steiauf and M. Fähnle, "Elliott-Yafet mechanism and the discussion of femtosecond magnetization dynamics", Phys. Rev. B **79**, 140401 (2009).

[99] R.J. Elliott "Theory of the effect of spin-orbit coupling on magnetic resonance in some semiconductors", Phys. Rev. **96**, 266 (1954).

[100] Y.Yafet, in "Solid State Physics", edited by F. Seitz and D. Turnbull, Vol. 14, Academic, New York (1963).

[101] B. Koopmans, J.J.M. Ruigrok, F. Dalla Longa, and W.J.M. de Jonge "Unifying Ultrafast Magnetization Dynamics", Phys. Rev. Lett. **95**, 267207 (2005).

[102] P.D. Desai "Thermodynamic properties of iron and silicon", J. Phys. Chem. Ref. Data **15**, 967 (1986).

[103] L.D. Landau, E.M. Lifshitz "For the theory of the magnetic permittivity dispersion of ferromagnets", M. Nauka (1969).

[104] A.G. Gurevich, G.A. Melkov "Magnetic oscillations and waves", M.:Fizmatlit (1994).

[105] E. Carpene, E. Mancini, D. Dazzi, C. Dallera, E. Puppin, and S. De Silvestri "Ultrafast three-dimensional magnetization precession and magnetic anisotropy of a photoexcited thin film of iron", Phys. Rev. B **81**, 060415 (2010).

[106] A. Melnikov, I. Razdolski, T.O. Wehling, Evangelos Th. Papaioannou, V. Roddatis, P. Fumagalli, O. Aktsipetrow, A.I. Lichtenstein, and U. Bovensiepen "Ultrafast transport of laser-excited spin-polarized carriers in Au/Fe/MgO(001)", Phys. Rev. Lett. **107**, 076601 (2011).

[107] H.A. Mook and R.M. Nicklow "Neutron scattering investigation of the magnetic excitations in iron", Phys. Rev. B **7**, 336 (1973).

[108] J. Prokop, W.X. Tang, Y. Zhang, I. Tudosa, T.R.F. Peixoto, Kh. Zakeri, and J. Kirschner "Magnons in a ferromagnetic monolayer", Phys. Rev. Lett. **102**, 177206 (2009).

[109] Y.R. Shen "The principles of Nonlinear Optics". Wiley-Interscience, John Wiley and Sons, 1st edition, (1984).

[110] M. Faraday "On the magnetization of light and the illumination of magnetic lines of force", Trans. Roy. Soc. (London), no. 5, 592, (1846).

[111] J. Kerr "On the rotation of the plance of polarization by reflection from the pole of a magnet", Phil. Mag. no. 3, 339 (1877).

[112] W. Voigt "Magneto- and electro-optic" (B.G. Teubner, Leipzig, 1908); and ""Handbook der Elekrizitt und des Magnetismums", Vol. IV:2, p. 393 (J.A. Barth, Leipzig, 1915).

[113] P.N. Argyres "Theory of the Faraday and Kerr Effects in Ferromagnetics", Phys. Rev. **97**, 334 (1955).

[114] U. Pustogowa, W. Hübner, and K.H. Bennemann "Theory for the nonlinear magneto-optical Kerr effect at ferromagnetic transition-metal surfaces", Phys. Rev. B **48**, 8607 (1993).

[115] H. Ehrenreich, M.H. Cohen "Self-consistent field approach to the many-electron problem", Phys. Rev. **115**, 786 (1959).

[116] R.P. Pan, H.D. Wei, Y.R. Shen "Optical second harmonic generation from magnetized surfaces", Phys. Rev. B **39**, 1229 (1989).

[117] J. Reif, J.C. Zink, C.-M. Schneider, and J. Kirschner "Effects of surface magnetism on optical second harmonic generation", Phys. Rev. Lett. **67**, 2878 (1991).

[118] A. Kirilyuk, Th. Rasing "Magnetization-induced-second-harmonic generation from surfaces and interfaces", J. Opt. Soc. Am. B **22**, 148 (2005).

[119] N. Bloembergen, P.S. Pershan "Light Waves at the Boundary of Nonlinear Media", Phys. Rev. **128**, 606 (1962).

[120] K.C. Rustagi "Bilinear optical polarizability of silver", Il Nuovo Cimento LIII, 346 (1968).

[121] T.F. Heinz, C.K. Chen, D. Ricard, and Y.R. Shen "Spectroscopy of molecular monolayers by resonant second-harmonic generation", Phys. Rev. Lett. **48**, 478 (1982).

[122] G. Traeger, L. Wenzel, A. Hubert "Computer experiments on the information and the figure of merit and magnetooptics", Phys. Stat. Sol. **131**, 201 (1992).

[123] B.A. Ruzicka, L.K. Werake, G. Xu, J.B. Khurgin, E.Ya. Sherman, J.Z. Wu, and H. Zhao "Second-harmonic generation induced by electric currents in GaAs", Phys. Rev. Lett. **108**, 077403 (2012).

[124] L.K. Werake and H. Zhao "Observation of second-harminc generation induced by pure spin currents", Nat. Phys. **6**, 875 (2010).

[125] A.Y. Bykov, T.V. Murzina, M.G. Rybin, and E.D. Obraztsova "Second harmonic generation in multilayer graphene induced by direct electric current", Phys. Rev. B **85**, 121413 (2012).

[126] C. Hirlimann. "Femtosecond Laser Pulses: Principles and Experiments", Springer (1998).

[127] Operator's Manual Mantis Modelocked Titanium:Sapphire Laser System. Coherent.

[128] J.-C. Diels, W. Rudolph "Ultrashort Laser Pulse Phenomena: Fundamentals, Techniques, and Applications on a Femtosecond Time Scale", Elsevier (2006).

[129] Cavity Dumper Pulse Switch Manual. Angewandte Physik&Elektronik GmbH.

[130] A. Glaubitz 'Laser-induced femtosecond spin dynamics in metallic multilayers', Diploma thesis at the Free University of Berlin (2010).

[131] T.Mühge, A. Stierle, N. Metoki, H. Zabel, U.Pietsch "Structural properties of high-quality sputtered Fe films on $Al_2O_3(11\bar{2}0)$ and MgO(001) substrates", Appl. Phys. A **59**, 659 (1994).

[132] D.T. Dekadjevi, P.A. Ryan, and B.J. Hickey "Experimental evidence for electron channeling in Fe/Au(100) Superlattices", Phys. Rev. Lett. **86**, 5787 (2001).

[133] Hans Lüth, "Surfaces and Interfaces of Solid Materials", Springer-Verlag, Berlin, (1995).

[134] E. Carpene, H. Hedayat, F. Boschini, and C. Dallera "Ultrafast demagnetization of metals: collapsed exchange versus collective excitations", Phys. Rev. B **91**, 174414 (2015).

[135] R.M. Costescu, M.A. Wall, and D.G. Gahill "Thermal conductance of epitaxial interfaces", Phys. Rev. B **67**, 054302 (2003).

[136] A.Goris, K.M. Döbrich, I. Panzer, A.B. Schmidt, M.Donath, and M. Weinelt "Role of spin-flip exchange scattering for hot-electron lifetimes in cobalt", Phys. Rev. Lett. **107**, 026601 (2011).

[137] F. Körmann, A. Dick, B. Grabowski, B. Hallstedt, T. Hickel, and J. Neugebauer "Free energy of bcc iron: Integrated ab initio derivation of vibrational, electronic and magnetic contributions", Phys. Rev. B **78**, 033102 (2008).

[138] M. Djordjevic, M. Lüttich, P. Moschkau, P. Guderian, T. Kampfrath, R.G. Ulbrich, M. Münzenberg, W. Felsch, and J.S. Moodera "Comprehensive view on ultrafast dynamics of ferromagnetic films", Phys. Stat. Sol. **3**, 1347 (2006).

[139] Z. Lin, L.V. Zhigilei, and V. Celli "Electron-phonon coupling and electron heat capacity of metals under conditions of strong electron-phonon nonequilibrium", Phys. Rev. B 77, 075133 (2008). http://www.faculty.virginia.edu/CompMat/electron-phonon-coupling/

[140] R.E. Stephens and I.H. Malitson "Index of Refraction of Magnesium Oxide", Journal of Research of the National Bureau of Standards, Vol. **49**, No. 4, 249-252 (1952).

[141] G.S. Krinchik and V.A. Artem'ev "Magneto-optical properties of Ni, Co, and Fe in the ultraviolet, visible, and infrared parts of the spectrum", Sov. Phys. JETP, Vol. **26**, No. 6, 1080-1085 (1968).

[142] D. Rudolf, C. La-O-Vorakiat, M. Battiato, R. Adam, J.M. Shaw, E. Turgut, P. Maldonado, S. Mathias, P. Grychtol, H.T. Nembach, T.J. Silva, M. Aeschlimann, H.C. Kapteyn, M.M. Murnane, C.M. Schneider, and P.M. Oppeneer "Ultrafast magnetization enhancement in metallic multilayers driven by superdiffusive spin current", Nature Commun. **3**, 1037 (2012).

[143] S. Kaltenborn, Yao-Hui Zhu, and Hans Christian Schneider "Wave-diffusion theory of spin transport in metals after ultrashort-pulse excitation", Phys. Rev. B **85**, 235101 (2012).

[144] B.Y. Mueller, A. Baral, S. Vollmar, M. Cinchetti, M. Aeschlimann, H.C. Schneider, and B. Rethfeld "Feedback Effect during Ultrafast Demagnetization Dynamics in Ferromagnets", Phys. Rev. Lett. **111**, 167204 (2013).

[145] P. Blaha, K. Schwarz, G. Madsen, D. Kvasnicka, J. Luitz "WIEN2K, An Augmented Plane Wave + Local Orbitals Program for Calculating Crystal Properties", Vienna University of Technology, Austria (2001).

[146] J.P. Perdew, K. Burke, and M. Ernzerhof "Generalized gradient approximation made simple", Phys. Rev. Lett. **77**, 3865 (1996).

[147] J.M. Soler, E. Artacho, J.D. Gale, A. Garcia, J. Junquera, P. Ordejón, and D. Sánchez-Portal "The SIESTA method for ab initio order-N materials simulation", J. Phys.: Condens. Matter **14**, 2745 (2002).

[148] A.R. Rocha, V.M. Garcia-Suárez, S. Bailey, C. Lambert, J. Ferrer, and S. Sanvito "Spin and molecular electronics in atomically generated orbital landscapes", Phys. Rev. B **73**, 085414 (2006).

[149] CRONOS project report "D5.6.1 Determination of ultrafast magnetization dynamics in MgO/Fe/Au" (2013). www.cronostheory.eu

[150] F.X. Wang, F.J. Rodríguez, W.M. Albers, R. Ahorinta, J.S. Sipe, and M. Kauranen "Surface and bulk contributions to the second-order nonlinear optical response of a gold film", Phys. Rev. B **80**, 233402 (2009).

[151] A. Borisov, D. Sanchez-Portal, R. Diez Muino, P.M. Echenique "Building up the screening below the femtosecond scale", Chem. Phys. Lett. **387**, 95-100 (2004).

[152] K. Uchida, S. Takahaschi, K. Harii, J. Ieda, W. Koshibae, K. Ando, S. Maekawa, and E. Saitoh "Observation of the spin Seebeck effect", Nat. Letters **455**, 778 (2008).

[153] J.M. Florczak and E.D. Dahlberg "Magnetization reversal in (100)Fe thin films", Phys. Rev. B **44**, 9338 (1991).

[154] G.-M. Choi, C.-H. Moon, B.-C. Min, K.-J. Lee, and D.G. Cahill "Thermal spin-transfer torque driven by the spin-dependent Seebeck effect in metallic spin-valves", Nat. Phys. **11**, 576 (2015).

[155] J.C. McGroddy, A.J. McAlister, and E.A. Stern "Polar reflection Faraday effect in silver and gold", Phys. Rev. **139**, A 1844 (1965).

Selbstständigkeitserklärung gemäß §7 der Promotionsordnung

Sämtliche verwendeten Hilfsmittel, Hilfen und Quellen sind an der entsprechenden Stelle angegeben. Ich versichere, dass ich auf dieser Grundlage diese Arbeit selbstständig verfasst habe. Diese Arbeit wurde bisher weder in gleicher noch ähnlicher Form einer anderen Prüfungskomission vorgelegt order veröffentlicht.

Berlin, den

Alexandr Alekhin